

EFFECTS OF SHOCK STRENGTH, CONFINEMENT, AND  
GEOMETRIC PERTURBATIONS ON SHOCK BOUNDARY  
LAYER INTERACTIONS

A DISSERTATION  
SUBMITTED TO THE DEPARTMENT OF MECHANICAL  
ENGINEERING  
AND THE COMMITTEE ON GRADUATE STUDIES  
OF STANFORD UNIVERSITY  
IN PARTIAL FULFILLMENT OF THE REQUIREMENTS  
FOR THE DEGREE OF  
DOCTOR OF PHILOSOPHY

Laura M. Campo

July 2014

© Copyright by Laura M. Campo 2014

All Rights Reserved

I certify that I have read this dissertation and that, in my opinion, it is fully adequate in scope and quality as a dissertation for the degree of Doctor of Philosophy.

**John Eaton, Primary Adviser**

I certify that I have read this dissertation and that, in my opinion, it is fully adequate in scope and quality as a dissertation for the degree of Doctor of Philosophy.

**Mark Cappelli**

I certify that I have read this dissertation and that, in my opinion, it is fully adequate in scope and quality as a dissertation for the degree of Doctor of Philosophy.

**Gianluca Iaccarino**

Approved for the Stanford University Committee on Graduate Studies.

**Patricia J. Gumpert, Vice Provost for Graduate Education**

*This signature page was generated electronically upon submission of this dissertation in electronic format. An original signed hard copy of the signature page is on file in University Archives.*



# Abstract

The effects of confinement, shock strength, and inflow perturbations on shock boundary layer interaction (SBLI) flows in low aspect ratio ducts are studied using particle image velocimetry (PIV). The wind tunnel is operated continuously with a steady  $M_\infty = 2.05$  inflow, and the oblique shock is generated by a fully spanning  $20^\circ$  compression ramp on the top wall of the test section. The flow is documented for two ramp heights,  $h_{\text{ramp}} = 3\text{mm}$  and  $5\text{mm}$  ( $h_{\text{ramp}}/\delta_0 = 0.56$  and  $0.93$ ), using streamwise-vertical measurement planes at four locations across the span. The measurement domain includes two SBLIs – one at the foot of the compression ramp where the shock wave is generated and another at the first reflection of the shock from the opposite wall.

The flow fields for the two geometries show significant qualitative and quantitative differences. The  $h_{\text{ramp}}/\delta_0 = 0.56$  flowfield includes a regular reflection of the incident shock wave, whereas the larger ramp case involves a Mach reflection with a subsonic wake downstream of the Mach stem in the core of the duct. The  $h_{\text{ramp}}/\delta_0 = 0.93$  case also has larger regions of mean flow reversal in both SBLI regions and a greater degree of three-dimensionality and confinement due to thickening of the side wall boundary layers. In both cases, the separation of the top and bottom wall boundary layers is most severe close to the spanwise centerline. The blockage due to mean flow reversal in the center region forces higher momentum fluid to divert upward and toward the side walls, mitigating the boundary layer thickening in off-center locations.

In the  $h_{\text{ramp}}/\delta_0 = 0.93$  incident shock interaction, the maximum streamwise velocity fluctuations,  $u'$ , occur at the same locations where the mean streamwise velocity profiles exhibit inflection points. Despite the compressible and 3D nature of this SBLI flow, this is the same behavior as in a subsonic mixing layer or reattaching boundary layer flow. The shock features in both test cases show a low degree of unsteadiness compared to previous studies reported in the literature, as characterized by the shock excursion length relative to the incoming boundary layer height,  $L_{\text{ex}}/\delta_0$ .

An uncertainty quantification (UQ) experiment is carried out using the  $h_{\text{ramp}} = 1.1\text{mm}$  ( $h_{\text{ramp}}/\delta_0 = 0.20$ ) geometry of Helmer (2011). Small, steady, well-characterized bumps of varying sizes ( $h_{\text{bump}} = 0.1$  to  $0.9\text{mm}$ ) and locations ( $x_{\text{bump}} \in [-80, -40]\text{mm}$ ) are set in the wall surface. The flow is very sensitive to perturbations in the range  $x_{\text{bump}} \in [-69, -48]\text{mm}$ , and insensitive to perturbations outside this area. The most notable effect caused by the perturbations in the sensitive region is their tendency to force the whole SBLI to shift upstream. The shift in the shock crossing point,  $\Delta x_{\text{scp}}$ , strongly depends on both the position and size of the perturbations. A quantitative integral metric describing the differences between the perturbed and unperturbed velocity fields is greatly reduced when the shock features are aligned, indicating that the main discrepancies between perturbed and unperturbed cases arise as a result of a global shift in position of the SBLI as opposed to local changes within the interaction.

A framework for quantitative comparisons between PIV data and CFD results for high speed compressible flows is developed. Bias errors inherent in PIV measurements, including particle inertia, interrogation region size, and particle travel between image exposures, are modeled and propagated through a CFD-generated flow field. The modified CFD result, which accounts for PIV biases, can then be directly compared to the PIV data. The biases are most significant in the immediate vicinity of shock waves where the convective acceleration terms are very large, but can be large elsewhere if too large seeding particles are used.

# Acknowledgement

I would like to acknowledge the generous funding I received from the NSF Graduate Research Fellowship and the Gabilan Stanford Graduate Fellowship. These fellowships gave me great flexibility in defining the direction and scope of my Ph.D. work. My research project was also supported by the Predictive Sciences Academic Alliance Program of the U.S. Department of Energy.

Special thanks are due to my collaborators David Helmer and Ivan Bermejo-Moreno. David was my mentor when I first joined the Eaton lab. Throughout my first year he taught me a lot about experimental fluid mechanics and helped me to get started on my own Ph.D. project. Ivan provided RANS and LES simulations to complement the experiments I performed. Together we came up with ideas for new experimental tests, and this close collaboration inspired my interest in validation and bridging the gap between experiments and simulations.

Many thanks to Chris Elkins and Lester Su for giving me helpful advice on setting up and troubleshooting my experiments. I am grateful for all of Lakhbir Johal's hard work in machining all of the many intricate pieces for my supersonic wind tunnel. Thanks very much to Rika Bosmans, Marlene Lomuljo-Bautista, and Rosa Fernandez for providing administrative support that kept the lab running smoothly.

I gratefully acknowledge all of the help and support I received from past and present students in the Eaton lab. In particular, thank you to Kevin Ryan for helping me with all manner of electronics and computer issues, to Emily Sayles for sharing

her PIV expertise, and to Julia Ling and Sayuri Yapa for their insights and helpful comments at lab meetings.

I am extremely thankful to have had the opportunity to do my Ph.D. under the supervision of Professor John Eaton. He taught me how to think critically and practically about fluid mechanics and heat transfer problems, and helped me build confidence in my abilities as an engineer and as a researcher. John's dedication to his students is remarkable, and I am truly grateful to have had his unwavering support throughout my time at Stanford.

To my friends and family – thank you for your support and love over the past several years. Thank you for listening, for always encouraging me to do my best, for helping me get through stressful times, and for sharing lots of fun and exciting adventures with me.

# Contents

<b>Abstract</b>	<b>v</b>
<b>Acknowledgement</b>	<b>vii</b>
<b>1 Introduction</b>	<b>1</b>
1.1 Motivation . . . . .	1
1.2 Background . . . . .	4
1.2.1 Physical description . . . . .	4
1.2.2 Literature review . . . . .	10
1.3 Objectives of present work . . . . .	19
<b>2 Experimental Setup</b>	<b>23</b>
2.1 Facility overview . . . . .	23
2.2 Test section details . . . . .	24
2.3 PIV measurements . . . . .	29
2.3.1 Measurement domain & data acquisition . . . . .	29
2.3.2 Flow seeding . . . . .	32
2.3.3 PIV data processing . . . . .	36
2.4 Uncertainty analysis . . . . .	42
2.4.1 Peak-locking . . . . .	43

2.4.2	Sampling	45
2.4.3	Alignment	46
<b>3</b>	<b>Effects of Confinement &amp; Shock Strength</b>	<b>49</b>
3.1	Inflow & boundary conditions	49
3.2	Overview of shock & interaction features	55
3.3	Mean velocity	58
3.3.1	Compression ramp SBLI region	68
3.3.2	Incident SBLI region	72
3.4	Turbulence quantities	74
3.5	Spatial scales of the interactions	94
<b>4</b>	<b>Effects of Geometric Perturbations</b>	<b>101</b>
4.1	Experimental setup	101
4.2	Perturbation device design	102
4.3	Characterization of perturbations	105
4.4	Qualitative comparisons	108
4.5	Quantitative comparisons	131
4.5.1	Velocity profile comparisons	131
4.5.2	Integral difference metric	135
4.5.3	Scalar quantity of interest	141
4.6	Utility for CFD validation	146
<b>5</b>	<b>PIV Measurement Biases in SBLI Flows</b>	<b>149</b>
5.1	Methodology	149
5.2	Particle inertia	151
5.2.1	Numerical setup	151
5.2.2	Simulation results using $\tau_p = 1\mu s$	156

5.2.3	Simulation results using $\tau_p = 0.25\mu s$ and $\tau_p = 4\mu s$	163
5.3	PIV measurement resolution	171
5.3.1	Interrogation region size and overlap	171
5.3.2	Particle travel between image exposures	172
5.4	Results	176
5.4.1	Simulations of PIV bias error magnitudes	176
5.4.2	Comparisons to PIV data	183
<b>6</b>	<b>Conclusions</b>	<b>193</b>
6.1	Effects of shock strength & confinement	193
6.2	Effects of geometric perturbations	197
6.3	PIV measurement biases for SBLI flows	198
6.4	Recommendations for future work	200
<b>A</b>	<b>Characterization &amp; Modeling of Perturbation Shapes</b>	<b>203</b>
A.1	Confocal microscopy	203
A.2	Polynomial & Gaussian fits for single bumps	205
A.3	Modeling a spanwise row of 5 bumps	206
<b>B</b>	<b>Experimental database</b>	<b>209</b>



# List of Tables

2.1	Summary of PIV parameters.	39
2.2	Uncertainty on mean velocities due to finite sampling	46
2.3	Uncertainty on turbulence statistics due to finite sampling	46
3.1	Experimental operating conditions	50
3.2	Characterization of incoming boundary layer	50
3.3	Summary of shock angles	58
3.4	Shock excursion length, $L_{\text{ex}}$	98
4.1	$\Delta x_{\text{scp}}$ for cases with perturbations at $x_{\text{bump}} = -57.2\text{mm}$	116
4.2	$\Delta x_{\text{scp}}$ for cases with perturbations at $x_{\text{bump}} = -75.2\text{mm}$	122
4.3	Coefficients for equation 4.7.	144
4.4	Summary of UQ experiment results	144
5.1	Parameters used to filter CFD data to simulate PIV biases	177
A.1	Coefficients for 5th order polynomial fits to single bump profiles	205
A.2	Parameters for Gaussian fits to single bump profiles	206
A.3	Parameters for defining piecewise fit to 5-bump profile shape	208



# List of Figures

1.1	Canonical geometries for SBLI flows . . . . .	5
1.2	Schematic of a compression ramp SBLI . . . . .	6
1.3	Schematic of a compression-expansion ramp SBLI . . . . .	7
1.4	Schematic of an incident/reflecting SBLI with regular reflection . . .	9
1.5	Schematic of an incident/reflecting SBLI with Mach reflection . . .	9
2.1	Overview of wind tunnel test facility and PIV setup . . . . .	25
2.2	Test section, including upstream nozzles . . . . .	26
2.3	Sample PIV images with and without oil streaking . . . . .	27
2.4	Exploded view of side wall oil removal device. . . . .	28
2.5	Location of PIV measurement planes. . . . .	30
2.6	Approximate profile of laser sheet intensity . . . . .	31
2.7	Experimental evaluation of particle time constant . . . . .	35
2.8	Histograms of peak-locked and non-peak-locked data . . . . .	40
2.9	Sample 2D PIV correlation peak . . . . .	41
2.10	Sub-pixel estimation using Gaussian fits . . . . .	42
2.11	Illustration of peak-locking error analysis for $v'$ . . . . .	44
3.1	Boundary layer profiles of undisturbed inlet flow . . . . .	51
3.2	Schematic of SBLI features near the centerplane for $h_{\text{ramp}}/\delta_0 = 0.56$ .	56
3.3	Schematic of SBLI features near the centerplane for $h_{\text{ramp}}/\delta_0 = 0.93$ .	57

3.4	Mean streamwise velocity for $h_{\text{ramp}}/\delta_0 = 0.56$ at $z/\delta_0 = 3.89$	60
3.5	Mean streamwise velocity for $h_{\text{ramp}}/\delta_0 = 0.56$ at $z/\delta_0 = 1.02$	60
3.6	Mean streamwise velocity for $h_{\text{ramp}}/\delta_0 = 0.56$ at $z/\delta_0 = 0.74$	61
3.7	Mean streamwise velocity for $h_{\text{ramp}}/\delta_0 = 0.56$ at $z/\delta_0 = 0.46$	61
3.8	Mean streamwise velocity for $h_{\text{ramp}}/\delta_0 = 0.93$ at $z/\delta_0 = 3.89$	62
3.9	Mean streamwise velocity for $h_{\text{ramp}}/\delta_0 = 0.93$ at $z/\delta_0 = 1.48$	62
3.10	Mean streamwise velocity for $h_{\text{ramp}}/\delta_0 = 0.93$ at $z/\delta_0 = 1.02$	63
3.11	Mean streamwise velocity for $h_{\text{ramp}}/\delta_0 = 0.93$ at $z/\delta_0 = 0.74$	63
3.12	Mean vertical velocity for $h_{\text{ramp}}/\delta_0 = 0.56$ at $z/\delta_0 = 3.89$	64
3.13	Mean vertical velocity for $h_{\text{ramp}}/\delta_0 = 0.56$ at $z/\delta_0 = 1.02$	64
3.14	Mean vertical velocity for $h_{\text{ramp}}/\delta_0 = 0.56$ at $z/\delta_0 = 0.74$	65
3.15	Mean vertical velocity for $h_{\text{ramp}}/\delta_0 = 0.56$ at $z/\delta_0 = 0.46$	65
3.16	Mean vertical velocity for $h_{\text{ramp}}/\delta_0 = 0.93$ at $z/\delta_0 = 3.89$	66
3.17	Mean vertical velocity for $h_{\text{ramp}}/\delta_0 = 0.93$ at $z/\delta_0 = 1.48$	66
3.18	Mean vertical velocity for $h_{\text{ramp}}/\delta_0 = 0.93$ at $z/\delta_0 = 1.02$	67
3.19	Mean vertical velocity for $h_{\text{ramp}}/\delta_0 = 0.93$ at $z/\delta_0 = 0.74$	67
3.20	Mean streamwise velocity profiles on top wall downstream of ramp	70
3.21	Mean vertical velocity profiles on top wall downstream of ramp	71
3.22	Streamwise velocity fluctuations for $h_{\text{ramp}}/\delta_0 = 0.56$ at $z/\delta_0 = 3.89$	75
3.23	Streamwise velocity fluctuations for $h_{\text{ramp}}/\delta_0 = 0.56$ at $z/\delta_0 = 1.02$	75
3.24	Streamwise velocity fluctuations for $h_{\text{ramp}}/\delta_0 = 0.56$ at $z/\delta_0 = 0.74$	76
3.25	Streamwise velocity fluctuations for $h_{\text{ramp}}/\delta_0 = 0.56$ at $z/\delta_0 = 0.46$	76
3.26	Streamwise velocity fluctuations for $h_{\text{ramp}}/\delta_0 = 0.93$ at $z/\delta_0 = 3.89$	77
3.27	Streamwise velocity fluctuations for $h_{\text{ramp}}/\delta_0 = 0.93$ at $z/\delta_0 = 1.48$	77
3.28	Streamwise velocity fluctuations for $h_{\text{ramp}}/\delta_0 = 0.93$ at $z/\delta_0 = 1.02$	78
3.29	Streamwise velocity fluctuations for $h_{\text{ramp}}/\delta_0 = 0.93$ at $z/\delta_0 = 0.74$	78
3.30	Vertical velocity fluctuations for $h_{\text{ramp}}/\delta_0 = 0.56$ at $z/\delta_0 = 3.89$	79

3.31	Vertical velocity fluctuations for $h_{\text{ramp}}/\delta_0 = 0.56$ at $z/\delta_0 = 1.02$ . . . . .	79
3.32	Vertical velocity fluctuations for $h_{\text{ramp}}/\delta_0 = 0.56$ at $z/\delta_0 = 0.74$ . . . . .	80
3.33	Vertical velocity fluctuations for $h_{\text{ramp}}/\delta_0 = 0.56$ at $z/\delta_0 = 0.46$ . . . . .	80
3.34	Vertical velocity fluctuations for $h_{\text{ramp}}/\delta_0 = 0.93$ at $z/\delta_0 = 3.89$ . . . . .	81
3.35	Vertical velocity fluctuations for $h_{\text{ramp}}/\delta_0 = 0.93$ at $z/\delta_0 = 1.48$ . . . . .	81
3.36	Vertical velocity fluctuations for $h_{\text{ramp}}/\delta_0 = 0.93$ at $z/\delta_0 = 1.02$ . . . . .	82
3.37	Vertical velocity fluctuations for $h_{\text{ramp}}/\delta_0 = 0.93$ at $z/\delta_0 = 0.74$ . . . . .	82
3.38	Reynolds shear stress for $h_{\text{ramp}}/\delta_0 = 0.56$ at $z/\delta_0 = 3.89$ . . . . .	83
3.39	Reynolds shear stress for $h_{\text{ramp}}/\delta_0 = 0.56$ at $z/\delta_0 = 1.48$ . . . . .	83
3.40	Reynolds shear stress for $h_{\text{ramp}}/\delta_0 = 0.56$ at $z/\delta_0 = 1.02$ . . . . .	84
3.41	Reynolds shear stress for $h_{\text{ramp}}/\delta_0 = 0.56$ at $z/\delta_0 = 0.74$ . . . . .	84
3.42	Reynolds shear stress for $h_{\text{ramp}}/\delta_0 = 0.93$ at $z/\delta_0 = 3.89$ . . . . .	85
3.43	Reynolds shear stress for $h_{\text{ramp}}/\delta_0 = 0.93$ at $z/\delta_0 = 1.48$ . . . . .	85
3.44	Reynolds shear stress for $h_{\text{ramp}}/\delta_0 = 0.93$ at $z/\delta_0 = 1.02$ . . . . .	86
3.45	Reynolds shear stress for $h_{\text{ramp}}/\delta_0 = 0.93$ at $z/\delta_0 = 0.74$ . . . . .	86
3.46	Profiles of mean streamwise velocity along incident SBLI . . . . .	90
3.47	Profiles of streamwise velocity fluctuations along incident SBLI . . . . .	90
3.48	Loci of $\max(u')$ and velocity profile inflection points . . . . .	92
3.49	Profiles of $\langle u'v' \rangle$ and $\partial U / \partial y$ in incident SBLI . . . . .	94
3.50	Illustration of method for determining $L_{\text{ex}}$ . . . . .	97
4.1	Detailed view of perturbation device in bottom wall . . . . .	104
4.2	Overview of UQ experiment geometry and flow features . . . . .	104
4.3	Perturbation height vs. number of screw turns . . . . .	106
4.4	Profiles of axisymmetric single-bump perturbations of 5 heights . . .	107
4.5	Perturbation surface profile for five-bump spanwise configurations . .	108
4.6	Mean streamwise velocity for perturbations at $x_{\text{bump}} = -57.2\text{mm}$ . .	110

4.7	Mean vertical velocity for perturbations at $x_{\text{bump}} = -57.2\text{mm}$	111
4.8	$\Delta U$ for perturbations at $x_{\text{bump}} = -57.2\text{mm}$	113
4.9	$\Delta V$ for perturbations at $x_{\text{bump}} = -57.2\text{mm}$	114
4.10	$\Delta U$ ( $x_{\text{scp}}$ aligned) for perturbations at $x_{\text{bump}} = -57.2\text{mm}$	117
4.11	$\Delta V$ ( $x_{\text{scp}}$ aligned) for perturbations at $x_{\text{bump}} = -57.2\text{mm}$	118
4.12	$\Delta U$ ( $x_{\text{scp}}$ and $y_{\text{scp}}$ aligned) for perturbations at $x_{\text{bump}} = -57.2\text{mm}$	120
4.13	$\Delta V$ ( $x_{\text{scp}}$ and $y_{\text{scp}}$ aligned) for perturbations at $x_{\text{bump}} = -57.2\text{mm}$	121
4.14	Mean streamwise velocity for perturbations at $x_{\text{bump}} = -75.2\text{mm}$	123
4.15	Mean vertical velocity for perturbations at $x_{\text{bump}} = -75.2\text{mm}$	124
4.16	$\Delta U$ for perturbations at $x_{\text{bump}} = -75.2\text{mm}$	125
4.17	$\Delta V$ for perturbations at $x_{\text{bump}} = -75.2\text{mm}$	126
4.18	$\Delta U$ ( $x_{\text{scp}}$ aligned) for perturbations at $x_{\text{bump}} = -75.2\text{mm}$	127
4.19	$\Delta V$ ( $x_{\text{scp}}$ aligned) for perturbations at $x_{\text{bump}} = -75.2\text{mm}$	128
4.20	$\Delta U$ ( $x_{\text{scp}}$ and $y_{\text{scp}}$ aligned) for perturbations at $x_{\text{bump}} = -75.2\text{mm}$	129
4.21	$\Delta V$ ( $x_{\text{scp}}$ and $y_{\text{scp}}$ aligned) for perturbations at $x_{\text{bump}} = -75.2\text{mm}$	130
4.22	$U$ profiles showing range of variability for all perturbed cases	132
4.23	$\Delta U$ profiles showing range of variability for all perturbed cases	133
4.24	$V$ profiles showing range of variability for all perturbed cases	134
4.25	$\Delta V$ profiles showing range of variability for all perturbed cases	134
4.26	Region of interest over which $\Lambda$ is computed	137
4.27	Correlation between $\Lambda$ and $\Delta x_{\text{scp}}$	138
4.28	Correlation between $\Delta y_{\text{scp}}$ and $\Delta x_{\text{scp}}$	140
4.29	Results of shock crossing point location algorithm	142
4.30	$\Delta x_{\text{scp}}$ plotted against $x_{\text{bump}}$ for various values of $h_{\text{bump}}$	143
4.31	2D polynomial fit to $\Delta x_{\text{scp}}$ data as a function of $(x_{\text{bump}}, h_{\text{bump}})$	143
5.1	Illustration of force balance on a particle	153

5.2	Streamlines and particle paths in incident SBLI for $h_{\text{ramp}}/\delta_0 = 0.56$	157
5.3	$U_p - U_f$ for $h_{\text{ramp}}/\delta_0 = 0.56$ using $\tau_p = 1\mu\text{s}$	158
5.4	$V_p - V_f$ for $h_{\text{ramp}}/\delta_0 = 0.56$ using $\tau_p = 1\mu\text{s}$	158
5.5	$U_p - U_f$ for $h_{\text{ramp}}/\delta_0 = 0.93$ using $\tau_p = 1\mu\text{s}$	160
5.6	$V_p - V_f$ for $h_{\text{ramp}}/\delta_0 = 0.93$ using $\tau_p = 1\mu\text{s}$	160
5.7	Convective acceleration terms for the $h_{\text{ramp}}/\delta_0 = 0.56$ case	161
5.8	Convective acceleration terms for the $h_{\text{ramp}}/\delta_0 = 0.93$ case	161
5.9	Particle velocity biases & convective accel. terms, $h_{\text{ramp}}/\delta_0 = 0.56$	162
5.10	Particle velocity biases & convective accel. terms, $h_{\text{ramp}}/\delta_0 = 0.93$	162
5.11	$U_p - U_f$ for $h_{\text{ramp}}/\delta_0 = 0.56$ using $\tau_p = 4\mu\text{s}$	164
5.12	$V_p - V_f$ for $h_{\text{ramp}}/\delta_0 = 0.56$ using $\tau_p = 4\mu\text{s}$	164
5.13	$U_p - U_f$ for $h_{\text{ramp}}/\delta_0 = 0.93$ using $\tau_p = 4\mu\text{s}$	165
5.14	$V_p - V_f$ for $h_{\text{ramp}}/\delta_0 = 0.93$ using $\tau_p = 4\mu\text{s}$	165
5.15	$U_p - U_f$ for $h_{\text{ramp}}/\delta_0 = 0.56$ using $\tau_p = 0.25\mu\text{s}$	167
5.16	$V_p - V_f$ for $h_{\text{ramp}}/\delta_0 = 0.56$ using $\tau_p = 0.25\mu\text{s}$	167
5.17	$U_p - U_f$ for $h_{\text{ramp}}/\delta_0 = 0.93$ using $\tau_p = 0.25\mu\text{s}$	168
5.18	$V_p - V_f$ for $h_{\text{ramp}}/\delta_0 = 0.93$ using $\tau_p = 0.25\mu\text{s}$	168
5.19	Mean velocity at constant $y$ for different values of $\tau_p$	170
5.20	PIV vector grid overlaid on CFD mesh	172
5.21	PIV velocity calculation for large & small particle displacements	173
5.22	PIV particle trajectories overlaid on CFD mesh	175
5.23	Mean streamwise velocity surface plots from unmodified CFD	177
5.24	Velocity profiles with simulated PIV biases, $h_{\text{ramp}}/\delta_0 = 0.93$	179
5.25	Velocity profiles with simulated PIV biases, $h_{\text{ramp}}/\delta_0 = 0.56$	182
5.26	PIV vs. CFD velocity surface plot comparison, $h_{\text{ramp}}/\delta_0 = 0.56$	184
5.27	PIV vs. CFD velocity profile comparisons, $h_{\text{ramp}}/\delta_0 = 0.56$	186
5.28	PIV vs. CFD velocity surface plot comparison, $h_{\text{ramp}}/\delta_0 = 0.93$	188

5.29 PIV vs. CFD velocity profile comparisons, $h_{\text{ramp}}/\delta_0 = 0.93$ . . . . .	189
A.1 Sample raw images from confocal microscopy of perturbation surface	204
A.2 Surface reconstruction from confocal microscopy data . . . . .	204

# List of Acronyms & Symbols

CFD	computational fluid dynamics
DNS	direct numerical simulation
LES	large eddy simulation
PIV	particle image velocimetry
RANS	Reynolds-averaged Navier Stokes
RK4	4th order Runge Kutta numerical integration scheme
SBLI	shock boundary layer interaction
UQ	uncertainty quantification
$d_p$	particle physical diameter [ $\mu\text{m}$ ]
$d_{pix}$	camera pixel physical size [ $\mu\text{m}$ ]
$d_\tau$	particle image diameter [ $\mu\text{m}$ ]
$F_D$	particle drag force [N]
$h_{\text{ramp}}$	height of shock-generating ramp [mm]
$h_{\text{bump}}$	peak height of a geometric perturbation [mm]
$h$	RK4 integration time step [s]
$L_{\text{ex}}$	shock excursion length [mm]
$L_{\text{int}}$	interaction length [mm]
$\dot{m}$	mass flow rate [kg/s]

$M_\infty$	incoming freestream Mach number
$M_o$	image magnification
$m_p$	particle mass [kg]
$N$	number of valid vectors
$n$	number of particle paths started inside an interrogation region
$P_0$	stagnation pressure [kPa]
$R$	correlation coefficient
$Re$	Reynolds number
$Re_p$	particle Reynolds number
$St_p$	particle Stokes number, $\tau_p/t^*$
$t$	time [s]
$\Delta t$	time delay between laser pulses [ns]
$T_\infty$	incoming freestream static temperature [K]
$T_0$	stagnation temperature [K]
$t^*$	incoming boundary layer time scale, $\delta_0/U_\infty$ [s]
$U$	streamwise mean velocity [m/s]
$U_\infty$	incoming freestream streamwise mean velocity [m/s]
$U_p^*$	normalized particle velocity normal to shock wave [m/s]
$U_\tau$	incoming friction velocity [m/s]
$\mathbf{U}_f$	fluid velocity vector [m/s]
$\mathbf{U}_p$	particle velocity vector [m/s]
$u'$	RMS of streamwise velocity fluctuations [m/s]
$\langle u'v' \rangle$	Reynolds shear stress [ $\text{m}^2/\text{s}^2$ ]
$V$	vertical mean velocity [m/s]
$v'$	RMS of vertical velocity fluctuations [m/s]
$W$	spanwise mean velocity [m/s]
$x$	streamwise coordinate, origin at foot of ramp [mm]

$\Delta x$	streamwise displacement between image pairs [pixels]
$x_0$	projected impingement of separation shock on bottom wall [mm]
$x^*$	non-dimensional streamwise position in incident SBLI, $(x - x_0)/L_{\text{int}}$
$x_\perp$	shock-normal coordinate [mm]
$x_{\text{rampend}}$	streamwise location of the end of the compression ramp [mm]
$x_{\text{bump}}$	streamwise location of a geometric perturbation [mm]
$x_{\text{scp}}$	streamwise location of shock crossing point [mm]
$x_{\text{scp,unperturbed}}$	streamwise location of shock crossing point in unperturbed case [mm]
$\Delta x_{\text{scp}}$	$x_{\text{scp}} - x_{\text{scp,unperturbed}}$ [mm]
$x_{IR}$	streamwise location of center of interrogation region [mm]
$\Delta x_{IR}$	half-width of interrogation region [mm]
$y$	vertical coordinate, origin on bottom wall [mm]
$\Delta y$	vertical displacement between image pairs [pixels]
$y_{\text{scp}}$	vertical location of shock crossing point [mm]
$y_{\text{scp,unperturbed}}$	vertical location of shock crossing point in unperturbed case [mm]
$\Delta y_{\text{scp}}$	$y_{\text{scp}} - y_{\text{scp,unperturbed}}$ [mm]
$y_{\text{topwall}}$	vertical location of the tunnel top wall [mm]
$y_{IR}$	vertical location of center of interrogation region [mm]
$\Delta y_{IR}$	half-height of interrogation region [mm]
$z$	spanwise coordinate, origin on back wall [mm]
$\delta_0$	incoming boundary layer thickness [mm]
$\Lambda$	integral difference parameter for comparing velocity fields [m/s]
$\lambda$	wavelength of laser light [nm]
$\mu$	air kinematic viscosity [N·s/m <sup>2</sup> ]
$\phi$	misalignment error [deg]
$\rho$	air density [kg/m <sup>3</sup> ]

$\rho_p$	particle density [kg/m <sup>3</sup> ]
$\rho_w$	air density at the wall [kg/m <sup>3</sup> ]
$\theta$	incoming boundary layer momentum thickness [mm]
$\tau_p$	particle time constant [s]
$\xi_p$	particle relaxation distance [mm]

# Chapter 1

## Introduction

### 1.1 Motivation

Shock boundary layer interactions (SBLIs) are present in nearly all flows of practical relevance in the transonic, supersonic, and hypersonic regimes. A variety of different types of interactions can occur, but all of them involve a shock wave coming into contact with the boundary layer growing on a surface. The flow across a shock wave experiences a very abrupt rise in pressure, temperature, and density accompanied by a sharp deceleration. Depending on the strength of the shock wave involved in the interaction, the boundary layer may separate in response to the imposed adverse pressure gradient. Particularly in the hypersonic regime, the temperature rise throughout the interaction can cause extreme heat transfer rates to the surface and may result in structural damage if not properly mitigated. Furthermore, any unsteadiness in the shock features causes fluctuating pressure and thermal loads which can impact

---

Portions of the text in sections 1.2.2 and 1.3 have been adapted from a manuscript submitted to *Int. J. Heat Fluid Flow* as Campo, L.M. & Eaton, J.K. (2014) Shock boundary layer interactions in a low aspect ratio duct.

performance and lead to fatigue failure.

These effects occur in a wide variety of applications including supersonic combustion ramjet (scramjet) engines, overexpanded rocket engine nozzles, high speed turbomachinery, spacecraft and missiles re-entering the atmosphere, and external aerodynamic and control surfaces on high speed flight vehicles. The particular application motivating the research presented in this thesis is the shock train system in the inlet and isolator sections of a scramjet engine. The successful operation of a scramjet engine depends heavily on the ability of the inlet and isolator sections to robustly set up the correct supersonic conditions at the inlet to the combustor stage. A common failure mode for these engines is unstart, in which the shock system is ejected out the front of the inlet duct. This condition causes high transient pressure loads and can lead to catastrophic loss of engine thrust. The unstart process can be initiated by the blockage associated with shock induced boundary layer separation (Wagner et al. (2009)). In addition, the state of the boundary layers in the isolator duct is known to influence unstart induced by mass injection, with thicker boundary layers leading to accelerated unstart (Do et al. (2011)).

SBLI flows have been studied for over 60 years, yet they still present formidable challenges to both experiments and computations. The ever increasing power of computational resources means that direct numerical simulation (DNS) can be performed for some low Reynolds number SBLI flows. In order to simulate more realistic higher Reynolds number SBLI flows, large eddy simulation (LES) can be employed. However, the grid requirements for resolving the smallest scales can still be prohibitive, necessitating the use of wall models or spanwise periodic boundary conditions to relax the computational cost. Reynolds averaged Navier Stokes (RANS) computations generally have tractable grid resolution requirements but often have difficulty capturing the physics of the highly non-equilibrium separated boundary layer. Before any simulation can be trusted to give accurate results it must be carefully validated

against an experimental dataset.

On the experimental side, many studies over the years have provided valuable insight into the physics of SBLI phenomena. However most of these experiments were not specifically designed with the goal of validating computational fluid dynamics (CFD) simulations in mind and are therefore not optimal for this purpose. For example, incomplete specification of boundary conditions or the use of complex geometries including aerodynamic fences which cannot be included in simulations hinders direct comparison between experiment and computation. Specifically, there is a need for experimental measurements that address the confinement effects imposed by the thickening of side wall boundary layers in realistic low aspect ratio duct geometries. These effects cannot be eliminated in real applications such as the scramjet inlet, and it is therefore important to both understand the physics and ensure that simulations can sufficiently predict these complex three-dimensional flows.

Furthermore, the inlet and boundary conditions for the scramjet engine are uncertain. Scramjets are subject to very harsh operating environments where pressure and thermal stresses may cause defects or deformations in the nominal engine geometry. Like many separated flows, SBLIs can be extremely sensitive to small changes in the inlet flow and boundary conditions. Therefore if simulations are to be used as a predictive tool for robust design, the methods and models must be validated not only for a nominal geometry but for a wide range of conditions. This is an uncertainty quantification (UQ) approach to computations, and it requires an appropriate UQ experimental database for validation. This data set must represent a systematic and quantitative documentation of the effects of small geometric perturbations on the SBLI flow features. In addition to their utility for CFD validation, these measurements are needed to provide fundamental insight into where and why the flow is sensitive to perturbations.

Finally, in order to make a meaningful comparison between simulation results

and experimental data, it is critical to understand the uncertainties and bias errors associated with the technique used to acquire the measurements. In the past decade, the most commonly used technique for making velocity and turbulence measurements in SBLI flows has been particle image velocimetry (PIV). This technique provides a wealth of information about both the mean and fluctuating velocity components, but it is subject to a few important limitations. In particular it is necessary to quantify how the measurement resolution, finite time delay between images, and particle inertia affect the accuracy of the measurements. These effects vary significantly depending on the local flow features, and are particularly important in high speed compressible flows where shock waves impose extremely high velocity gradients.

## 1.2 Background

### 1.2.1 Physical description

A few simple canonical geometries have been used widely in both laboratory experiments and simulations to study various aspects of shock boundary layer interactions. These include the compression ramp, the compression-expansion ramp, the oblique incident/reflected shock wave, the normal shock wave in a duct, the blunt fin, and the crossing of two shock waves. Schematics of these test geometries are shown in Figure 1.1. Note that the features are exaggerated for illustrative purposes and are not necessarily to scale. This thesis will focus specifically on interactions occurring near a compression-expansion ramp and in the vicinity of an oblique incident/reflected shock wave.

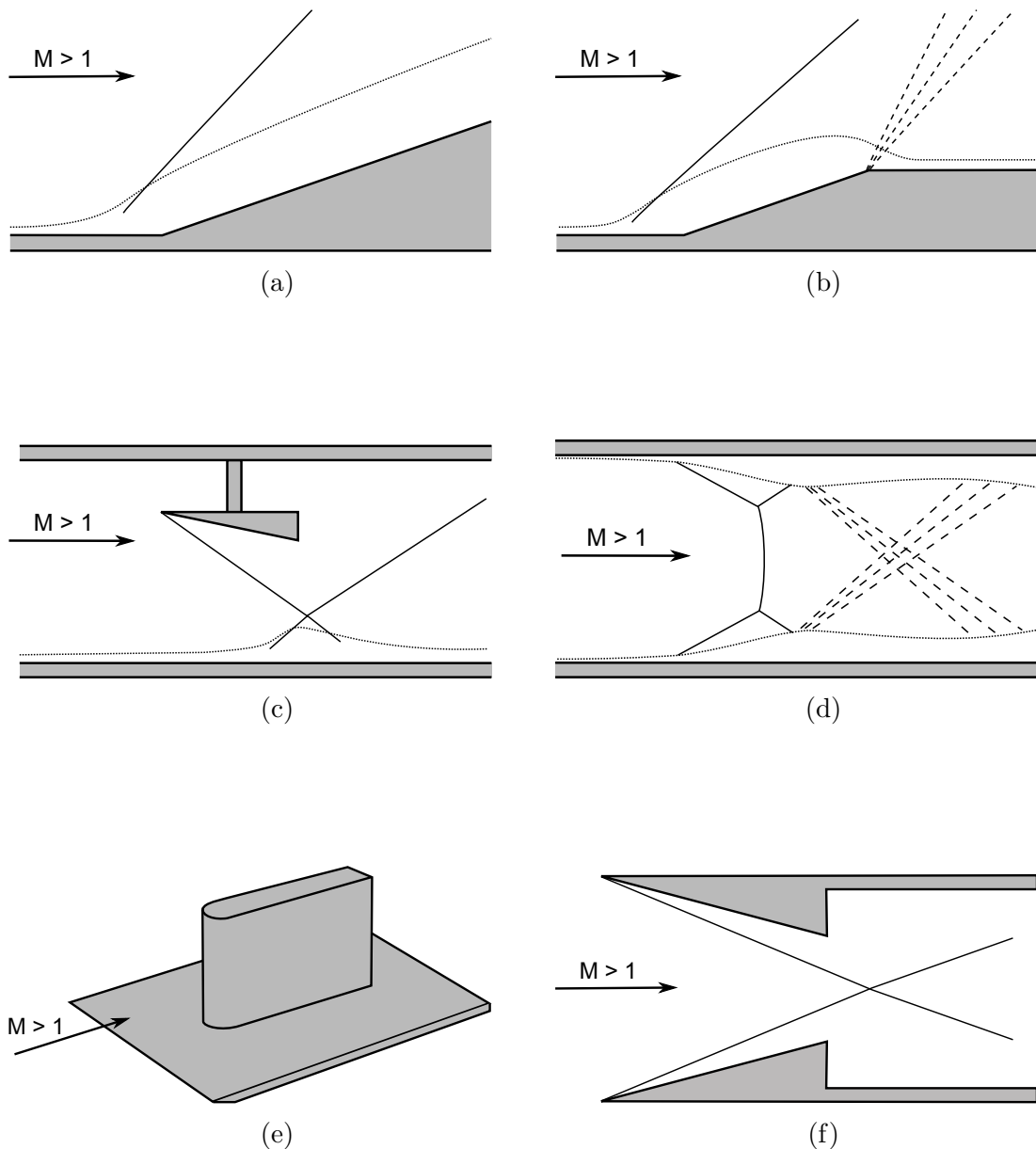


Figure 1.1: Canonical geometries for SBLI flows: (a) compression ramp; (b) compression-expansion ramp; (c) oblique incident/reflected shock; (d) normal shock in a duct; (e) blunt fin; (f) two crossing shock waves.

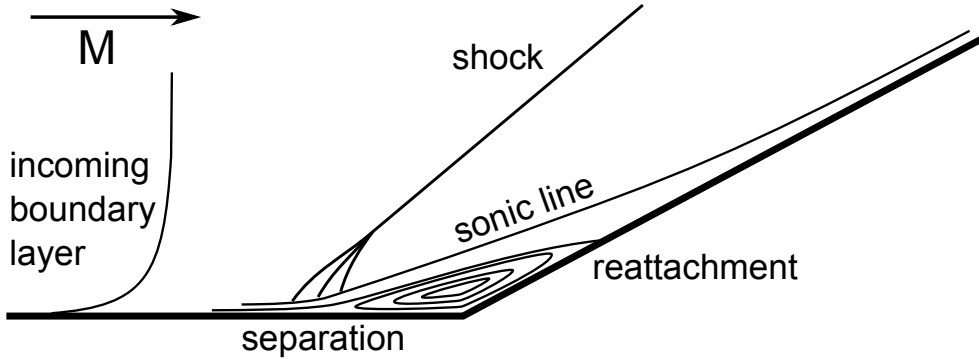


Figure 1.2: Schematic of a compression ramp SBLI

### Compression ramps

In the compression ramp and compression-expansion ramp configurations, shown schematically in Figures 1.2 and 1.3, a supersonic inflow encounters an angled ramp. The incoming flow “feels” the presence of the ramp upstream of its actual location due to the upstream propagation of pressure signal through the subsonic portion of the turbulent boundary layer. Compression waves emanate from a point upstream of the ramp foot and coalesce into a shock wave further from the wall. The system of compression waves and the shock wave deflect the supersonic flow over the ramp. The adverse pressure gradient imposed by the shock wave may cause the boundary layer to separate in the vicinity of the compression corner. The presence and size of a separated region is dependent upon the Reynolds number, the incoming boundary layer thickness, the freestream Mach number, and the ramp angle. Délery & Marvin (1986) summarize the following trends for two-dimensional compression ramp SBLIs at a fixed Reynolds number:

- the separation length relative to the boundary layer thickness increases with increasing ramp angle at constant Mach number
- the separation length relative to the boundary layer thickness decreases with increasing Mach number at constant ramp angle

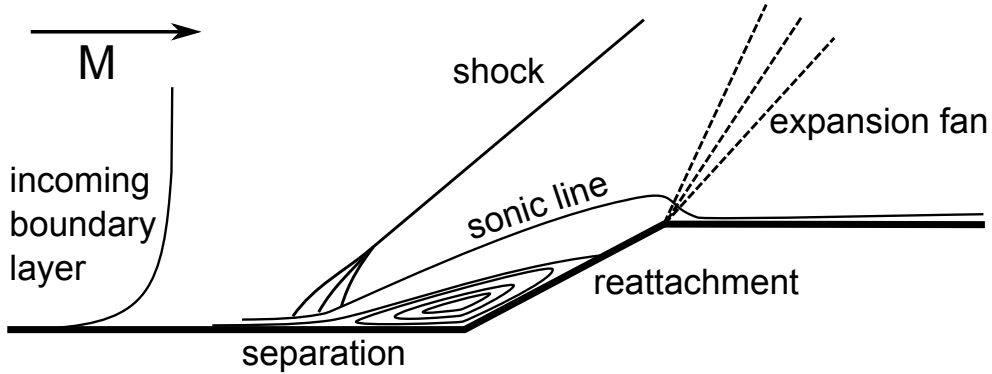


Figure 1.3: Schematic of a compression-expansion ramp SBLI

The difference between the compression ramp and compression-expansion ramp geometries is that the latter includes a section where the angled ramp turns back to horizontal, as shown in Figure 1.3. An expansion wave emanates from this second corner, causing the flow to accelerate and turn back to horizontal to match the wall angle downstream. This geometry, although less common in the literature than the compression ramp, is of practical interest as both shock waves and expansion fans are relevant in real world applications such as the intake of a scramjet engine (Krishnan et al. (2009), White & Ault (1996)). Hunter & Reeves (1971) investigated the effect of compression ramp length on separation in compression-expansion ramp configurations and found that for short enough ramps (or equivalently for small enough ramp height relative to the incoming boundary layer thickness), the upstream influence of the expansion fan affects flow properties over the ramp. Therefore in the small ramp case, the four parameters listed by Délery & Marvin (1986) – Reynolds number, Mach number, boundary layer thickness, and ramp angle – are not sufficient to define a scaling for the separation length. The effect of the ramp height on shock strength, interaction size, and degree of boundary layer separation are directly investigated in the work presented in this thesis.

### Oblique incident/reflected shock waves

In the oblique incident/reflected shock configuration, an externally generated shock wave impinges on a wall which has a turbulent boundary layer, as shown in Figure 1.4. The incident shock is typically generated by a sharp-edged wedge or angled plate suspended in the supersonic freestream flow. This configuration causes a known incident shock angle and flow deflection according to the inviscid oblique shock relations. The incident shock wave steepens as it penetrates into the boundary layer due to the decrease in the local Mach number closer to the wall. The incident shock terminates at the sonic line and reflects as a set of expansion waves. The adverse pressure gradient imposed by the incident shock wave is communicated upstream through the subsonic portion of the boundary layer, causing boundary layer distortion and blockage. Depending on the strength of the incident shock wave, a region of recirculating flow may exist. The thickening of the boundary layer in this region displaces the streamlines of the outer flow, effectively acting like a compression ramp. This generates compression waves that coalesce into the reflected shock wave outside the boundary layer, similar to the compression ramp case described above. In the case where the interaction is strong enough to cause boundary layer separation, an additional set of compression waves emanates from the downstream reattachment point.

If the incident shock wave is sufficiently strong, the reflection of the shock transitions from regular reflection (as described above) to Mach reflection, shown in Figure 1.5. The Mach reflection involves a nearly normal shock wave – the Mach stem – situated between the incident shock wave and the separation shock. In an ideal two-dimensional inviscid flow the transition from regular reflection to Mach reflection is defined by the von Neumann condition (von Neumann (1943)). This condition exists when the deflection through the reflected shock required to turn the flow to a compatible downstream condition exceeds the maximum deflection that can occur

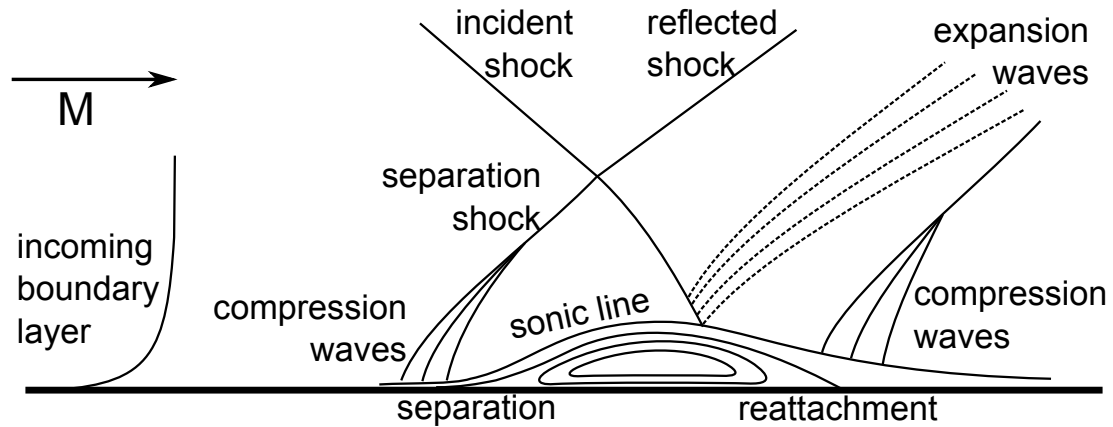


Figure 1.4: Schematic of an oblique incident/reflecting SBLI with a regular reflection

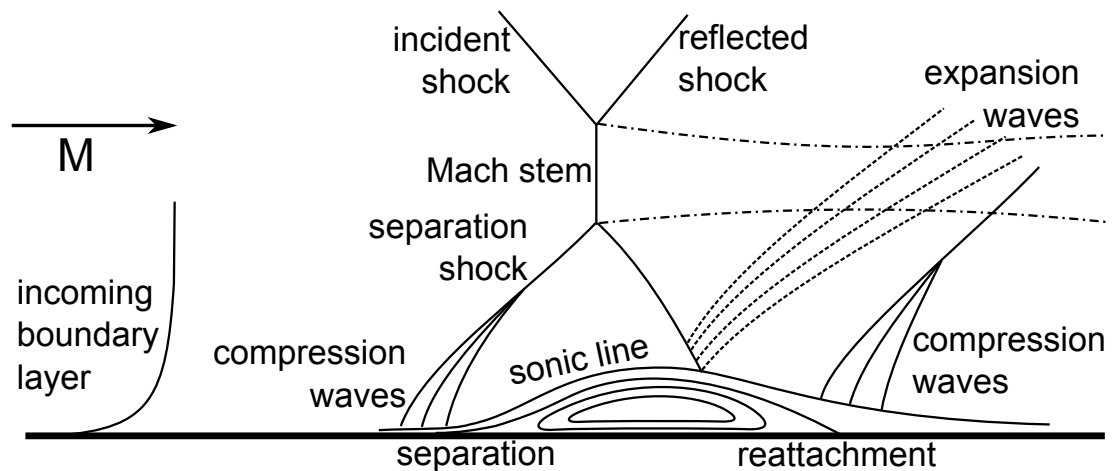


Figure 1.5: Schematic of an oblique incident/reflecting SBLI with a Mach reflection

through a weak shock at the given Mach number. The Mach stem allows for a downstream condition including a slip line across which the pressure is continuous but the velocity is discontinuous. In real flows with viscous and three-dimensional effects, the transition criterion is significantly more complicated (Ivanov et al. (2001)). In a shock-shock interaction generated by two symmetric wedges, Skews (1997) and Ivanov et al. (1998) found that ratio of the width of the wedges to the span of the test section heavily influenced whether or not the flow was two-dimensional and the condition at which the Mach reflection was observed. Bermejo-Moreno et al. (2014) also noted that three-dimensional confinement by side walls affected whether or not a Mach stem was predicted in a wall-modeled large eddy simulation of an incident SBLI in a duct. The experiments presented in this thesis discuss SBLIs involving both regular and Mach reflection of the incident shock wave.

### 1.2.2 Literature review

The shock wave boundary layer interaction has been an active area of research since the first documented experimental observation by Ferri (1940). Much of the early experimental work was carried out using qualitative techniques such as oil flow visualizations, shadowgraph imaging, and Schlieren photographs as well as quantitative measurements of wall pressure distributions. Pitot-static tube traverses and hot-wire anemometry were used to extract boundary layer profiles; however these intrusive methods are particularly challenging in supersonic flows since the probes cause shock waves and may significantly alter the flow field in the vicinity of the measurement.

Prior to the widespread application of numerical methods to SBLI flows, theoretical descriptions of the interaction properties were of great importance. Two of the most prominent advancements were the introduction of the free-interaction concept by Chapman et al. (1958) and the development of the triple-deck theory by Stewartson & Williams (1969) and Neiland (1969). A detailed review of early experimental

and theoretical studies of a number of different SBLI configurations was compiled by Green (1970). Adamson & Messiter (1980) summarize the first attempts to compute SBLI flows using the Reynolds averaged Navier-Stokes equations with zero-, one-, and two-equation turbulence models. They noted that reasonably good agreement between computations and experiments could be achieved in weak interactions where the flow remained attached, and that two-equation models could be tuned to give decent agreement with individual experiments. However, no turbulence model performed well enough to be considered universally applicable to separated interactions.

Settles et al. (1979) used oil flow visualization, shadowgrams, surface pressure measurements, and Preston tube readings to record mean flow and surface measurements in a Mach 2.85 flow over compression ramps of four different angles. They demonstrated that the flow over an  $8^\circ$  compression ramp was fully attached, while the flow over a  $16^\circ$  ramp was incipiently separated. The shock boundary layer interactions due to flow over a  $20^\circ$  ramp and a  $24^\circ$  ramp both exhibited significant regions of fully separated flow.

Unsteady motion of shock waves in a variety of SBLI flows was noted qualitatively in early studies (e.g. Bogdonoff (1955), Chapman et al. (1958)), and later studied quantitatively in an effort to determine the root cause for the shock motion. Kistler (1964) made the first quantitative measurements of the fluctuating wall pressure signal, which indicated a low frequency unsteadiness associated with the shock wave in a separated supersonic flow over a forward facing step. The mechanism driving this low frequency unsteadiness has been the subject of much debate, with most studies supporting either an upstream or downstream mechanism. Highlights of several past experimental and numerical studies on shock wave unsteadiness are summarized briefly here.

Dolling & Murphy (1983) and Dolling & Or (1985) investigated the unsteadiness associated with the shock foot in several compression ramp SBLI flows using unsteady

pressure measurements. They discovered large peaks in pressure fluctuations associated with both the separation and reattachment points, as well as an intermittent region underneath the shock structure. The power spectra of the pressure fluctuations in the intermittent region indicated that a significant fraction of the energy was associated with frequencies one to two orders of magnitude lower than the characteristic frequency of the incoming boundary layer,  $U_\infty/\delta_0$ . Andreopoulos & Muck (1987) performed a similar study and found that the frequency of the shock motion was comparable to the bursting frequency of the upstream boundary layer and independent of the downstream separated flow. Ünalmis & Dolling (1994) proposed that low frequency unsteady thickening and thinning of the upstream boundary layer were responsible for the upstream and downstream motion of the shock foot. Beresh et al. (2002) and Hou et al. (2003) used PIV measurements in the upstream boundary layer combined with the fluctuating pressure signal to show that instantaneously fuller velocity profiles were associated with downstream motion of the shock wave and vice versa. Ganapathisubramani et al. (2007) discovered streamwise oriented elongated superstructures in the incoming boundary layer of length up to  $8\delta_0$ , which correlated with the low frequency shock foot oscillation.

A study by Erengil & Dolling (1991) disagreed with the upstream mechanism proposed by Andreopoulos & Muck (1987), finding only weak evidence of a correlation between the incoming boundary layer and the shock motion. They argued that coherent structures with extremely large streamwise extent would need to be present in the incoming flow in order to explain the very low frequency shock motion and that instead, a low frequency mechanism associated with the downstream separation was the more likely cause. Thomas et al. (1994) also observed no correlation between burst events in the incoming boundary layer and motion of the shock foot; however they did find evidence that the fluctuations in the reattachment region were correlated with fluctuations in the intermittent region, indicating a downstream mechanism for

the unsteadiness. Experimental studies by Dupont et al. (2005), Dupont et al. (2006), and Piponnaiu et al. (2009), as well as large eddy simulations by Touber & Sandham (2009) and Hadjadj et al. (2010) and direct numerical simulations by Wu & Martin (2008) and Priebe & Martin (2012) also supported a downstream mechanism related to the pulsation of the separation bubble.

These conclusions should be taken with caution since correlation does not imply causation; Brusniak & Dolling (1994) noted that it was possible that upstream structures could influence the dynamics of the separated flow which could in turn cause the motion of the shock foot. Souverein et al. (2010) studied incident/reflected shock boundary layer interactions of varying strengths and concluded that both upstream and downstream mechanisms were at work, and the severity of the boundary layer separation dictated which mechanism was dominant. A comprehensive review of the subject of shock wave unsteadiness was given by Clemens & Narayanaswamy (2014), who also argued that both upstream and downstream mechanisms were present in all interactions. They suggested that a downstream mechanism related to the separation bubble dynamics was dominant for highly separated flows and that a combined upstream and downstream mechanism dominated in weakly separated flows.

The structure of turbulence in SBLI flows is also of great interest, both for a fundamental understanding of the flow physics as well as to inform modeling choices for CFD simulations. Accurate measurements of turbulence quantities in the harsh environment of a shock boundary layer interaction are challenging and require large data records, which is why only relatively few early studies report any turbulence measurements. The widespread use of blowdown type facilities with limited test times makes collection of these large datasets difficult, and raises the question of whether transient effects are unintentionally represented in the data.

Rose & Johnson (1975) used laser doppler velocimetry and hot wire anemometry to measure the mean and fluctuating components of velocity upstream and downstream

of an unseparated incident shock boundary layer interaction generated by a flat plate inclined at  $7^\circ$  to a Mach 2.9 inflow. They found that the gradients in the Reynolds normal stresses were significantly smaller than the streamwise pressure gradient and proposed that the Reynolds shear stresses could be described using a hybrid approach with both an equilibrium and frozen mixing length model. Ardoneau et al. (1980) studied the turbulence structure in a Mach 2.25 flow over compression ramps of angles  $8^\circ$ ,  $13^\circ$ , and  $18^\circ$ , corresponding to attached, incipiently separated, and fully separated flows. The streamwise and wall-normal mean velocity and fluctuations were measured using laser doppler anemometry and the state of separation was deduced using wall pressure measurements and oil surface flow visualization. They noted large values of streamwise velocity fluctuations and a highly anisotropic turbulence state, particularly in the shear layer above the separation bubble. Downstream along the ramp, the streamwise fluctuations decayed and the turbulence recovered to a more isotropic state. These effects were greatest for the fully separated interaction generated by the steepest compression ramp.

Smits & Muck (1987) used hot wire anemometry measurements to document the turbulence structure in SBLIs produced by a Mach 2.9 flow over compression ramps inclined at  $8^\circ$ ,  $16^\circ$ , and  $20^\circ$ . They made measurements of the longitudinal mass-flux fluctuations and the mass-weighted turbulent shear stresses. They found that the interaction dramatically amplified the turbulent stresses, and that the amplification increased with increasing turning angle. They also noted that different stress components were amplified by different amounts, leading to significant anisotropy within the interaction.

More recent studies of the turbulence structure in a variety of SBLI configurations have been carried out using non-intrusive laser based techniques including PIV. PIV experiments on incident/reflected SBLIs by Humble et al. (2007), Dupont et al. (2008), and Souverein et al. (2010) showed that high levels of streamwise velocity

fluctuations were associated with the separation shock foot and the highest intensity turbulence was confined to a region beneath the impingement of the incident shock. They noted significant anisotropy and a distinct elongated region of large negative Reynolds shear stress associated with the redeveloping boundary layer downstream of the interaction.

Recently, large-eddy simulations (LES) and direct numerical simulations (DNS) also have been used to investigate turbulence in SBLI flows. Loginov et al. (2007) performed a wall-resolved LES of the Mach 2.95 flow over a compression-expansion ramp geometry used in experiments by Zheltovodov & Yakovlev (1986). They confirmed that significant amplification of turbulence occurred across the interaction region. They also described large-scale streamwise vortices in the vicinity of the compression and expansion corners, and attributed their development to a Görtler-like mechanism. DNS of an impinging SBLI by Priebe et al. (2009) also showed amplified turbulence in the interaction region. They noted significant deviations from the strong Reynolds analogy, which relates the streamwise velocity fluctuations and temperature fluctuations in a compressible boundary layer on an adiabatic flat plate. This analogy assumes a perfect anticorrelation between the temperature and velocity fluctuations (Morkovin (1962)) and allows incompressible turbulence models to be adapted for compressible flows. Pirozzoli & Bernardini (2011) produced a DNS database of impinging SBLI flows to be used as a reference in the development of advanced turbulence models for non-equilibrium flows. One major limitation of DNS databases for SBLI flows is that only low Reynolds number flows can be simulated.

Another topic that has been widely studied is the control of shock-induced boundary layer separation for applications such as the inlet/isolator of a scramjet engine or external aerodynamic surfaces of high speed vehicles. One commonly used technique for control involves blowing and suction in the boundary layer near the separation point. This can be done passively using recirculation chambers (Raghunathan (1987),

Raghunathan & Mabey (1987), Chyu et al. (1995), Bur et al. (1998), Smith et al. (2004), Holden & Babinsky (2005)) or actively using pressurized injectors (Viswanath et al. (1983), White et al. (1991)) or plasma actuators (Kalra et al. (2009), Kalra et al. (2010), Narayanaswamy et al. (2012), Bisek et al. (2013)). Geometric control devices including ramps and vortex generators (Cohen & Motallebi (2008), Babinsky et al. (2009), Lapsa (2009), Herges et al. (2010)) and 3D devices (Ogawa et al. (2008), Bruce & Babinsky (2012), Colliss et al. (2013)) have also been used. All studies noted significant changes in the SBLI flow field, with varying degrees of success at controlling the separation and drag associated with the interactions.

Reda & Murphy (1973) demonstrated that the sidewall boundary layers had a significant influence on a separated incident/reflecting shock wave boundary layer interaction in a rectangular duct. They developed a system of side plates to isolate the main flow from the side wall boundary layers. The addition of these side plates did not completely remove three-dimensional effects; however it did significantly reduce the scale of the interaction region. Many subsequent experimental studies made efforts to two-dimensionalize the SBLI of interest by focusing only on a nominally two-dimensional region in the center of a channel (Beresh et al. (2002), Hou et al. (2003), Humble et al. (2007), Dupont et al. (2008), Souverein et al. (2010)) or by employing aerodynamic fences and/or non-fully-spanning shock generators (Settles et al. (1979), Dolling & Or (1985), Andreopoulos & Muck (1987), Erengil & Dolling (1991), Bookey et al. (2005), Ringuette et al. (2009), Lapsa (2009)).

These studies provided a wealth of knowledge about a nominally two-dimensional region of the flow, including measurements of the low frequency unsteadiness of the shock wave, separation and interaction length scales, and the effect of increasing ramp angle on shock strength and boundary layer separation. However, questions remain about how the flow outside this region is affected by corner vortices and confinement by side walls. Several researchers have concluded that the separation bubble size

is underpredicted in simulations with spanwise periodic boundary conditions when compared to experiments in which confinement effects cannot be completely avoided (Adamson & Messiter (1980), Hadjadj et al. (2010), Pirozzoli et al. (2010)). Furthermore, Touber & Sandham (2009) reported that the size of the separation bubble varied with changes in the spanwise extent of the computational domain even when spanwise periodic boundary conditions were employed. Galbraith et al. (2013) performed compressible RANS computations of a Mach 2.75 incident shock boundary layer interaction in geometries of aspect ratio one and two. They found significant differences in the amount of blockage and boundary layer separation between the two cases. Furthermore, they reported that the flow field is highly three dimensional even with an extruded 2D geometry and that a centerline view of the results could not be considered as representative of a 2D solution even for the larger aspect ratio tunnel. Dussauge et al. (2006) suggested that the low frequency motion of the shock wave may be coupled to or perhaps caused by three-dimensional effects and specifically proposed the question of “what is the effect of sidewalls?”

Ganapathisubramani et al. (2007) used planar laser scattering and wide field PIV measurements in streamwise-spanwise planes to investigate low frequency unsteadiness in a Mach 2 SBLI generated by a  $20^\circ$  compression ramp. The measurement domain focused on a central region of the tunnel span far from the side walls, but instantaneous coherent 3D structures were still identified in this region. Elongated instantaneous regions of high and low momentum in the streamwise direction were found across the span, but these features were not stationary and therefore not visible in the mean velocity field. Humble et al. (2009) used tomographic PIV to investigate the three-dimensional instantaneous structure of an incident shock boundary layer interaction. These measurements provided insight into the organization of vortical structures and the relationship between coherent large scale motions in the incoming

boundary layer with the shock motion. However, similar to the study by Ganapathisubramani, the measurement domain did not extend into a region affected by the side wall boundary layers and corner/sidewall effects were not specifically addressed.

Recently a handful of studies have shifted attention toward directly investigating three-dimensionality induced by side walls and corner effects in SBLI flows. Gaitonde et al. (2001) used a Reynolds-averaged compressible Navier Stokes solver with a  $k-\epsilon$  turbulence model to investigate the sidewall interaction in a simulated scramjet inlet configuration. With appropriate tuning of a limiting term on turbulence energy production, the simulation results agreed qualitatively with the experimental oil flow visualizations of Zheltovodov et al. (1994); however more rigorous quantitative comparisons were not possible. The study concluded that the SBLI flowfield was highly sensitive to the state of the sidewall boundary layers. Hanada et al. (2005) investigated a three-dimensional normal shock interaction in a duct with inlet Mach number of 1.68. Using laser induced fluorescence measurements in several streamwise-spanwise planes, they found that the Mach number immediately downstream of the initial shock wave was highly non-uniform over the cross section, with a higher Mach number near the corner regions than in the core of the flow. Burton & Babinsky (2012) studied corner separation for a normal shock boundary layer interaction at Mach 1.5 using oil flow visualization, laser Doppler anemometry, pitot probe traverses, and pressure sensitive paint. They were able to alter the corner separations using suction and micro-vortex generators and observed that the degree of separation near the centerline increased with decreasing corner separation and vice versa.

Eagle (2012) added to the understanding of 3D separation in a Mach 2.75 incident oblique SBLI using stereo PIV and oil flow visualization. These measurements indicated significant three-dimensionality throughout the interaction, and that no regions of the flow could be accurately represented as nominally two-dimensional. Helmer (2011) & Helmer et al. (2012) initiated the study upon which the current

work expands, making the first high resolution 2D PIV measurements inside the side-wall boundary layer of an oblique SBLI. Bermejo-Moreno et al. (2014) performed wall-modeled LES of the test geometries presented in this thesis, using part of the present experimental database for validation. They compared simulations performed with spanwise periodic boundary conditions to simulations including no-slip side walls and noted drastic differences in the SBLI features, including the degree of boundary layer separation and whether or not a Mach stem was present.

### 1.3 Objectives of present work

The experiments presented in this thesis take into account several recommendations by previous researchers. In particular, Dolling (2001) highlights the importance of focusing on three-dimensional SBLI flows and acquiring detailed high quality measurements that are well suited to CFD validation. Settles & Dodson (1994) recommend concentrating on using non-intrusive measurement techniques to acquire both mean and fluctuating velocity components as well as introducing new and slightly more complex “building block” type experiments. The present experiments include PIV measurements of the mean and turbulent velocity fields in both the core of the SBLI flow as well as within the sidewall boundary layers. Experiments are performed in a low aspect ratio ( $AR \approx 1$ ) duct with a fully spanning  $20^\circ$  shock-generating ramp machined into the top wall. These features are specifically selected so that confinement effects and spanwise non-uniformities in flow features due to interaction of the shock wave with the sidewall boundary layers can be documented.

In all test cases the shock generating ramp has a height smaller than the incoming boundary layer thickness. This geometry causes a coupling between the viscous effects in the SBLI near the compression ramp foot and the freestream flow deflection; e.g. the shock strength can be increased by increasing the ramp size while holding its angle

constant. Several previous studies have altered the strength of the shock wave using shock generators of varying angles (see e.g. Settles et al. (1979), Dupont et al. (2006), Souverein et al. (2010)), but to the authors' knowledge this is the first study that achieves the strengthening or weakening effect by changing ramp height at constant angle. Measurements are made both in the vicinity of the compression ramp where the shock is generated as well as on the opposite wall where the shock wave impinges and reflects, allowing both types of interactions to be investigated in a single test case.

The combination of these unique features makes this experiment a slightly more complex “building block” case, while still allowing for the inlet and boundary conditions to be accurately controlled and documented as is necessary for any dataset which is intended for CFD validation. Wide field mean and fluctuating measurements of the streamwise and vertical velocity components are provided at several stations across the span of the tunnel, allowing for detailed assessment of a simulation’s ability to capture the relevant physics in many different regions of the flow. The simple low aspect ratio test section with side walls can be simulated at a lower computational cost than a fully three-dimensional simulation of a higher aspect ratio geometry or one with more complex features like aerodynamic fences or non-fully spanning shock generators. The combination of a simple, low aspect ratio geometry, well-defined boundary conditions, and highly stable freestream conditions means that the flow can be directly replicated by high fidelity simulations. Once such simulations are validated using the converged mean flow and turbulence statistics, the simulation results can be used to further explore the flow physics, including features that are difficult to measure in experiments. The design, acquisition of data, and discussion of findings of these experiments are presented in chapters 2 and 3.

As summarized in the previous section, past research on control techniques for

SBLIs indicates that these flows are highly sensitive to changes in inlet and boundary conditions. This has important implications for robust design of systems where SBLIs are relevant, including scramjet engines. This thesis presents a systematic documentation of the sensitivity of SBLI features to a wide range of small ( $< 0.2\delta_0$  in height) well-defined geometric perturbations. This is done not specifically to attempt to control the interaction, but rather to provide validation data for CFD simulations of SBLI flows including uncertainty quantification. The “UQ experiment” described in chapter 4 was initiated in collaboration with Dr. David Helmer (Helmer et al. (2011), Helmer (2011)) and expanded to include measurements of the incident shock boundary layer interaction (Campo et al. (2012)). This experiment introduces small steady geometric perturbations into the bottom wall of the inlet section to the experimental test section studied in detail by Helmer (2011). A two-dimensional parameter space – the size and location of the geometric perturbations – is explored in order to quantify the response of the SBLI features. In total,  $\approx 50$  perturbation cases are documented and compared to two- and three-dimensional RANS computations carried out by Dr. Ivan Bermejo-Moreno.

In keeping with the purpose of using the data set for CFD validation, an accurate assessment of experimental uncertainty and bias errors is required. This is critical for PIV measurements where traditional uncertainty sources do not account for all of the issues that arise in supersonic flows with shock waves. A detailed analysis of the biases inherent in PIV measurements of such flows is developed in chapter 5. The approach involves modeling and propagating the sources of bias errors through the flow field computed by an LES of the same test geometry. This provides quantitative information about the magnitude of errors and the regions of the flow where they are most severe. It also highlights the importance of choosing appropriate parameters in the experimental design to mitigate these errors. Using this method, the modified

CFD dataset can be directly compared to the experimental result knowing that discrepancies due to the main sources of PIV bias errors have been eliminated from the comparison.

The present experiments are tightly coupled to numerical simulations of the same flow configurations performed by Dr. Ivan Bermejo-Moreno under the direction of Professor Gianluca Iaccarino. The purpose of this collaboration was to ensure that the experimental design and test procedures produced well-documented inflow and boundary conditions that could be accurately implemented in CFD. Throughout the experimental campaign, the simulations provided by Dr. Bermejo-Moreno were used to highlight areas where further measurements were necessary as well as to explore potentially interesting additional test cases. Furthermore, validated CFD simulations were helpful in the interpretation of the experimental measurements and they allowed for investigation of flow quantities that could not be directly measured.

# Chapter 2

## Experimental Setup

### 2.1 Facility overview

Experiments are conducted in a low aspect ratio continuous flow Mach 2.05 wind tunnel. The open-loop tunnel sources air from a compressor (Ingersoll Rand SSRXF400) upstream and exhausts downstream to a muffler and 6-inch duct to atmospheric conditions. Moisture, oil, and particulates are removed from the compressed air supply by a refrigerated air dryer (Ingersoll Rand TM1900-KTE4) which includes an oil separator and air filter. The flow then passes through another filter (Norgren F18-C00-A3DA) and a regulator (Norgren R18-C00-RNXA) which is used to control the incoming stagnation pressure. The flow can be cooled by a chilled water shell and tube heat exchanger or heated by a series of 2kW electrical resistance heaters. This allows for a constant inlet stagnation temperature to be maintained throughout the experiments, regardless of the ambient temperature. The air is delivered to the upstream section of the experiment via a long 3-inch diameter copper pipe.

The upstream flow conditioning and inlet sections are adapted from previous experiments in the facility including Vicharelli & Eaton (2006) and Helmer (2011). The upstream section of the experiment consists of a 1.54-meter long duct containing two

coarse grids, two fine grids, and a honeycomb (2-inch long with 1/4-inch cells) to condition the flow. The inlet duct is made from custom machined half-inch thick aluminum plates bolted together and sealed using RTV silicone adhesive. The steel grids are fixed in place at flanged joints which are sealed using rubber gaskets.

The stagnation quantities,  $P_0$  and  $T_0$ , are measured at the exit of the flow conditioning section.  $P_0$  is measured by a United Sensor Kiel probe connected to a Setra 204D differential pressure transducer referenced to atmospheric pressure. The stagnation temperature,  $T_0$ , is measured by an Omega TJ36-44004 thermistor. The stagnation quantities are continuously monitored and controlled throughout the experiments.

Next, the flow passes through a three-dimensional contraction and then a two-dimensional symmetric converging-diverging nozzle. This establishes a clean  $M_\infty = 2.05$  inflow with very thin boundary layers and low freestream turbulence. The wall geometries for the converging nozzle sections are defined by fifth order polynomials with zero slope and curvature at the endpoints. The wall shape in the diverging nozzle section is designed using the method of characteristics to cancel expansion waves and minimize flow disturbances. Coordinates of the full converging-diverging nozzle shape can be found in Helmer (2011). A schematic overview of the full wind tunnel facility is presented in Figure 2.1.

## 2.2 Test section details

The test section inlet consists of a constant area duct with a cross section of 45mm  $\times$  47.5mm which allows the boundary layers to develop over a length of 325mm downstream of the converging-diverging nozzle exit. This section is followed by a small fully-spanning compression ramp on the top wall which generates an oblique shock wave. Experiments are performed for shocks generated by ramps of three different

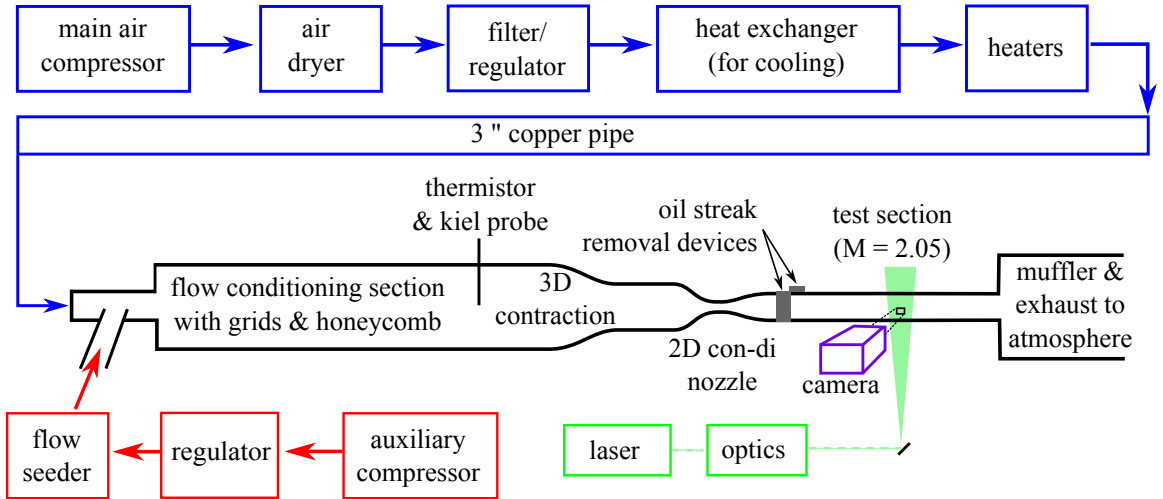


Figure 2.1: Overview of wind tunnel test facility and PIV setup

heights:  $h_{\text{ramp}} = 1.1, 3.0 and  $5.0\text{mm}$ . Previous measurements were performed for the smallest ramp case by Helmer (2011) and Helmer et al. (2012). Selected results from those experiments will be referenced for comparison.$

In each case, the ramp is inclined at an angle of  $20^\circ$  to the incoming flow. The ramps are all smaller than the undisturbed incoming boundary layer thickness,  $\delta_0 = 5.4\text{mm}$ , and will henceforth be referred to in non-dimensional form as  $h_{\text{ramp}}/\delta_0 = 0.20, 0.56$ , and  $0.93$ . The three ramp heights will also be called “small”, “mid-size”, and “large”; however it is important to keep in mind that even the “large” ramp is embedded in the incoming boundary layer. Downstream of the ramp, the top wall of the tunnel turns back to horizontal and the flow continues through a constant area duct with cross section  $(45 - h_{\text{ramp}})\text{mm} \times 47.5\text{mm}$  before dumping into a muffler which exhausts to atmospheric conditions. The test section geometry, including the inlet nozzles, is depicted in Figure 2.2.

The front and back walls of the wind tunnel test section are made from half-inch thick black anodized aluminum to minimize unwanted reflections of laser light. The top and bottom walls are machined from cast acrylic and polished to optical clarity

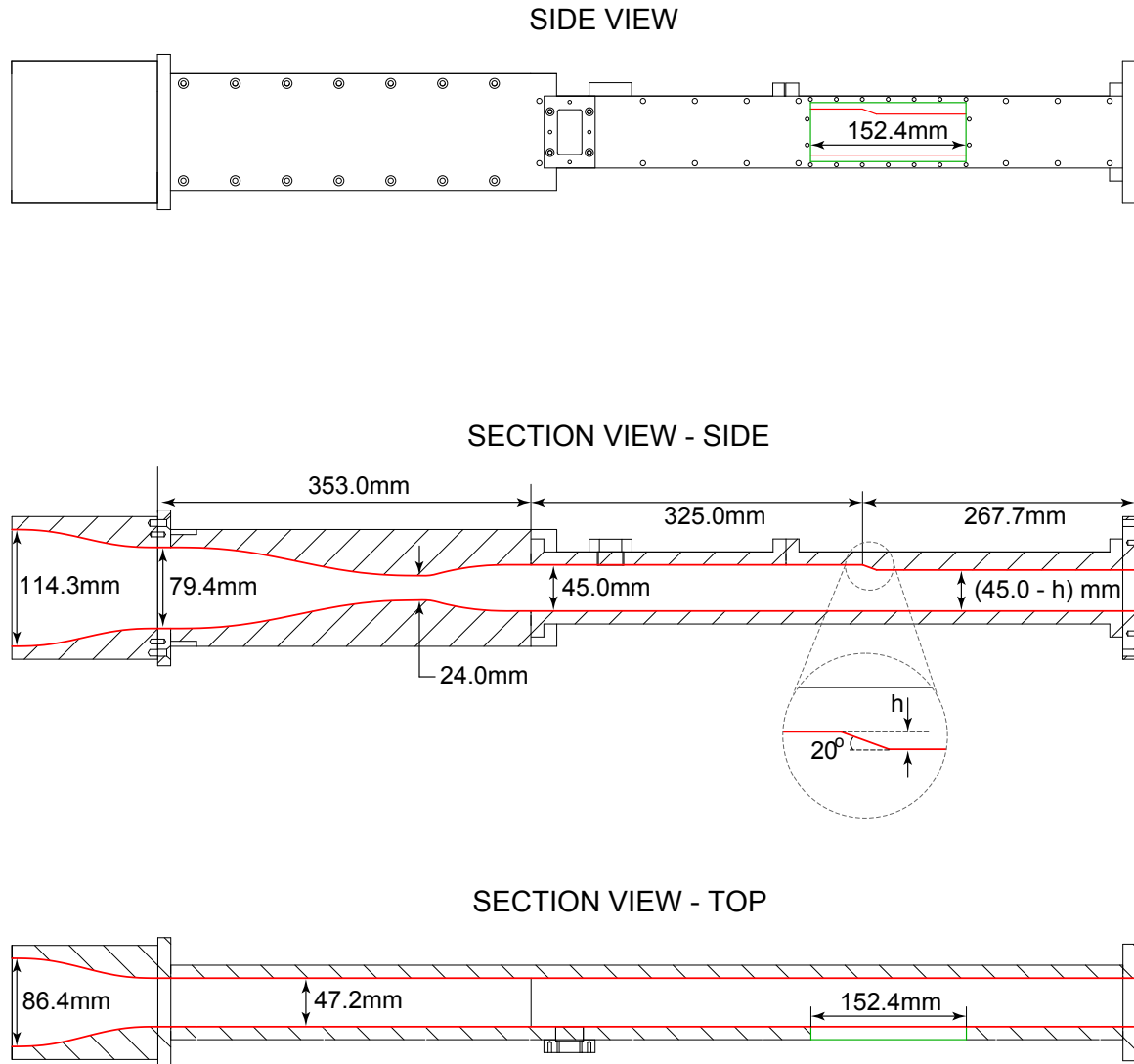


Figure 2.2: Test section assembly, including upstream nozzles. The interior surfaces defining the flow path are shown in red. The imaging window cutout is shown in green. These figures are to scale.

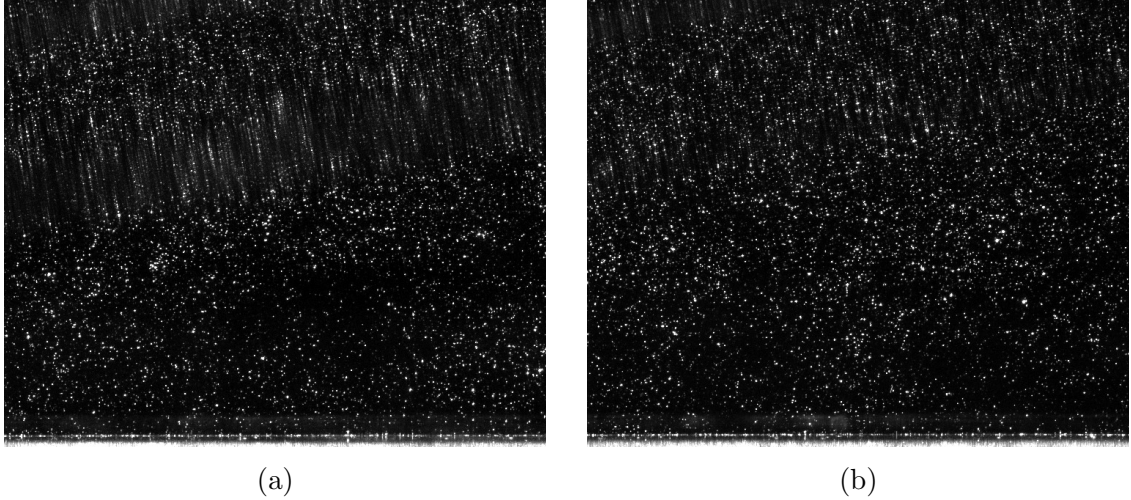


Figure 2.3: Sample PIV images (a) with significant blurring due to oil streaks running across the imaging window; (b) with less blurring due to mitigation of oil streaks by oil removal device.

to allow access for the laser sheet. A polished cast acrylic window insert fits into the front wall of the test section and is held in place by an aluminum compression flange. The window is 15.2cm long and spans the full height of the tunnel, allowing a large region of the flow to be imaged. The window is precisely machined and carefully aligned to ensure that there are no gaps or steps in the interior surface of the wind tunnel.

The inlet section includes two oil removal devices which reduce the presence of oil streaks along the top and side walls of the test section. These oil streaks are caused by agglomeration of the olive oil droplets used to seed the flow. If not properly mitigated, the oil streaks along the imaging window can defocus particle images and cause regions of very low valid vector yield. Oil streaks along the top wall are problematic because the adverse pressure gradient can trap oil just upstream of the compression ramp. The pooled oil in this region causes unwanted laser light reflections which obscure particle images and degrade the overall quality of the PIV dataset. Sample PIV images acquired with and without the oil removal devices are shown in Figure 2.3.

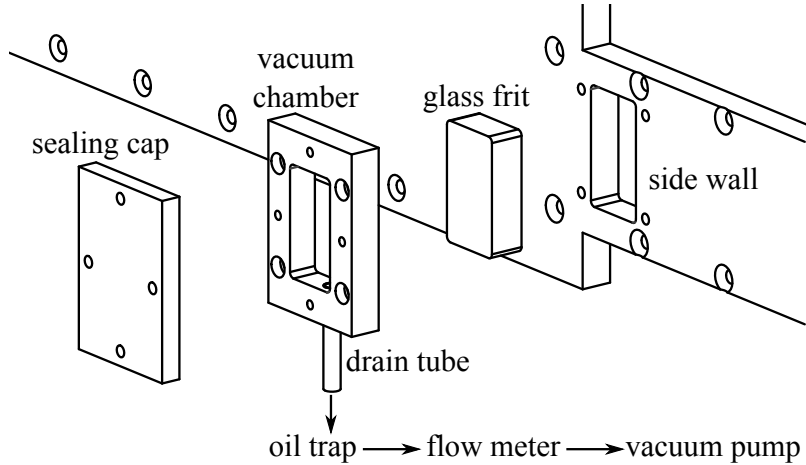


Figure 2.4: Exploded view of side wall oil removal device.

Each of the oil removal devices consists of a porous wall insert and a sealed chamber fixed to the wind tunnel wall. A vacuum pump is connected to each chamber in order to drive flow through the porous material, wicking oil away from the interior surfaces of the wind tunnel. Oil removed from the test section is trapped in filter flasks in order to prevent damage to the vacuum pumps. An exploded view schematic of the oil removal device for the side wall is shown in Figure 2.4. The concept for the top wall oil removal device is the same.

The porous inserts are made of half-inch thick sintered glass pieces machined to precisely fit into the top and side walls with no gaps or discontinuities across the inner surface of the wind tunnel. The supplier of the glass frits, Adams & Chittenden Scientific Glass, specifies a nominal pore size of 10-16  $\mu\text{m}$  and a pore volume of 42%. The side wall vacuum chamber is machined from aluminum and bolted to the aluminum side wall of the tunnel. The top wall vacuum chamber is machined from cast acrylic and attached to the top wall piece using acrylic cement.

Rotameters are used to measure the air flow rate through each of the oil removal systems. The total flow rate through both devices never exceeds 25 standard cubic feet per hour ( $2.3 \times 10^{-4} \text{ kg/sec}$ ), and is roughly equally split between the top and

side wall oil removal devices. This flow rate is only  $\approx 0.3\%$  of the primary mass flow rate of  $\dot{m} = 0.67$  kg/sec through the experiment, and may therefore be considered negligible. The porous inserts are located far upstream of the compression ramp to minimize any local flow disturbances near the SBLIs of interest. Furthermore, PIV measurements show that the top wall boundary layer in the test section is unaffected by the presence of the oil removal devices.

In order to further minimize fouling of the optical window by oil streaks, seed is supplied only during image acquisition, which is done in batches of 125 – 500 image pairs at a time. In between these batches of data collection, the main air flow remains on but the auxiliary flow supplying the olive oil seed is shut off for a period of 3 – 5 minutes. This method of seeding is recommended by Adrian & Westerweel (2011) because it allows the unseeded flow to clean the wind tunnel inner surfaces prior to collection of the next batch of data. Despite the cycling of the seed flow, the wind tunnel still effectively runs at a continuous steady state because the additional flow due to the seeding accounts for a very small fraction ( $< 1\%$ ) of the overall flow through the experiment.

## 2.3 PIV measurements

### 2.3.1 Measurement domain & data acquisition

Velocity measurements are acquired using high resolution two-component particle image velocimetry (PIV) in streamwise-vertical planes at  $z/\delta_0 = 0.74, 1.01$ , and  $3.89$ , with the origin of the  $z$ -coordinate fixed to the back wall of the duct. For the mid-size ramp geometry ( $h_{\text{ramp}}/\delta_0 = 0.56$ ), an additional plane of PIV data is obtained further inside the side wall boundary layer at  $z/\delta_0 = 0.46$ . For the largest ramp geometry ( $h_{\text{ramp}}/\delta_0 = 0.93$ ), the three-dimensional effects imposed by the side wall

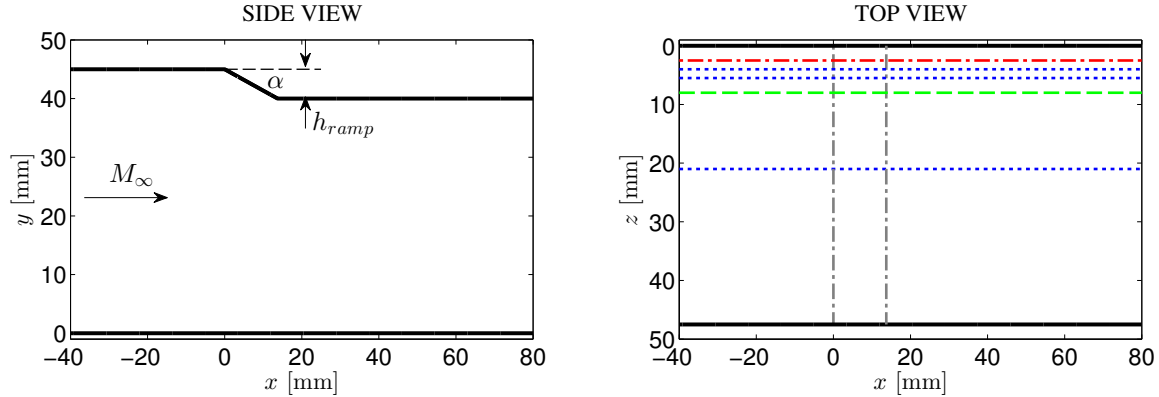


Figure 2.5: Measurement domain with locations of PIV measurement planes:

- wall geometry —
- extent of compression ramp - - -
- PIV measurement plane: all cases ..... blue
- PIV measurement plane:  $h_{\text{ramp}}/\delta_0 = 0.93$  case ..... green
- PIV measurement plane:  $h_{\text{ramp}}/\delta_0 = 0.56$  case ..... red

interaction extend further outside the side wall boundary layer so an additional PIV measurement plane at  $z/\delta_0 = 1.48$  is added. Top and side views of the measurement domain with the PIV planes superimposed are shown in Figure 2.5.

For the cases with  $h_{\text{ramp}}/\delta_0 = 0.20$  and  $0.56$ , PIV image pairs are recorded at 4Hz by a TSI model 630047 PIV camera with a  $1024 \times 1280$  pixel array and a Nikon AF Micro-Nikkor 200mm lens. For the case with the larger compression ramp ( $h_{\text{ramp}}/\delta_0 = 0.93$ ), data are acquired at 7Hz using a newer TSI PowerPlus 4MP camera with a  $2048 \times 2048$  pixel array and the same lens. In order to achieve a wide-field representation of the flow at high resolution, PIV data at many different locations throughout the test section are acquired in sequence by a single camera. Data from each camera position are located in space using reference images of an alignment grid with fiducial markings. A composite representation of the full domain is achieved by stitching all the individual PIV data tiles together. Neighboring tiles overlap by  $\approx 3\text{mm}$  in the streamwise direction, which allows the accuracy of the tile placement to be confirmed

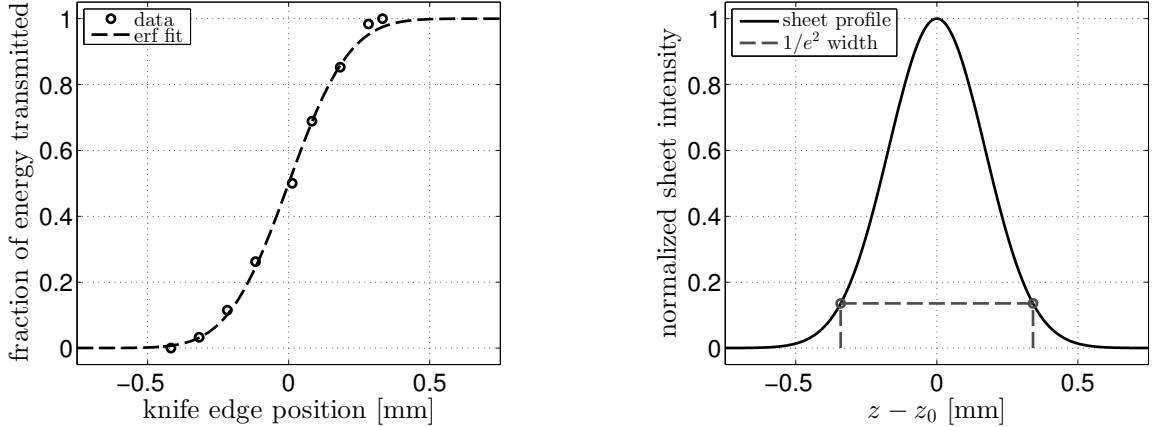


Figure 2.6: Measurement of the laser sheet width: laser sheet energy transmitted vs. position of knife edge with error function fit (left panel) and approximate Gaussian sheet profile with  $1/e^2$  width shown (right panel).

based on ensuring good agreement of flow features from one tile to the next. A minimum of 5000 image pairs are recorded at each camera position to give well-converged mean velocity and turbulence statistics.

A New Wave Solo-200XT dual-pulse PIV laser with a wavelength of  $\lambda = 532\text{nm}$  and a pulse separation of  $\Delta t = 0.8\mu\text{s}$  is used to illuminate the images. The beam path originates in a horizontal plane below the test section and is expanded through a spherical diverging-converging lens pair of focal lengths  $f = -150\text{mm}$  and  $f = 250\text{mm}$ , separated by a distance of  $100\text{mm}$ . The beam is further expanded by an area ratio of 2.3 by a TSI model 9188 beam expander and then passes through a spherical converging lens of focal length  $f = 2\text{m}$ . The beam then passes through a cylindrical diverging lens with focal length  $f = -150\text{mm}$  to form the laser sheet, which is directed vertically toward the test section by an angled mirror. Due to the long focal length of the spherical converging lens, the laser sheet thickness is approximately constant over the full height of the test section.

The width of the laser sheet in the test section is obtained by measuring the fraction of the total laser energy transmitted as a knife edge is traversed through the

width of the beam. An error function is fit to this data, representing the cumulative distribution function (CDF) of the laser sheet's energy. The intensity of the sheet is approximately Gaussian with standard deviation,  $\sigma = 0.17\text{mm}$ . The CDF of laser sheet energy and the approximate laser sheet intensity profile are shown in Figure 2.6. The  $1/e^2$  width of the laser sheet is  $\approx 0.7\text{mm}$  throughout the test section.

### 2.3.2 Flow seeding

Aerosolized olive oil particles are used to seed the flow for imaging. The seed is generated by forcing compressed air through six Laskin nozzles immersed in olive oil inside a sealed chamber (TSI model 9307-6 oil droplet generator). The auxiliary flow of compressed air is supplied by an Ingersoll Rand 2340L5-V compressor and controlled by a Norgren B74G-4AK-AD1-RMG filter/regulator. Seed is introduced upstream of the flow conditioning section to minimize any disturbances to the downstream flow.

The particle response through an oblique shock wave is investigated experimentally in order to characterize the particle response time,  $\tau_p$ . This quantity gives an estimate of how well the particles track the underlying air velocity field. The characteristic time scale of the incoming boundary layer is  $t^* = \delta_0/U_\infty$ , and the particle Stokes number is defined as the ratio of the particle time scale to the flow time scale:  $St_p = \tau_p/t^*$ . To ensure that the particles faithfully track the flow field,  $St_p \leq 0.1$  is desired.

In the following analysis of the particle response time, an ideal shock wave situated at shock-normal coordinate  $x_\perp = 0$  is assumed. Subscript  $p$  denotes a quantity related to the particle, and subscript  $\perp$  denotes the component normal to the shock wave. The air velocity normal to the shock wave is given by a step function:

$$U_\perp = \begin{cases} U_1 : x_\perp \leq 0 \\ U_2 : x_\perp > 0 \end{cases} \quad (2.1)$$

A spherical particle of diameter  $d_p$  and density  $\rho_p$  traveling through this flow field experiences an inertial force and a viscous drag force due to the difference between the local particle and air velocities. The equation governing the particle's velocity normal to the shock wave is:

$$\frac{dU_{\perp,p}}{dt} = \frac{F_D}{m_p} = \frac{6F_D}{\pi d_p^2 \rho_p} \quad (2.2)$$

The drag force can be modeled as Stokes drag such that  $F_D = -3\pi\mu d_p(U_{\perp,p} - U_{\perp})$ . The validity of this assumption is confirmed later by computing  $St_p$  and comparing experimental and theoretical results. The particle velocity is normalized as  $U_p^* = (U_{\perp,p} - U_2)/(U_1 - U_2)$ , and the Stokes drag term is substituted into equation 2.2, leading to the simplified form:

$$\frac{dU_p^*}{dt} = - \left( \frac{18\mu}{d_p^2 \rho_p} \right) U_p^* \quad (2.3)$$

The bracketed term on the right hand side of equation 2.3 has dimension 1/s, and is the analytical expression for the inverse of the particle relaxation time scale,  $1/\tau_p$ . At this point, it is possible to estimate the particle time scale by simply substituting  $\mu$ ,  $d_p$ , and  $\rho_p$  into the expression for  $\tau_p$ . According to the manufacturer's specifications, the seed particles have a mean diameter of  $d_p \approx 1\mu\text{m}$ . The density of olive oil is  $\rho_p \approx 900 \text{ kg/m}^3$ , and the viscosity of the freestream flow (air at  $T_\infty \approx 160\text{K}$ ) is  $\mu \approx 1.1 \times 10^{-5} \text{ kg/m}\cdot\text{s}$ . Substituting these parameters into  $\tau_p = d_p^2 \rho_p / 18\mu$  gives the result  $\tau_p \approx 4.5\mu\text{s}$ . However, because the actual mean particle diameter has not been confirmed experimentally, the uncertainty on this estimate of  $\tau_p$  is high. Mitchell et al. (2011) report significant variations in particle response time for particle distributions with the same mean size and varying degrees of polydispersity, meaning that experimental determination of  $\tau_p$  is necessary. Therefore, we continue the analysis with the goal of obtaining expressions for the particle's velocity,  $U_p^*(t)$ , and trajectory,  $x_{\perp,p}(t)$ , for

comparison with the experimental data.

Assuming that the particle and air velocities are equal upstream of the shock and that the particle arrives at the shock wave at time  $t = 0$ , the appropriate initial condition for equation 2.3 is:

$$U_p^*(t = 0) = \frac{U_{\perp,p}(t = 0) - U_2}{U_1 - U_2} = 1 \quad (2.4)$$

Integrating (2.3) and applying the initial condition (2.4) yields:

$$U_p^*(t) = \exp\left(\frac{-18\mu}{\rho_p d_p} t\right) = \exp(-t/\tau_p) \quad (2.5)$$

Integrating equation 2.5 again and applying the initial condition of  $x_{\perp,p}(t = 0) = 0$  yields an expression for the shock-normal trajectory of the particle as a function of time:

$$x_{\perp,p}(t) = U_2 t + \tau_p(U_1 - U_2)[1 - \exp(-t/\tau_p)] \quad (2.6)$$

Experimental measurements of  $U_p^*$  vs.  $x_{\perp,p}$  can be extracted from the PIV data across the oblique shock. Figure 2.7 shows these data, as well as parametric curves of  $U_p^*(t)$  vs.  $x_{\perp,p}(t)$  generated for varying values of  $\tau_p$  using equations 2.5 and 2.6. The curve for  $\tau_p = 1\mu s$  fits the experimental data well, indicating that the particles track the flow significantly better than indicated by the previous estimate of  $\tau_p \approx 4.5\mu s$ . The reason for this is likely a discrepancy between the actual distribution of particle sizes as compared to the mean particle diameter of  $d_p \approx 1\mu m$  supplied by the manufacturer of the seeder. Based on these results, the actual mean particle diameter is probably closer to  $d_p \approx 0.5\mu m$ .

The characteristic time scale of the incoming boundary layer is  $t^* = \delta_0/U_\infty \approx 10.3\mu s$ , which leads to a particle Stokes number of  $St_p = \tau_p/t^* \approx 0.1$ . The low value of particle Stokes number and good agreement of the experimental data to the

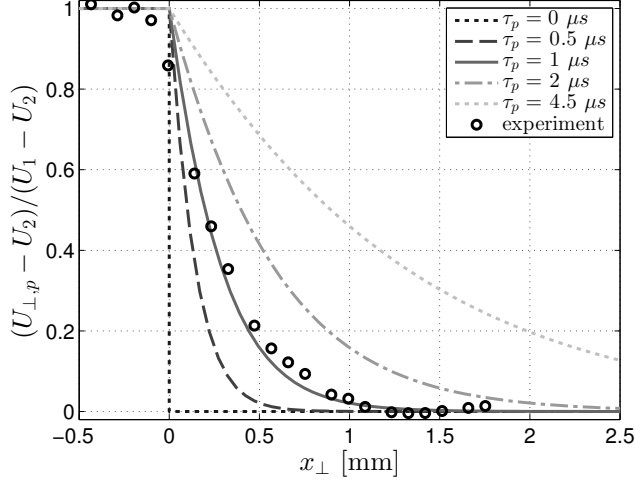


Figure 2.7: Experimental evaluation of particle time constant by comparison to theory based on Stokes drag.

analytical curve for  $\tau_p = 1\mu\text{s}$  in Figure 2.7 are consistent with the assumed linear drag law.

Figure 2.7 also shows that the PIV measurements “feel” the influence of the shock wave slightly upstream of its actual location. This is not due to the particle’s inertia, but rather to the finite area represented by a single PIV vector. An interrogation window centered slightly upstream of the shock wave encompasses both the high velocity incoming flow and the region behind the shock where the particle velocity begins to relax to the downstream air velocity. Therefore, PIV measurements slightly upstream of the shock wave are biased to lower velocities due to the finite measurement resolution. Downstream of the shock wave, the particle velocities are higher than the air velocity due to the finite distance over which the particles decelerate.

The particle relaxation distance is the distance over which particle relaxation effects are important and cause significant measurement errors. It can be defined as the particle displacement corresponding to  $t = \tau_p$ :

$$\xi_{\perp,p} = x_{\perp,p}(t = \tau_p) = \tau_p [U_1 - (U_1 - U_2)e^{-1}] \quad (2.7)$$

This length scale is sensitive to the upstream and downstream values of the velocity normal to the shock wave, so unlike the particle relaxation time, it varies depending on the local flow features. As an example, for the  $-37^\circ$  angle oblique shock wave used in this analysis, the particle relaxation distance is  $\xi_{\perp,p} = 0.28\text{mm}$  in the shock-normal coordinate, which corresponds to  $\xi_p = 0.21\text{mm}$  in the streamwise  $x$  direction. The choice of using a  $1/e$  cutoff to define the particle relaxation distance is somewhat arbitrary. If instead a threshold of 0.1 is chosen, the particle relaxation distances are significantly larger:  $\xi_{\perp,p} = 0.62\text{mm}$  and  $\xi_p = 0.50\text{mm}$ .

### 2.3.3 PIV data processing

The PIV data processing code was first developed by Han (2001) and subsequently modified by Helmer (2011) for application to high speed flows with a large dynamic range of particle displacements. Further modifications to the code made specifically for the current study include:

- A new scheme is implemented for generating the initial guess for interrogation window offsets used in the first round of processing. Previously, the initial guess of pixel offsets was generated by hand based on inspection of raw image pairs. Now the initial guess is automatically generated by a low-resolution first pass at PIV processing using  $64 \times 64$  pixel interrogation windows and 50% overlap. For each interrogation region, the cross-correlation functions for each of  $\approx 150$  image pairs are computed and summed to improve the signal to noise ratio. Then the most likely mean pixel displacement for each interrogation region, determined by locating the peak in the summed correlation function, is extracted and used as the initial guess for the first round of processing.
- A new method for determining the physical vertical position of each tile of data is developed. This method directly uses the pixel locations of the top

and bottom walls as seen in the background images in order to ensure that the data are correctly positioned and aligned relative to the geometric features of the wind tunnel. As in Helmer (2011), a precisely machined grid with fiducial markings is used to determine image resolution ( $\mu\text{m}/\text{pixel}$ ) and to define the streamwise position of each data tile.

- Several subfunctions within the PIV processing and post-processing codes are optimized for faster processing and lower memory requirements. These subfunctions perform operations including interpolation, mean and median calculation, and file I/O.

Raw images are acquired in batches of 125 – 500 images as described in section 2.2. The image data are background subtracted prior to processing. Background images are generated by averaging all of the images in a batch. This is done individually for images from the first and second exposures in a pair in order to account for any differences in light sheet intensity between the two laser pulses.

The background-subtracted data are processed using an FFT-based cross-correlation algorithm with an iterative interrogation scheme. The first iteration uses  $64 \times 64$  pixel interrogation regions and a spatially varying initial guess for the pixel displacement between interrogation regions, generated as described above. The algorithm then iterates twice at  $32 \times 32$  pixel window sizes and does a final pass with  $16 \times 16$  pixel windows. The image resolution is  $15\mu\text{m}/\text{pixel}$ , leading to a final vector spacing of 0.12mm with 50% overlap. This high resolution means that incoming boundary layer profiles include  $\approx 45$  data points between the wall and the edge of the boundary layer at  $y = \delta_0 = 5.4\text{mm}$ . Helmer (2011) acquired data for the smaller ramp case ( $h_{\text{ramp}}/\delta_0=0.20$ ) at an even higher resolution.

The vector field of pixel displacements is computed individually for each image pair. This is in contrast to the method used to generate the initial guess, in which

the correlation functions for many individual realizations are summed. The benefit of computing a vector field from each image pair is that it provides independent instantaneous snapshots of the flow, allowing for computation of turbulence statistics and analysis of quantities like reverse flow probability. Furthermore, the computation of one vector field from a given image pair is independent of the calculation of all the other vector fields, allowing for the code to be easily parallelized.

In order to achieve a high dynamic range of particle displacements for accurate measurement of both low and high velocity regions, the freestream particle displacement between frames is larger than the size of the final interrogation windows. Therefore in fast regions of the flow, the actual resolution of the velocity vectors in the streamwise direction is dictated by the physical distance traveled by particles between image frames. In the incoming freestream where the mean velocity is 530 m/s, this distance is approximately  $425\mu\text{m}$ . Even considering the effects of particle travel, the measurements presented in this thesis are of considerably higher resolution than most previous PIV studies of SBLI flows.

The drawback of having such high resolution measurements is that the field of view in each camera location is small, meaning that it is impossible to capture instantaneous snapshots of large scale structures in the flow or to examine correlations between widely spaced points. This trade off between velocity dynamic range and spatial dynamic range is described by Adrian (1997). However, by stitching together the tiles of data, a statistical representation of  $U$ ,  $V$ ,  $u'$ ,  $v'$ , and  $\langle u'v' \rangle$  is possible over a large area. The PIV acquisition parameters are summarized in Table 2.1.

Instantaneous velocity vector fields are validated using several criteria. First, a correlation coefficient of at least 0.5 is required to consider the cross-correlation peak between interrogation windows valid. Secondly, a range filter is implemented to remove spurious vectors that fall outside a pre-determined span of  $U \in [-130, 740]$  m/s and  $V \in [-250, 250]$  m/s. Thirdly, a filter is used to remove outliers, defined

Table 2.1: Summary of PIV parameters.

aperture setting, $f\#$	$f/8$
lens focal length	200 mm
image magnification, $M_o$	0.45
image resolution	15 $\mu\text{m}/\text{pixel}$
final interrogation region size	16 $\times$ 16 pixels
vector spacing (50% overlap)	0.12 mm
laser sheet thickness	0.7 mm
laser light wavelength, $\lambda$	532 nm
inter-frame time, $\Delta t$	0.8 $\mu\text{s}$
particle time constant, $\tau_p$	1.0 $\mu\text{s}$
number of image pairs per tile	5000
camera field of view	19.2 mm $\times$ 15.4 mm (TSI 630047) 28.4 mm $\times$ 28.4 mm (TSI PowerPlus 4MP)
pixel array	1280 $\times$ 1024 (TSI 630047) 2048 $\times$ 2048 (TSI PowerPlus 4MP)
physical pixel size, $d_{pix}$	6.45 $\mu\text{m}$ (TSI 630047) 6.70 $\mu\text{m}$ (TSI PowerPlus 4MP)

as any instantaneous velocity vectors which deviate from the local mean velocity by more than three standard deviations. In regions where false correlations with reflections from the walls may occur, the histograms of instantaneous velocity samples are carefully examined to ensure the data quality. Finally, data are cropped from the flow field representation in any region in which the yield of valid vectors is less than 10%.

Peak locking is a phenomenon where the pixel displacements calculated by the PIV processing algorithm are biased toward integer values. This effect is most severe when particle images are under-sampled; i.e. the size of the particle image is smaller than the physical size of a pixel on the camera sensor. It can also occur in regions of the flow with low seeding density. Histograms of instantaneous velocity realizations from the present experiments exhibit moderate peak-locking in some regions of the flow, particularly inside the boundary layers where seed density is lower. Figure

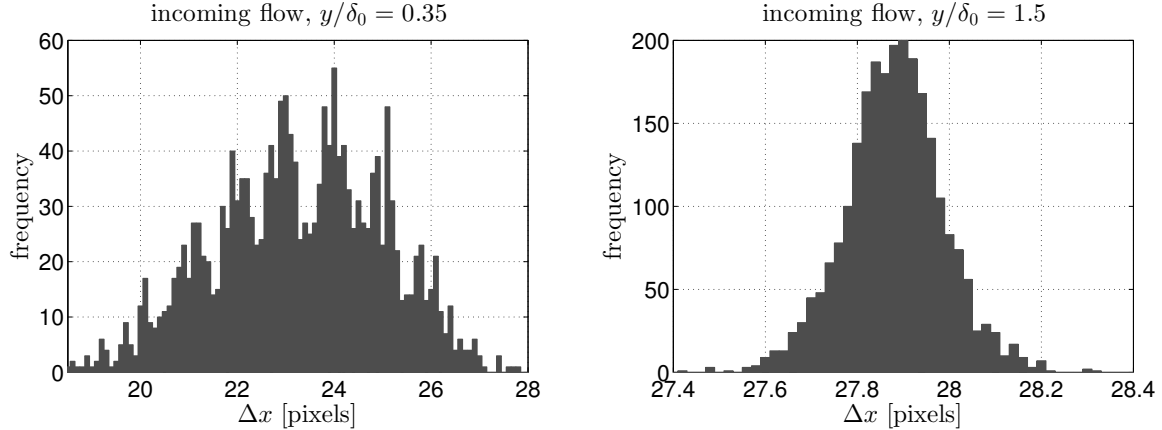


Figure 2.8: Histograms of peak-locked streamwise pixel displacements inside the incoming boundary layer (left panel) and non-peak-locked streamwise pixel displacements in the incoming freestream (right panel).

2.8 shows histograms of pixel displacements in the incoming boundary layer where moderate peak-locking is present and the incoming freestream which does not exhibit peak-locking. Note that the  $x$ -axes are scaled differently on the two plots and that the dynamic range of the measurements is large in regions where peak-locking is significant.

The image magnification and aperture settings are chosen to ensure that the particle images are resolved ( $d_\tau/d_{pix} > 2$ , where  $d_\tau$  is the particle image diameter and  $d_{pix}$  is the physical size of a pixel) in order to reduce the severity of the peak-locking. The particle images are diffraction-limited, so their size can be accurately estimated by the diffraction-limited spot size (Raffel et al. (2007)):

$$d_\tau \approx 2.44(1 + M_o)f^\# \lambda \quad (2.8)$$

The image magnification ( $M_o$ ),  $f$ -number ( $f^\#$ ), wavelength ( $\lambda$ ), and pixel size ( $d_{pix}$ ) are all listed in Table 2.1.

In order to determine the displacement associated with well-resolved particle images more accurately than  $\pm 0.5$  pixels, a sub-pixel estimation scheme is required.

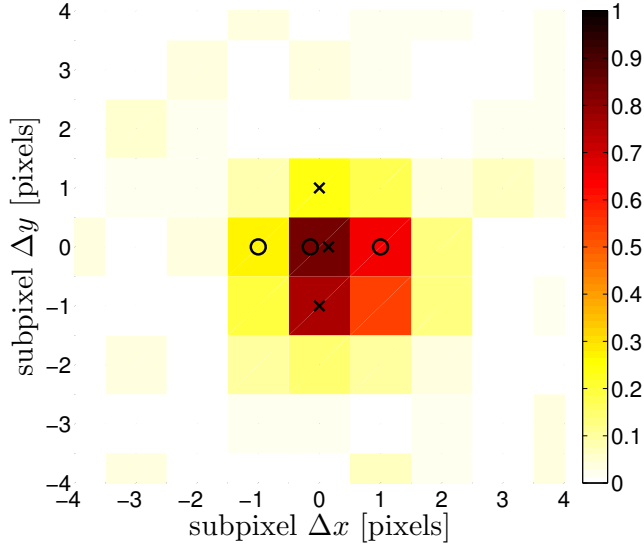


Figure 2.9: Sample 2D PIV correlation peak. Circles and  $\times$ -marks show which points are used in the sub-pixel estimation schemes for the  $x$  and  $y$  displacements, respectively.

Three commonly used estimators include centroid, parabolic fit, and Gaussian fit. Each of these methods uses five points on the 2D correlation peak to estimate the location of the “true” peak for the two in-plane directions at sub-pixel resolution. The Gaussian sub-pixel estimator yields the most accurate results in most practical situations (Adrian & Westerweel (2011)), and is therefore employed in the current PIV processing algorithm.

An example correlation peak is shown in Figure 2.9. The maximum sampled value of the correlation occurs at  $\Delta x = \Delta y = 0$ . However, the actual peak of the underlying distribution is slightly offset (by  $< 0.5$  pixels) in both the  $x$  and  $y$  directions. In order to estimate this sub-pixel offset, the values of the correlation function at the points labeled with circles and  $\times$  marks are extracted and used in determining a Gaussian fit to the correlation data in each direction. The estimates of the sub-pixel offsets,  $\hat{\varepsilon}_x$  and  $\hat{\varepsilon}_y$ , are equal to the mean values of the fitted Gaussians.

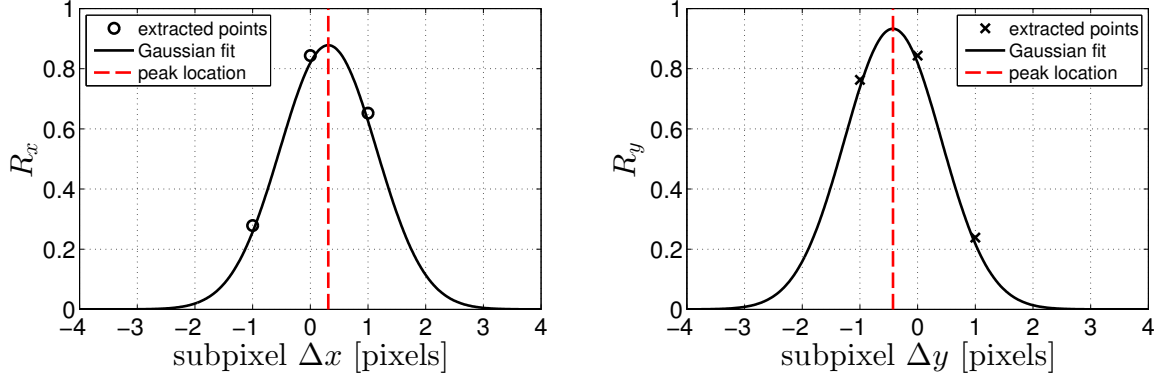


Figure 2.10: Gaussian fits to the correlation function for estimation of sub-pixel displacements in the  $x$  (left panel) and  $y$  (right panel) directions. The sub-pixel displacement estimates,  $\hat{\varepsilon}_x$  and  $\hat{\varepsilon}_y$ , are marked by dashed red lines.

Because the logarithm of a Gaussian is a parabola, a simple explicit relation for the mean of the fitted Gaussian can be written as:

$$\hat{\varepsilon}_x = \frac{\ln(R_{-1}) - \ln(R_{+1})}{2 [\ln(R_{-1}) + \ln(R_{+1}) - 2\ln(R_0)]} \quad (2.9)$$

where  $R_n$  represents values of the correlation function at the upstream ( $n = -1$ ), centered ( $n = 0$ ), and downstream ( $n = +1$ ) locations marked by circles in Figure 2.9. The same formula can be applied in the  $y$  direction, using the vertically oriented points labeled with  $\times$ -marks instead. The Gaussian sub-pixel estimation scheme is applied to the correlation function from Figure 2.9, with the resulting fits shown in Figure 2.10. The computed sub-pixel displacement estimates are  $\hat{\varepsilon}_x = 0.31$  pixels and  $\hat{\varepsilon}_y = -0.43$  pixels.

## 2.4 Uncertainty analysis

The error sources considered in the uncertainty analysis presented here include peak-locking, finite number of velocity samples, and misalignment. The uncertainties due to these types of errors can be estimated using traditional methods, and representative

estimates or ranges are provided. However, the most significant errors in the mean velocity are due to the effects of particle travel between image frames, finite resolution of interrogation regions, and particle inertia. These sources of PIV measurement bias are significantly more complicated and vary greatly across the flow field depending on the local flow features. Therefore Chapter 5 is devoted to the development of a much more quantitative and detailed analysis of the effects of these error sources.

### 2.4.1 Peak-locking

According to Adrian & Westerweel (2011) and Raffel et al. (2007) the error in mean velocity due to peak locking is small. Christensen (2004) finds that even in the limiting case of complete peak-locking (integer values only), the mean velocity is not affected. This is true for data where the dynamic range of particle displacements is at least 3-4 pixels, which is the case in the current experiments for all regions of the flow that exhibit peak-locking. Therefore peak-locking is not a source of uncertainty in the mean velocity measurements presented in this work.

However, peak-locking does affect the computation of turbulence statistics from PIV data ensembles. Fortunately, the large dynamic range of pixel displacements in the present experiments mitigates these effects. For example, the pixel displacement associated with the freestream velocity ( $U_\infty = 530$  m/s) is 28.3 pixels. Streamwise velocity fluctuations up to 30% of  $U_\infty$  and wall-normal velocity fluctuations up to 15% of  $U_\infty$  are observed in the SBLI regions. These RMS velocities represent displacements of 8.4 and 4.2 pixels, respectively. Therefore, even for moderate to severely peak-locked data, the dynamic range of these measurements significantly reduces the bias errors due to peak-locking in the turbulent fluctuations (Christensen (2004)).

Upper bounds on the uncertainties of  $u'$ ,  $v'$ , and  $\langle u'v' \rangle$  associated with peak-locking are established using the following procedure. First all three statistics are computed at several points in the upstream boundary layer using the appropriate

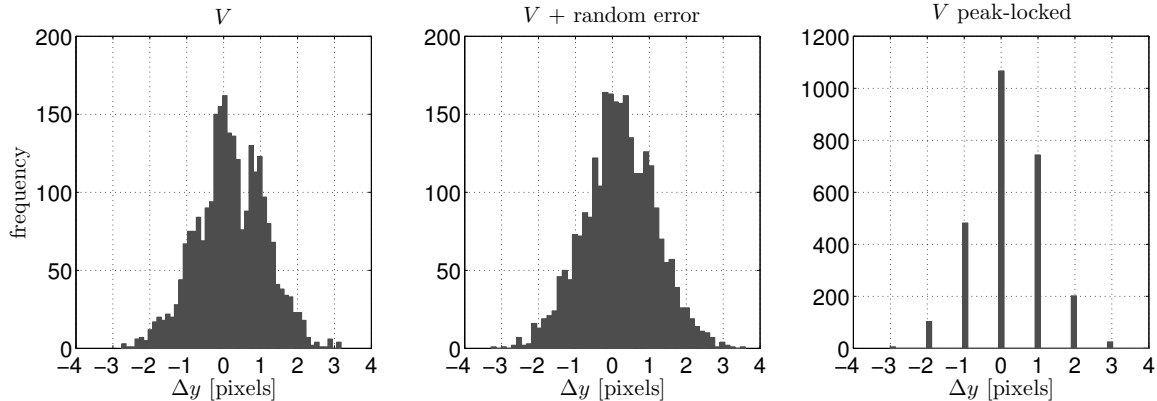


Figure 2.11: Illustration of process for analyzing uncertainty in  $v'$ . The original data are moderately peak-locked (left panel). Then the original data are randomly perturbed by samples from a zero-mean normal distribution with  $\sigma = 0.25$  (center panel). Finally, the perturbed data are rounded to the nearest integer value to simulate complete peak-locking (right panel).

ensembles of valid pixel displacements in the streamwise and wall-normal directions. Next, the data in these pixel-displacement ensembles are perturbed by independent samples from a zero-mean normal distribution with a standard deviation of 0.25 pixels, corresponding to the estimated peak-locking error. The velocity statistics are then recomputed using these perturbed ensembles of pixel displacements and compared to the original estimates. Differences between the statistics computed using the original data and the randomly perturbed data are very small. To simulate the most severe case of peak-locking possible, the statistics are again computed after rounding all of the perturbed pixel displacements to their nearest integer values. This process is illustrated for the wall-normal velocity component in Figure 2.11.

The differences between the statistics computed from the original dataset and the completely peaklocked dataset were small, and they represent the absolute upper bound on the peak-locking error. The estimated maximum uncertainties using this method were 0.15% of  $U_\infty$  for  $u'$ , 0.25% of  $U_\infty$  for  $v'$ , and < 0.001% of  $U_\infty^2$  for  $\langle u'v' \rangle$ . The true uncertainties due to peak locking are probably significantly smaller because

the degree of peak-locking is much less severe than the worst case presented here.

### 2.4.2 Sampling

Estimates of the mean velocities,  $U$  and  $V$ , are obtained by ensemble averaging the  $N$  valid vectors at each point in the flow. Therefore, the finite number of velocity realizations causes a small uncertainty in the estimated values of  $U$  and  $V$ . An estimate for the standard deviation of the distribution of the sample mean velocity,  $U$ , based on  $N$  valid instantaneous realizations, is given by:  $\sigma_U \approx u'/\sqrt{N}$ . For the wall-normal component, the result is analogous:  $\sigma_V \approx v'/\sqrt{N}$ . The magnitude of this effect varies throughout the flow field because of the spatial variability of both the turbulence intensities and the number of valid vectors.

The minimum number of valid vectors at any point in the flow is  $N = 500$ , corresponding to 10% yield. However, in most regions of the flow over 50% yield is observed ( $N \geq 2500$ ). In the incoming freestream, the velocity fluctuations in the streamwise and wall-normal directions are well below  $0.01U_\infty$ . The maximum values of  $u'$  and  $v'$  are  $0.3U_\infty$  and  $0.15U_\infty$ , respectively. In the following analysis, the quoted uncertainty values are  $\pm 1.96\sigma_U$  and  $\pm 1.96\sigma_V$ , corresponding to 95% confidence intervals on  $U$  and  $V$ .

In the absolute worst case (minimum  $N$  and maximum  $u'$  or  $v'$ ), the uncertainty on  $U$  due to finite sample size is  $\pm 14$  m/s ( $\pm 2.6\%$  of  $U_\infty$ ) and the uncertainty on  $V$  is  $\pm 7$  m/s ( $\pm 1.3\%$  of  $U_\infty$ ). In the incoming freestream flow where  $u'$  and  $v'$  are very low and yield is at least 90%, the uncertainty on  $U$  and  $V$  is less than  $\pm 0.1$  m/s ( $< \pm 0.02\%$  of  $U_\infty$ ). In most regions outside the incoming freestream, the uncertainties on  $U$  and  $V$  due to finite sample size fall somewhere between these upper and lower bounds. Representative estimates of mean velocity uncertainties based on moderate values of velocity fluctuations and valid vector yield ( $u' = 0.15U_\infty$ ,  $v' = 0.075U_\infty$ , and  $N = 2500$ ) are  $\pm 3.2$  m/s ( $\pm 0.6\%$  of  $U_\infty$ ) for  $U$  and  $\pm 1.6$  m/s ( $\pm 0.3\%$  of  $U_\infty$ ) for  $V$ ,

Table 2.2: Uncertainty on mean velocities due to finite sampling

	$u'/U_\infty$	$v'/U_\infty$	$N$	$U$ uncertainty (% of $U_\infty$ )	$V$ uncertainty (% of $U_\infty$ )
worst case	0.3	0.15	500	$\pm 2.6$	$\pm 1.3$
best case	0.005	0.005	4500	$\pm 0.015$	$\pm 0.015$
representative	0.15	0.075	2500	$\pm 0.6$	$\pm 0.3$

Table 2.3: Uncertainty on turbulence statistics due to finite sampling

$z/\delta_0$	3.89	1.48	1.02	0.74	0.46
$u'$ and $v'$ uncertainty (% of $U_\infty$ )	0.1	0.1	0.2	0.25	0.5
$\langle u'v' \rangle$ uncertainty (% of $U_\infty^2$ )	0.01	0.01	0.02	0.05	0.1

respectively. These results are summarized in Table 2.2.

The uncertainty involved in the computation of  $u'$ ,  $v'$ , and  $\langle u'v' \rangle$  from a finite number of instantaneous velocity samples is more difficult to assess. Following the analysis of Helmer (2011), these uncertainties are estimated by examining the noise level in the  $u'$ ,  $v'$ , and  $\langle u'v' \rangle$  profiles in the incoming flow far from the top wall where the values should be relatively constant. The results of this analysis are presented in Table 2.3. The reason for higher uncertainties in the data planes closer to the side wall is that the seeding density decreases within the side wall boundary layer, leading to lower overall yields of valid vectors.

### 2.4.3 Alignment

The measurement resolution and alignment of data tiles are based on images of a grid with precisely machined horizontal and vertical lines at 3mm intervals. If the camera is not aligned perfectly such that a horizontal row of pixels is at a constant  $y$ -coordinate in the wind tunnel, this misalignment is measured in both the angle of the grid lines and the angle of the wall in the background images. The pixel

displacements computed in the PIV processing algorithm are rotated to correct for this misalignment. The maximum possible misalignment after this procedure is performed is  $\phi = \pm 0.05^\circ$ . Misalignment errors in mean streamwise velocity,  $U$ , and mean wall-normal velocity,  $V$ , are given by the following equations:

$$\begin{aligned} U_{error} &= U(\cos\phi - 1) - V\sin\phi \\ V_{error} &= U\sin\phi + V(\cos\phi - 1) \end{aligned} \quad (2.10)$$

For very small angles,  $|\sin(\phi)| \gg |1 - \cos(\phi)|$ . Therefore,  $\max\{|U_{error}|\}$  occurs where  $|V|$  is largest – directly downstream of the oblique shockwave where  $V \approx -100$  m/s. Similarly  $\max\{|V_{error}|\}$  occurs where  $|U|$  is largest – the incoming freestream where  $U = 530$  m/s. Then the maximum possible errors due to a misalignment of  $\phi = \pm 0.05^\circ$  are:

$$\begin{aligned} \max\{U_{error}\} &= \pm 0.1 \text{m/s} < \pm 0.02\% \text{ of } U_\infty \\ \max\{V_{error}\} &= \pm 0.5 \text{m/s} < \pm 0.1\% \text{ of } U_\infty \end{aligned} \quad (2.11)$$

By neglecting the very small  $(\cos\phi - 1)$  terms in equation 2.10, it is possible to derive an analytical expression for the error incurred in the turbulence quantities due to a small misalignment. These expressions are:

$$\begin{aligned} \langle u'^2 \rangle_{error} &= -2\langle u'v' \rangle \sin\phi + \langle v'^2 \rangle \sin^2\phi \\ \langle v'^2 \rangle_{error} &= 2\langle u'v' \rangle \sin\phi + \langle u'^2 \rangle \sin^2\phi \\ \langle u'v' \rangle_{error} &= (\langle u'^2 \rangle - \langle v'^2 \rangle) \sin\phi - \langle u'v' \rangle \sin^2\phi \end{aligned} \quad (2.12)$$

For small misalignments, the  $\sin^2\phi$  terms can be neglected, and thus the magnitude of the errors in the turbulent fluctuations can be written simply as:

$$\begin{aligned}|u'_{error}| &= |v'_{error}| = \sqrt{|2\langle u'v' \rangle \sin\phi|} \\ \langle u'v' \rangle_{error} &= (\langle u'^2 \rangle - \langle v'^2 \rangle) \sin\phi\end{aligned}\tag{2.13}$$

The errors in  $u'$  and  $v'$  are largest in the regions of the flow where  $|\langle u'v' \rangle|$  are largest. In the SBLI flows investigated in this thesis, the highest values of  $|\langle u'v' \rangle|$  are  $\approx 5 \times 10^{-3}U_\infty^2$ . Therefore, the upper bound on the misalignment error on the turbulent fluctuations can be established as:

$$\begin{aligned}\max\{|u'_{error}|\} &= \max\{|v'_{error}|\} = \pm 0.003U_\infty &= \pm 1.6 \text{ m/s} \\ \max\{|\langle u'v' \rangle_{error}|\} &= \pm 7 \times 10^{-5}U_\infty^2 &= \pm 20 \text{ m}^2/\text{s}^2\end{aligned}\tag{2.14}$$

# Chapter 3

## Effects of Confinement & Shock Strength

### 3.1 Inflow & boundary conditions

Documentation of the inflow and boundary conditions is critical for data sets intended for CFD validation. In the present experiments, the inflow is a simple rectangular duct flow with thin turbulent boundary layers on all four walls. The flow supply conditions are monitored and controlled continuously throughout the experiments to maintain a constant stagnation temperature of  $T_0 = 303 \pm 1$  K and stagnation pressure of  $P_0 = 255.3 \pm 1$  kPa. The incoming freestream flow has a streamwise velocity of  $U_\infty = 530$  m/s and a Mach number of  $M_\infty = 2.05 \pm 0.03$ . These operating conditions are listed in Table 3.1.

---

This chapter includes large portions of a manuscript submitted to the International Journal of Heat and Fluid Flow as Campo, L.M. and Eaton, J.K. (2014) Shock Boundary Layer Interactions in a Low Aspect Ratio Duct.

Table 3.1: Experimental operating conditions

$M_\infty$	$U_\infty$ [m/s]	$T_0$ [K]	$P_0$ [kPa]	$\dot{m}$ [kg/s]
$2.05 \pm 0.03$	530	$303 \pm 1$	$255.3 \pm 1$	0.67

Table 3.2: Characterization of incoming boundary layer

$\delta_0$ [mm]	$Re_{\delta_0}$	$\theta$ [mm]	$Re_\theta$	$U_\tau$ [m/s]
5.4	$1.82 \times 10^5$	0.47	$1.60 \times 10^4$	22.1

The flowfield at the upstream measurement station is unaffected by the shock-generating ramp height because the flow is supersonic. Detailed measurements of the incoming boundary layer on the top wall are made for both the  $h_{\text{ramp}}/\delta_0 = 0.56$  and 0.93 geometries, confirming that the inflow conditions are consistent between test cases. To avoid confusion in the following discussion, the boundary layers growing on the top and bottom walls will be referred to as vertical boundary layers, while the boundary layers on the side walls will be called the side wall boundary layers. Profiles of the mean and fluctuating velocity components in the undisturbed incoming vertical boundary layer were extracted from PIV measurements on the upper surface at a station 35mm upstream of the foot of the shock-generating ramp. These profiles are shown in Figure 3.1. Note that only every third data point is plotted to make the figures more readable.

The undisturbed incoming vertical boundary layer has 99% velocity thickness  $\delta_0 = 5.4\text{mm}$ , and momentum thickness  $\theta = 0.47\text{mm}$  near the spanwise centerline of the duct ( $z/\delta_0 = 3.89$ ). The appropriate Reynolds numbers associated with the incoming boundary layer are  $Re_{\delta_0} = 1.82 \times 10^5$  and  $Re_\theta = 1.60 \times 10^4$ , based on the freestream viscosity and density. These boundary layer properties are summarized in Table 3.2.

The profiles in Figure 3.1 are plotted from the top wall ( $y/\delta_0 = 0$ ) to the duct's vertical half-height ( $y/\delta_0 = 4.17$ ). The turbulence quantities are not density-weighted

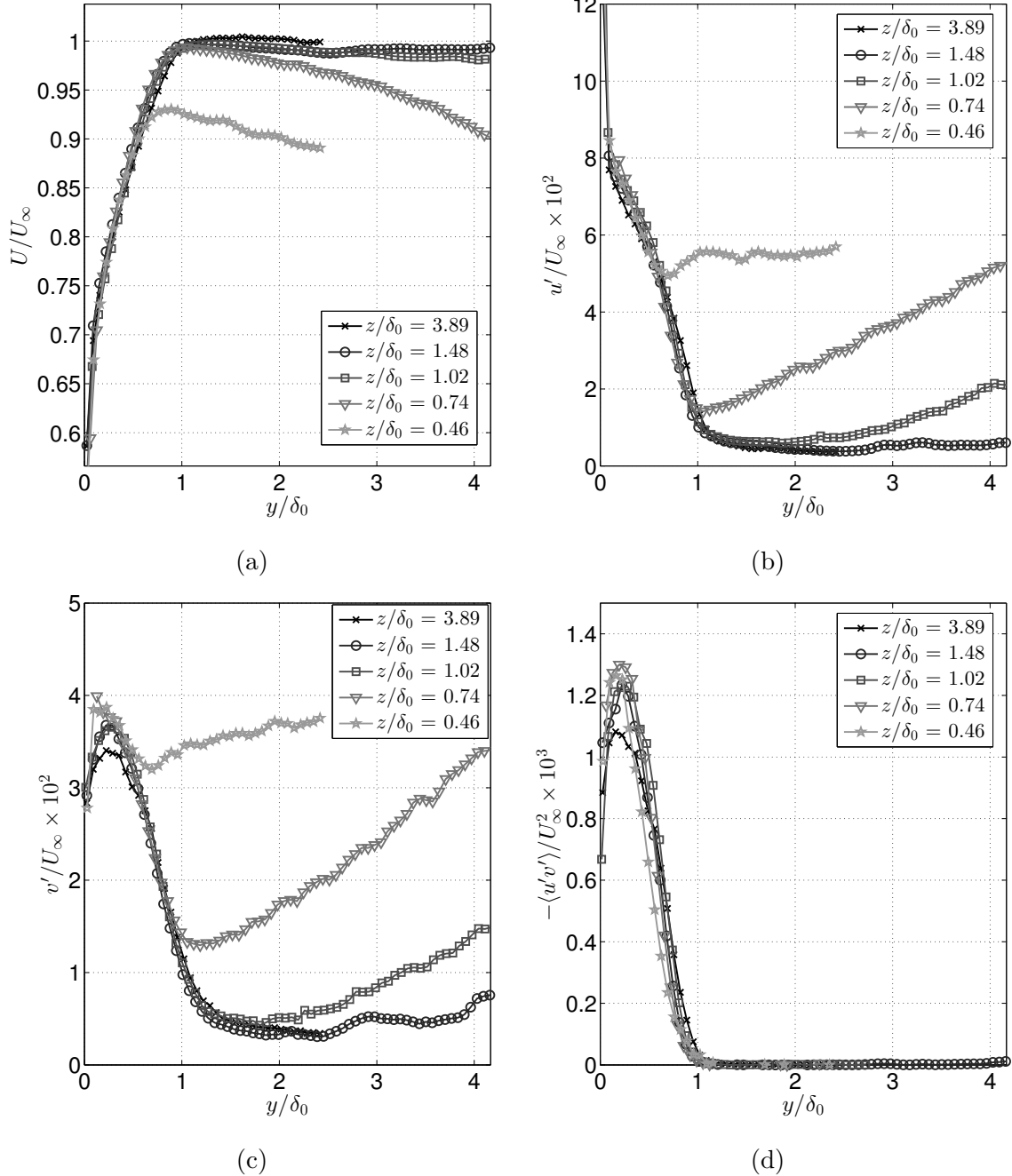


Figure 3.1: Profiles of (a) streamwise mean velocity; (b) streamwise velocity fluctuations; (c) vertical velocity fluctuations; (d) Reynolds shear stresses; at four stations across the tunnel span. Profiles are taken at a fixed streamwise position of  $x = -35\text{mm}$  ( $x/\delta_0 = -6.48$ ), which is upstream of any influence of the compression ramp. The vertical ( $y$ ) coordinate extends to the vertical half-height of the tunnel.

$(\sqrt{\rho/\rho_w})$  because accurate computation of the local density for the profiles inside the side wall boundary layer is not possible. Positive vertical velocities are defined as away from the top wall. The mean velocity and normal stresses may be assumed to be symmetric about the vertical half-height of the duct, while the shear stresses are anti-symmetric.

The mean streamwise velocity profiles at different spanwise locations in Figure 3.1a collapse within the inner half of the vertical boundary layer,  $y/\delta_0 \leq 0.5$ . This suggests that the wall shear stress does not vary significantly across the span in the undisturbed inlet section. However, outside of  $y/\delta_0 = 0.5$  the profiles deviate significantly. The profiles inside the side wall boundary layer ( $z/\delta_0 = 0.74$  and  $0.46$ ) show a distinct non-monotonic shape and do not asymptote to  $U_\infty$ . The profile closest to the side wall attains a maximum of  $\approx 0.93U_\infty$  around  $y/\delta_0 = 0.8$  and decreases toward the center of the duct. The profile at  $z/\delta_0 = 0.74$  reaches a maximum velocity of  $\approx U_\infty$  at the edge of the vertical boundary layer ( $y/\delta_0 = 1$ ) and decays to  $\approx 0.9U_\infty$  at the half-height of the duct. This overshoot effect is also present in the velocity profile at  $z/\delta_0 = 1.02$ , but it is far less pronounced. The velocity profile at  $z/\delta_0 = 1.48$  agrees very closely with the near-centerline profile ( $z/\delta_0 = 3.89$ ); the only difference is a very slightly ( $\approx 1\%$ ) lower freestream asymptotic velocity. The mean vertical velocity everywhere in the inlet section deviates from zero by no more than  $+4\%$  and  $-2\%$  of  $U_\infty$ , and is within  $\pm 1\%$  of  $U_\infty$  in most regions of the inlet.

Profiles of the streamwise and vertical velocity fluctuations at four locations across the span are shown in Figures 3.1b and 3.1c, respectively. Similar to the behavior of the mean streamwise velocity, the profiles of velocity fluctuations collapse within the vertical boundary layer,  $y/\delta_0 \leq 0.5$ , and deviate outside this region. The streamwise and vertical velocity fluctuations in the  $z/\delta_0 = 0.74$  and  $1.02$  measurement planes exhibit minima near  $y/\delta_0 = 1$  and then increase toward the half-height of the duct. For the  $u'$  and  $v'$  profiles in the  $z/\delta_0 = 0.46$  plane, the minimum is attained deeper

within the vertical boundary layer ( $y/\delta_0 \approx 0.6$ ). The turbulence intensity far from the top wall increases with decreasing distance to the side wall. In particular, the values of  $v'$  far from the wall in the  $z/\delta_0 = 0.46$  plane are comparable to the maximum level of vertical velocity fluctuations. Near the centerline ( $z/\delta_0 = 3.89$ ) and outside the vertical boundary layer ( $y/\delta_0 > 1$ ), the magnitude of the streamwise and vertical fluctuations decay to  $< 1\%$  of  $U_\infty$ . This measurement represents both the freestream turbulence level as well as any overall unsteadiness, and therefore indicates that the inlet flow is clean and does not exhibit any significant unsteadiness. Unlike the mean velocity and normal stresses, the shear stress profiles (Figure 3.1d) collapse everywhere. The only deviation is a slightly lower peak in  $-\langle u'v' \rangle$  near the centerline ( $z/\delta_0 = 3.89$ ).

These profiles upstream of the interaction show that the flow is clearly three-dimensional in the inlet section. The non-monotonic profiles at the edge and inside the side wall boundary layer are consistent with the presence of corner vortices as expected in a supersonic duct flow (see e.g. Davis et al. (1986) or Davis & Gessner (1989)). In a supersonic duct flow with counter rotating corner vortices, the secondary flow forces a jet of high momentum air directed at  $45^\circ$  into the corner. These vortices also sweep lower momentum fluid away from the walls at locations away from the corner. Therefore, a vertically oriented mean velocity profile extracted within the side wall boundary layer should show the mean velocity first increasing with increasing distance from the top wall, then reaching a maximum which is less than the freestream velocity in the core, and then decreasing further from the top wall as it passes through the part of the side wall boundary layer that is thickened by the corner vortex. Unfortunately the secondary flows cannot be directly resolved in the current experiments. However, it is interesting to note that the non-monotonic behavior noted in the 1D mean velocity profiles is at least qualitatively consistent with the type of secondary flow that is expected in this configuration. Based on collaborations with Bermejo-Moreno

et al. (2014), it is evident that correct representation of these secondary flow features in the inlet section is critical for accurate CFD prediction of the rest of the flowfield.

The PIV data do not include measurements of the spanwise velocity component and are not sufficiently resolved in the corner to fully describe these secondary flows. Therefore, CFD simulations should begin as far upstream as possible, perhaps even at the nozzle throat where the inflow conditions are well defined based on the isentropic relations at  $M = 1$  and the known stagnation quantities,  $P_0$  and  $T_0$ . The nozzle acceleration is strong and the boundary layers are extremely thin at that point. Furthermore, the Reynolds number is high enough that transition occurs shortly downstream of the nozzle exit.

If it is necessary to start the simulations at a point further downstream in the duct, then the inflow should be generated by a method similar to that used by Bermejo-Moreno et al. (2014). This process involves generating synthetic inflow turbulence using a digital filtering technique and matching the experimental mean and turbulent velocity profiles at the inflow location. To construct an appropriate spanwise-vertical plane of inlet data, Bermejo-Moreno et al. (2014) reflect the experimental 1D profiles at varying locations across the span across the corner bisector to approximate the side wall boundary layer. The intermediate regions where experimental data are unavailable are filled by interpolation. The inflow may be considered symmetric across both the vertical and spanwise centerplanes.

The side wall boundary layers are expected to be very similar to the top wall boundary layer where the inlet profile measurements are made. While direct measurements of the side wall boundary layers are not available, this assumption can be justified using the following reasoning. The inlet contraction used to accelerate the flow to  $M = 1$  is designed using a 5th order polynomial with zero curvature at both endpoints. Furthermore the nozzle length to contraction ratio is  $L/H = 10$ , indicating gentle and continuous curvature throughout. This design is known to minimize

secondary flows due to transverse pressure gradients caused by streamline curvature. Any differences in the boundary layers at the exit of the converging-diverging nozzle are minimal because all four boundary layers are extremely thin due to the large favorable pressure gradient. The boundary layers on all walls become fully turbulent a short distance downstream ( $\approx 6\text{mm}$ ) and develop similarly through the approximately zero pressure gradient square duct upstream of the measurement domain.

The wind tunnel is allowed to run continuously for at least 20 minutes prior to any data acquisition, allowing the whole system to achieve a thermal steady state. For all experiments, the adiabatic wall temperature in the test section inlet is  $T_{aw} = 288\text{K}$ , based on a recovery factor of  $r = 0.89$  and stagnation temperature of  $T_0 = 303\text{ K}$ . This temperature is very close to the ambient temperature, and therefore the small heat flux due to natural convection on the outer surfaces of the wind tunnel may be considered negligible. For CFD simulations of this experimental configuration, adiabatic wall boundary conditions are recommended.

## 3.2 Overview of shock & interaction features

Figures 3.2 and 3.3 depict the primary flow features near the spanwise centerplane of the duct for the  $h_{\text{ramp}}/\delta_0 = 0.56$  and  $h_{\text{ramp}}/\delta_0 = 0.93$  test section geometries, respectively. In both cases, the incident shock wave (IS) is generated by the  $20^\circ$  compression ramp on the top wall. An expansion fan is generated at the downstream end of the ramp where the top wall turns back to horizontal. The small and mid-size ramp configurations ( $h_{\text{ramp}}/\delta_0 = 0.20$  and  $0.56$ ) cause regular reflection of the incident shock wave, whereas the large ramp geometry ( $h_{\text{ramp}}/\delta_0 = 0.93$ ) causes a Mach reflection. In both types of reflections, compression waves emanate from the bottom wall upstream of the projected impingement point of the incident shock, and these waves coalesce into the separation shock (SS). In the case of the larger

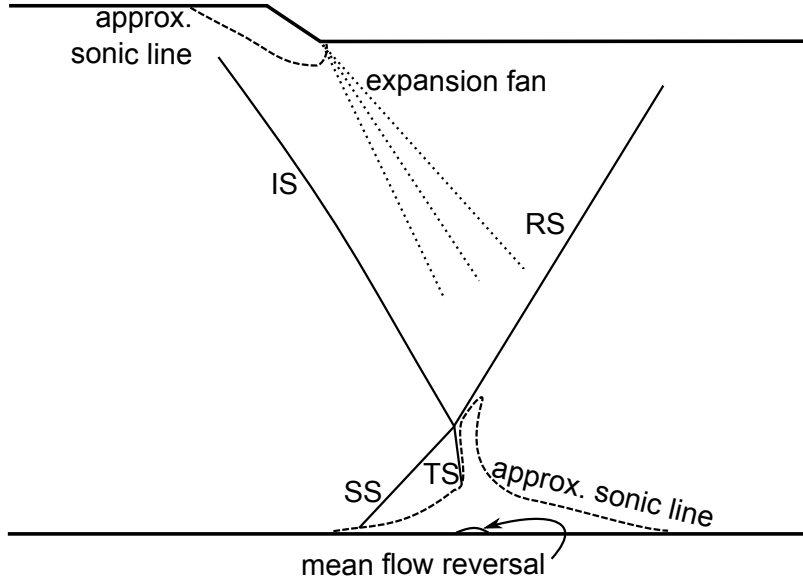


Figure 3.2: Shock and interaction features near the spanwise centerplane for the  $h_{\text{ramp}}/\delta_0 = 0.56$  geometry. This case has a regular reflection of the incident shock.

ramp, the Mach stem (MS) sits near the core of the duct, resulting in a large region of subsonic flow downstream, as indicated by the approximate sonic line in Figure 3.3. The subsonic flow caused by the Mach stem is re-accelerated downstream by the expansion fans, and shear layers are evident at the top and bottom of the wake region. In both cases, the transmitted shock (TS) extends down toward the bottom wall until the point where the boundary layer becomes subsonic. The reflected shock (RS) departs from the intersection of the incident shock and Mach stem in the case of the Mach reflection, and from the intersection of the incident and separation shocks for the case of the regular reflection. In the large ramp geometry, a second reflection off of the top wall (RS2) occurs and this shock interacts with the wake downstream of the Mach stem; however these downstream features are not the primary focus of this investigation.

The shock angles vary with the size of the compression ramp, and for a given geometry there is a high degree of non-uniformity in the shock features across the

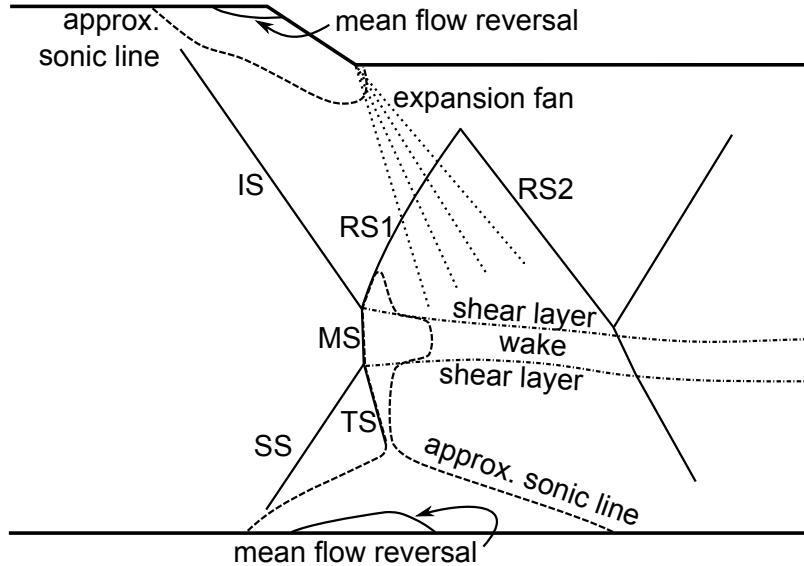


Figure 3.3: Shock and interaction features near the spanwise centerplane for the  $h_{\text{ramp}}/\delta_0 = 0.93$  geometry. This case has a Mach reflection of the incident shock.

span. The incident and reflected shock angles for both test geometries are reported in Table 3.3 and compared to the results of Helmer (2011) and Helmer et al. (2012), who investigated the flow field for the smaller ramp geometry ( $h_{\text{ramp}}/\delta_0 = 0.20$ ) with all of the other test parameters matching the current experiments. In some cases, the shock waves are curved so a range of angles are reported. The shock angles generally steepen as the side wall is approached, which is consistent with the fact that the incoming flow is slower in the vicinity of the side wall boundary layers. The steepening shock angle could also be related to oblique shock waves emanating from the side wall; however without data in streamwise-spanwise planes this is difficult to confirm. In all cases, the angle of the incident shock wave is considerably shallower than the  $-52^\circ$  angle predicted by inviscid theory for a Mach 2 flow impinging on a  $20^\circ$  ramp. This indicates that the small ramp height relative to the incoming boundary layer, viscous effects near the foot of the ramp, and confinement effects due to the side walls play an important role in determining the freestream behavior of the incident

Table 3.3: Summary of shock angles

$h_{\text{ramp}}/\delta_0$	$z/\delta_0$	incident shock angle	reflected shock angle
0.93	3.89	$-37^\circ$	$54^\circ$ to $44^\circ$
	1.48	$-41^\circ$	$47^\circ$
	1.02	$-45^\circ$	$47^\circ$
	0.74	$-47^\circ$	can't be identified
0.56	3.89	$-38^\circ$ to $-44^\circ$	$44^\circ$
	1.02	$-39^\circ$ to $-47^\circ$	$46^\circ$
	0.74	$-40^\circ$ to $-48^\circ$	$48^\circ$
	0.46	$-41^\circ$ to $-47^\circ$	can't be identified
0.20 Helmer (2011)	3.89	$-37^\circ$	$38^\circ$
	1.02	$-39^\circ$	$38^\circ$
	0.74	$-40^\circ$	$40^\circ$
	0.46	can't be identified	can't be identified

shock wave.

In the case of the largest ramp geometry, the angles of the separation and transmitted shocks can also be identified in the  $z/\delta_0 = 3.89$  and  $1.48$  planes. In the planes closer to the side wall, these features are no longer identifiable due to the high levels of velocity fluctuations associated with the thickening of the side wall boundary layer. Near the centerplane ( $z/\delta_0 = 3.89$ ), the separation and transmitted shocks have angles  $38^\circ$  and  $-60^\circ$ , respectively. Off center, but outside the side wall boundary layer ( $z/\delta_0 = 1.48$ ), the separation and transmitted shock angles are  $43^\circ$  and  $-76^\circ$ , respectively. These results are consistent with the trend of steeper shocks away from the centerline that was noted in the incident and reflected shock angles in Table 3.3.

### 3.3 Mean velocity

Mean streamwise velocity contours in each measurement plane for the mid-size ramp ( $h_{\text{ramp}}/\delta_0 = 0.56$ ) are shown in Figures 3.4 – 3.7. The mean streamwise velocity measurements for the large ramp ( $h_{\text{ramp}}/\delta_0 = 0.93$ ) are shown in Figures 3.8 – 3.11.

Similarly, mean vertical velocity contours for both ramp geometries are shown in Figures 3.12 – 3.19. Blank areas in the plots correspond to regions where data were not acquired or where data were deemed invalid based on the criteria described in section 2.3. In the mid-size ramp case the interaction regions are largely confined to the vicinity of the compression ramp and the impingement point of the incident shock, so measurements are acquired selectively in these regions. The SBLI caused by the larger ramp geometry is considerably stronger and exhibits a higher degree of three-dimensionality. Therefore, for the large ramp case the  $z/\delta_0 = 0.46$  measurement plane is eliminated and PIV data are acquired instead at an off-center plane outside the incoming side wall boundary layer,  $z/\delta_0 = 1.48$ .

The most prominent difference between the shock structures produced by the mid-size ( $h_{\text{ramp}}/\delta_0 = 0.56$ ) and large ( $h_{\text{ramp}}/\delta_0 = 0.93$ ) ramps is the presence of a Mach stem for the larger ramp geometry, as described in section 3.2. This feature is evident in the mean velocity data near the center of the span ( $z/\delta_0 = 3.89$ ), but it vanishes closer to the side wall. Even though the  $z/\delta_0 = 1.48$  plane resides outside the undisturbed upstream side wall boundary layer, the shock wave pattern and interaction zone in this plane are strongly affected by the interaction of the shocks with the side wall boundary layer. As the side wall is approached, the streamwise deceleration of the flow begins further upstream and is more gradual than the sharp deceleration across the incident shock wave in the core of the flow. In addition, subsonic flow is observed in the vicinity of the duct's vertical half height for the  $z/\delta_0 = 1.02$  and  $0.74$  planes. This is not due to the presence of a Mach stem in these planes, but rather due to the thickening of the side wall boundary layer as it interacts with the shock waves. These results are qualitatively consistent with the observations of Hanada et al. (2005), who report a high degree of spanwise non-uniformity in a normal shock boundary layer interaction in a duct, including a large low velocity region in the core of the flow and higher velocities off-center.

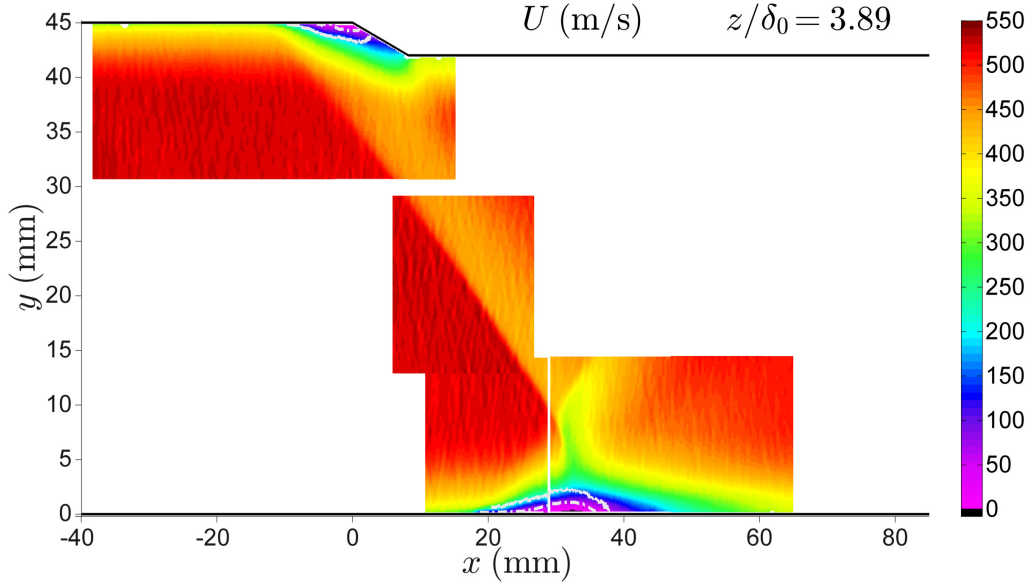


Figure 3.4: Mean streamwise velocity for the mid-size ramp ( $h_{\text{ramp}}/\delta_0 = 0.56$ ) at  $z/\delta_0 = 3.89$  (near centerline). Isocontours of reversed flow probability (— 5% and - - - 25%) are superimposed in white.

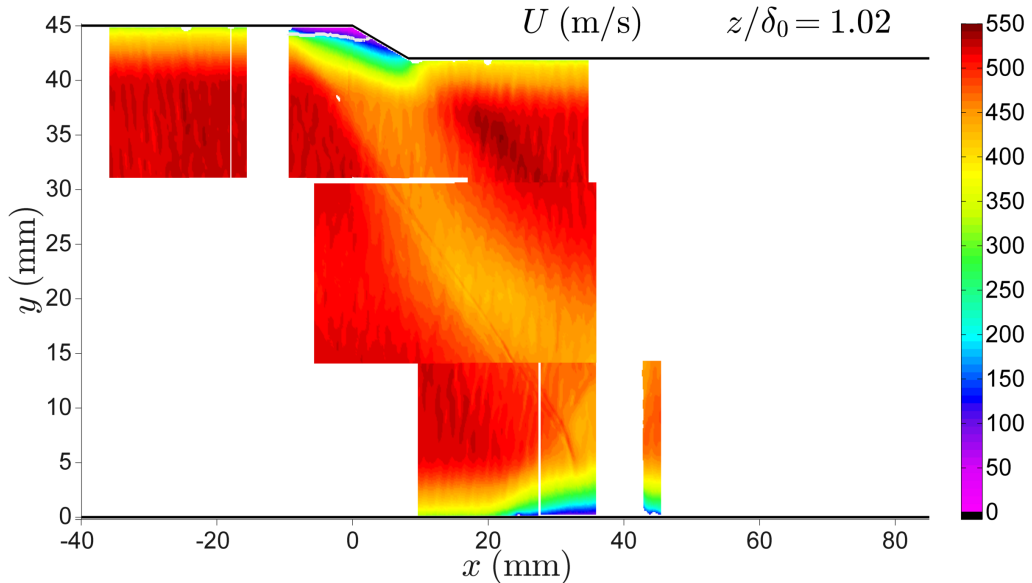


Figure 3.5: Mean streamwise velocity for the mid-size ramp ( $h_{\text{ramp}}/\delta_0 = 0.56$ ) at  $z/\delta_0 = 1.02$ . An isocontour of reversed flow probability (— 5%) is superimposed in white.

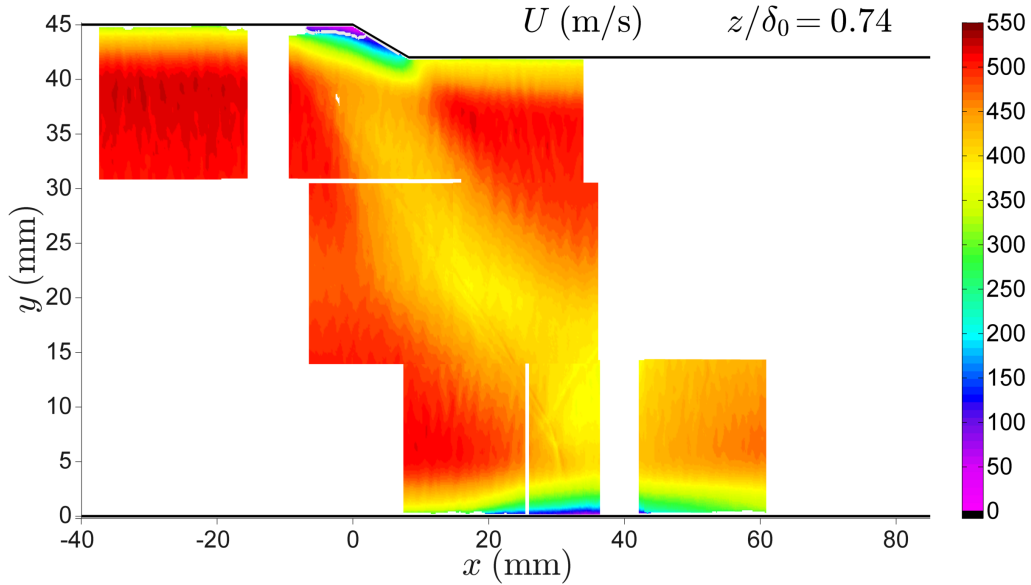


Figure 3.6: Mean streamwise velocity for the mid-size ramp ( $h_{\text{ramp}}/\delta_0 = 0.56$ ) at  $z/\delta_0 = 0.74$ . An isocontour of reversed flow probability (— 5%) is superimposed in white.

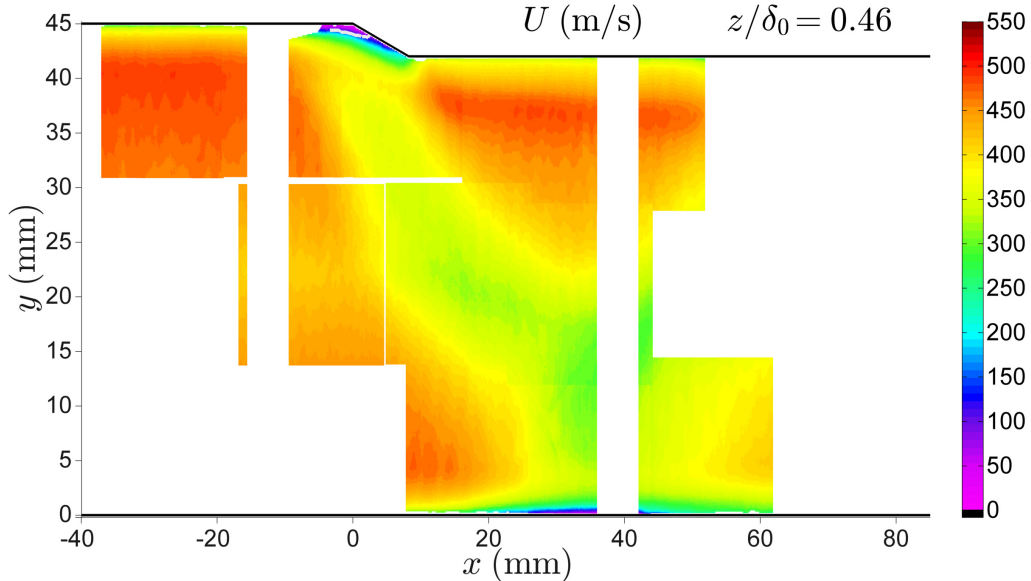


Figure 3.7: Mean streamwise velocity for the mid-size ramp ( $h_{\text{ramp}}/\delta_0 = 0.56$ ) at  $z/\delta_0 = 0.46$ . An isocontour of reversed flow probability (— 5%) is superimposed in white.

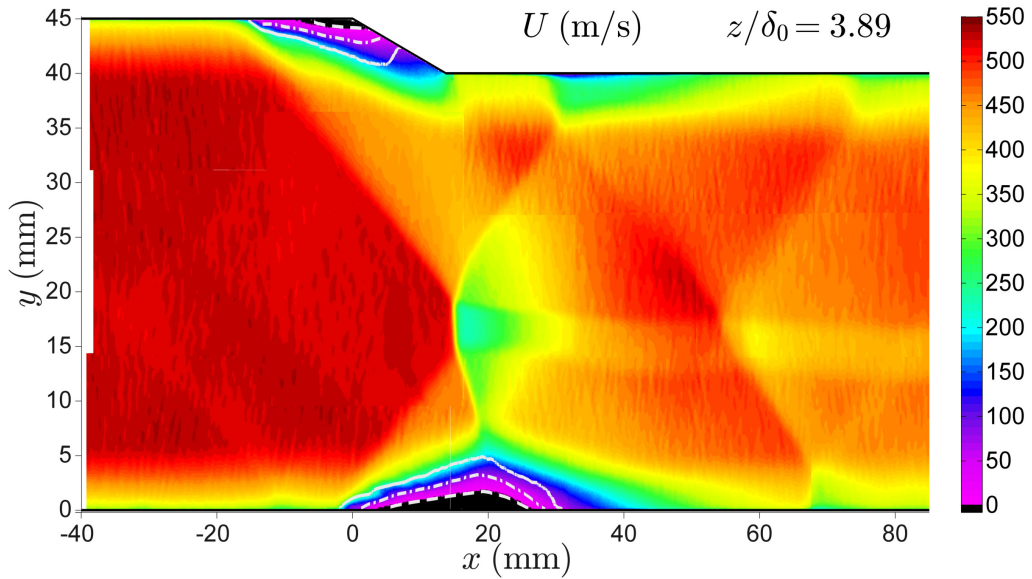


Figure 3.8: Mean streamwise velocity for the large ramp ( $h_{\text{ramp}}/\delta_0 = 0.93$ ) at  $z/\delta_0 = 3.89$  (near centerline). Reversed flow probability isocontours (— 5%; -·- 25%; and -··- 60%) are superimposed in white.

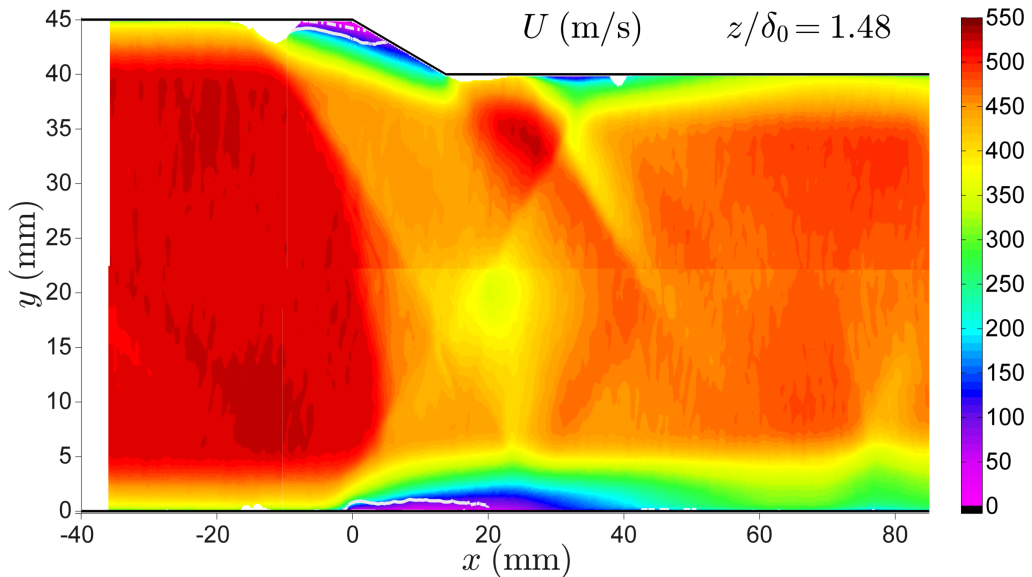


Figure 3.9: Mean streamwise velocity for the large ramp ( $h_{\text{ramp}}/\delta_0 = 0.93$ ) at  $z/\delta_0 = 1.48$ . Reversed flow probability isocontours (— 5% and -·- 25%) are superimposed in white.

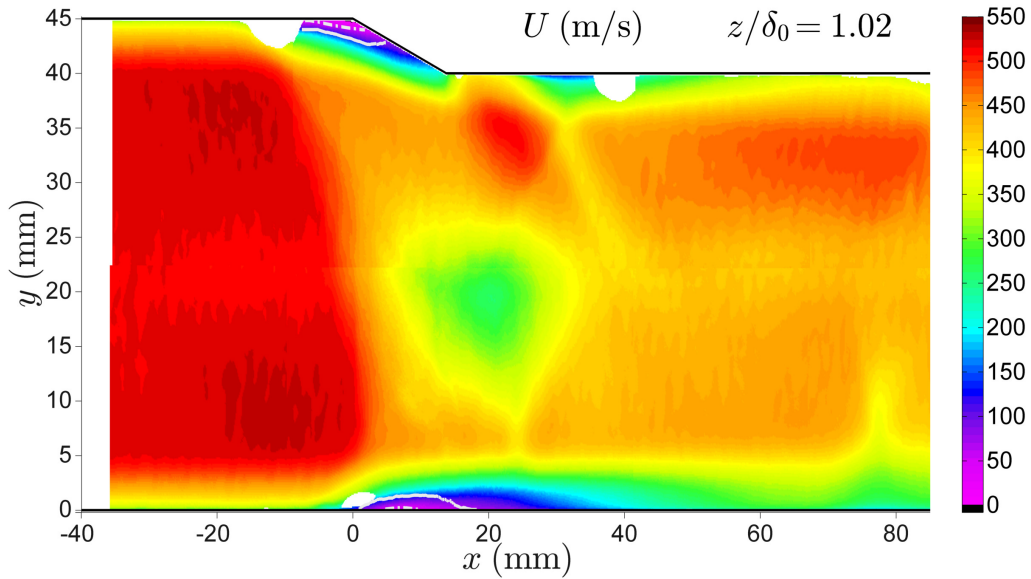


Figure 3.10: Mean streamwise velocity for the large ramp ( $h_{\text{ramp}}/\delta_0 = 0.93$ ) at  $z/\delta_0 = 1.02$ . Reversed flow probability isocontours (— 5% and - - - 25%) are superimposed in white.

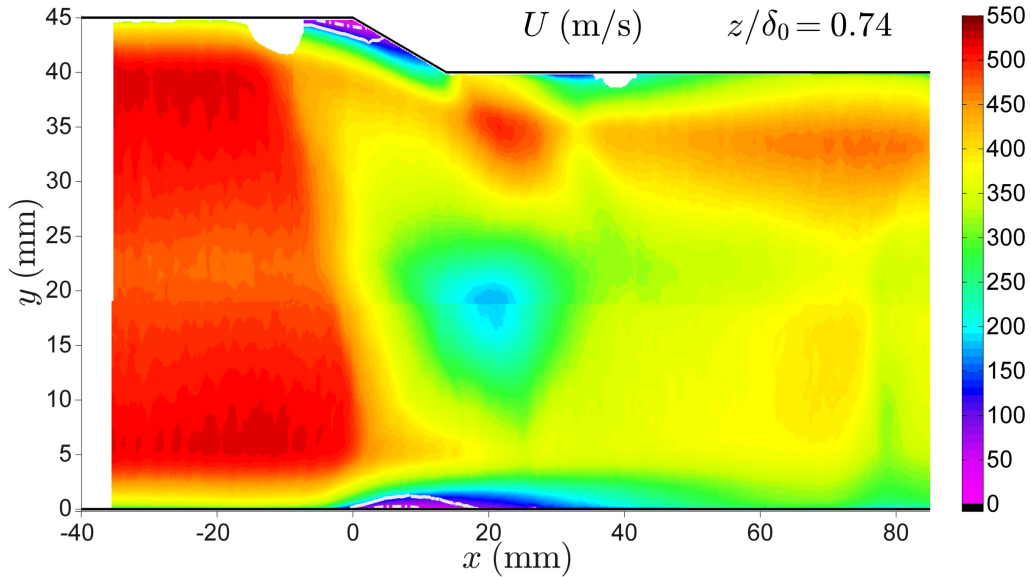


Figure 3.11: Mean streamwise velocity for the large ramp ( $h_{\text{ramp}}/\delta_0 = 0.93$ ) at  $z/\delta_0 = 0.74$ . Reversed flow probability isocontours (— 5% and - - - 25%) are superimposed in white.

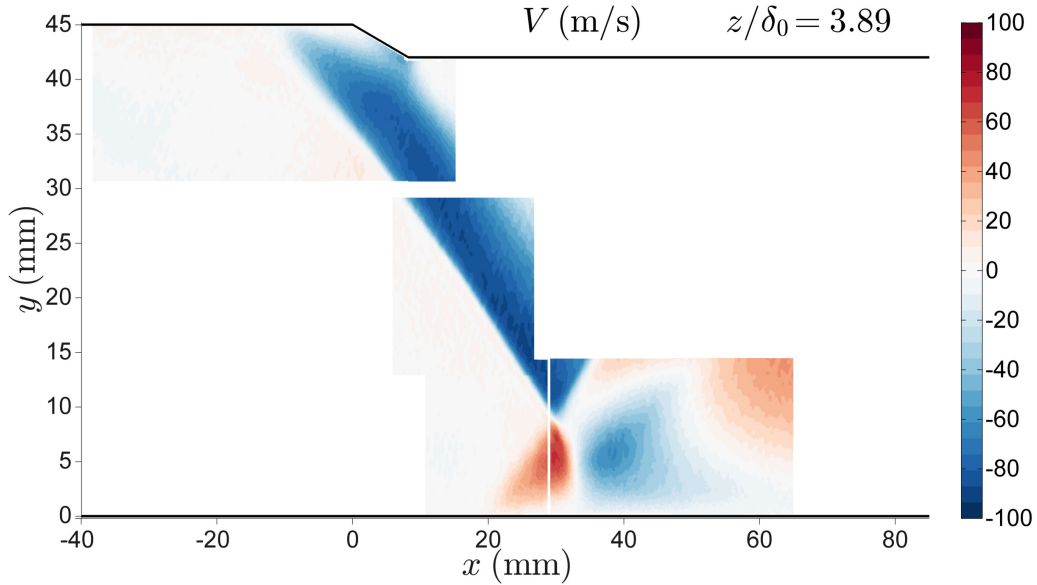


Figure 3.12: Mean vertical velocity for the mid-size ramp ( $h_{\text{ramp}}/\delta_0 = 0.56$ ) at  $z/\delta_0 = 3.89$  (near centerline).

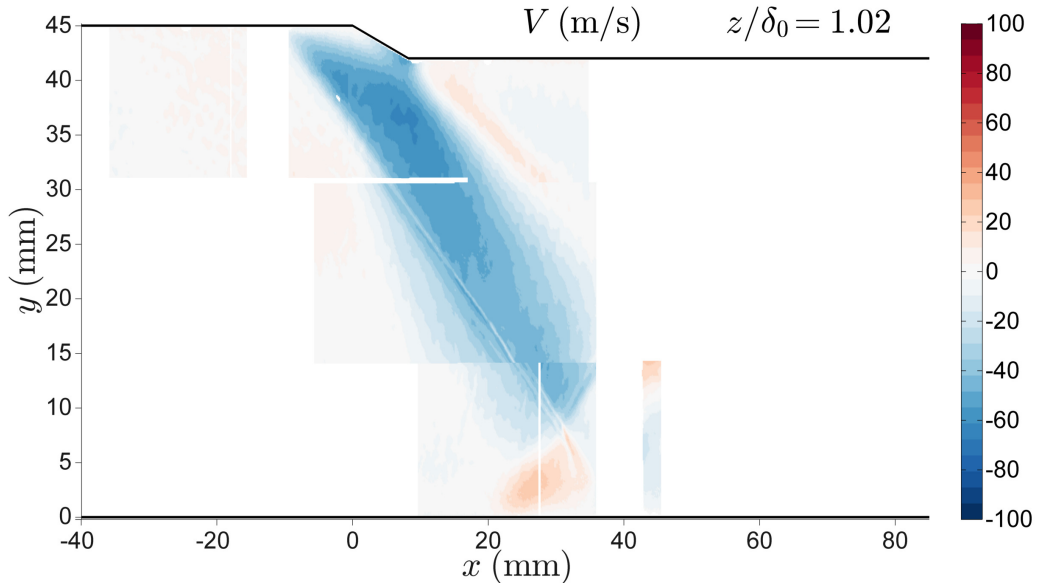


Figure 3.13: Mean vertical velocity for the mid-size ramp ( $h_{\text{ramp}}/\delta_0 = 0.56$ ) at  $z/\delta_0 = 1.02$ .

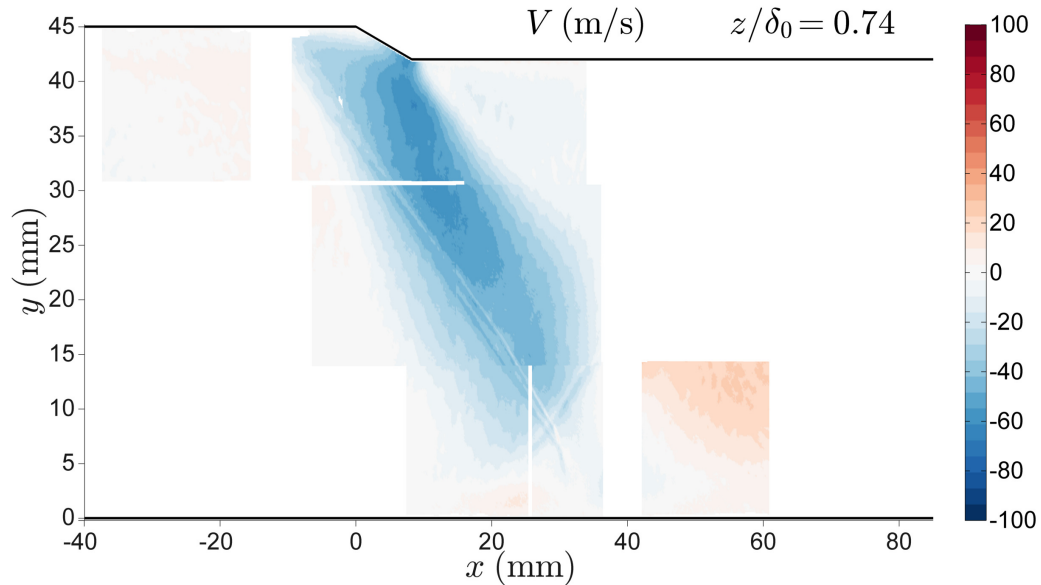


Figure 3.14: Mean vertical velocity for the mid-size ramp ( $h_{\text{ramp}}/\delta_0 = 0.56$ ) at  $z/\delta_0 = 0.74$ .

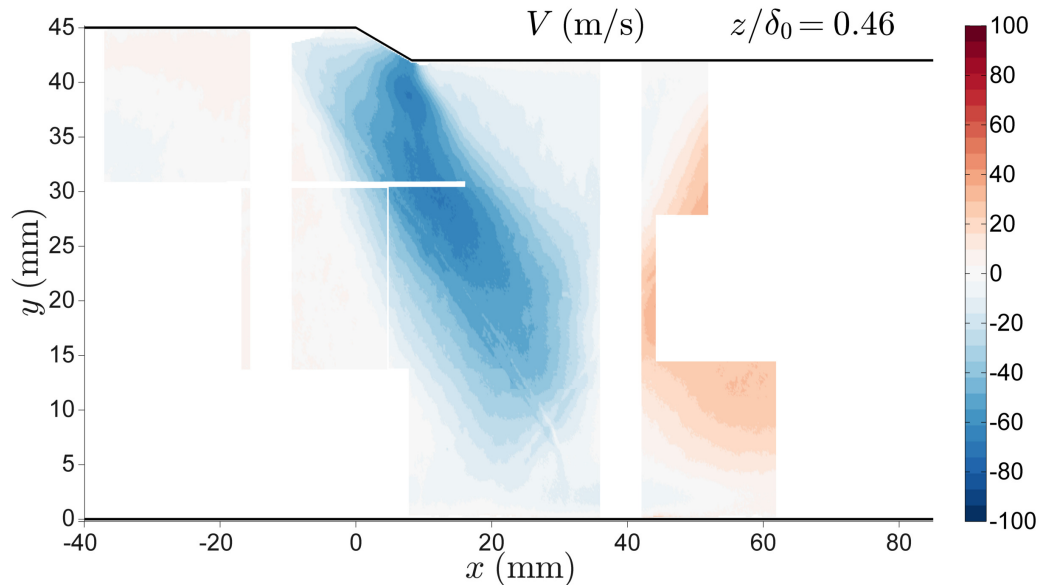


Figure 3.15: Mean vertical velocity for the mid-size ramp ( $h_{\text{ramp}}/\delta_0 = 0.56$ ) at  $z/\delta_0 = 0.46$ .

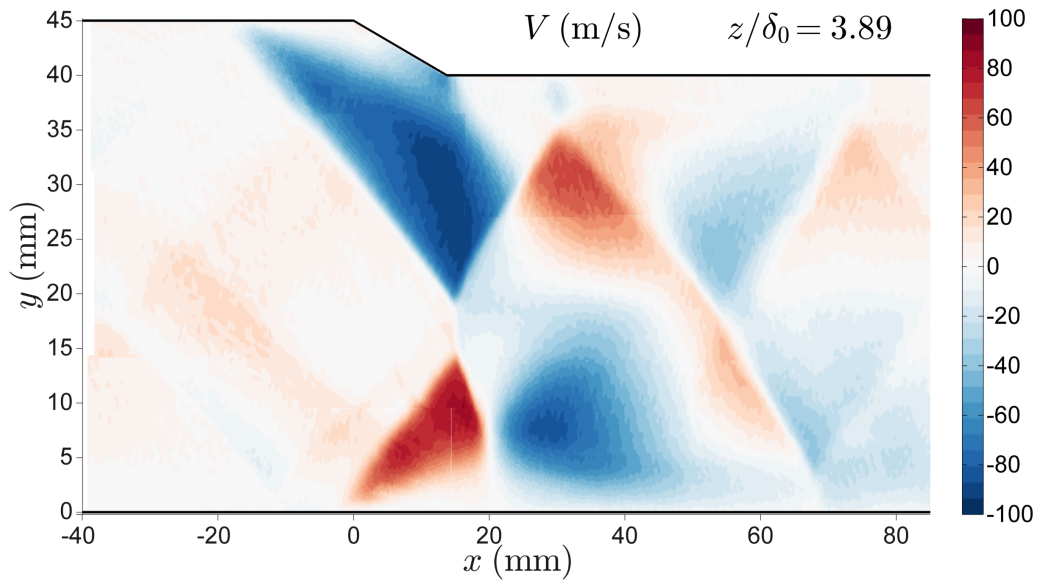


Figure 3.16: Mean vertical velocity for the large ramp ( $h_{\text{ramp}}/\delta_0 = 0.93$ ) at  $z/\delta_0 = 3.89$  (near centerline).

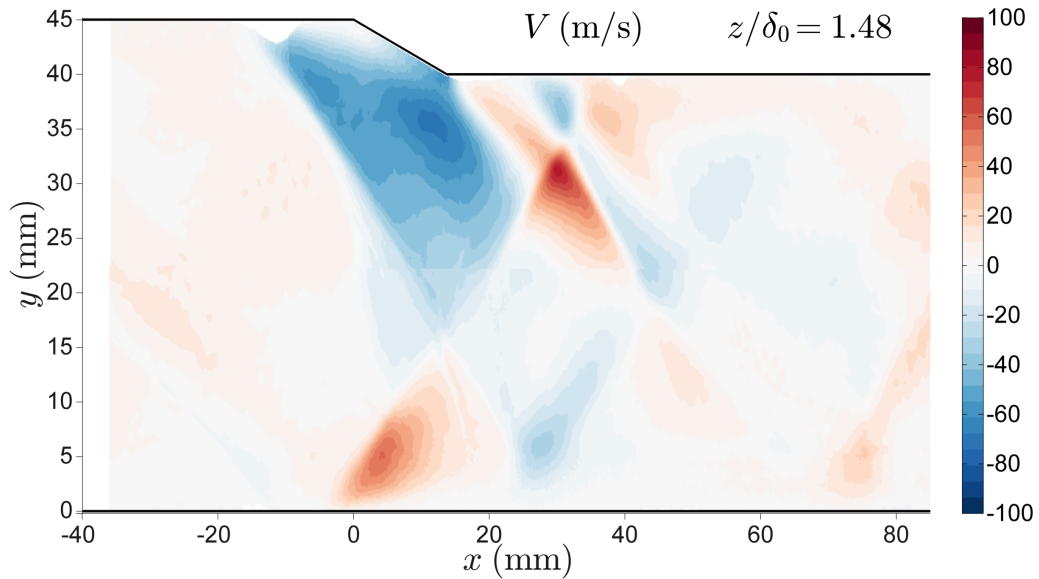


Figure 3.17: Mean vertical velocity for the large ramp ( $h_{\text{ramp}}/\delta_0 = 0.93$ ) at  $z/\delta_0 = 1.48$ .

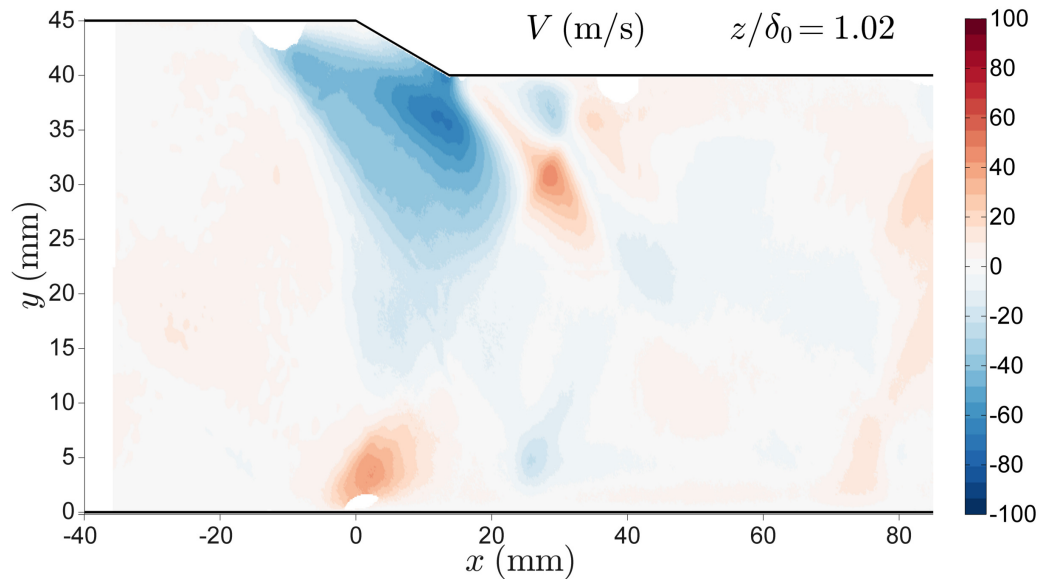


Figure 3.18: Mean vertical velocity for the large ramp ( $h_{\text{ramp}}/\delta_0 = 0.93$ ) at  $z/\delta_0 = 1.02$ .

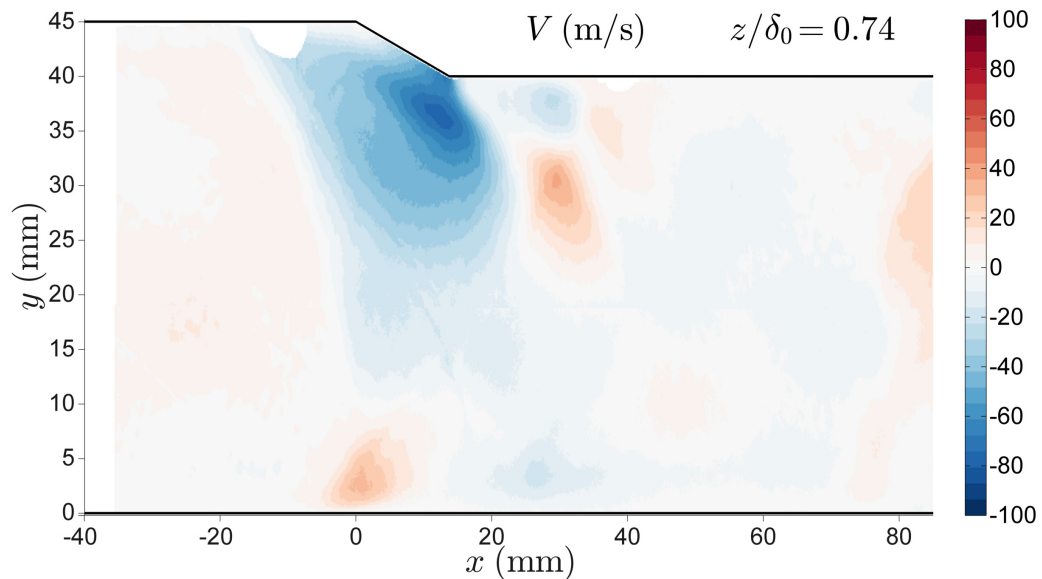


Figure 3.19: Mean vertical velocity for the large ramp ( $h_{\text{ramp}}/\delta_0 = 0.93$ ) at  $z/\delta_0 = 0.74$ .

The transition from regular reflection to Mach reflection has been well studied for shock-shock interactions generated by two symmetric wedges (see e.g. Hornung & Robinson (1982), Skews (2000), or Ivanov et al. (2001)), but fewer studies have been done where the Mach reflection is part of an incident/reflected SBLI. Tieng et al. (1992) investigate this phenomenon using holographic interferography for a number of test cases in which both the incoming Mach number and deflection angle across the incident shock are altered. Mattheis et al. (2013) examine the transition from regular reflection to Mach reflection in a Mach 2 incident shock boundary layer interaction using large eddy simulations. They present spanwise-averaged results which show that the nominal transition from regular reflection to Mach reflection occurs when a flow deflection of  $13^\circ$  is achieved across the incident shock wave. Bermejo-Moreno et al. (2014) provide two wall-modeled large eddy simulations of the current  $h_{\text{ramp}}/\delta_0 = 0.93$  ramp – one treating the side walls as no-slip surfaces and one using spanwise periodic boundary conditions for the side walls. They find that for the case with no-slip side walls, a Mach stem is predicted; however for the same geometry but with spanwise periodic boundary conditions, a regular shock reflection is predicted. This indicates that the effects of confinement by the side wall boundary layers are critical in accurately predicting the flow throughout the domain.

### 3.3.1 Compression ramp SBLI region

In the SBLI on the top wall near the foot of the compression ramp, no mean flow reversal is observed anywhere across the span for the mid-size ramp geometry ( $h_{\text{ramp}}/\delta_0 = 0.56$ ). However the flow is intermittently reversed, with probabilities of reversed flow up to  $\approx 53\%$  at the foot of the compression ramp near the spanwise centerline. As the side wall is approached ( $z/\delta_0 = 1.02, 0.74$ , and  $0.46$ ), the region of non-zero reversed flow probability is confined closer to the foot of the compression ramp. In these planes, the maximum probability of observing reversed flow is reduced to  $\approx 45\%$ .

The stronger compression ramp SBLI produced by the larger ramp ( $h_{\text{ramp}}/\delta_0 = 0.93$ ) involves a small zone of mean flow reversal at the foot of the compression ramp near the spanwise centerline, denoted by the black region in Figure 3.8. Although the flow is reversed on average, the maximum probability of instantaneously reversed flow observed in this region is only  $\approx 79\%$ . Away from the spanwise centerline of the duct, the region of intermittent flow reversal decreases in size, as can be seen by the isocontours of reversed flow probability superimposed on the mean streamwise velocity plots in Figures 3.8 – 3.11. Furthermore, the maximum probability of reversed flow observed at the foot of the  $h_{\text{ramp}}/\delta_0 = 0.93$  compression ramp drops to  $\approx 58\%$ ,  $55\%$ , and  $52\%$  at  $z/\delta_0 = 1.48$ ,  $1.02$ , and  $0.74$ , respectively. This behavior is qualitatively consistent with the observations for the mid-size ramp case.

At the end of the compression ramp, an expansion fan turns the flow back to horizontal. This is seen most clearly in the vertical velocity contours (Figures 3.12 – 3.19), where the region of negative velocity (blue) caused by the primary oblique shock wave turns back to zero vertical velocity (white). The strength of the expansion fan is non-uniform across the tunnel span, and does not perfectly match the strength of the incident shock wave in some planes. This is most notable in the  $z/\delta_0 = 1.02$  and  $1.48$  data planes (Figures 3.13, 3.17 and 3.18), where a region of positive vertical velocity (red) exists at the downstream of the expansion fan. This feature indicates an over-correction of the vertical velocity through the expansion fan, and it is also observed in the  $z/\delta_0 = 1.02$  data for the smallest ramp case presented by Helmer et al. (2012).

In all data planes, the expansion fan re-accelerates the top wall boundary layer downstream of the compression ramp; however the strength of the re-acceleration is strongly dependent on the local vertical velocity. This effect is demonstrated in Figures 3.20 and 3.21, which show mean streamwise and vertical velocity profiles in each plane at four stations downstream of the end of the  $h_{\text{ramp}}/\delta_0 = 0.93$  compression

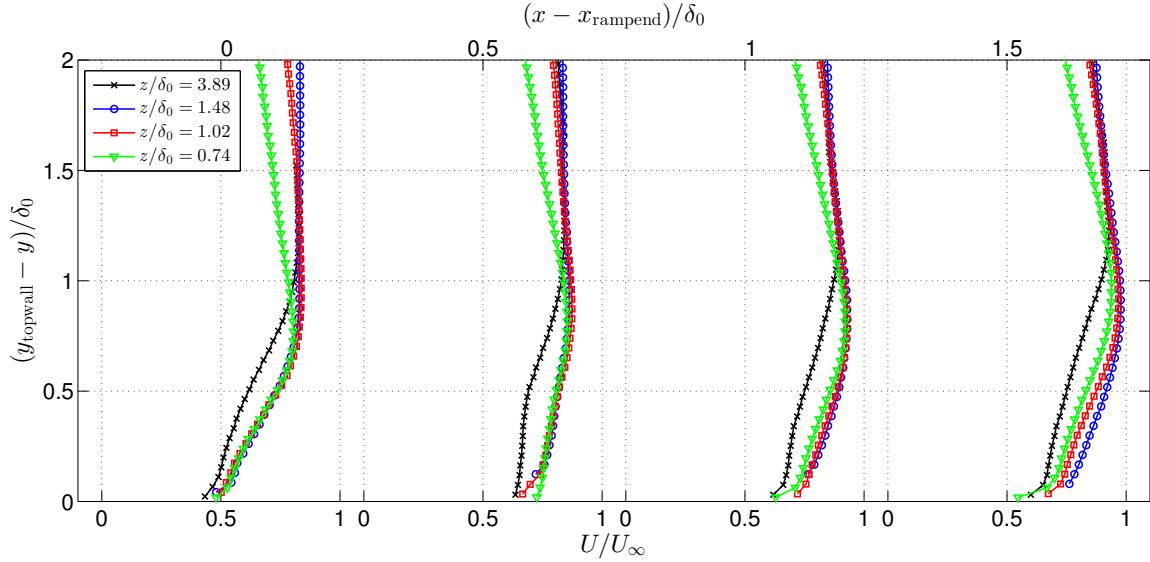


Figure 3.20: Profiles of mean streamwise velocity on top wall downstream of ramp end for the  $h_{\text{ramp}}/\delta_0 = 0.93$  test case.

ramp. The first set of profiles is extracted at the location where the top wall turns back to horizontal:  $x = 13.74$  mm, or  $(x - x_{\text{rampend}})/\delta_0 = 0$ . Subsequent profiles are extracted at streamwise locations of  $x = 16.44$ mm,  $19.14$ mm, and  $21.84$ mm ( $(x - x_{\text{rampend}})/\delta_0 = 0.5$ ,  $1$ , and  $1.5$ ). At the end of the compression ramp, the top wall boundary layer is most severely distorted near the spanwise center ( $z/\delta_0 = 3.89$ ). In the planes closer to the side wall, the profiles are less distorted and collapse inside of  $(y_{\text{topwall}} - y)/\delta_0 \approx 0.7$ . As the flow evolves downstream, the top wall boundary layer begins to recover. Of the three off-center planes, the  $z/\delta_0 = 1.48$  profile recovers fastest and the  $z/\delta_0 = 0.74$  plane recovers slowest, as indicated by the differences in the fullness of each profile at the last streamwise station.

The spanwise non-uniformity of the top wall boundary layer re-acceleration can be explained by the trends in the mean vertical velocity profiles presented in Figure 3.21. At the end of the compression ramp, all of the planes show negative vertical velocities (away from the top wall). At the downstream stations, the vertical velocities

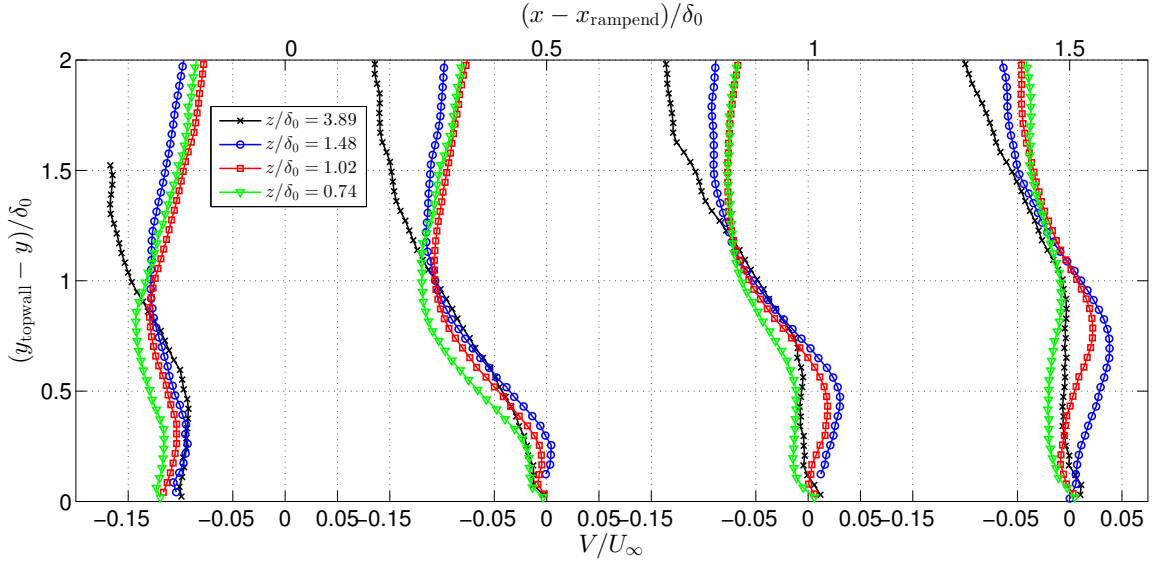


Figure 3.21: Profiles of mean vertical velocity on top wall downstream of ramp end for the  $h_{\text{ramp}}/\delta_0 = 0.93$  test case. Positive velocities are toward the top wall.

become less negative due to the turning of the flow through the expansion fan. The overcorrection of the vertical velocity in the  $z/\delta_0 = 1.02$  and  $1.48$  planes is apparent in the profiles at  $(x - x_{\text{rampend}})/\delta_0 = 1$  and  $1.5$ . These regions of positive vertical velocity bring higher momentum toward to the top wall, re-energizing the top wall boundary layer.

The top wall boundary layer does not fully recover before the reflected shock wave impinges on the top wall, causing another region of severe distortion. The influence of the reflected shock wave on the top wall boundary layer is felt further upstream for the planes closer to the side wall. This secondary SBLI on the top wall is not the primary focus of this work; however it is worth noting that this flow is considerably more complicated than either the compression corner SBLI or the primary incident SBLI. The reason for the added complexity is that both the strength of the reflected shock wave and the state of the top wall boundary layer upstream of the shock impingement vary significantly across the span. As such, accurate prediction of this

secondary SBLI will likely be very challenging for numerical simulations.

### 3.3.2 Incident SBLI region

In the SBLI caused by the incident shock impinging on the bottom wall boundary layer, a small region of mean flow reversal is observed near the centerline in the mid-size ( $h_{\text{ramp}}/\delta_0 = 0.56$ ) ramp geometry. A significantly larger region of mean flow reversal occurs in the stronger incident SBLI caused by the large ( $h_{\text{ramp}}/\delta_0 = 0.93$ ) ramp configuration. These zones are denoted by the black regions near the bottom wall in Figures 3.4 and 3.8. To give an idea of the sizes of the separated zones, isocontours of reversed flow probability at levels of 5%, 25%, and 60% are superimposed on top of the mean streamwise velocity plots. No mean flow reversal is observed in any of the off-center planes for either test geometry; however there are still significant regions of intermittently reversed flow. Helmer (2011) reports no mean flow reversal anywhere in the SBLIs generated by the small ( $h_{\text{ramp}}/\delta_0 = 0.20$ ) ramp, and a maximum probability of flow reversal of  $\approx 20\%$ , which is significantly lower than the levels observed in the larger ramp cases.

In both the mid-size and large ramp geometries, the bottom wall boundary layer thickens rapidly due to the adverse pressure gradient imposed by the incident shock wave. The thickening is most severe near the centerline of the tunnel for both geometries. This effect is partially due to the non-uniform shock strength across the span of the tunnel. In addition, the region of mean flow reversal on the bottom wall causes a large blockage near the center of the duct, forcing higher momentum fluid to divert upward and toward the side walls. This energizes the bottom wall boundary layer at locations away from the spanwise centerplane of the duct, mitigating the thickening due to the shock interaction. The variation across the span is strongest for the interaction caused by the largest ramp geometry.

Another interesting characteristic of the incident shock interaction for the large

ramp geometry is that near the spanwise centerline ( $z/\delta_0 = 3.89$ ), the bottom wall boundary layer thins rapidly downstream of the transmitted shock. However, this boundary layer thinning occurs much more gradually in the off-center planes ( $z/\delta_0 = 1.48, 1.02, 0.74$ ). This is the opposite of the trend in the top wall boundary layer re-acceleration noted in the previous section. As before, the effect can be examined by looking at the mean vertical velocity contours in Figures 3.16 – 3.19. The incident shock interaction involves a region of strong positive vertical velocity due to the separation shock, followed downstream by a region of strong negative velocity caused by the transmitted shock and the expansion fan emanating from the point where it impinges on the sonic line. The vertical velocities are strongest near the spanwise centerline, with comparable positive and negative velocity magnitudes (Figure 3.16). Off the spanwise centerline, the vertical velocities are weaker overall, and the positive vertical velocity region pushing flow away from the wall dominates over the negative vertical velocities driving the recovery (Figures 3.17 – 3.19). This is due to a mismatch in the strengths of the separation and transmitted shocks at these off-center locations.

The bottom wall boundary layer does not recover fully before the next shock impingement at  $x \approx 70\text{mm}$ . Unlike the secondary impingement on the top wall, the effect of the second reflected shock on the bottom wall boundary layer is felt furthest upstream at the spanwise centerline of the duct. This is likely due to the steepening of the second reflected shock wave as it interacts with the wake of the Mach stem near the core of the duct (most clearly visible in Figure 3.16). As with the secondary SBLI on the top wall, the features of the third incident SBLI have a complex dependence upon the spanwise non-uniformity of all of the upstream flow features.

The overall degree of vertical boundary layer thickening and thinning is less severe in the mid size ramp case (Figures 3.4 – 3.7 and 3.12 – 3.15), and the discrepancies between the center and off-center planes appear less drastic. These effects are present, but significantly weaker, in the smallest ramp case investigated by Helmer (2011).

A side-by-side comparison of the datasets for each of the three geometries clearly indicates that increasing the compression ramp height causes increased confinement due to boundary layer thickening as well as stronger three-dimensionality of the flow. The incident shock strength also increases with increasing ramp height, and because a stronger incident shock wave leads to larger blockage by separated flow regions, it is impossible to de-couple the shock strength and confinement effects.

### 3.4 Turbulence quantities

Contour plots of the normalized streamwise velocity fluctuations,  $u'/U_\infty$ , in each of the PIV measurement planes for the  $h_{\text{ramp}}/\delta_0 = 0.56$  and  $0.93$  geometries are shown in Figures 3.22 – 3.29. The normalized vertical velocity fluctuations,  $v'/U_\infty$ , appear in Figures 3.30 – 3.37, and the Reynolds shear stresses,  $\langle u'v' \rangle / U_\infty^2$  are shown in Figures 3.38 – 3.45. Because  $u' > v'$  throughout most of the flow field, the range of values in the colorbar is scaled down by a factor of two for the vertical fluctuations.

The shock features are clearly distinguishable in all of the fluctuating quantities. In particular, the oblique shocks are most easily identified in  $v'$  and the nearly normal Mach stem is most apparent in  $u'$ . This is because of the steep gradient in velocity across the shocks, such that any slight unsteadiness in the shock feature position appears as an artificially inflated level of turbulence intensity. Shock wave unsteadiness is not the focus of the current investigation; however the length scales associated with any motion of the shock waves are discussed later in section 3.5. The positions of the shock features are clearest near the spanwise centerplane ( $z/\delta_0 = 3.89$ ) due to the very low levels of freestream turbulence in the core of the flow. The signature of the shock features becomes difficult to discern in the measurement planes closer to the side wall. This is because the levels of velocity fluctuations associated with the side wall boundary layer are much higher, masking the effects of the shock unsteadiness.

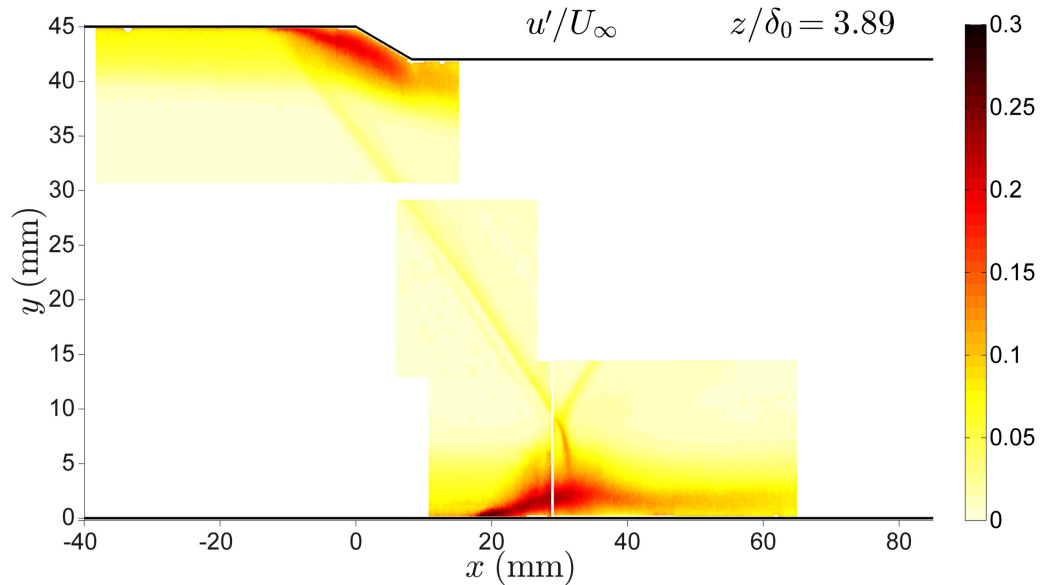


Figure 3.22: RMS of streamwise velocity fluctuations, normalized by  $U_\infty$  for the mid-size ramp ( $h_{\text{ramp}}/\delta_0 = 0.56$ ) at  $z/\delta_0 = 3.89$  (near centerline).

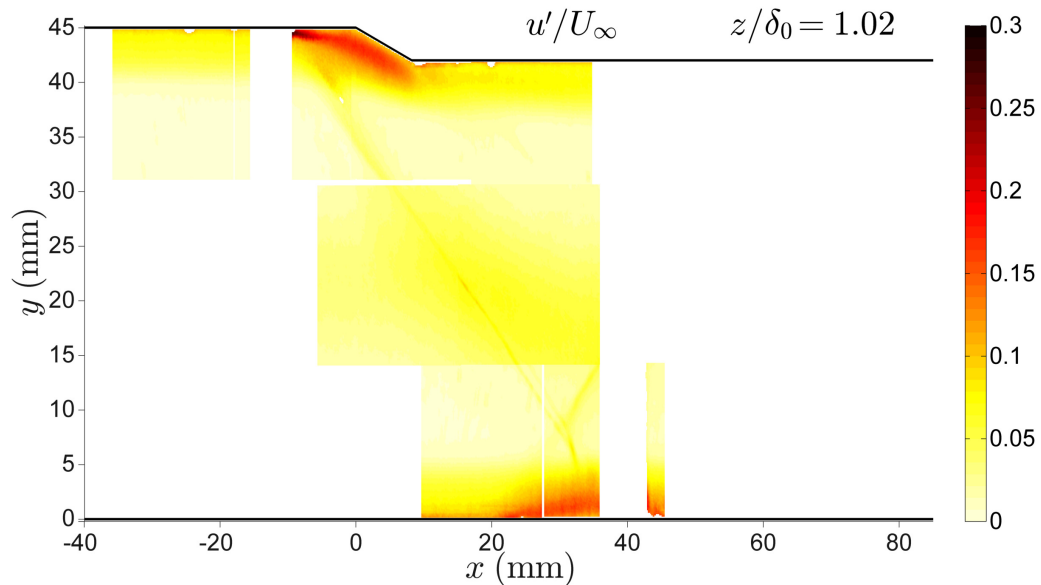


Figure 3.23: RMS of streamwise velocity fluctuations, normalized by  $U_\infty$  for the mid-size ramp ( $h_{\text{ramp}}/\delta_0 = 0.56$ ) at  $z/\delta_0 = 1.02$ .

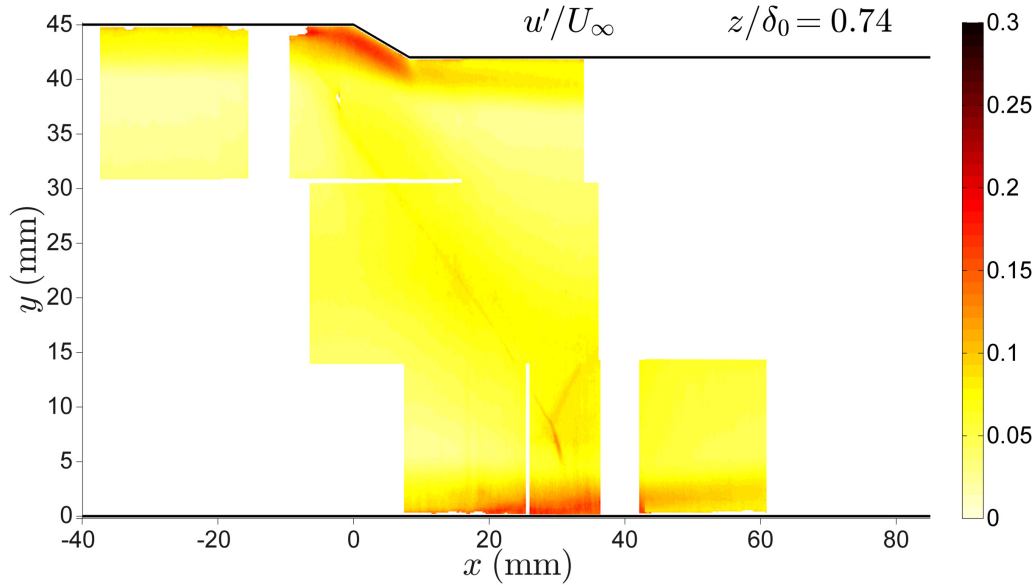


Figure 3.24: RMS of streamwise velocity fluctuations, normalized by  $U_\infty$  for the mid-size ramp ( $h_{\text{ramp}}/\delta_0 = 0.56$ ) at  $z/\delta_0 = 0.74$ .

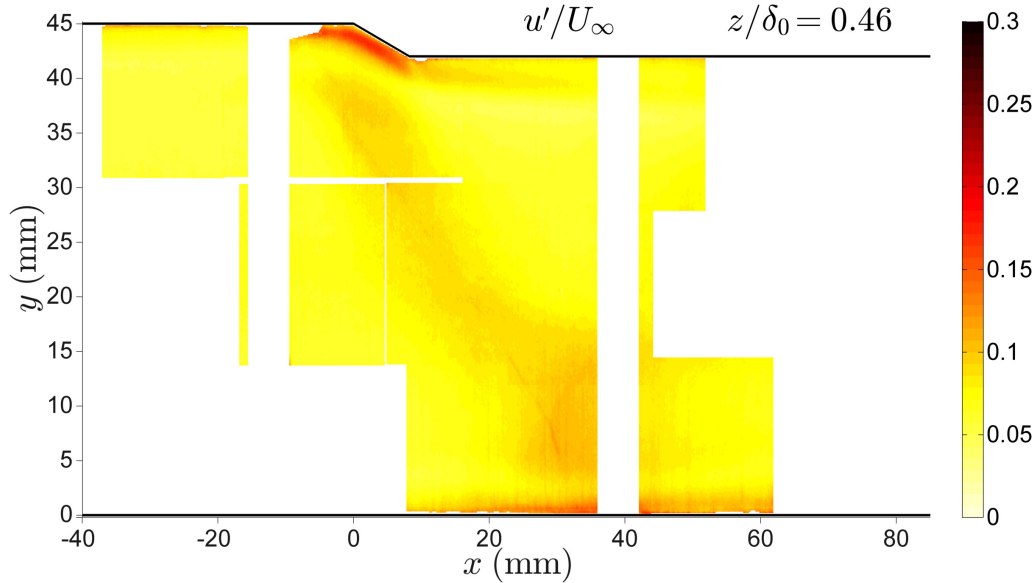


Figure 3.25: RMS of streamwise velocity fluctuations, normalized by  $U_\infty$  for the mid-size ramp ( $h_{\text{ramp}}/\delta_0 = 0.56$ ) at  $z/\delta_0 = 0.46$ .

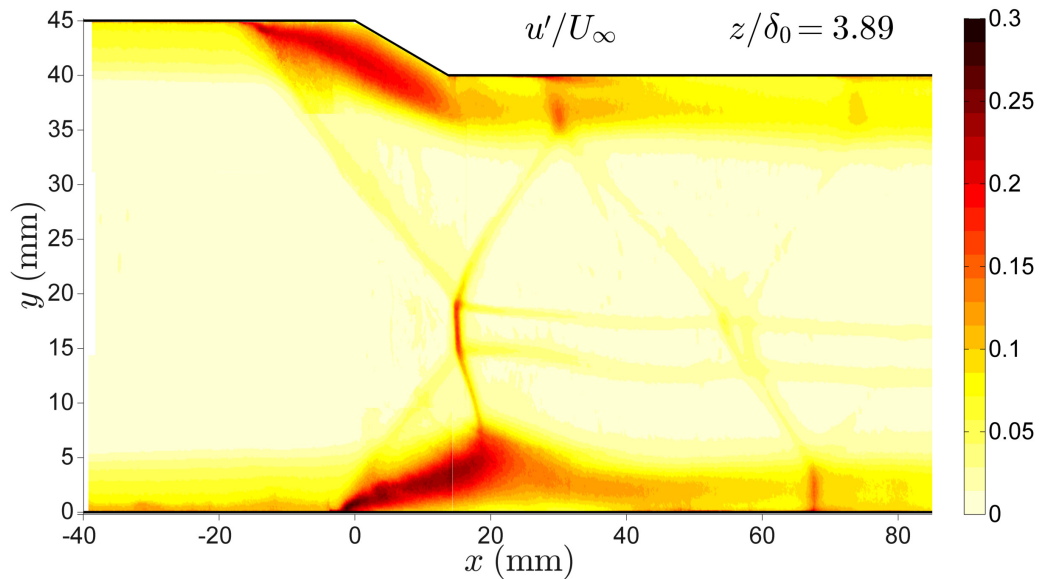


Figure 3.26: RMS of streamwise velocity fluctuations, normalized by  $U_\infty$  for the large ramp ( $h_{\text{ramp}}/\delta_0 = 0.93$ ) at  $z/\delta_0 = 3.89$  (near centerline).

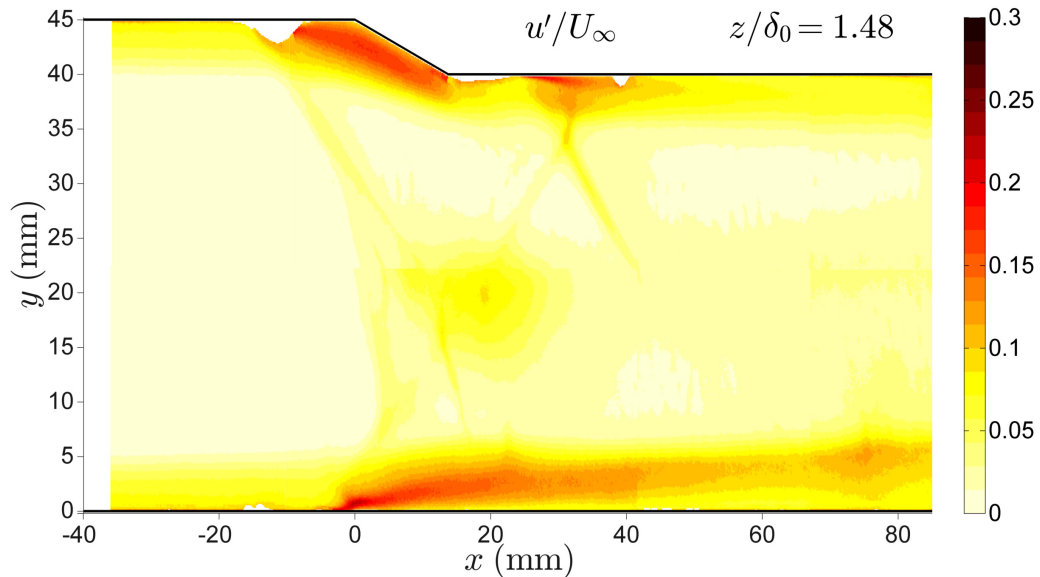


Figure 3.27: RMS of streamwise velocity fluctuations, normalized by  $U_\infty$  for the large ramp ( $h_{\text{ramp}}/\delta_0 = 0.93$ ) at  $z/\delta_0 = 1.48$ .

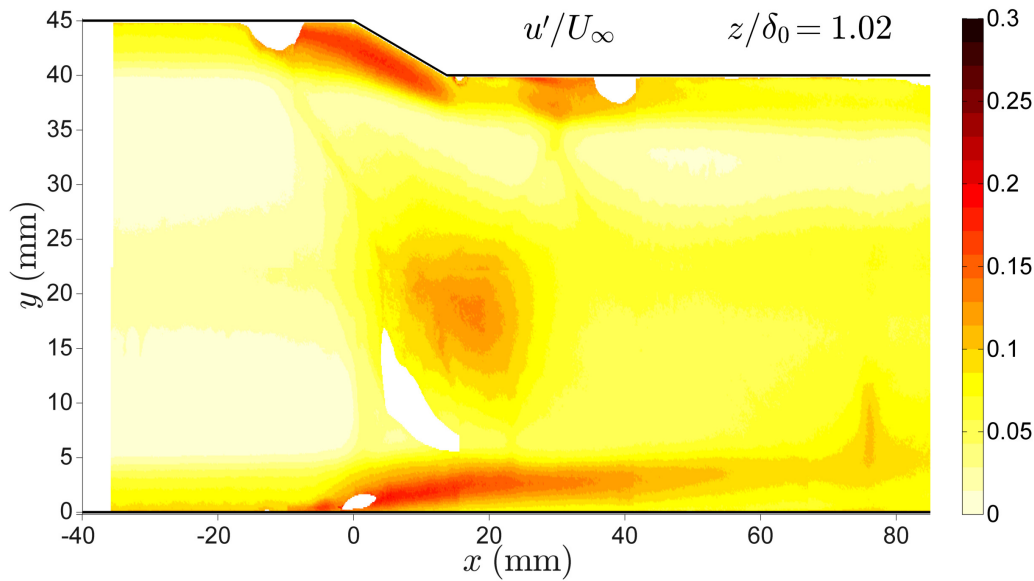


Figure 3.28: RMS of streamwise velocity fluctuations, normalized by  $U_\infty$  for the large ramp ( $h_{\text{ramp}}/\delta_0 = 0.93$ ) at  $z/\delta_0 = 1.02$ .

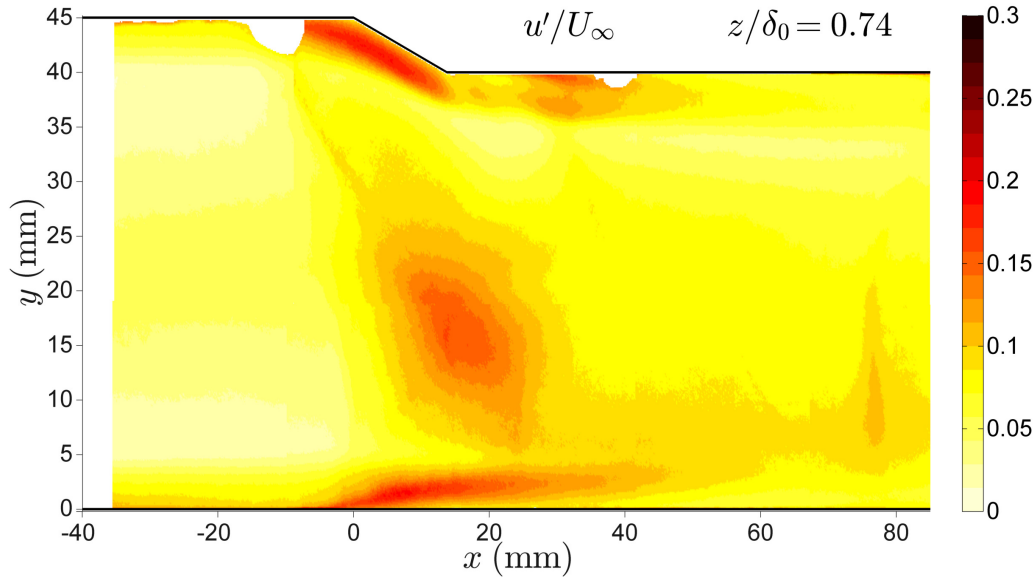


Figure 3.29: RMS of streamwise velocity fluctuations, normalized by  $U_\infty$  for the large ramp ( $h_{\text{ramp}}/\delta_0 = 0.93$ ) at  $z/\delta_0 = 0.74$ .

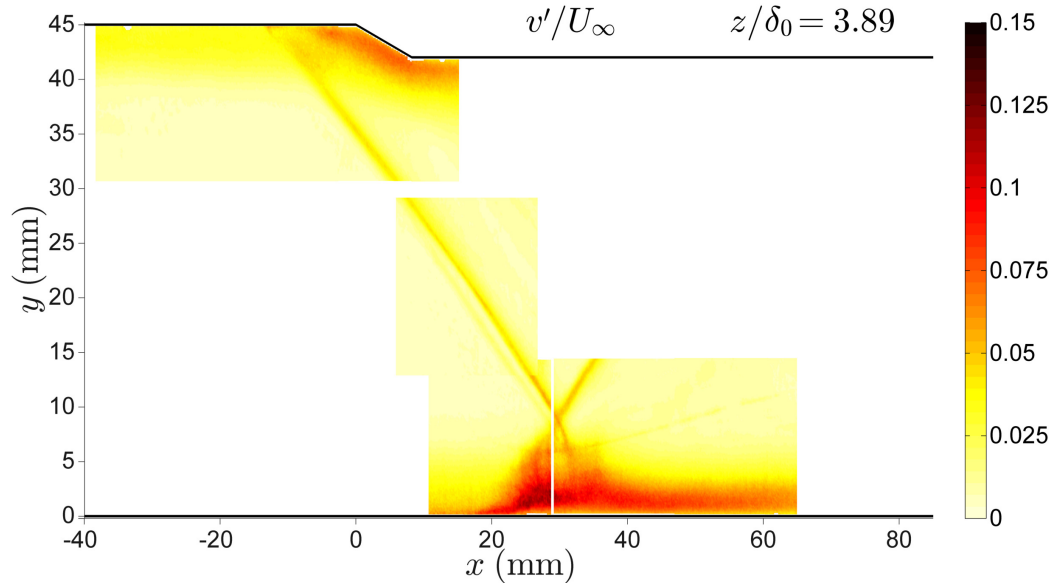


Figure 3.30: RMS of vertical velocity fluctuations, normalized by  $U_\infty$  for the mid-size ramp ( $h_{\text{ramp}}/\delta_0 = 0.56$ ) at  $z/\delta_0 = 3.89$  (near centerline).

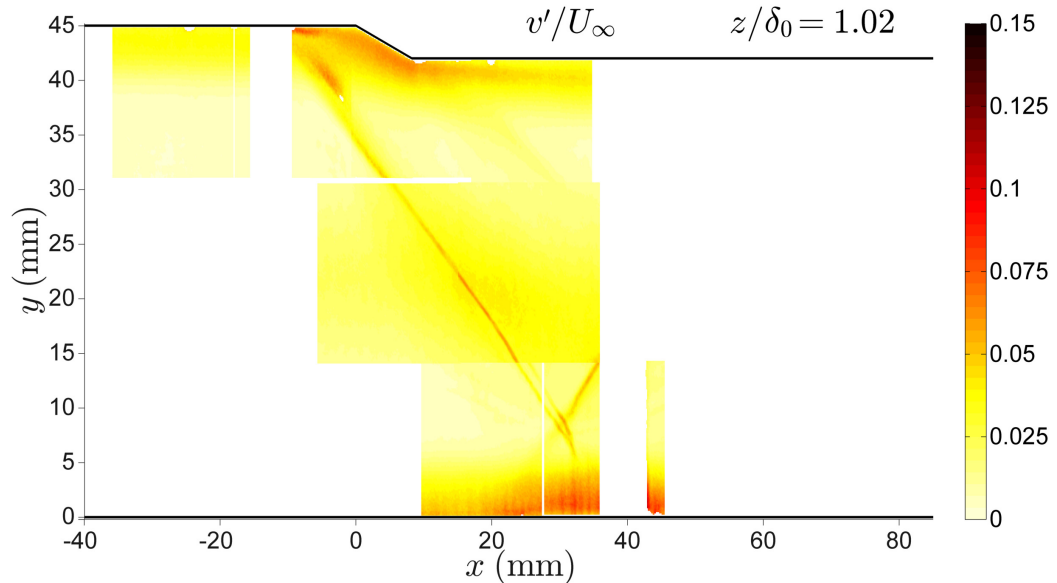


Figure 3.31: RMS of vertical velocity fluctuations, normalized by  $U_\infty$  for the mid-size ramp ( $h_{\text{ramp}}/\delta_0 = 0.56$ ) at  $z/\delta_0 = 1.02$ .

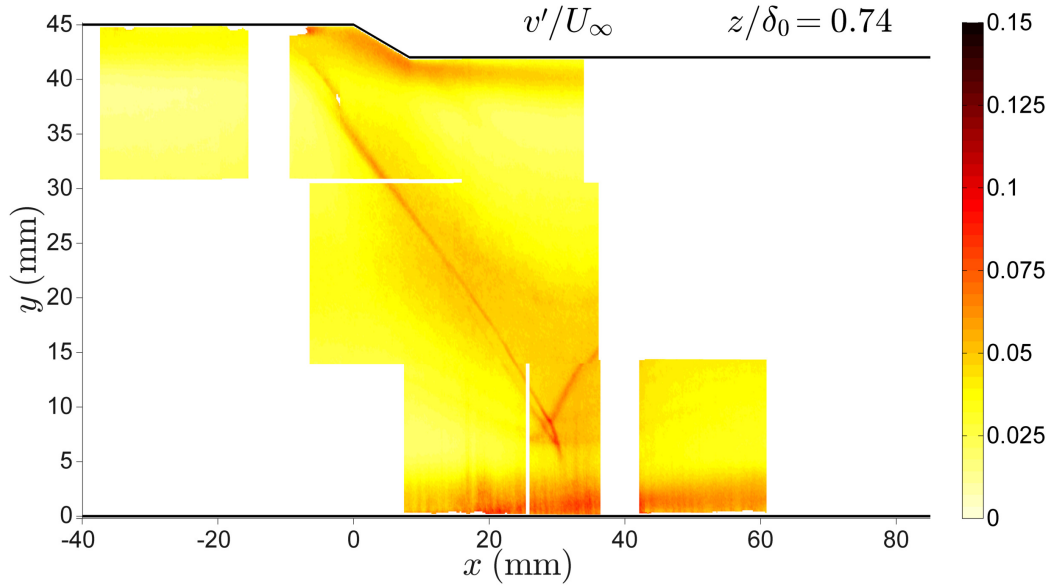


Figure 3.32: RMS of vertical velocity fluctuations, normalized by  $U_\infty$  for the mid-size ramp ( $h_{\text{ramp}}/\delta_0 = 0.56$ ) at  $z/\delta_0 = 0.74$ .

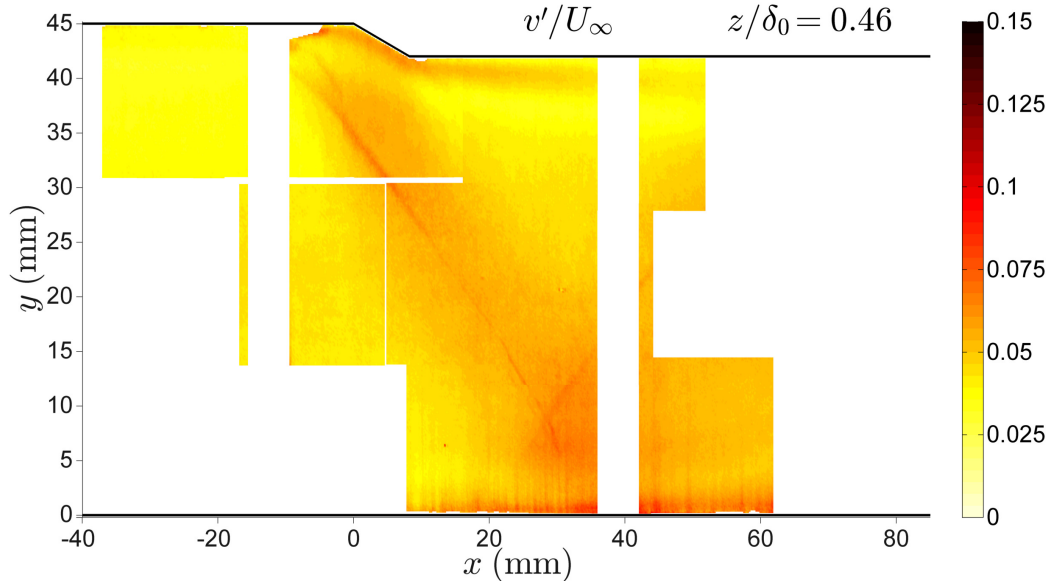


Figure 3.33: RMS of vertical velocity fluctuations, normalized by  $U_\infty$  for the mid-size ramp ( $h_{\text{ramp}}/\delta_0 = 0.56$ ) at  $z/\delta_0 = 0.46$ .

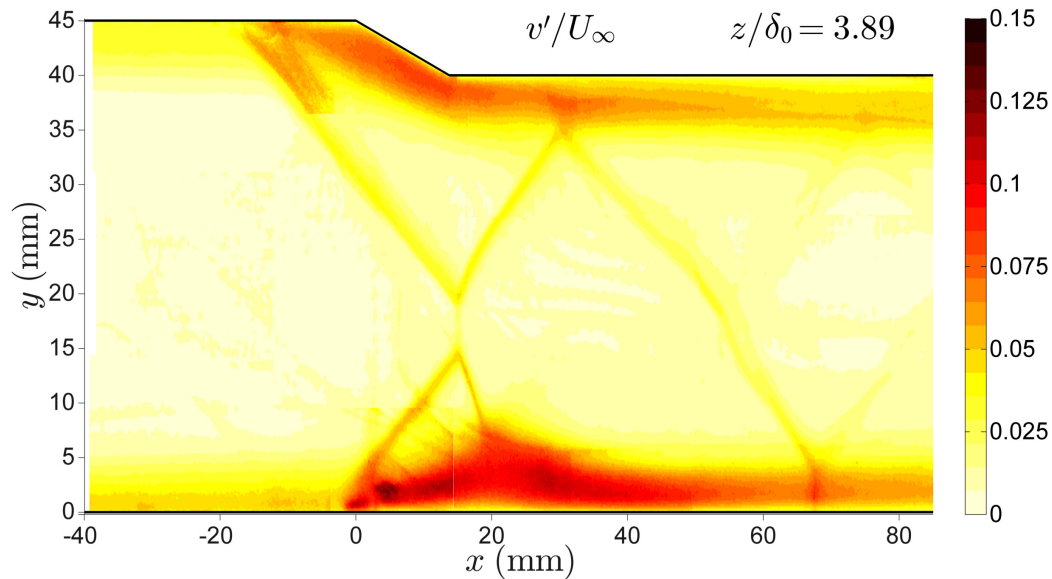


Figure 3.34: RMS of vertical velocity fluctuations, normalized by  $U_\infty$  for the large ramp ( $h_{\text{ramp}}/\delta_0 = 0.93$ ) at  $z/\delta_0 = 3.89$  (near centerline).

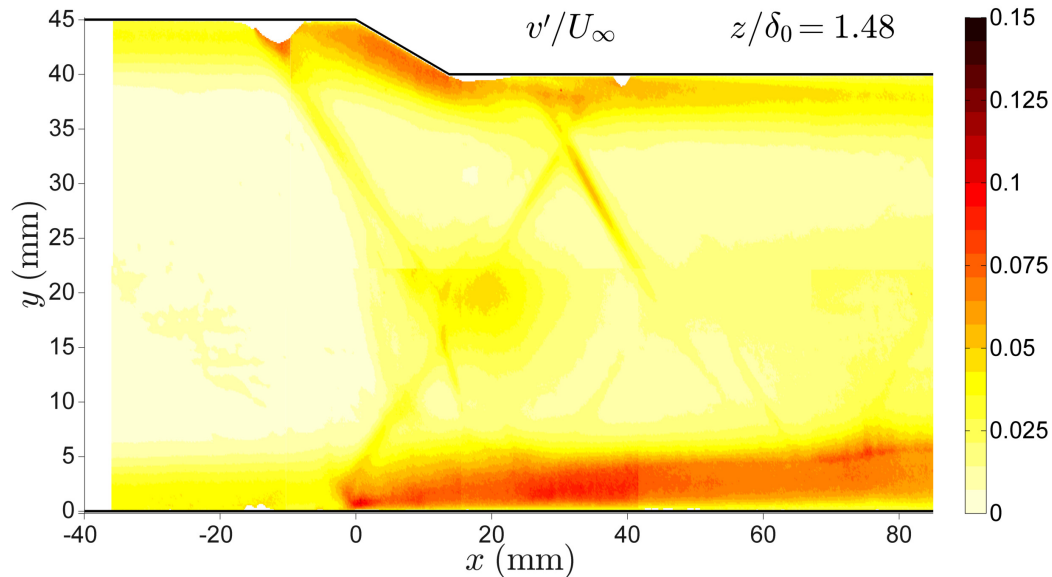


Figure 3.35: RMS of vertical velocity fluctuations, normalized by  $U_\infty$  for the large ramp ( $h_{\text{ramp}}/\delta_0 = 0.93$ ) at  $z/\delta_0 = 1.48$ .

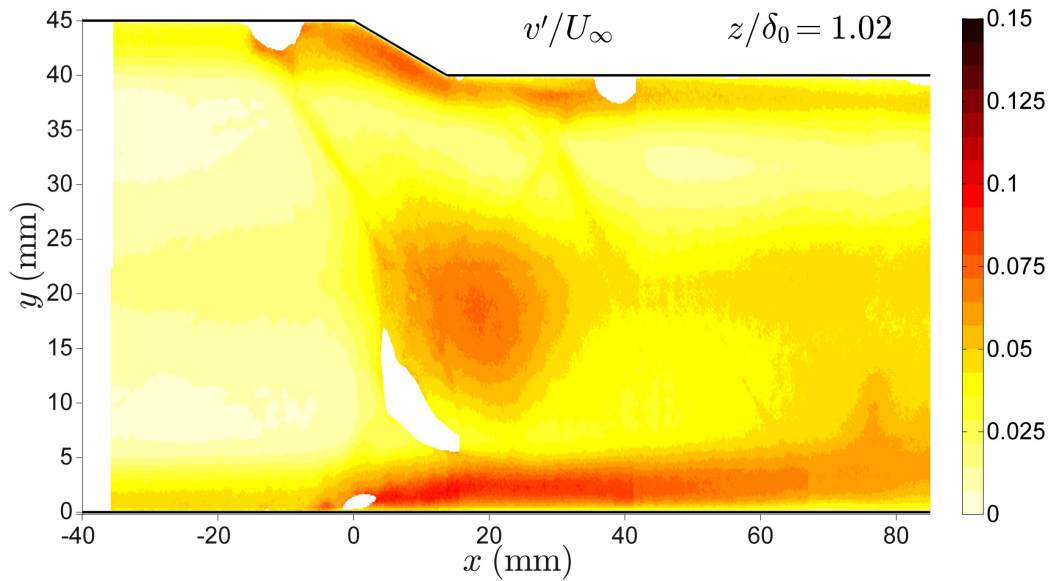


Figure 3.36: RMS of vertical velocity fluctuations, normalized by  $U_\infty$  for the large ramp ( $h_{\text{ramp}}/\delta_0 = 0.93$ ) at  $z/\delta_0 = 1.02$ .

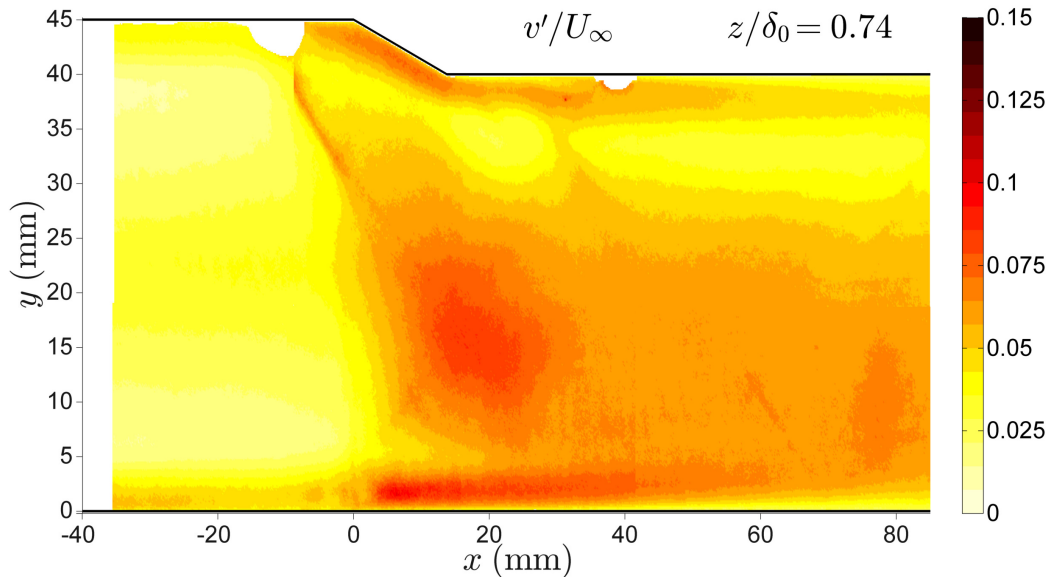


Figure 3.37: RMS of vertical velocity fluctuations, normalized by  $U_\infty$  for the large ramp ( $h_{\text{ramp}}/\delta_0 = 0.93$ ) at  $z/\delta_0 = 0.74$ .

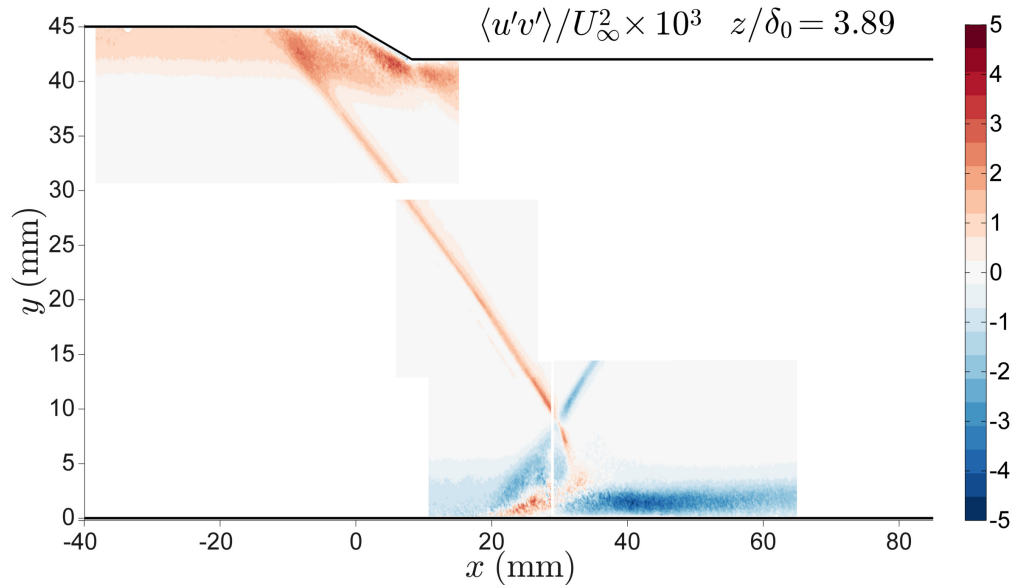


Figure 3.38: Reynolds shear stress, normalized by  $U_\infty^2$  for the mid-size ramp ( $h_{\text{ramp}}/\delta_0 = 0.56$ ) at  $z/\delta_0 = 3.89$  (near centerline).

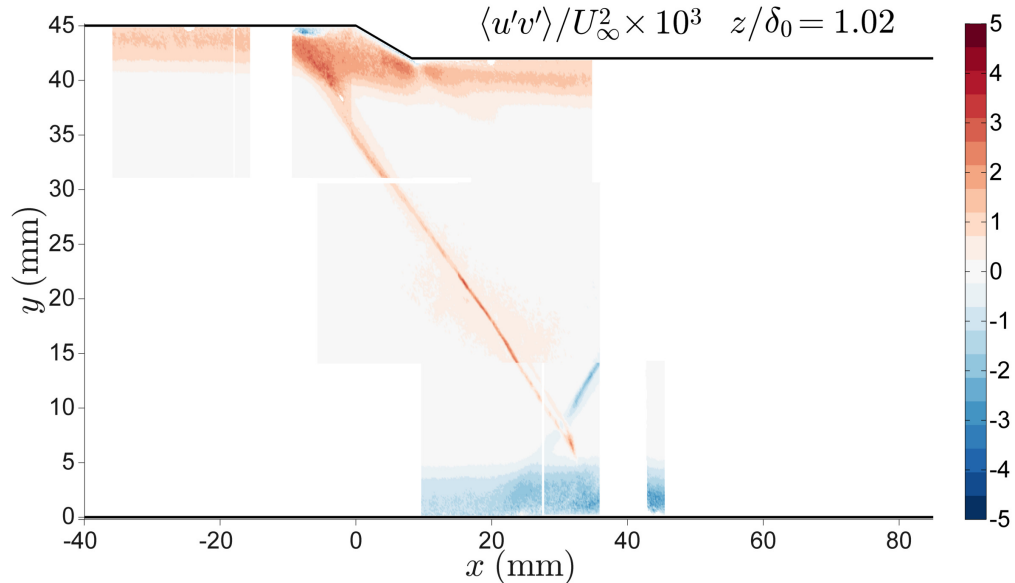


Figure 3.39: Reynolds shear stress, normalized by  $U_\infty^2$  for the mid-size ramp ( $h_{\text{ramp}}/\delta_0 = 0.56$ ) at  $z/\delta_0 = 1.02$ .

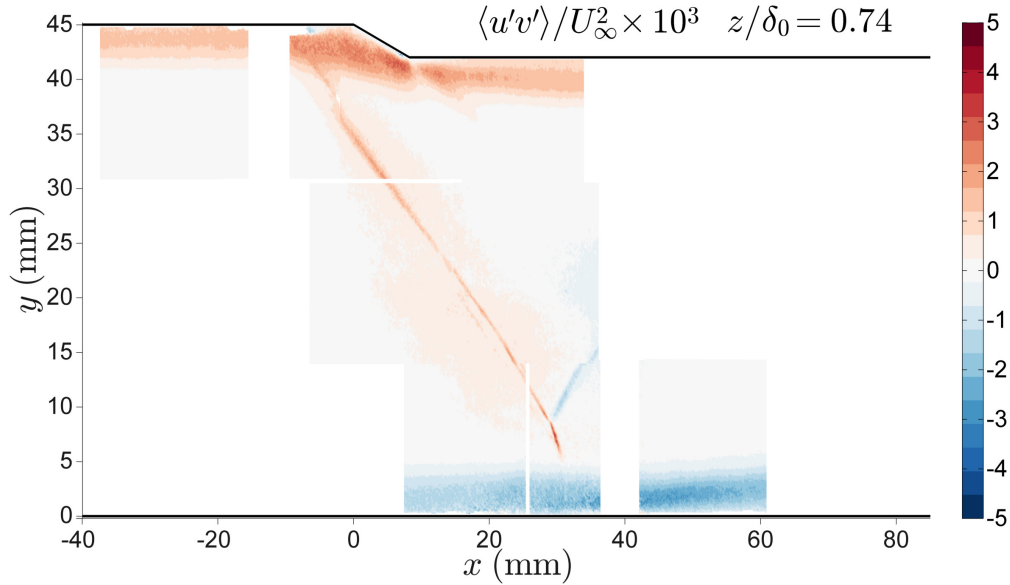


Figure 3.40: Reynolds shear stress, normalized by  $U_\infty^2$  for the mid-size ramp ( $h_{\text{ramp}}/\delta_0 = 0.56$ ) at  $z/\delta_0 = 0.74$ .

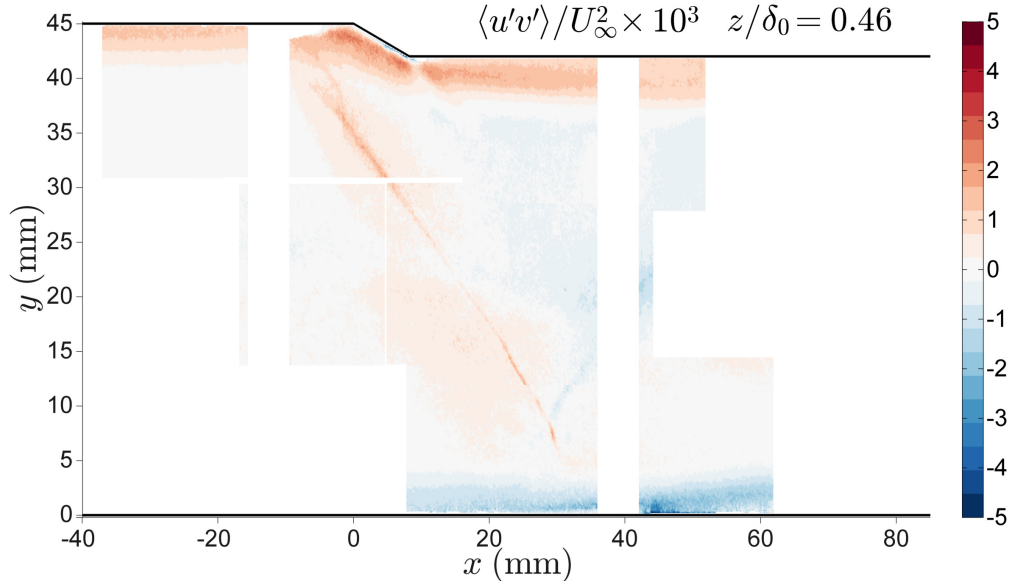


Figure 3.41: Reynolds shear stress, normalized by  $U_\infty^2$  for the mid-size ramp ( $h_{\text{ramp}}/\delta_0 = 0.56$ ) at  $z/\delta_0 = 0.46$ .

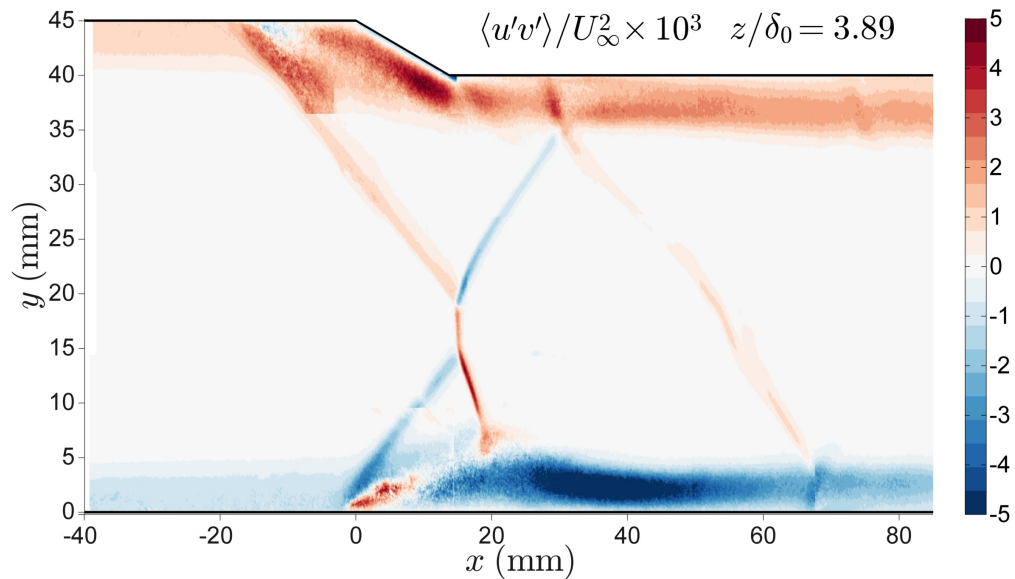


Figure 3.42: Reynolds shear stress, normalized by  $U_\infty^2$  for the large ramp ( $h_{\text{ramp}}/\delta_0 = 0.93$ ) at  $z/\delta_0 = 3.89$  (near centerline).

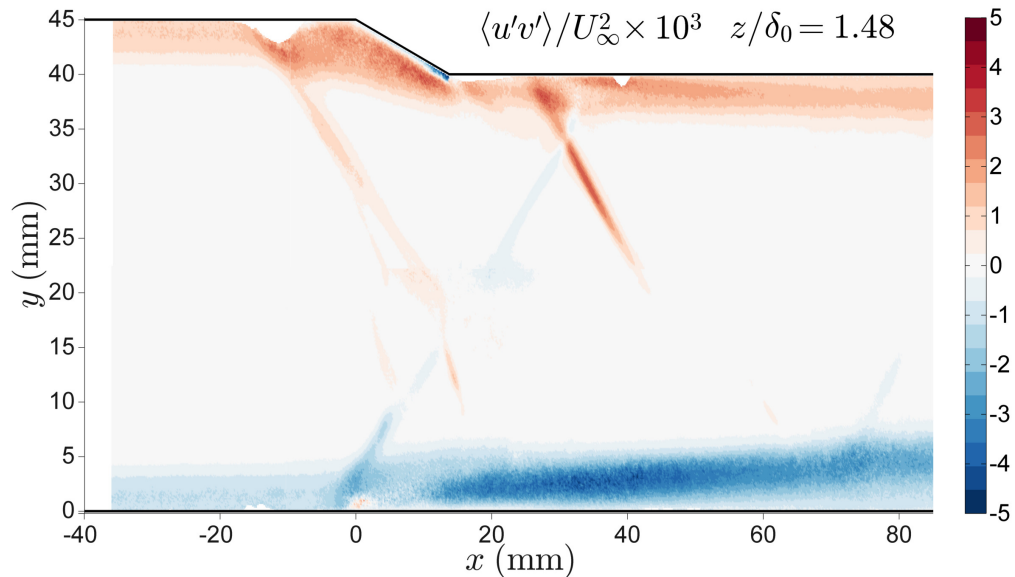


Figure 3.43: Reynolds shear stress, normalized by  $U_\infty^2$  for the large ramp ( $h_{\text{ramp}}/\delta_0 = 0.93$ ) at  $z/\delta_0 = 1.48$ .

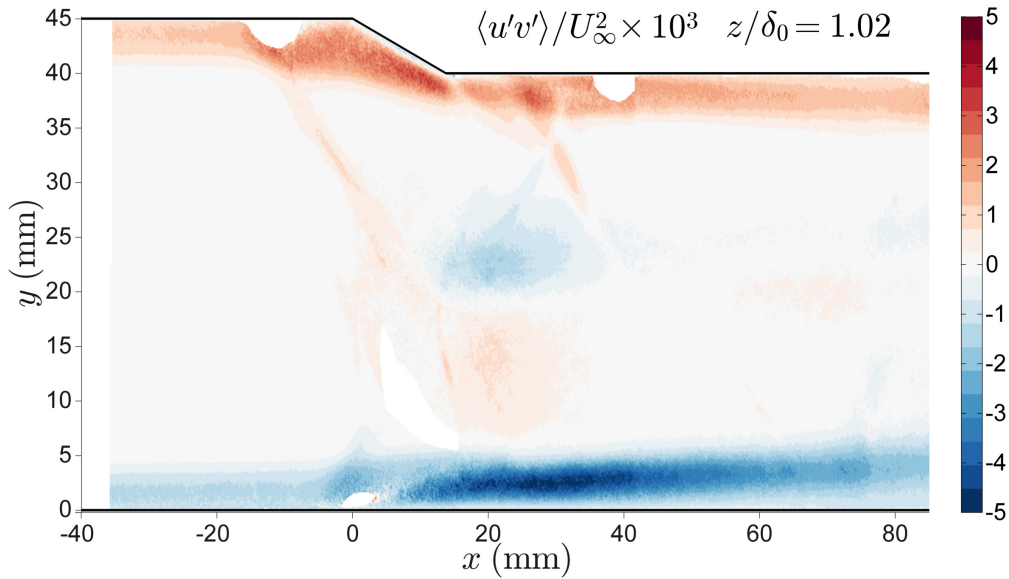


Figure 3.44: Reynolds shear stress, normalized by  $U_\infty^2$  for the large ramp ( $h_{\text{ramp}}/\delta_0 = 0.93$ ) at  $z/\delta_0 = 1.02$ .

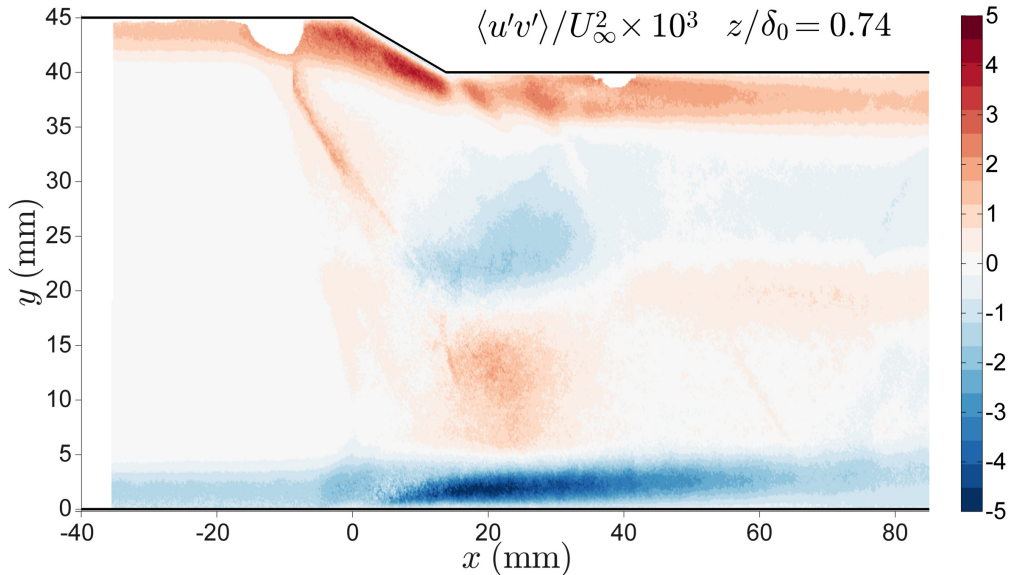


Figure 3.45: Reynolds shear stress, normalized by  $U_\infty^2$  for the large ramp ( $h_{\text{ramp}}/\delta_0 = 0.93$ ) at  $z/\delta_0 = 0.74$ .

Another prominent feature that appears in the streamwise fluctuations near the spanwise centerline for the larger ramp (Figure 3.26) is an elevated level of fluctuations associated with the shear layers downstream of the Mach stem. These features persist to the downstream limit of the measurement domain, and they mark the boundary between the wake and the surrounding faster fluid. Interestingly, the vertical distance between the top and bottom shear layers first decreases and then increases downstream of the Mach stem. This is consistent with the fact that the subsonic flow directly behind the Mach stem must pass through a minimum area sonic throat before being re-accelerated to supersonic speed. This minimum area occurs at a streamwise location of  $x \approx 30\text{mm}$ .

For both test geometries, a region of high turbulence intensity develops on the top wall upstream of the foot of the compression ramp and continues along its length. These fluctuations are associated with the thickening and separation of the boundary layer in this region of severe adverse pressure gradient as well as any unsteadiness in the position of the shock foot. The extent of the high turbulence intensity region is significantly larger for the larger ramp geometry; however the peak levels of turbulence intensity are comparable in both cases. As the side wall is approached, the size of the high turbulence region decreases and is confined to an area closer to the top wall, and the maximum level of turbulence intensity decreases. This is consistent with the lesser degree of boundary layer thickening observed in the mean velocity plots (Figures 3.4 – 3.11) as the measurement planes approach the side wall. Along the top wall downstream of the compression ramp where the expansion fan re-accelerates the boundary layer, the streamwise turbulence intensity drops significantly but the magnitude of the vertical fluctuations remains relatively constant. From the full-field data in the large ramp case (Figures 3.26 – 3.29, 3.34 – 3.37, and 3.42 – 3.45), it is evident that the turbulence in the top wall boundary layer does not fully recover downstream of the compression ramp prior to the impingement of the reflected shock

wave on the top wall.

On the bottom wall in the incident/reflected SBLI, there is a region of high intensity streamwise velocity fluctuations, particularly near the spanwise centerline of the duct (Figures 3.22 and 3.26). The trends in the velocity fluctuations in the incident shock interaction region across the span are similar between the two test cases but far more pronounced for the larger ramp geometry, so the discussion will focus primarily on the  $h_{\text{ramp}}/\delta_0 = 0.93$  case. The region of highest intensity streamwise fluctuations is confined to the area below the Mach stem between the separation shock and the projected impingement point of the transmitted shock. The locus of maximum streamwise velocity fluctuations starts near the foot of the separation shock and extends diagonally upward and away from the bottom wall, then turns back down toward the bottom wall downstream of where the transmitted shock impinges on the separated zone. This is in qualitative agreement with the results of previous studies including Dupont et al. (2005), Humble et al. (2007), and Souverein et al. (2010).

Downstream of the transmitted shock, the streamwise fluctuations in the accelerating boundary layer decay rapidly while the intensity of the vertical velocity fluctuations (Figures 3.34 – 3.37) remains elevated. This means that the turbulence anisotropy varies significantly in the streamwise direction throughout the incident shock interaction, first increasing and then decreasing downstream of the transmitted shock. This behavior was noted by Ardoneau et al. (1980), and is attributed to the redistribution of the turbulent kinetic energy in the interaction, primarily through the pressure-strain correlation terms. For the larger ramp geometry near the spanwise centerline ( $z/\delta_0 = 3.89$ ), the ratio of  $u'/v'$  just downstream of the separation shock is  $\approx 6$ , decaying to  $\approx 2.9$  in the region between the separation and transmitted shocks, and dropping further to  $\approx 1.3$  downstream of the transmitted shock.

In the planes closer to the side wall (Figures 3.27 – 3.29 and 3.35 – 3.37), the maximum observed levels of streamwise and vertical velocity fluctuations are lower

than for the spanwise centerplane. For these off-center planes, the ratio of  $u'/v'$  decreases everywhere in the flow except near the vertical half-height of the duct, where the rapid thickening of the side wall boundary layer intensifies both  $u'$  and  $v'$ . Furthermore, the loci of maximum streamwise and vertical velocity fluctuations in the  $z/\delta_0 = 1.48, 1.02$ , and  $0.74$  planes occur much closer to the bottom wall than in the spanwise centerplane. This observation is consistent with the fact that the thickening of the vertical boundary layer is less severe in these off-center planes.

In order to better highlight and quantify the non-uniformities across the span throughout the incident shock interaction for the  $h_{\text{ramp}}/\delta_0 = 0.93$  test case, profiles of mean streamwise velocity and streamwise velocity fluctuations are plotted in Figures 3.46 and 3.47. The quantity  $x^* = (x - x_0)/L_{\text{int}}$  describes a non-dimensional position within the interaction, where  $x_0$  is the projected point of impingement of the separation shock on the bottom wall and  $L_{\text{int}}$  is the interaction length, which is discussed in further detail in section 3.5. The profiles are plotted to a vertical height of  $y/\delta_0 = 3$ , which is contained below the Mach stem. Note that only every third data point is plotted in order to make the figures more readable.

Figure 3.46 shows that the mean velocity profiles in the disturbed turbulent boundary layer develop an inflection point due to the strong adverse pressure gradient in the interaction zone. This behavior is observed both near the centerline and toward the side wall, though it is most obvious in the profiles at  $z/\delta_0 = 3.89$ . The most significant distortion and blockage occurs near the spanwise centerline of the duct, as denoted by the evolution of the severe velocity deficit in the profiles at  $z/\delta_0 = 3.89$ . The variation in the profiles across the span is most notable near  $x^* = 0.5$  where the maximum mean flow reversal occurs near the spanwise centerline. This streamwise location is also where the side wall boundary layer experiences its most severe thickening, causing the velocity profiles at  $z/\delta_0 = 1.48, 1.02$ , and  $0.74$  to show a prominent non-monotonic behavior outside of  $y/\delta_0 = 1$ . It is remarkable to note how differently

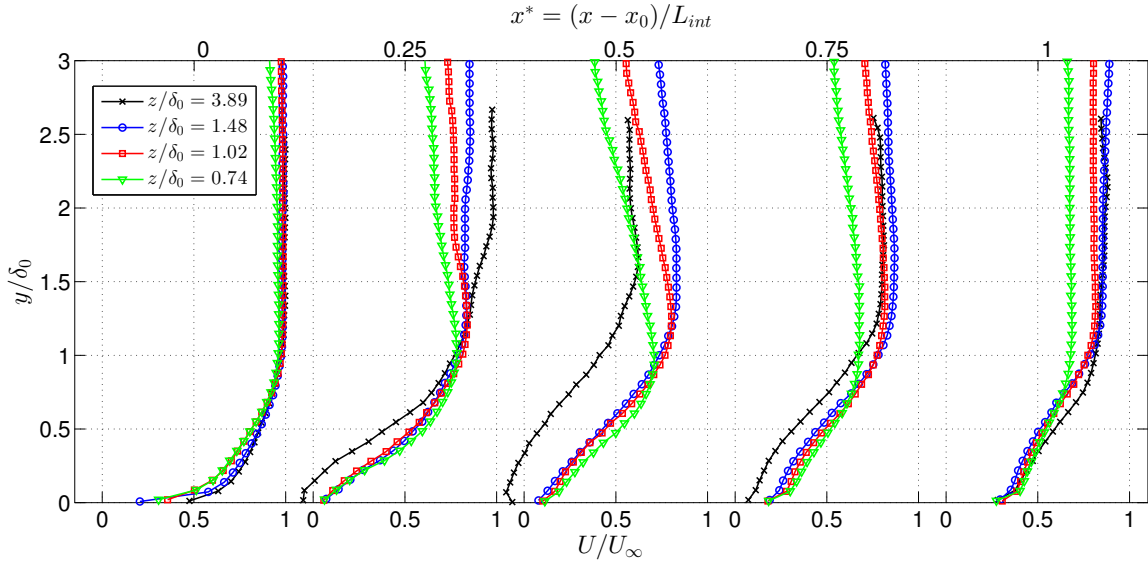


Figure 3.46: Streamwise evolution of the mean streamwise velocity profiles along the length of the incident shock interaction for the  $h_{\text{ramp}}/\delta_0 = 0.93$  test case.

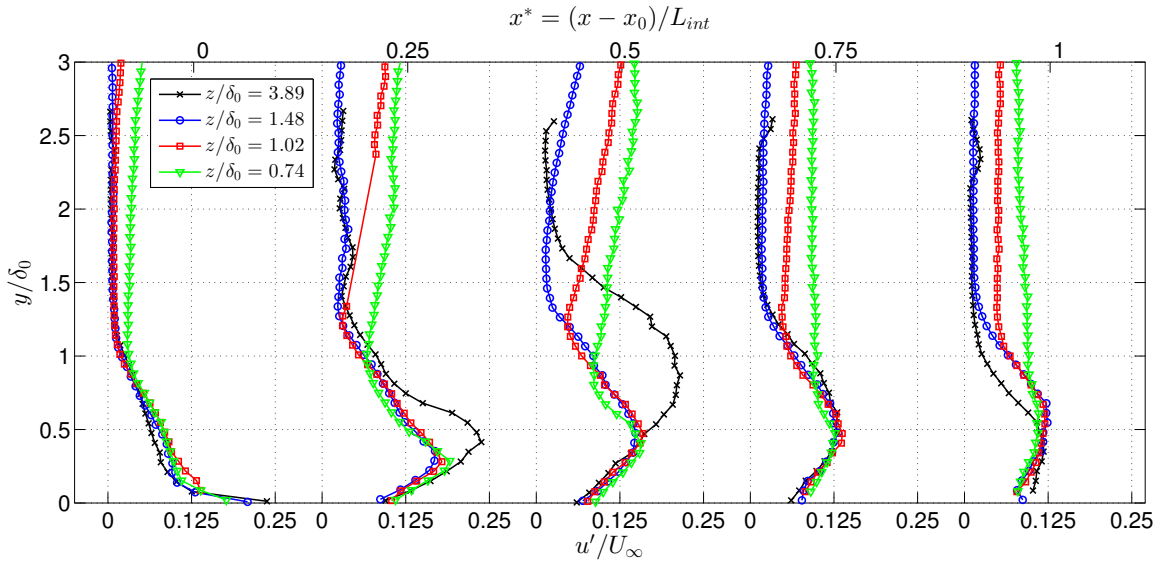


Figure 3.47: Streamwise evolution of the streamwise velocity fluctuation profiles along the length of the incident shock interaction for the  $h_{\text{ramp}}/\delta_0 = 0.93$  test case.

the profiles at  $z/\delta_0 = 1.48$  and  $3.89$  evolve in the streamwise direction. Even though the  $z/\delta_0 = 1.48$  measurement plane is well outside the side wall boundary layer in the inflow, it is heavily influenced by the thickening of the side wall boundary layer throughout the interaction. At the end of the interaction length, the profiles collapse below  $y/\delta_0 = 0.5$ , but asymptote to different values far from the bottom wall.

The profiles in Figure 3.47 show that the streamwise velocity fluctuations are amplified more near the spanwise centerline than closer to the side wall, particularly between  $x^* = 0.25$  and  $0.5$ . Outside of this streamwise region, there is fairly good agreement in the profiles across the span for  $y/\delta_0 < 1$ , with large discrepancies further from the bottom wall. Each profile shows a distinct maximum in  $u'$ , associated with the separated shear layer in the incident/reflected shock interaction.

The loci of  $\max(u')$  are extracted from the PIV data in planes near the spanwise centerline ( $z/\delta_0 = 3.89$ ) and at the edge of the incoming undisturbed side wall boundary layer ( $z/\delta_0 = 1.02$ ), and plotted in Figure 3.48. First, it is interesting to note that the shapes of the loci of  $\max(u')$  are both qualitatively and quantitatively different across the span. Near the spanwise centerplane, there is a clear peak around  $x^* \approx 0.5$  corresponding to the impingement point of the transmitted shock on the boundary layer; however closer to the side wall, the distance of  $\max(u')$  from the bottom wall increases monotonically throughout the interaction. Figure 3.48 also shows the loci of inflection points in the mean streamwise velocity profiles for the  $z/\delta_0 = 3.89$  and  $1.02$  data planes. In both planes there is very good agreement between the location of the inflection point in the  $U$  profile and the location of  $\max(u')$ . Despite the fact that this flow is compressible and three-dimensional, these results agree with the classic behavior observed in a subsonic mixing layer (Bell & Mehta (1990)) or subsonic reattaching turbulent boundary layer (Eaton & Johnston (1981)).

Contours of Reynolds shear stress for both ramp geometries are given in Figures 3.38 – 3.45. In compressible flows, the Reynolds shear stress term includes the local

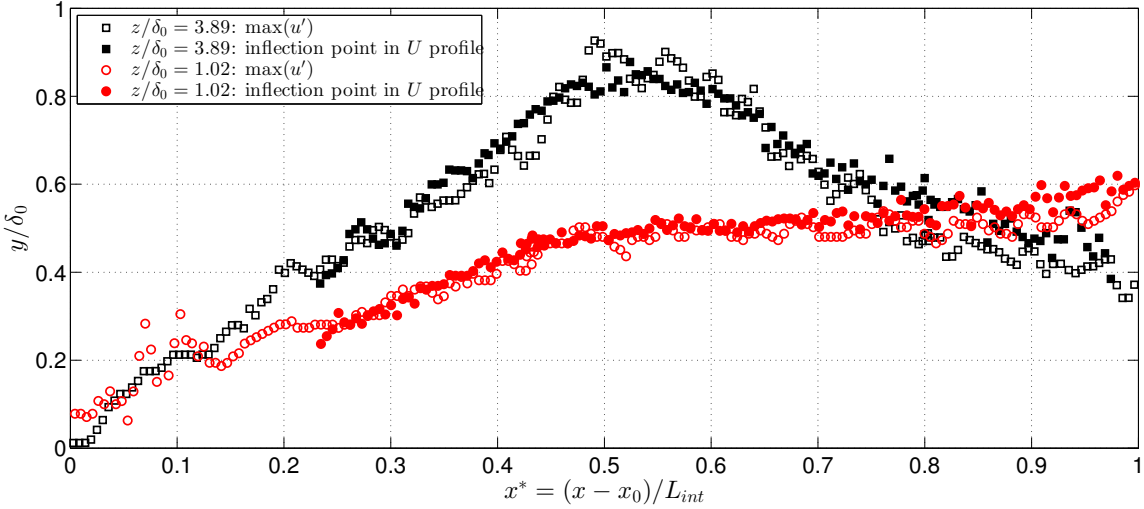


Figure 3.48: Loci of points corresponding to  $\max(u')$  and the inflection point of the  $U$  profiles throughout the incident shock interaction for the  $h_{\text{ramp}}/\delta_0 = 0.93$  case. The square symbols correspond to the plane near the spanwise centerline ( $z/\delta_0 = 3.89$ ) and circles correspond to data at  $z/\delta_0 = 1.02$ .

mean density; however since density measurements are not available, representative measurements of  $\langle u'v' \rangle$  are presented instead. These contours clearly show the shock waves due to small oscillations in their positions. Positive values of  $\langle u'v' \rangle$  are associated with shock waves that turn the flow downward (the incident and transmitted shocks) since negative fluctuations in the vertical velocity are correlated with deceleration in the streamwise direction. The opposite is true for shock waves that turn the flow upward. Toward the side wall boundary layer, the transmitted and reflected shock waves are no longer marked by sharp peaks in  $|\langle u'v' \rangle|$ . This is due to the thickening of the side wall boundary layer; the pressure signal is propagated through the large subsonic region, allowing the flow to decelerate and turn more gradually and effectively smearing out the effects in the streamwise direction (Figures 3.44 and 3.45).

In the incoming turbulent boundary layers, the Reynolds shear stress is positive on the top wall and negative on the bottom wall. The magnitude of  $\langle u'v' \rangle$  is amplified

by the interaction of the vertical boundary layers with the incident and reflected shock waves. In particular, strongly negative values of  $\langle u'v' \rangle$  are associated with the thinning of the bottom wall boundary layer downstream of the transmitted shock. This is consistent with the idea that a negative fluctuation in the vertical direction carries fluid with a higher streamwise momentum closer to the bottom wall, energizing and re-accelerating the boundary layer. This large streamwise-oriented region of high negative values of  $\langle u'v' \rangle$  is also in qualitative agreement with the results of Humble et al. (2007) and Piponnaiu (2009).

Close to the bottom wall and directly downstream of the separation shock near the spanwise centerline, there is a coherent region of positive Reynolds shear stress. This is interesting and counterintuitive because typically in a boundary layer positive values of  $\langle u'v' \rangle$  are associated with negative values of  $\partial U / \partial y$ , which is not the case here. A region of oppositely signed  $\langle u'v' \rangle$ , though less prominent, is observed on the top wall in the compression ramp interaction directly downstream of the foot of the incident shock. The effect is seen in both test geometries, but it is more significant in the stronger interactions produced by the  $h_{\text{ramp}}/\delta_0 = 0.93$  case. The region is oriented along the same direction as the locus of maximum  $u'$  near the spanwise centerplane in both the compression ramp and incident shock interactions. A similar region of positive  $\langle u'v' \rangle$  was observed by Humble et al. (2007) near the bottom wall downstream of the separation shock in an incident SBLI generated by an impinging shock with flow deflection of  $8^\circ$  in a  $M_\infty = 2.1$  flow. The consistent presence of this feature in both geometries investigated in this study, combined with the similar observation by Humble et al. (2007) suggest that the effect is physical; however the exact mechanism is unclear. Figure 3.49 shows profiles of the Reynolds shear stress plotted along with profiles of the mean velocity gradient,  $\partial U / \partial y$ . These profiles are extracted at four stations in the centerplane incident SBLI region of the  $h_{\text{ramp}}/\delta_0 = 0.93$  case. The furthest upstream profiles show the expected behavior of  $\langle u'v' \rangle < 0$  while  $\partial U / \partial y > 0$ .

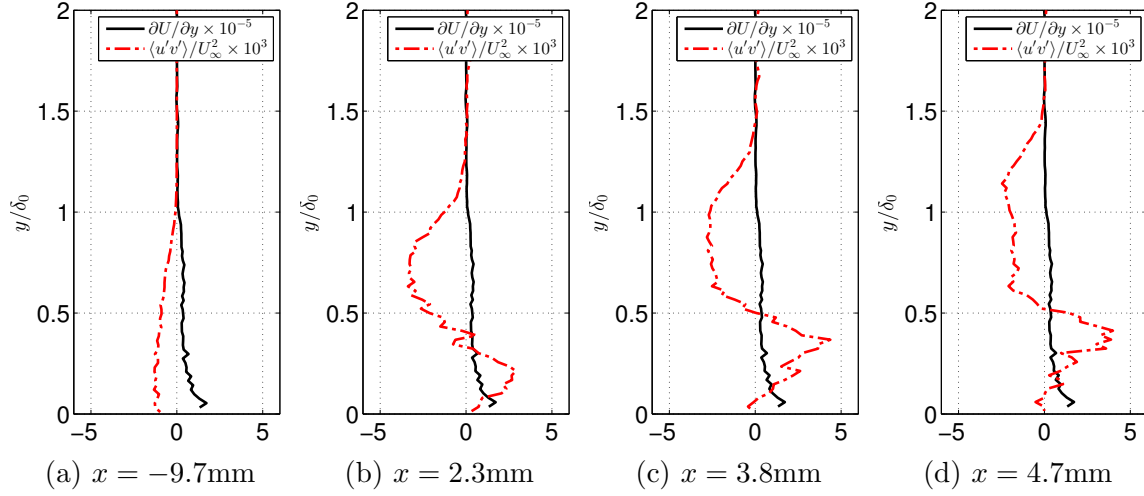


Figure 3.49: Profiles of  $\langle u'v' \rangle$  and  $\partial U / \partial y$ , extracted from the  $z/\delta_0 = 3.89$  data plane at four different streamwise positions in the incident shock interaction in the  $h_{\text{ramp}}/\delta_0 = 0.93$  geometry.

The three profiles at the downstream locations exhibit regions where this is not true.

### 3.5 Spatial scales of the interactions

One of the important spatial scales considered for shock boundary layer interactions is the interaction length,  $L_{\text{int}}$ . For SBLIs near compression ramps, this length is typically determined by the streamwise location upstream of the foot of the compression ramp where the mean wall pressure signal begins to rise. The interaction length can also be inferred by examining the mean streamwise velocity contours because the point where the wall pressure begins to rise corresponds directly to the location where strong boundary layer thickening begins, or alternatively where  $\partial U / \partial x$  begins rapidly decreasing, i.e. becoming more negative.

In the data of Helmer et al. (2012), the mean wall pressure signal upstream of the compression ramp is measured. The location of the first noticeable pressure rise matches well with the location where the rate of boundary layer thickening increases;

both occur at location  $\approx 1.4\delta_0$  upstream of the foot of the compression ramp near the spanwise centerline. No pressure measurements are made in the current experiments, so the interaction lengths are determined from the PIV measurements alone. The interaction lengths associated with the compression ramp SBLI flow near the spanwise centerline are  $L_{\text{int}} \approx 2.3\delta_0$  and  $L_{\text{int}} \approx 3.6\delta_0$  for the mid-size ( $h_{\text{ramp}}/\delta_0 = 0.56$ ) and large ( $h_{\text{ramp}}/\delta_0 = 0.93$ ) ramp geometries, respectively. Previous arguments for the scaling of  $L_{\text{int}}$  with the incoming Reynolds number, Mach number, boundary layer thickness, and compression ramp angle (see e.g. Délery & Marvin (1986)) assume large ramp geometries ( $h_{\text{ramp}} > \delta_0$ ) such that the size of the obstacle does not influence the interaction length. However, the results of the current experiments show that for smaller ramp sizes, the height of the ramp clearly also influences the interaction length.

In incident shock boundary layer interaction flows, the interaction length is related to the streamwise extent of the separated zone. Dupont et al. (2005) found that the length of the separated zone was well predicted by the distance between the projected impingement points of the incident and reflected shock waves on the bottom wall. Using this definition, the interaction lengths near the spanwise centerplane for the incident SBLIs are  $L_{\text{int}} \approx 3.5\delta_0$  and  $L_{\text{int}} \approx 8.0\delta_0$  for the mid-size and large ramps, respectively. Both of these interaction lengths are significantly larger than the value of  $L_{\text{int}} = 2.4\delta_0$  for the incident SBLI in the  $h_{\text{ramp}}/\delta_0 = 0.20$  investigated by Helmer (2011). Because this method of determining  $L_{\text{int}}$  is based on projected shock impingement points, both the shock angles and the vertical position of the intersection between the incident and reflected shocks play an important role. As the interaction strength increases, the influence of the separated zone is felt over a much greater vertical distance, pushing the shock crossing point away from the bottom wall. This effect is dominant over the steepening of the shock waves as the shock-generating ramp height increases (Table 3.3). Therefore an increase in  $L_{\text{int}}$  occurs as

the shock-generating ramp size increases.

Another way to quantify the size and strength of the incident shock interaction zone is to measure the length of the region over which mean flow reversal is observed on the bottom wall. This quantity does not correspond directly to the size of the separation bubble, but it provides valuable information for CFD validation, particularly given that accurately predicting the highly non-equilibrium separated boundary layer in this region is one of the most difficult challenges to numerical simulations. The lengths associated with mean flow reversal along the bottom wall are  $4.2\delta_0$ ,  $0.71\delta_0$ , and 0 for the  $h_{\text{ramp}}/\delta_0 = 0.93$ , 0.56, and 0.20 cases respectively.

Much work has been done to determine the frequency and length scales associated with the low frequency motion of the shock wave in SBLI flows (see Clemens & Narayanaswamy (2014) for review). The present experiments do not focus on identifying frequency content of the shock oscillation or the mechanism behind it. However, a related quantity – the shock excursion length  $L_{\text{ex}}$  – is computed.  $L_{\text{ex}}$  quantifies the streamwise distance traversed by the shock and is therefore a measure of the overall shock unsteadiness.

As described by Dupont et al. (2008), the position of the shock wave can be inferred from any quantity which has a step change across the shock wave, such as pressure, density, or a component of velocity. This work adopts the convention presented by Dupont et al. (2008) and Souverein et al. (2010), using the vertical velocity across the oblique shock waves to determine  $L_{\text{ex}}$ . The median position of the shock wave corresponds to the location of  $\max(v')$ . Then, the upstream and downstream extents of the shock oscillations are defined as the points corresponding to  $v' = (1/e) \max(v')$ . In these calculations, the low background level of freestream turbulence intensity is neglected. The process of determining  $L_{\text{ex}}$  is illustrated in Figure 3.50. In the case of the nearly normal Mach stem, it is necessary to use the streamwise fluctuations,  $u'$ , instead of the vertical fluctuations as there is very little change in vertical velocity

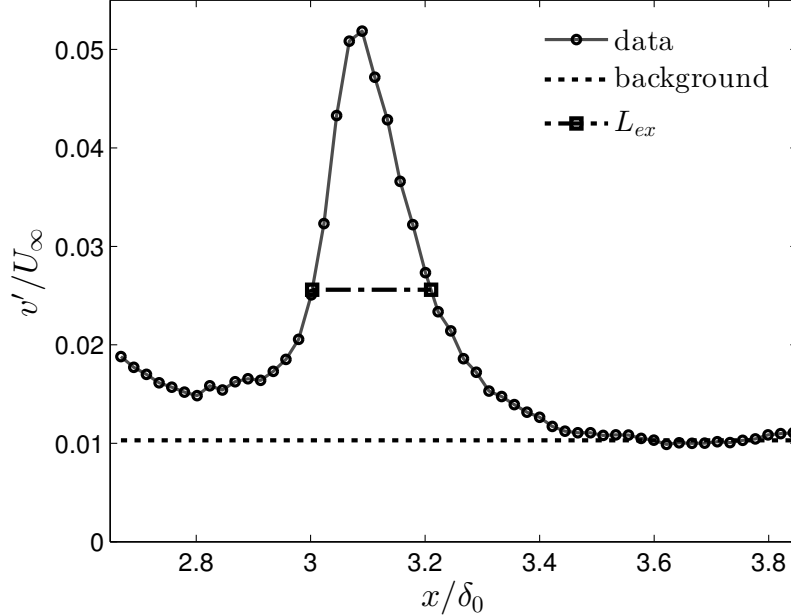


Figure 3.50: Streamwise evolution of  $v'/U_\infty$  for illustrating the method for determining  $L_{ex}$ . Data are from the transmitted shock at a vertical location of  $y/\delta_0 = 2.22$  in the  $h_{\text{ramp}}/\delta_0 = 0.93$  test geometry.

across this shock. It is important to note that this definition based on the velocity fluctuations does not allow  $L_{ex}$  to be determined in the high turbulence regions close to the walls, but it can be measured closer to the core of the duct. Table 3.4 presents a summary of  $L_{ex}$  near the spanwise centerplane of the duct for all of the shock waves in the test geometries presented. In addition,  $L_{ex}$  of the incident and reflected shocks has been extracted from the dataset of Helmer (2011) for comparison.

In general, the shock excursion lengths associated with all of the shock features are small relative to the incoming boundary layer size. The flow deflection across the incident shock wave ranges from  $8^\circ$  for the smallest ramp geometry to  $11.5^\circ$  for the largest ramp geometry. Dupont et al. (2006) report a value of  $L_{ex}/\delta_0 = 0.58$  for the reflected shock outside the boundary layer ( $y/\delta_0 = 3.45$ ) for a similar interaction where the flow deflection angle across the incident shock wave is  $9.5^\circ$  and the boundary

Table 3.4: Shock excursion length,  $L_{\text{ex}}$ , measured for various shock structures near the spanwise centerplane ( $z/\delta_0 = 3.89$ ) for the  $h_{\text{ramp}}/\delta_0 = 0.56$  and  $0.93$  test geometries.  $L_{\text{ex}}$  was also extracted from the data of Helmer et al. for the  $h_{\text{ramp}}/\delta_0 = 0.20$  for comparison.

$h_{\text{ramp}}/\delta_0$	shock type	$y/\delta_0$	$L_{\text{ex}}/\delta_0$
0.20 (Helmer)	incident	2.22	0.33
0.56	incident	2.22	0.40
0.93	incident	2.22	0.76
0.20 (Helmer)	reflected	2.22	0.37
0.56	reflected	2.22	0.38
0.93	reflected	4.07	0.36
0.93	separation	2.22	0.50
0.93	transmitted	2.22	0.22
0.93	Mach stem	3.15	0.23

layer is separated. This value is about a factor 1.5 larger than  $L_{\text{ex}}/\delta_0$  for the reflected shock in all of the test cases presented in Table 3.4; however it is comparable to the value of  $L_{\text{ex}}$  for the separation shock in the  $h_{\text{ramp}}/\delta_0 = 0.93$  case. In their experiments, Dupont et al. (2006) also observed an increase in  $L_{\text{ex}}/\delta_0$  of the reflected shock with increasing strength of incident shock wave. This trend is not seen in the current experiments; instead the value of  $L_{\text{ex}}/\delta_0$  appears to be constant across the three test cases, regardless of the strength of the incident shock wave or the degree to which the bottom wall boundary layer is separated.

Furthermore, previous experimental studies by Humble et al. (2007) noted much larger values of velocity fluctuations associated with the reflected shock wave as compared to the incident shock wave. They attributed this to the larger degree of unsteadiness observed in the reflected shock wave. However, in the current study the peak values of the velocity fluctuations associated with the incident and reflected shock waves are approximately equal (see Figures 3.30 – 3.37), further supporting the conclusion that the reflected shock wave in the current experiments does not exhibit

significant unsteadiness.

For the strongest interaction considered here ( $h_{\text{ramp}}/\delta_0 = 0.93$  test geometry), the least steady shock feature is the incident shock wave, with  $L_{\text{ex}}/\delta_0 = 0.76$ . This indicates that the maximum excursion of the incident shock from its median position is about  $\pm 2\text{mm}$  in the streamwise direction. The transmitted shock and Mach stem are the steadiest features, with very low values of  $L_{\text{ex}}/\delta_0$  of 0.22 and 0.23, respectively. In dimensional terms, this means that any oscillations of these shocks about their median positions are limited to a region of less than  $\pm 0.6\text{mm}$  in the streamwise direction. The consistently low values of  $L_{\text{ex}}$  for all of the shock features can be attributed to the very carefully controlled steady inflow conditions in the continuously operated wind tunnel facility.

While it would be interesting and informative to have measurements of the interaction and shock excursion length scales for the data planes away from the spanwise centerline of the duct, these values unfortunately cannot be inferred from the PIV measurements. The reason for this is that the techniques for calculating  $L_{\text{int}}$  and  $L_{\text{ex}}$  rely on identifying the shock features based on the elevated levels of velocity fluctuations in their vicinity. Closer to the side wall, the elevated levels of turbulence intensity associated with the side wall boundary layer and its interaction of the shock features obscures the signature of the shock waves.



# Chapter 4

## Effects of Geometric Perturbations

This chapter describes a novel uncertainty quantification (UQ) experiment for SBLI flows that was initiated in collaboration with Dr. David Helmer. A special purpose apparatus was jointly designed in order to introduce geometric perturbations to the inflow of the test section. Characterization of the sizes and shapes of perturbations produced by this device is part of the present work. Dr. Helmer's thesis (Helmer (2011)) includes descriptions of both the apparatus design and characterization for completeness. An entirely new description has been written for the present thesis. Helmer (2011) provides results from the initial stages of the UQ experiment, focusing on an SBLI in the vicinity of a  $h_{\text{ramp}}/\delta_0 = 0.20$  compression ramp. The present work explores an incident shock boundary layer interaction with the primary shock wave generated by that same  $h_{\text{ramp}}/\delta_0 = 0.20$  compression ramp. The experimental data and analysis contained within this chapter were all done as part of the present work.

### 4.1 Experimental setup

The UQ experiment is carried out using the same wind tunnel facility, measurement system, and data processing techniques as described in Chapter 2. Furthermore, the

inflow and boundary conditions are the same as described in Section 3.1 of Chapter 3. The important modifications are:

- The primary oblique shock wave is generated by a smaller  $20^\circ$  compression ramp with height  $h_{\text{ramp}} = 1.1\text{mm}$  ( $h_{\text{ramp}}/\delta_0 = 0.20$ ). This is the same compression ramp as used by Helmer (2011).
- Small geometric bumps of varying sizes and locations are introduced into the bottom wall surface upstream of the compression ramp. This is accomplished by installing a custom designed perturbation device, described in Section 4.2
- Acquiring full-field PIV measurements in multiple planes for a large number of different perturbed cases is not feasible. Therefore, data are acquired only in a single streamwise-vertical plane stationed near the centerline ( $z/\delta_0 = 3.89$ ), and the measurements for each case are focused on a small region near the impingement of the incident shock wave.
- Ensembles of 2500 PIV image pairs are acquired for each perturbed case, as opposed to the 5000 image pairs obtained at each camera location in the experiments from the previous chapter. The smaller sample size leads to higher uncertainties in turbulence quantities, and therefore only mean velocity measurements are provided for each of the perturbed configurations.

## 4.2 Perturbation device design

The objective of the UQ experiment is to quantitatively document the sensitivity of an SBLI to a large number of small, steady, geometric perturbations. A set of 2D RANS computations performed by Dr. Tonkid Chantrasmi was used to inform the initial experimental design. Each of the simulations had a slightly different perturbed

geometry, with a small bump placed somewhere in the inlet section on either the top or bottom wall of the wind tunnel. This study helped to narrow down the perturbation locations which should be included in the experimental test matrix. The RANS simulations indicated that bumps located on the bottom wall at streamwise positions between  $x = -50\text{mm}$  and  $x = -30\text{mm}$  would cause the largest changes in the downstream SBLI features. Based on these results, the initial design of the experiment allowed for bumps to be placed at streamwise locations between  $x = -54.2\text{mm}$  and  $x = -24.9\text{mm}$ . PIV measurements indicated that the sensitive region extended further upstream than initially predicted by RANS. Therefore an additional set of PIV measurements were acquired after relocating the perturbation device upstream to a position that allowed bumps to be placed between  $x = -82.2\text{mm}$  and  $x = -52.9\text{mm}$ .

In order to create bumps of varying size and position, the wind tunnel bottom wall is modified slightly to accommodate a custom designed perturbation device. This device consists of a  $5 \times 5$  array of  $1\frac{1}{2}''$  long 2-56 machine screws set vertically in a block which can be traversed in the streamwise direction. The screws extend up through slots machined in the bottom wall of the tunnel. The height of each screw can be individually set in order to deform a  $1/16''$  thick neoprene rubber sheet covering the slots. The rubber deforming surface fits precisely into a recessed area on the bottom wall, and it is glued in place at its edges. This flush mounting ensures that the bottom wall surface is as smooth as possible, and that the only disturbance to the flow is caused by the intentionally introduced bumps.

Schematics of the bottom wall with the perturbation device installed are shown in Figure 4.1. The top view shows that the spanwise arrangement of the screw slots is not symmetric about the spanwise centerline. The spanwise locations of each of the slots are  $z = 5.75, 14.75, 23.75, 28.25$ , and  $37.25\text{mm}$ , with the origin of the  $z$ -coordinate fixed to the back wall of the tunnel as before. The non-dimensional spanwise slot locations are  $z/\delta_0 = 1.06, 2.73, 4.40, 5.23$ , and  $6.90$ . The center slot

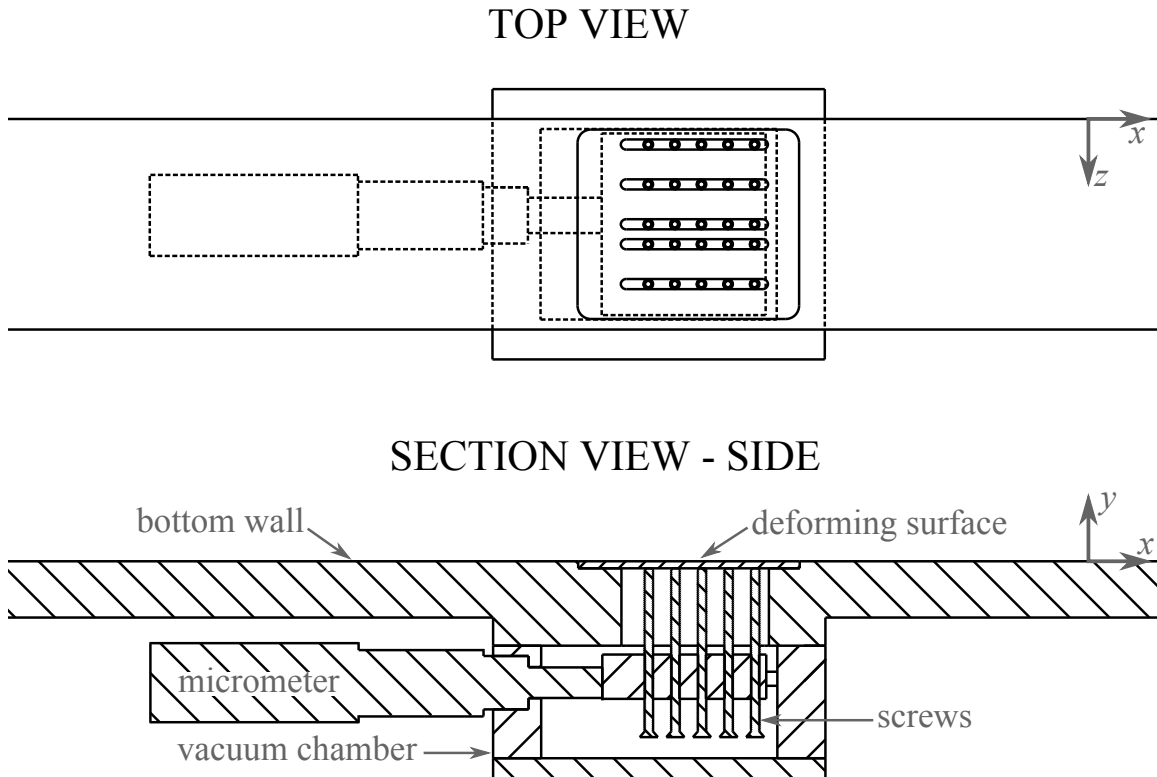


Figure 4.1: Top and side views of the perturbation device installed in the bottom wall. The figures are to scale, and the side view is a section cutaway at the spanwise centerline of the duct, showing the features enclosed in the vacuum chamber.

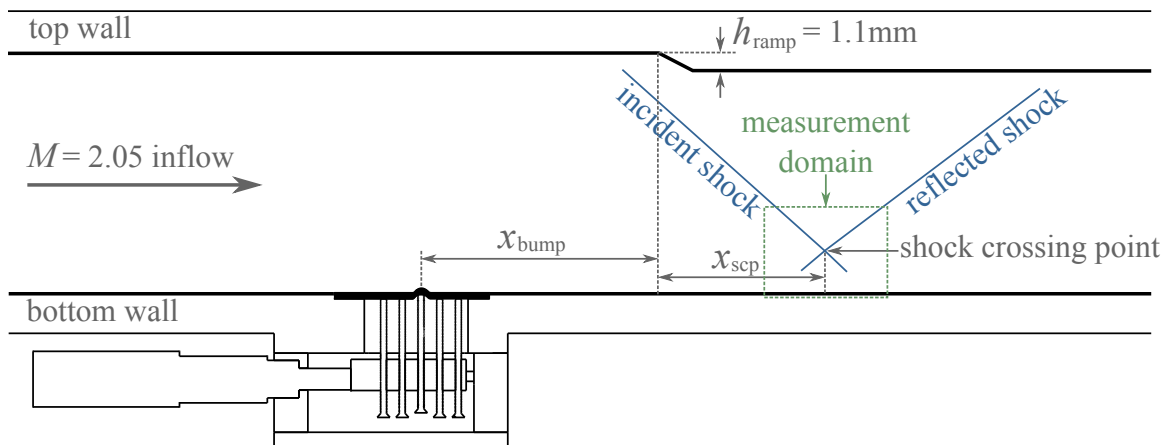


Figure 4.2: Overview of the perturbation device location relative to other important features of the experiment. Note that the ramp height is exaggerated for clarity.

( $z/\delta_0 = 4.40$ ) is located on the spanwise centerline of the duct. The spacing of the screws in the streamwise direction is 6mm, and the position of the screw block can be adjusted over a streamwise range of 5.3mm, accurate to  $\pm 0.05$ mm. This allows for a bump to be placed at almost any streamwise location over the full range of the device.

The whole assembly is encased in a sealed chamber which is connected to a vacuum pump. The differential pressure between the vacuum chamber and the inside of the wind tunnel inlet section is continuously monitored and maintained at  $-17 \pm 0.5$  kPa. This ensures that the pressure forces on the neoprene deforming surface are constant for all experiments and that the bump shapes and sizes are repeatable.

An overview of the location of the perturbation device relative to other important features of the wind tunnel is shown in Figure 4.2. The streamwise location of a given perturbation is called  $x_{\text{bump}}$ . All streamwise distances are measured relative to the  $x$ -coordinate origin at the foot of the compression ramp. The PIV measurement domain is indicated, as well as the approximate positions of the incident and reflected shock waves. It will be shown that the streamwise location of the shock crossing point ( $x_{\text{scp}}$ ) is sensitive to the upstream perturbations and is an important quantity of interest in the analysis of the UQ experiment results.

### 4.3 Characterization of perturbations

Bumps heights ranging from  $h_{\text{bump}} = 0.1$  mm to 0.9mm ( $h_{\text{bump}}/\delta_0 = 0.019$  to 0.17) can be reliably reproduced by turning the screws in half-turn increments. The zero position of each screw is determined by backing it out of the block until the head of the screw is flush with a custom machined zero-stop. The peak heights of individual bumps are measured using a dial indicator. These measurements are repeated multiple times, with the screws set to zero and reset to the desired height in between each

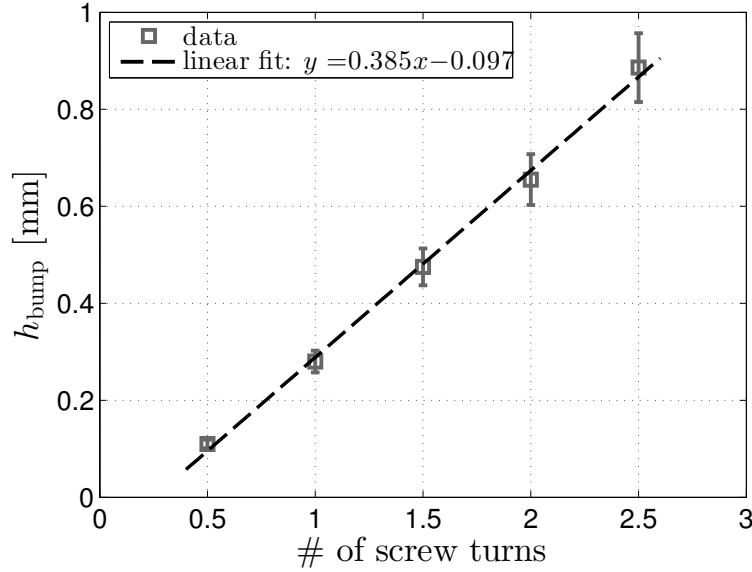


Figure 4.3: Bump height vs. number of screw turns.

measurement. Using this method, the uncertainty in the reported bump heights is  $\pm 8\%$ . As shown in Figure 4.3, the height of a bump is directly proportional to the number of screw turns. The bump shapes are not significantly altered when the surface temperature is decreased or when the the vacuum chamber differential pressure is changed by  $\pm 3.5$  kPa.

High resolution measurements of several single bump and two-bump configurations are made using confocal microscopy. A description of these measurements and details of the perturbation shapes can be found in Appendix A. Individual bumps are axisymmetric and can therefore be defined by a single profile shape. Profiles for single bumps of five different heights are shown in Figure 4.4. The shapes of these profiles can be well-approximated by fifth order polynomials or by Gaussians of the following forms:

$$h_{\text{poly5}}(z) = a_5 z^5 + a_4 z^4 + a_3 z^3 + a_2 z^2 + a_1 z + a_0 \quad (4.1)$$

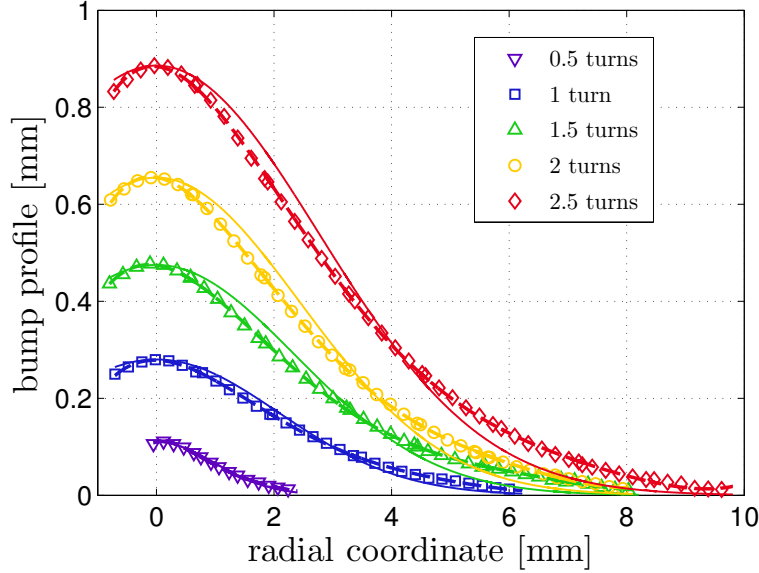


Figure 4.4: Profiles of axisymmetric perturbations of varying heights, created by a single screw at settings between 0.5 and 2.5 turns. Confocal microscope data (open symbols) are down-sampled by a factor of 25 to aid visualization. Fits using fifth order polynomials (---) and Gaussian distributions (—) are superimposed.

$$h_{\text{gauss}}(z) = A \exp \left( \frac{-(z - z_0)^2}{2\sigma^2} \right) \quad (4.2)$$

For single bumps, equation 4.1 is valid from  $z = 0 \rightarrow \infty$ , with the peak of the bump located at  $z = 0$ . Equation 4.2 is valid for  $z \in (-\infty, \infty)$ , with the peak of the bump located at  $z = z_0$ . The fifth-order polynomial and Gaussian approximations to each of the profiles are plotted on top of the confocal microscopy data in Figure 4.4 for comparison. The coefficients  $a_0, a_1, \dots, a_5$  of the polynomial approximations are given in Table A.1 in Appendix A. The parameters  $A$  and  $\sigma$  for each of the Gaussian fits are provided in Table A.2 of Appendix A.

Single-bump configurations have negligible overall effects on the SBLI features, at least in the  $z/\delta_0 = 3.89$  PIV measurement plane (Helmer (2011), Campo et al. (2012)). Therefore, the experiments presented in this chapter are conducted using

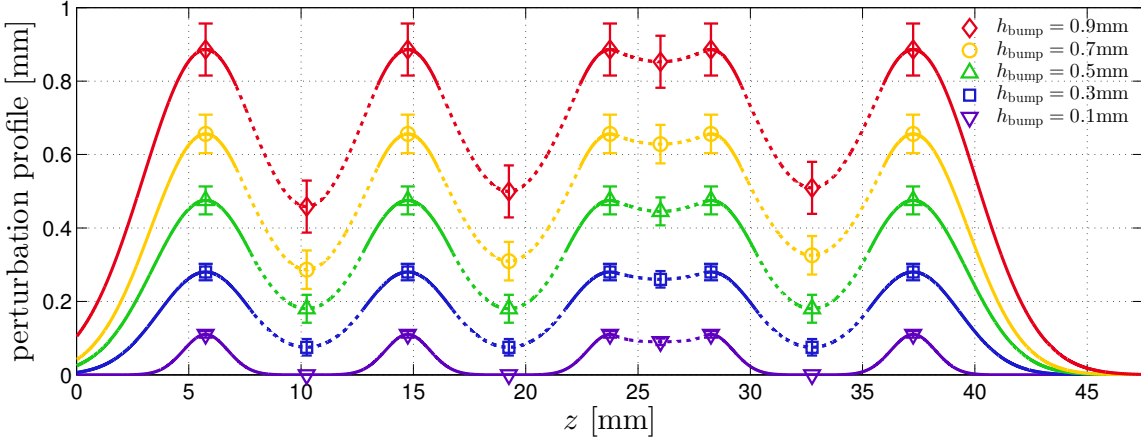


Figure 4.5: Perturbation surface profile analysis for a five-bump spanwise row configurations of five different heights. The shapes are modeled using Gaussian fits to the peaks (solid lines) and fifth order polynomial approximations to the valleys (dashed lines). Symbols represent macroscopic measurements made using a dial indicator.

larger quasi-2D perturbations, which are created by raising all five screws in a row across the span to the same height.

By combining the confocal microscopy and dial indicator measurements, the “ridge-line” of the five-bump perturbation across the tunnel span can be modeled. These shapes are shown in Figure 4.5 for all five of the different bump heights,  $h_{\text{bump}}$ , used in the perturbed cases presented in this chapter. The ridgeline profiles are described by Gaussians near the peaks (solid lines) and by fifth order polynomial splines near the vales (dashed lines). Details of the modeling of these shapes are provided in Appendix A.

## 4.4 Qualitative comparisons

All of the perturbations are configured as a spanwise row of five bumps of equal height (as shown in Figure 4.5). Five different bump heights are used:  $h_{\text{bump}} = 0.11, 0.28, 0.48, 0.66$ , and  $0.89\text{mm}$ . For each of these bump heights, nine different streamwise

placements are explored:  $x_{\text{bump}} = -72.2, -69.2, -63.2, -60.2, -57.2, -54.2, -51.2, -48.2$ , and  $-42.2\text{mm}$ , for a total of 45 different perturbed cases.

Several color contour plots of mean streamwise and vertical velocity components will be shown in this section. In all cases, the top left plot (a), shows the baseline unperturbed mean velocity field in the incident shock region of interest. The baseline velocity field will be used as a reference to examine how different perturbations alter the interaction, both qualitatively and quantitatively.

Mean streamwise and vertical velocity plots for the baseline case plus five different perturbed cases are shown in Figures 4.6 and 4.7. Subfigures (b) – (f) show the velocity field as perturbations of increasing height (0.1mm to 0.9mm) are added at a constant location  $x_{\text{bump}} = -57.2\text{mm}$ . These particular cases were chosen for illustrative purposes because bumps at this location produce some of the strongest velocity field disturbances. In each case, the streamwise coordinate is the absolute streamwise position minus the streamwise location of the shock crossing point in the unperturbed case,  $x_{\text{scp,unperturbed}}$ . The constant shift in  $x$  centers the unperturbed interaction zone about zero, and helps to highlight the fact that as perturbations are added at higher and higher heights, the perturbed SBLIs shift upstream. This trend is visible in both the streamwise (Figure 4.7) and vertical (Figure 4.6) velocity components, and the largest effect is felt for the tallest perturbations (subfigure (f), corresponding to  $h_{\text{bump}} = 0.9\text{mm}$ ). For the most perturbed case, the shift of the interaction is about 5mm in the upstream direction. This shift is significant relative to the other relevant length scales, representing  $\approx 90\%$  of the undisturbed boundary layer thickness,  $\delta_0$ , and  $\approx 11\%$  of the total duct height.

In the mean velocity plots, it appears that the incoming boundary layer thickens slightly, and that the outer portion of the boundary layer in the interaction is displaced further away from the bottom wall. This is most clearly noted by looking at the contour line corresponding to  $U = 450\text{m/s}$  in the streamwise velocity plots.

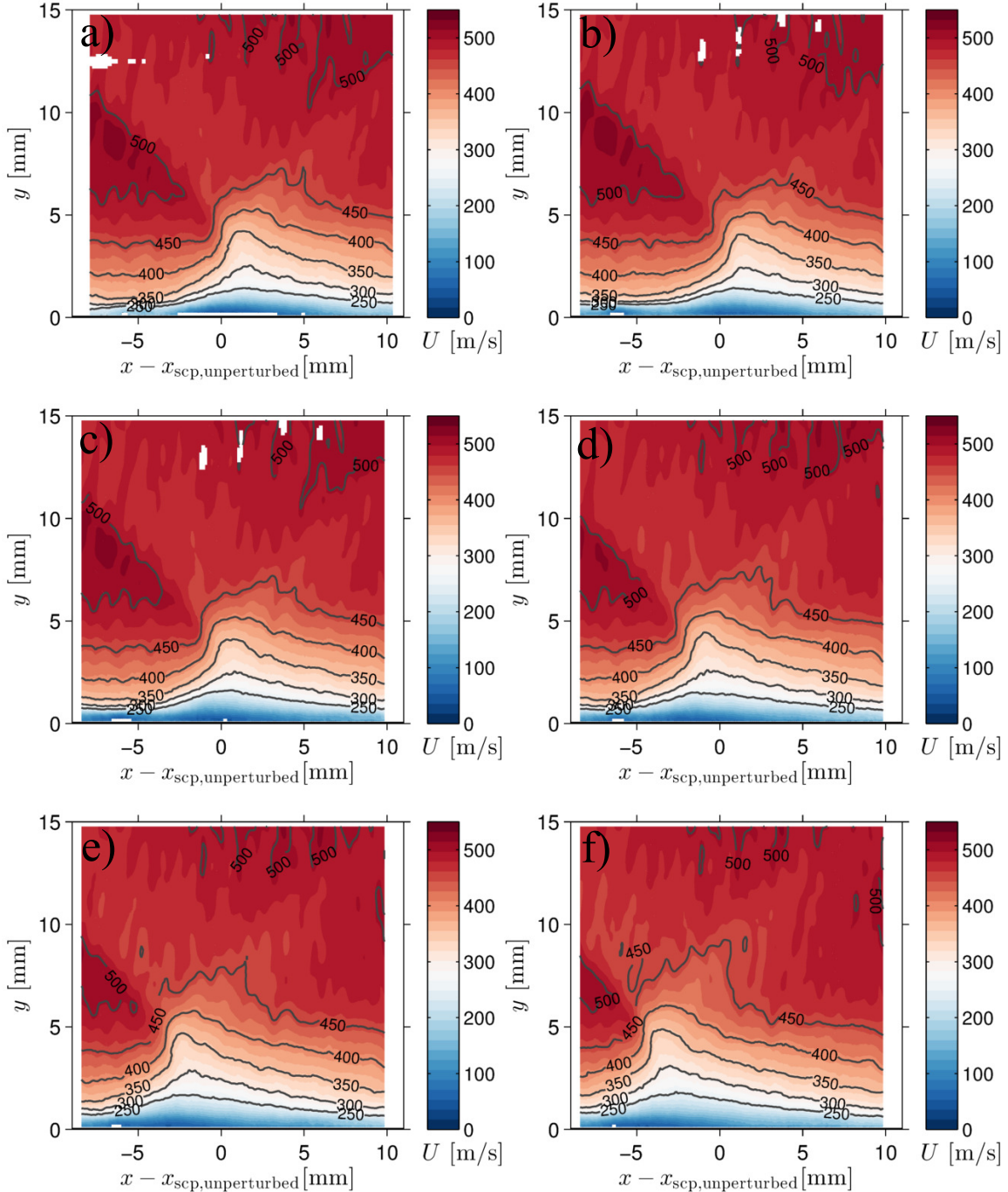


Figure 4.6: Mean streamwise velocity in the incident SBLI region for perturbations located at  $x_{\text{bump}} = -57.2\text{mm}$ . (a)  $h_{\text{bump}} = 0$  (unperturbed); (b)  $h_{\text{bump}} = 0.11\text{mm}$ ; (c)  $h_{\text{bump}} = 0.28\text{mm}$ ; (d)  $h_{\text{bump}} = 0.48\text{mm}$ ; (e)  $h_{\text{bump}} = 0.66\text{mm}$ ; (f)  $h_{\text{bump}} = 0.89\text{mm}$ .

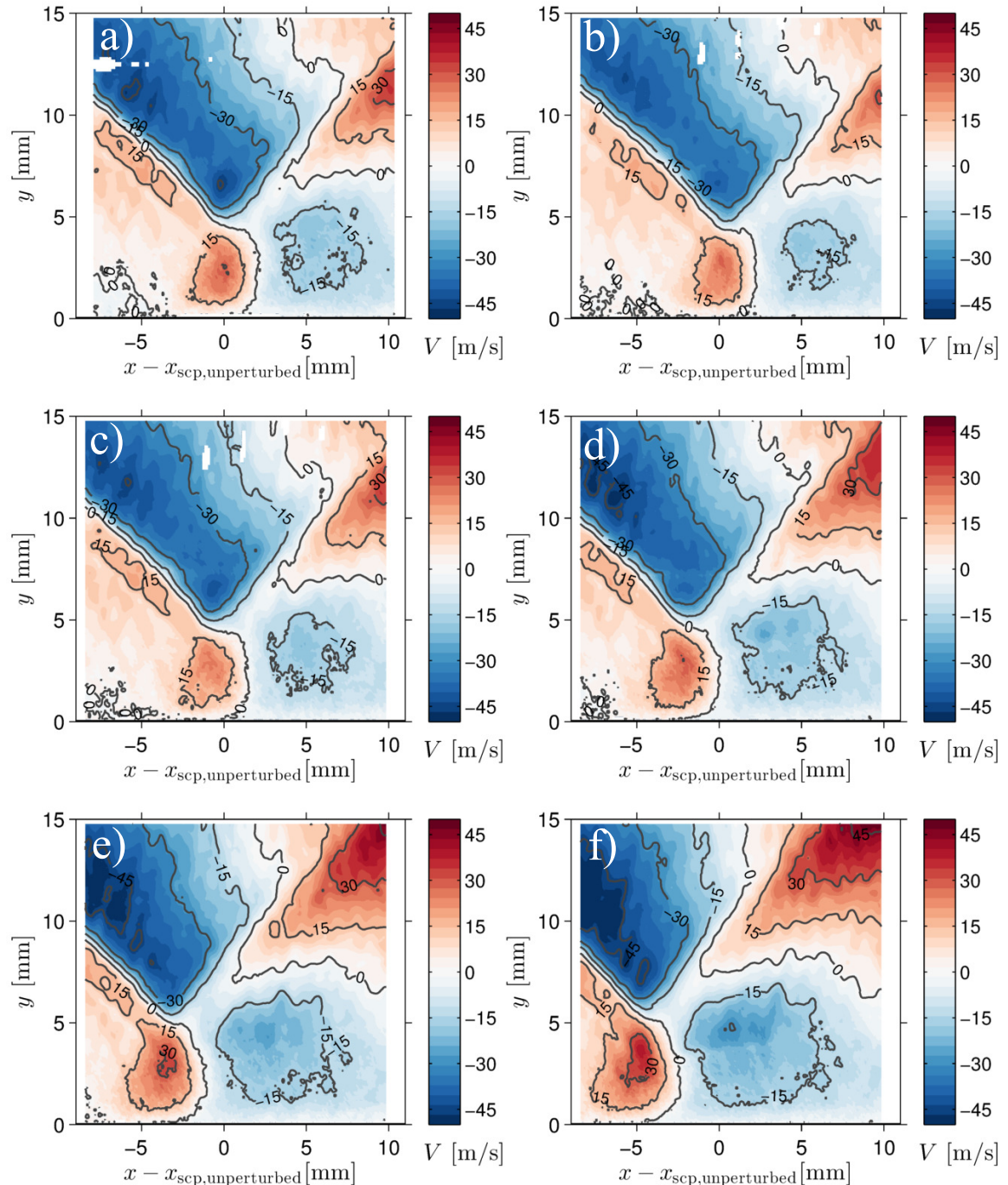


Figure 4.7: Mean vertical velocity in the incident SBLI region for perturbations located at  $x_{\text{bump}} = -57.2$  mm. (a)  $h_{\text{bump}} = 0$  (unperturbed); (b)  $h_{\text{bump}} = 0.11$  mm; (c)  $h_{\text{bump}} = 0.28$  mm; (d)  $h_{\text{bump}} = 0.48$  mm; (e)  $h_{\text{bump}} = 0.66$  mm; (f)  $h_{\text{bump}} = 0.89$  mm.

In the unperturbed case, this contour reaches a maximum height of  $\approx 7\text{mm}$ , but is displaced to  $\approx 9.5\text{mm}$  in the case with the largest perturbations. In the mean vertical velocity plots, the region of positive velocity associated with the reflected shock wave strengthens as the perturbation size is increased. Similarly, the region of negative velocity driving the boundary layer recovery downstream also strengthens with increasing bump height. Furthermore, the vertical velocity directly downstream of the incident oblique shock wave becomes more negative for larger perturbations at this streamwise location of  $x_{\text{bump}} = -57.2\text{mm}$ .

To further examine the specific differences between each case and the baseline unperturbed flow, Figures 4.8 and 4.9 show the velocity differences:

$$\Delta U = U(x - x_{\text{scp,unperturbed}}, y) - U_{\text{unperturbed}}(x - x_{\text{scp,unperturbed}}, y)$$

$$\Delta V = V(x - x_{\text{scp,unperturbed}}, y) - V_{\text{unperturbed}}(x - x_{\text{scp,unperturbed}}, y)$$

The top left subfigure (a) still represents the unperturbed baseline velocity for reference. Note that for the streamwise velocity difference plots (Figure 4.8), the range of values in the colormap is shifted and scaled down such that zero difference is represented by white and the features are distinguishable. These velocity difference figures confirm, at least in a qualitative sense, the trends that are noted in the previous figures. In both the mean streamwise and vertical velocity difference plots, the differences become monotonically larger as the size of the perturbations is increased while holding the position of the perturbations constant at  $x_{\text{bump}} = -57.2\text{mm}$ . The magnitude of the maximum local velocity differences for the most perturbed cases exceed  $150\text{m/s}$  ( $0.28U_\infty$ ) for the streamwise component and  $60\text{m/s}$  ( $0.28U_\infty$ ) in the vertical component.

Figure 4.8 highlights the thickening of the incoming boundary layer, denoted by

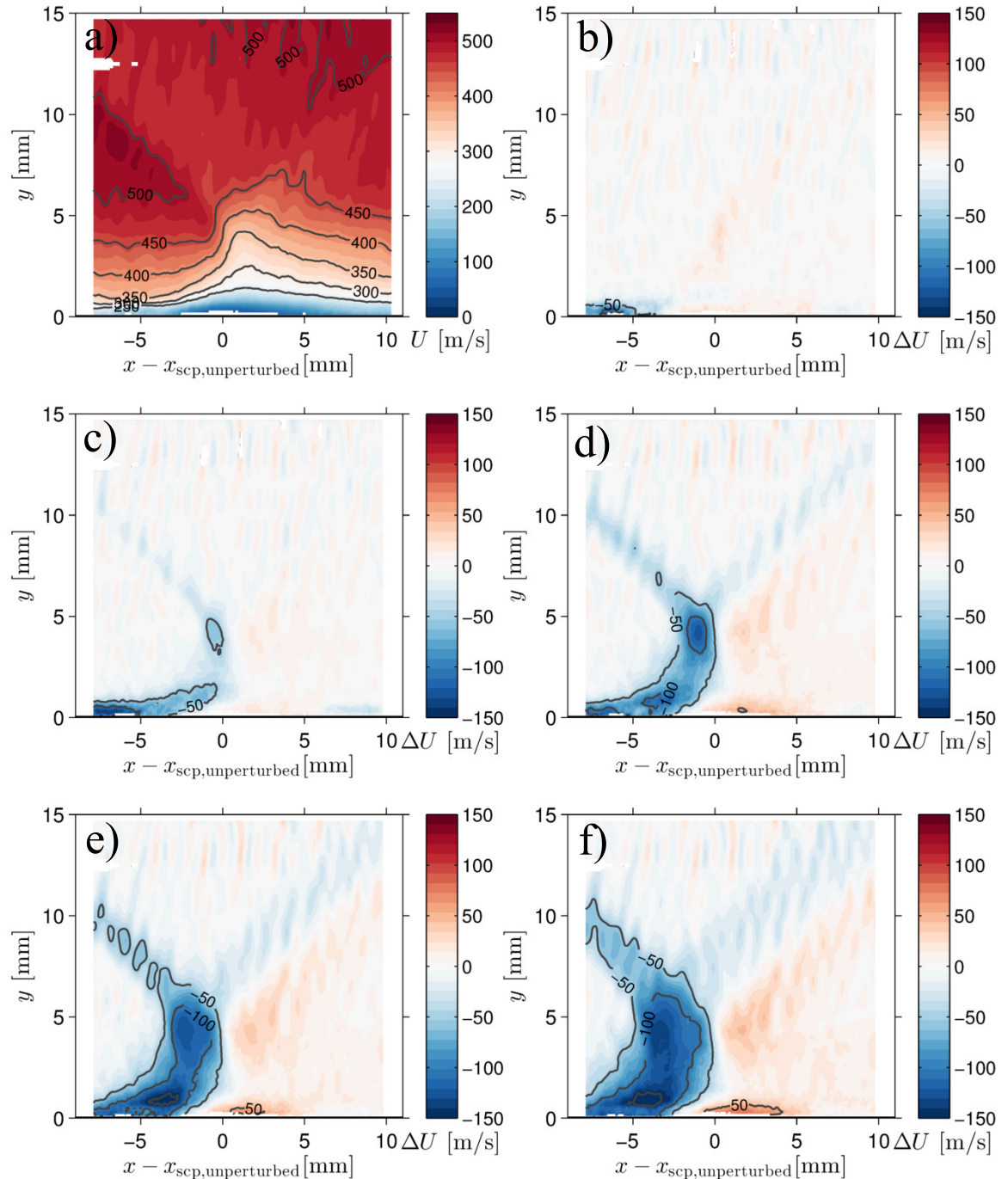


Figure 4.8: Mean streamwise velocity difference in the incident SBLI region for perturbations located at  $x_{bump} = -57.2\text{mm}$ . (a)  $h_{bump} = 0$  (unperturbed); (b)  $h_{bump} = 0.11\text{mm}$ ; (c)  $h_{bump} = 0.28\text{mm}$ ; (d)  $h_{bump} = 0.48\text{mm}$ ; (e)  $h_{bump} = 0.66\text{mm}$ ; (f)  $h_{bump} = 0.89\text{mm}$ .

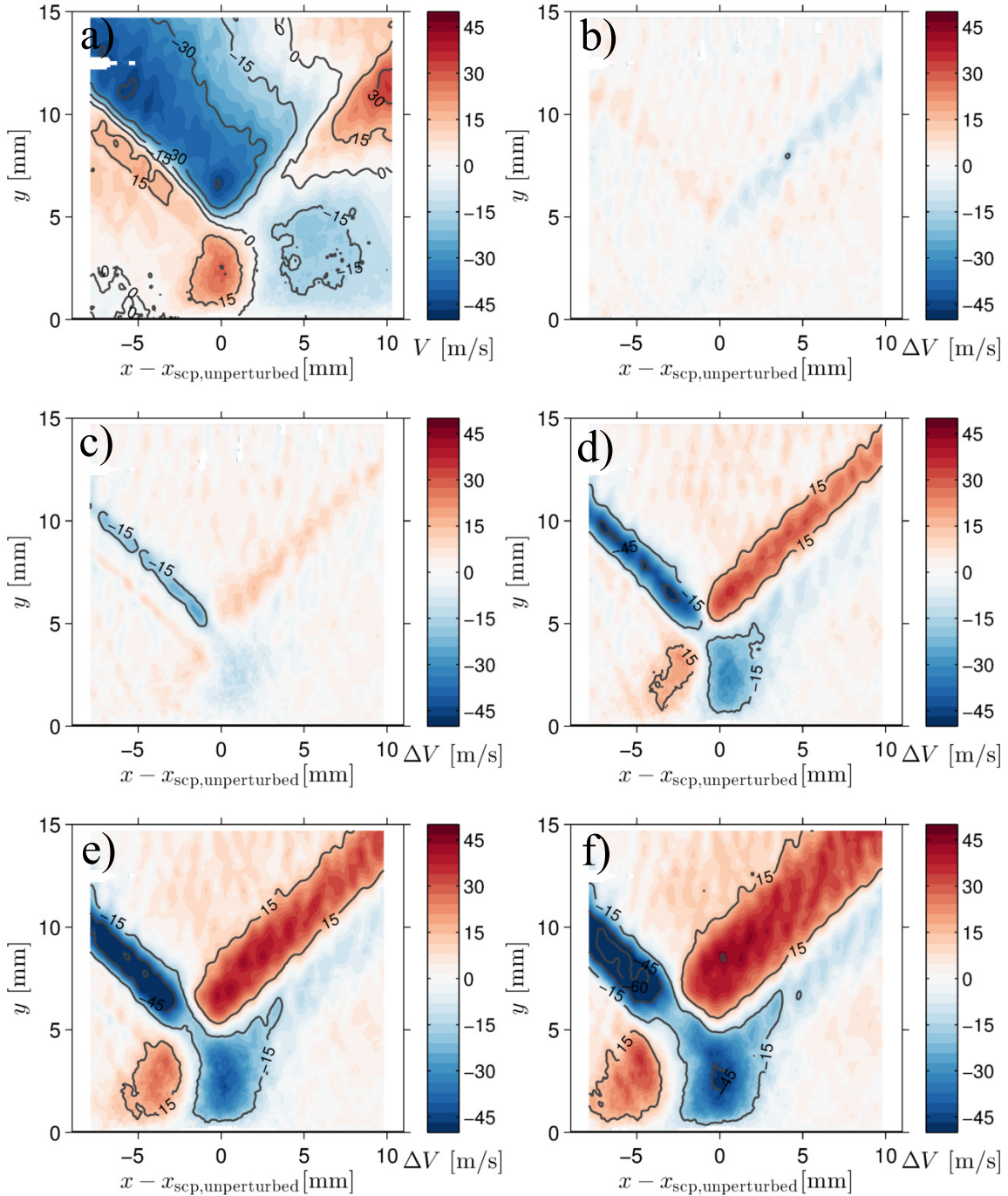


Figure 4.9: Mean vertical velocity difference in the incident SBLI region for perturbations located at  $x_{\text{bump}} = -57.2 \text{ mm}$ . (a)  $h_{\text{bump}} = 0$  (unperturbed); (b)  $h_{\text{bump}} = 0.11 \text{ mm}$ ; (c)  $h_{\text{bump}} = 0.28 \text{ mm}$ ; (d)  $h_{\text{bump}} = 0.48 \text{ mm}$ ; (e)  $h_{\text{bump}} = 0.66 \text{ mm}$ ; (f)  $h_{\text{bump}} = 0.89 \text{ mm}$ .

the negative (blue) contours at the bottom left corner of each figure. This incoming boundary layer thickening is the only noticeable difference for the case with the smallest perturbations (b). As the perturbations become larger (c) – (f), the negative  $\Delta U$  contours increase in size and strength. In the mean vertical velocity differences in Figure 4.9, a region of negative  $\Delta V$  is associated with the incident shock wave and a region of positive  $\Delta V$  is present in the vicinity of the reflected shock wave. These features are consistent with the overall upstream shift of the interaction as larger perturbations are introduced at  $x_{\text{bump}} = -57.2\text{mm}$ . As the shock features translate upstream, the downward deflection of the flow due to the incident shock wave and the upward deflection through the reflected shock wave both occur upstream relative to their unperturbed positions. For the cases with  $h_{\text{bump}} > 0.66\text{mm}$  in subfigures (c) – (f), there are also significant coherent regions of positive and negative  $\Delta V$  centered below the shock crossing point. These regions are also consistent with the overall upstream shift of the interaction. However, at this point it is impossible to say for sure whether these differences are due to the global shift in the position of the interaction with the addition of perturbations, or if these differences represent local changes in the structure of the interaction.

To separate the effects of local changes in the SBLI structures from the overall shift in its position, the mean velocity differences are recalculated after aligning the shock features in the streamwise direction. This transformation uses the streamwise position of the shock crossing point for each individual perturbed case as the shift in streamwise coordinate:  $x - x_{\text{sep}}$ . (Note that the specifics of how the shock crossing point is computed for each case are described in Section 4.5.3.)

Using this shifted  $x$  coordinate, the velocity differences are defined as:

$$\Delta U = U(x - x_{\text{sep}}, y) - U_{\text{unperturbed}}(x - x_{\text{sep,unperturbed}}, y)$$

$$\Delta V = V(x - x_{\text{scp}}, y) - V_{\text{unperturbed}}(x - x_{\text{scp,unperturbed}}, y)$$

The positions of the shock crossing point for each of the five perturbed cases with  $x_{\text{bump}} = -57.2\text{mm}$  are presented in Table 4.1.

This transformation centers all of the SBLIs about zero, and causes the incident and reflected shock waves to line up much more consistently. Figures 4.10 and 4.11 show the same five perturbed cases (b) – (f), with the velocity differences recomputed after shifting the streamwise coordinate to align all of the shock crossing points at zero. In the  $\Delta U$  plots, the only significant differences now appear in the bottom left corner where the incoming boundary layer is thicker than its unperturbed state. The velocity differences in the other regions of the flow are quite small, and a very noticeable overall reduction in  $\Delta U$  is achieved using the  $x_{\text{scp}}$  streamwise transformation (compare Figures 4.8 and 4.10).

The vertical velocity differences computed after aligning the shock crossing points in the streamwise direction (Figure 4.11) are also significantly reduced relative to their previous values (Figure 4.9). However, for the two largest perturbations (e) and (f), there is still a non-negligible vertical velocity difference associated with the incident shock wave. Whereas in the previous velocity difference computation this region had strong negative values of  $\Delta V$ , the incident shock wave is now associated with strong positive values of  $\Delta V$ . This new feature is consistent with a vertical misalignment of the incident shock wave, where the shock crossing point is pushed away from the bottom wall with increasing perturbation height. To determine whether or not a vertical shift of the shock crossing point is the cause for this region of large  $\Delta V$ , the

Table 4.1: Shock crossing point locations for cases with perturbations at  $x_{\text{bump}} = -57.2\text{mm}$ .  $\Delta x_{\text{scp}} = x_{\text{scp}} - x_{\text{scp,unperturbed}}$ .

$h_{\text{bump}}$ [mm]	0.11	0.28	0.48	0.66	0.89
$\Delta x_{\text{scp}}$ [mm]	0.36	-0.55	-1.96	-3.41	-4.76

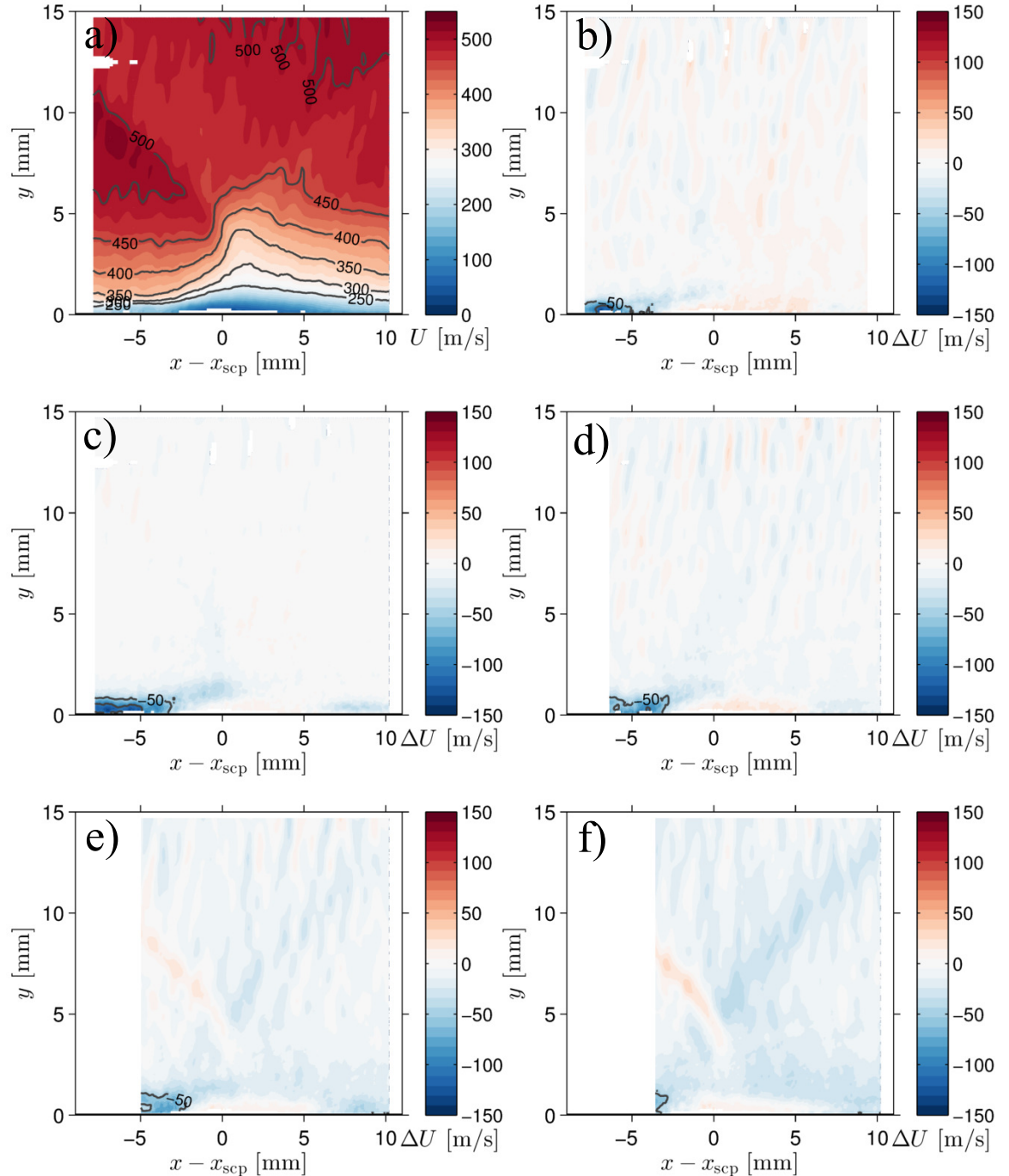


Figure 4.10: Mean streamwise velocity difference in the incident SBLI region for perturbations located at  $x_{\text{bump}} = -57.2\text{mm}$ . (a)  $h_{\text{bump}} = 0$  (unperturbed); (b)  $h_{\text{bump}} = 0.11\text{mm}$ ; (c)  $h_{\text{bump}} = 0.28\text{mm}$ ; (d)  $h_{\text{bump}} = 0.48\text{mm}$ ; (e)  $h_{\text{bump}} = 0.66\text{mm}$ ; (f)  $h_{\text{bump}} = 0.89\text{mm}$ . The data are shifted to align the shock crossing points in the streamwise direction.

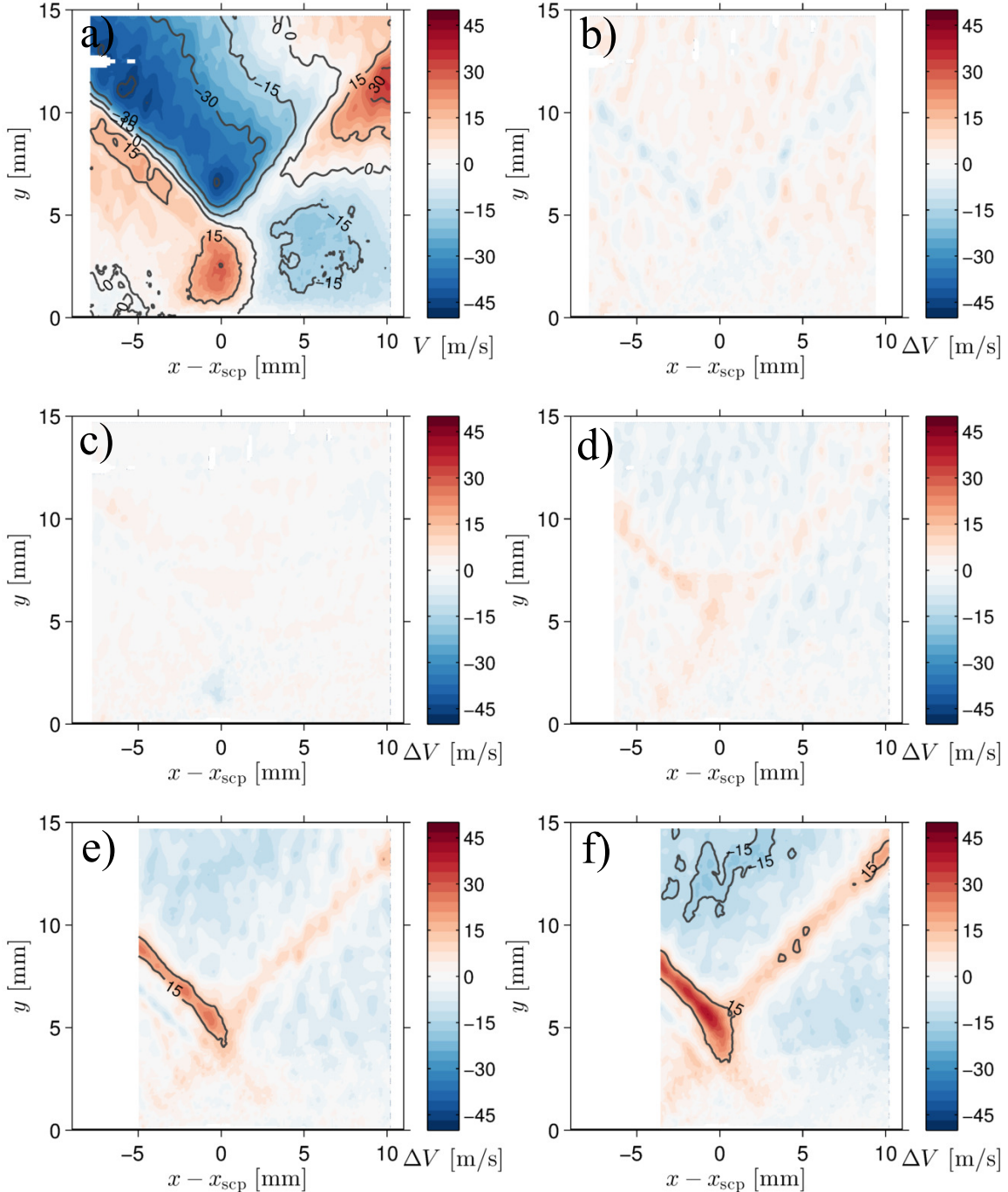


Figure 4.11: Mean vertical velocity difference in the incident SBLI region for perturbations located at  $x_{bump} = -57.2$  mm. (a)  $h_{bump} = 0$  (unperturbed); (b)  $h_{bump} = 0.11$  mm; (c)  $h_{bump} = 0.28$  mm; (d)  $h_{bump} = 0.48$  mm; (e)  $h_{bump} = 0.66$  mm; (f)  $h_{bump} = 0.89$  mm. The data are shifted to align the shock crossing points in the streamwise direction.

velocity differences can be recomputed once more after shifting both the streamwise and vertical coordinates to align the shock crossing point for all cases in both the vertical and horizontal directions; i.e. the shock crossing point is shifted to (0,0) in every case:

$$\Delta U = U(x - x_{\text{scp}}, y - y_{\text{scp}}) - U_{\text{unperturbed}}(x - x_{\text{scp}, \text{unperturbed}}, y - y_{\text{scp}, \text{unperturbed}})$$

$$\Delta V = V(x - x_{\text{scp}}, y - y_{\text{scp}}) - V_{\text{unperturbed}}(x - x_{\text{scp}, \text{unperturbed}}, y - y_{\text{scp}, \text{unperturbed}})$$

Figures 4.12 and 4.13 show the results of recomputing  $\Delta U$  and  $\Delta V$  with the shock crossing points aligned in both directions. The bottom wall is marked by a black line, and due to the vertical shift by  $y_{\text{scp}}$ , it is no longer fixed at zero. In regions where the velocity fields no longer overlap due to the horizontal and vertical shifting, the  $\Delta U$  and  $\Delta V$  plots appear white. This is due to a lack of data rather than a true difference of zero in these regions.

For the smallest bump cases (b) and (c), the vertical shift is small and the resulting plots are very similar to the ones in Figure 4.10. In the larger bump cases (d) – (f), a non-negligible shift in  $y$  is observed. This causes all features above the lower half of the boundary layer to better align, resulting in smaller  $\Delta U$  far from the wall. However, as expected, any relative vertical shift between the perturbed and unperturbed velocity fields causes a large discrepancy in the bottom part of the boundary layer where  $\partial U / \partial y$  is largest. Since the perturbed velocity fields must be shifted down relative to the unperturbed field in order to align the shock crossing point vertically, a long streamwise-oriented region of high positive  $\Delta U$  occurs near the bottom wall in Figures 4.12 (d) – (f).

By aligning the shock crossing points in both the streamwise and vertical directions, the recomputed  $\Delta V$  values are significantly reduced for the largest bump cases, as shown in Figure 4.13. Because the  $\partial V / \partial y \ll \partial U / \partial y$  in the boundary layer, there

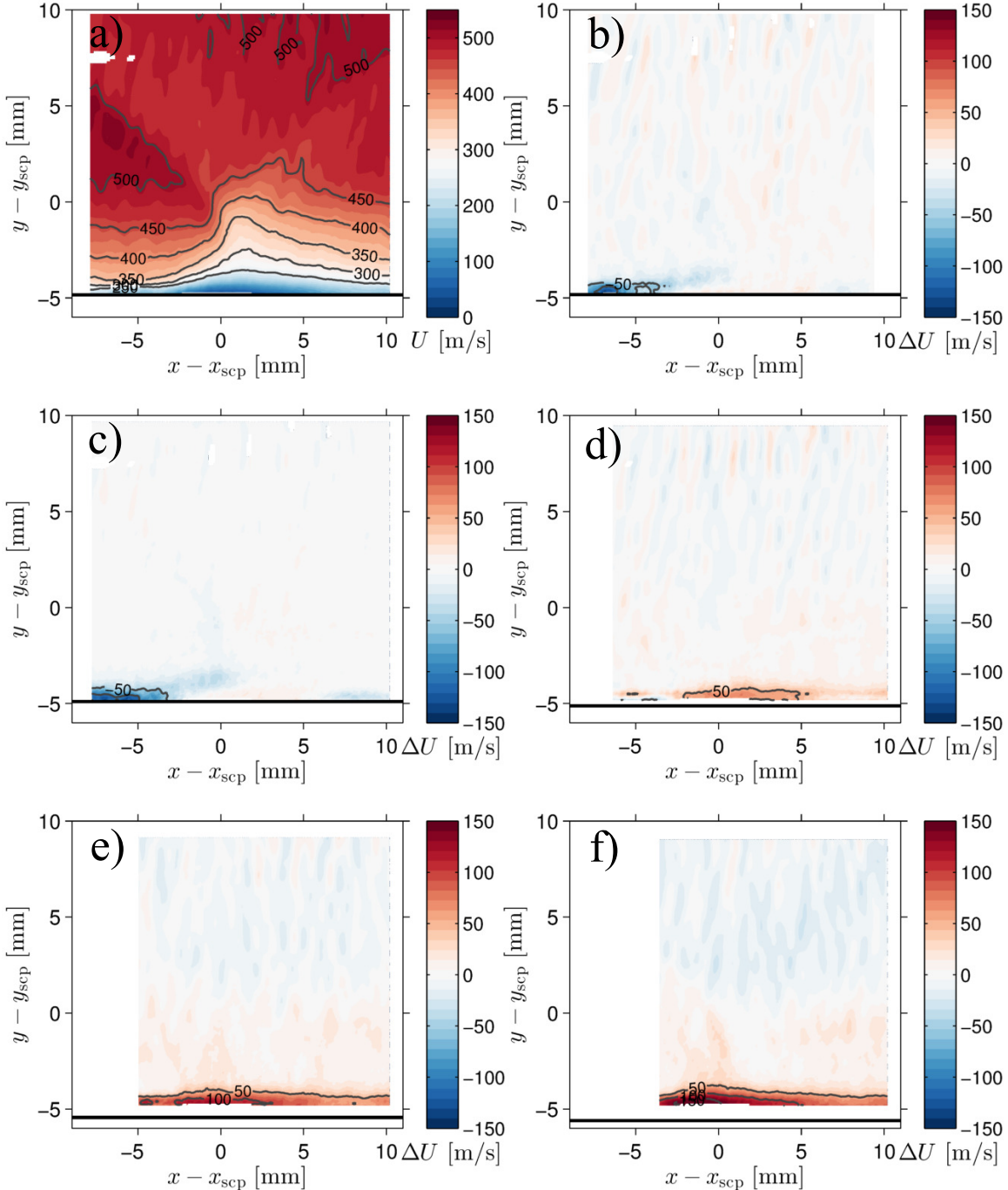


Figure 4.12: Mean streamwise velocity difference in the incident SBLI region for perturbations located at  $x_{\text{bump}} = -57.2\text{mm}$ . (a)  $h_{\text{bump}} = 0$  (unperturbed); (b)  $h_{\text{bump}} = 0.11\text{mm}$ ; (c)  $h_{\text{bump}} = 0.28\text{mm}$ ; (d)  $h_{\text{bump}} = 0.48\text{mm}$ ; (e)  $h_{\text{bump}} = 0.66\text{mm}$ ; (f)  $h_{\text{bump}} = 0.89\text{mm}$ . The data are shifted to align the shock crossing points in both the streamwise and vertical directions.

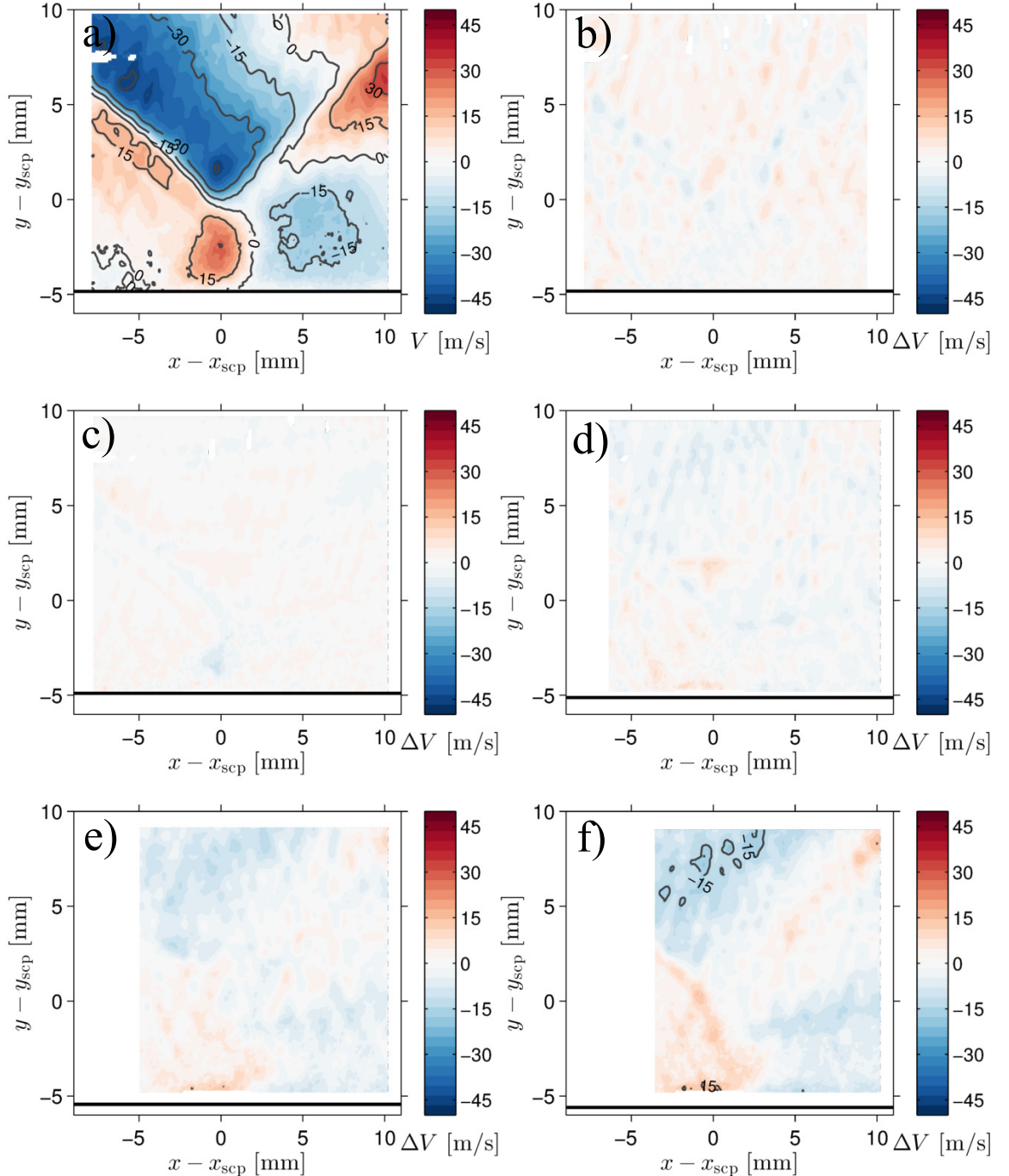


Figure 4.13: Mean vertical velocity difference in the incident SBLI region for perturbations located at  $x_{\text{bump}} = -57.2$  mm. (a)  $h_{\text{bump}} = 0$  (unperturbed); (b)  $h_{\text{bump}} = 0.11$  mm; (c)  $h_{\text{bump}} = 0.28$  mm; (d)  $h_{\text{bump}} = 0.48$  mm; (e)  $h_{\text{bump}} = 0.66$  mm; (f)  $h_{\text{bump}} = 0.89$  mm. The data are shifted to align the shock crossing points in both the streamwise and vertical directions.

Table 4.2: Positions of the shock crossing points for cases with perturbations at  $x_{\text{bump}} = -75.2\text{mm}$ .  $\Delta x_{\text{scp}} = x_{\text{scp}} - x_{\text{scp,unperturbed}}$ .

$h_{\text{bump}}$ [mm]	0.11	0.28	0.48	0.66	0.89
$\Delta x_{\text{scp}}$ [mm]	0.09	-0.62	-0.36	-0.42	-0.36

are no regions of particularly large  $\Delta V$  due to the vertical shifting.

All of the plots in Figures 4.6 – 4.13 correspond to the same five perturbed cases ( $x_{\text{bump}} = 57.2\text{mm}$ ,  $h_{\text{bump}} = 0.1, 0.3, 0.5, 0.7$ , and  $0.9\text{mm}$ ), plus the baseline unperturbed case. The reason for demonstrating the qualitative comparison process on these five specific perturbed cases is that they show some of the largest discrepancies between perturbed and unperturbed velocity fields. This makes the results of the shifting process easy to identify. However, some of the perturbed cases show much smaller differences from the baseline case, even when data are not shifted to correct for differences in  $x_{\text{scp}}$  and  $y_{\text{scp}}$ . Sample velocity and velocity difference plots from a set of these perturbed cases ( $x_{\text{bump}} = 75.2\text{mm}$ ,  $h_{\text{bump}} = 0.1, 0.3, 0.5, 0.7$ , and  $0.9\text{mm}$ ) are shown in 4.14 – 4.21. The positions of the shock crossing point for each of the five perturbed cases with  $x_{\text{bump}} = -75.2\text{mm}$  are presented in Table 4.2.

Figures 4.14 and 4.15 demonstrate that for perturbations located further upstream at  $x_{\text{bump}} = -75.2\text{mm}$ , the SBLI does not respond by translating upstream as it did for the same size perturbations located at  $x_{\text{bump}} = -57.2\text{mm}$ . When the difference between unshifted perturbed and unperturbed velocity fields is computed (4.16 and 4.17), the resulting  $\Delta U$  and  $\Delta V$  are small. The quantities  $\Delta U$  and  $\Delta V$  can be slightly reduced by shifting the streamwise coordinate by  $x_{\text{scp}}$  to align the shock crossing points in the streamwise direction (Figures 4.18 and 4.19). Marginally better agreement is achieved by aligning the shock crossing point in the vertical direction (Figures 4.20 and 4.21).

The differences for the case with the largest perturbations (f), shows the largest discrepancies of all the cases with perturbations at  $x_{\text{bump}} = -75.2\text{mm}$ , regardless of

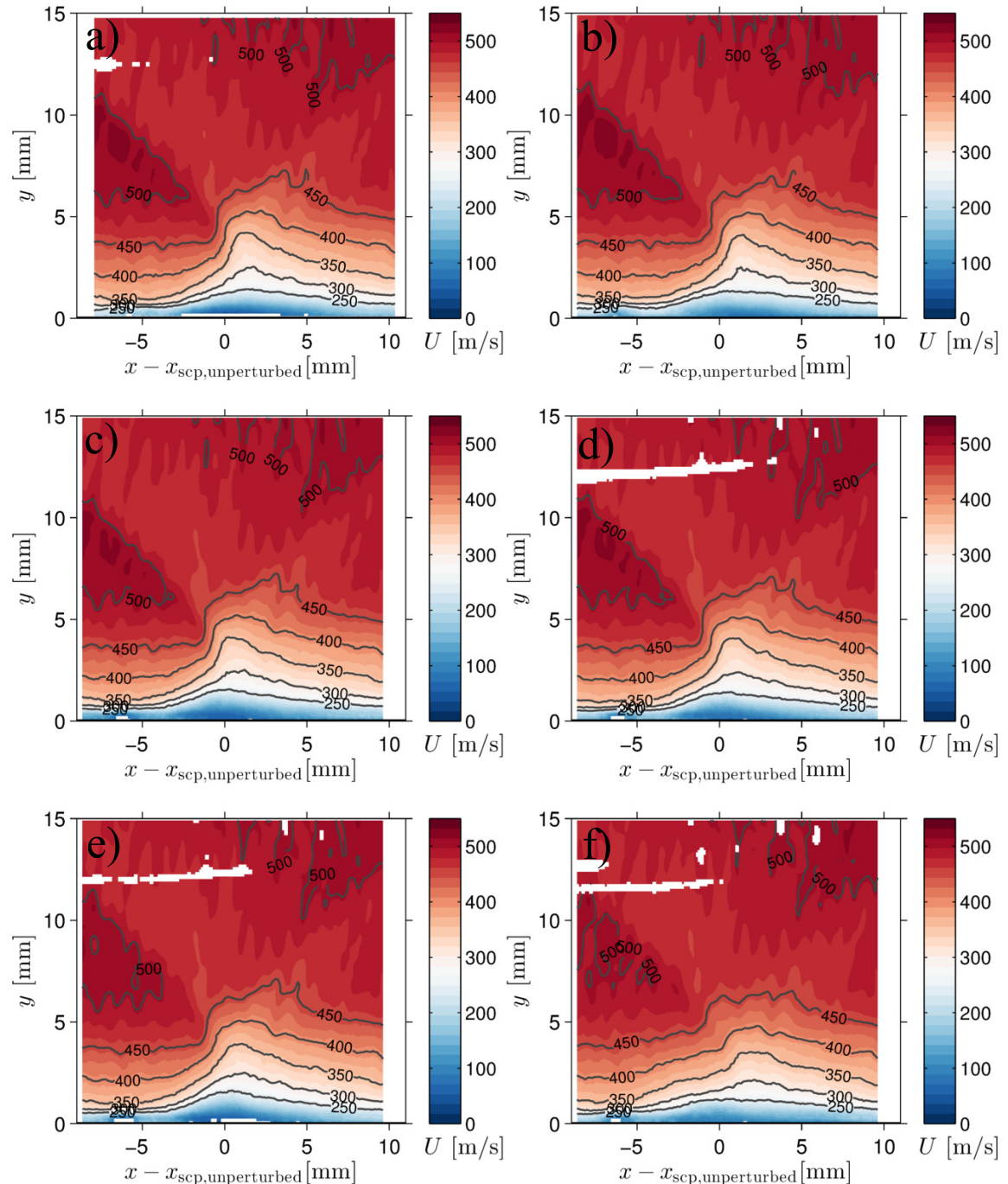


Figure 4.14: Mean streamwise velocity in the incident SBLI region for perturbations located at  $x_{\text{bump}} = -75.2\text{mm}$ . (a)  $h_{\text{bump}} = 0$  (unperturbed); (b)  $h_{\text{bump}} = 0.11\text{mm}$ ; (c)  $h_{\text{bump}} = 0.28\text{mm}$ ; (d)  $h_{\text{bump}} = 0.48\text{mm}$ ; (e)  $h_{\text{bump}} = 0.66\text{mm}$ ; (f)  $h_{\text{bump}} = 0.89\text{mm}$ .

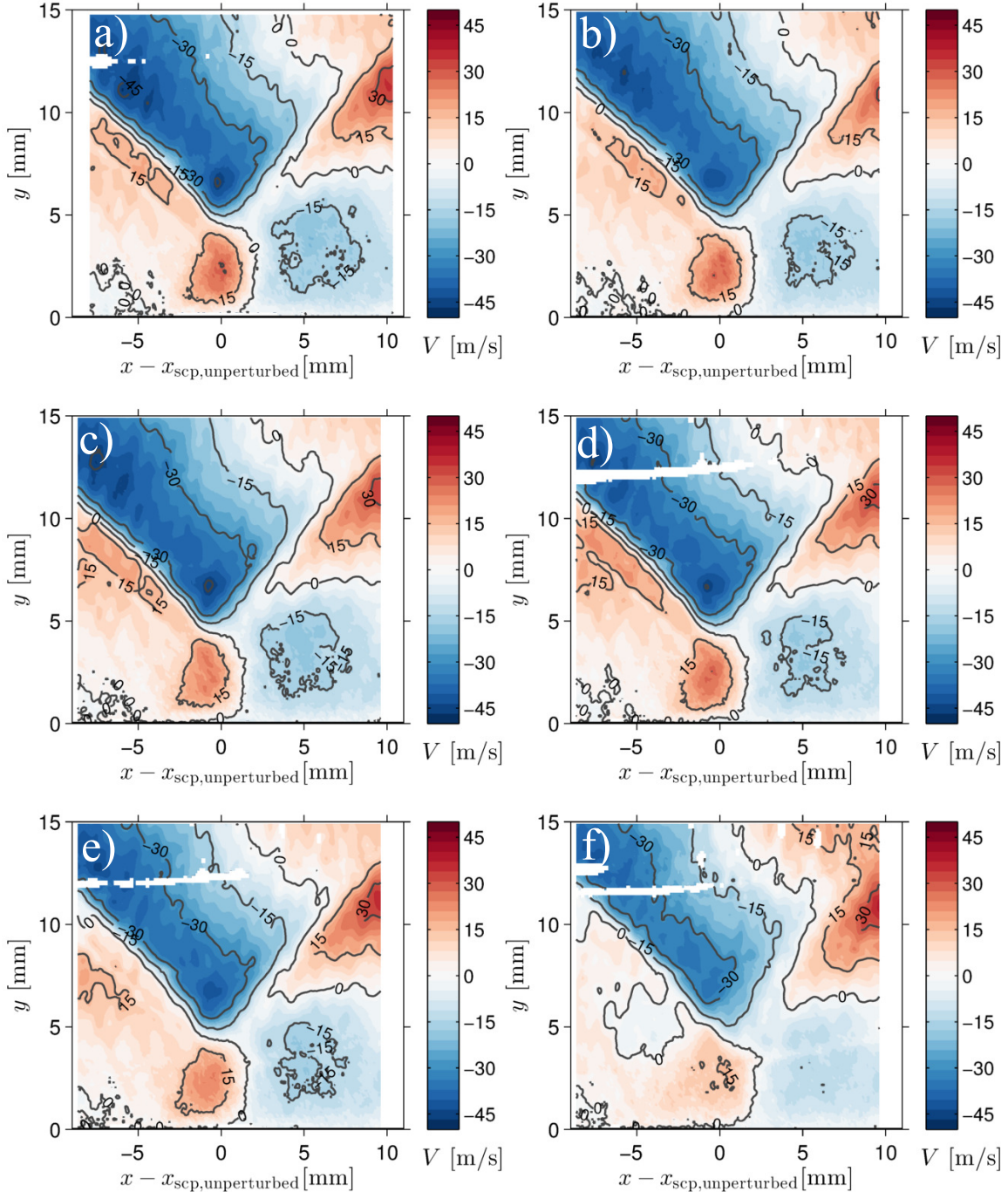


Figure 4.15: Mean vertical velocity in the incident SBLI region for perturbations located at  $x_{\text{bump}} = -75.2$  mm. (a)  $h_{\text{bump}} = 0$  (unperturbed); (b)  $h_{\text{bump}} = 0.11$  mm; (c)  $h_{\text{bump}} = 0.28$  mm; (d)  $h_{\text{bump}} = 0.48$  mm; (e)  $h_{\text{bump}} = 0.66$  mm; (f)  $h_{\text{bump}} = 0.89$  mm.

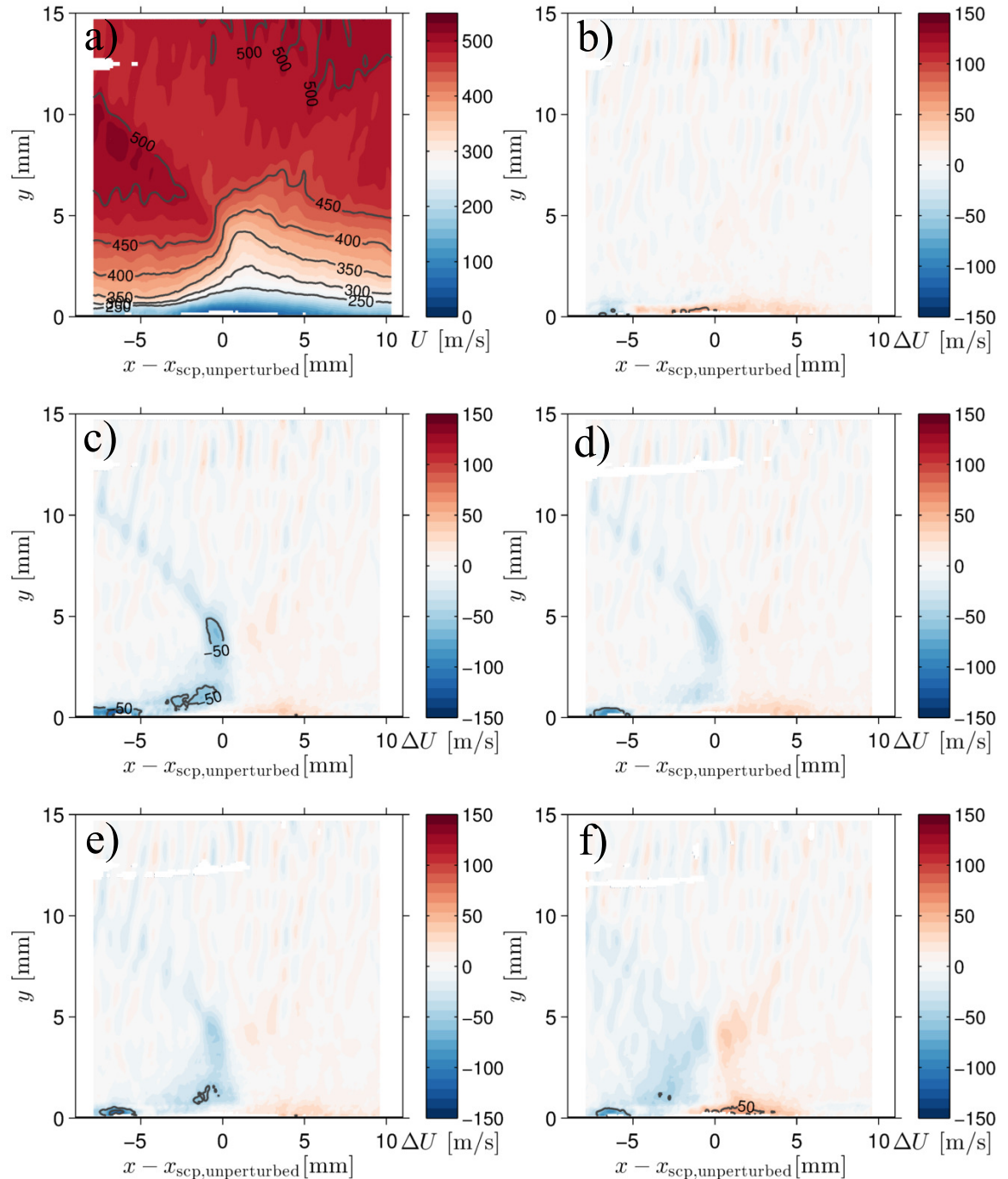


Figure 4.16: Mean streamwise velocity difference in the incident SBLI region for perturbations located at  $x_{\text{bump}} = -75.2\text{mm}$ . (a)  $h_{\text{bump}} = 0$  (unperturbed); (b)  $h_{\text{bump}} = 0.11\text{mm}$ ; (c)  $h_{\text{bump}} = 0.28\text{mm}$ ; (d)  $h_{\text{bump}} = 0.48\text{mm}$ ; (e)  $h_{\text{bump}} = 0.66\text{mm}$ ; (f)  $h_{\text{bump}} = 0.89\text{mm}$ .

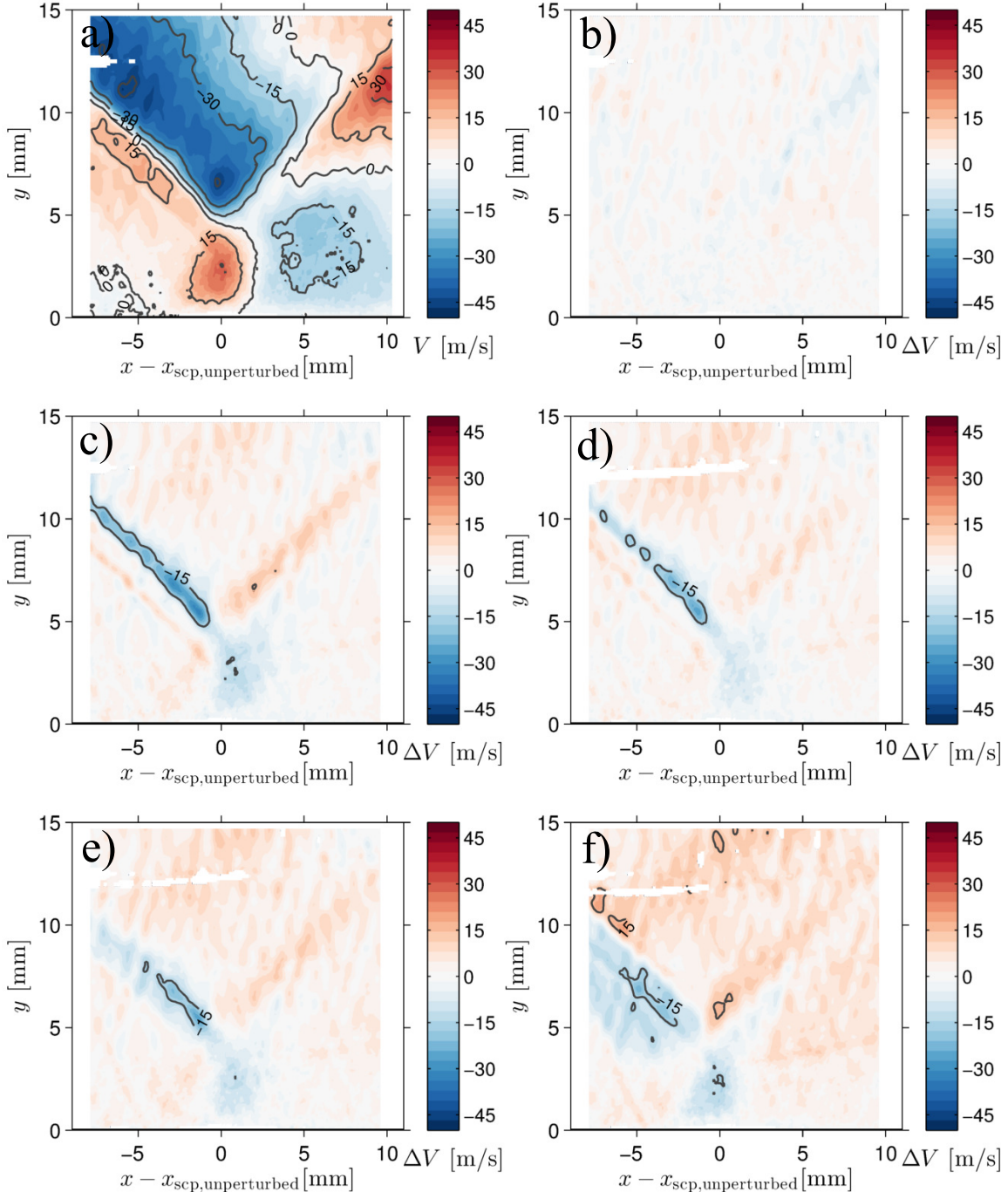


Figure 4.17: Mean vertical velocity difference in the incident SBLI region for perturbations located at  $x_{bump} = -75.2$  mm. (a)  $h_{bump} = 0$  (unperturbed); (b)  $h_{bump} = 0.11$  mm; (c)  $h_{bump} = 0.28$  mm; (d)  $h_{bump} = 0.48$  mm; (e)  $h_{bump} = 0.66$  mm; (f)  $h_{bump} = 0.89$  mm.

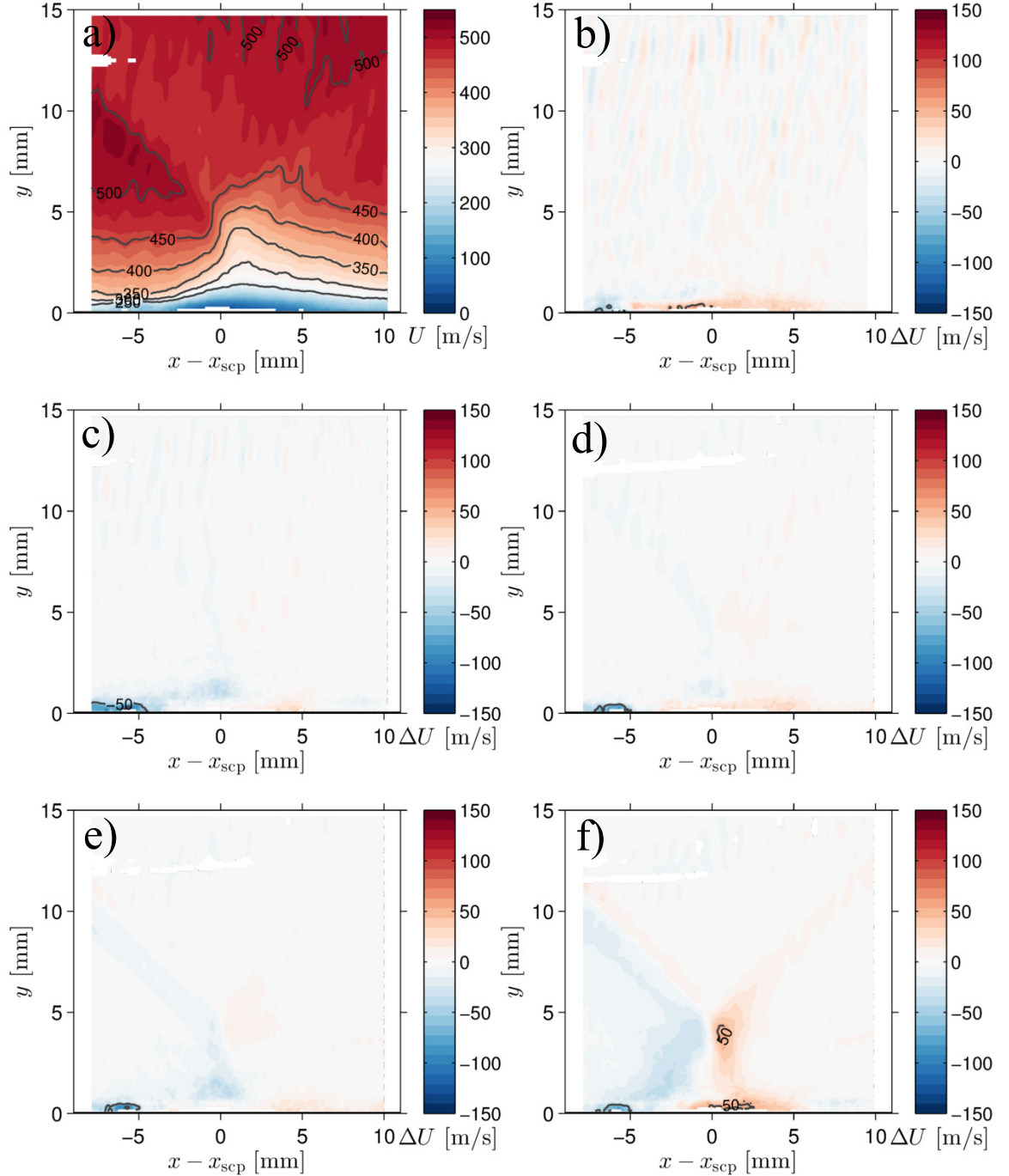


Figure 4.18: Mean streamwise velocity difference in the incident SBLI region for perturbations located at  $x_{\text{bump}} = -75.2\text{mm}$ . (a)  $h_{\text{bump}} = 0$  (unperturbed); (b)  $h_{\text{bump}} = 0.11\text{mm}$ ; (c)  $h_{\text{bump}} = 0.28\text{mm}$ ; (d)  $h_{\text{bump}} = 0.48\text{mm}$ ; (e)  $h_{\text{bump}} = 0.66\text{mm}$ ; (f)  $h_{\text{bump}} = 0.89\text{mm}$ . The data are shifted to align the shock crossing point in the streamwise direction.

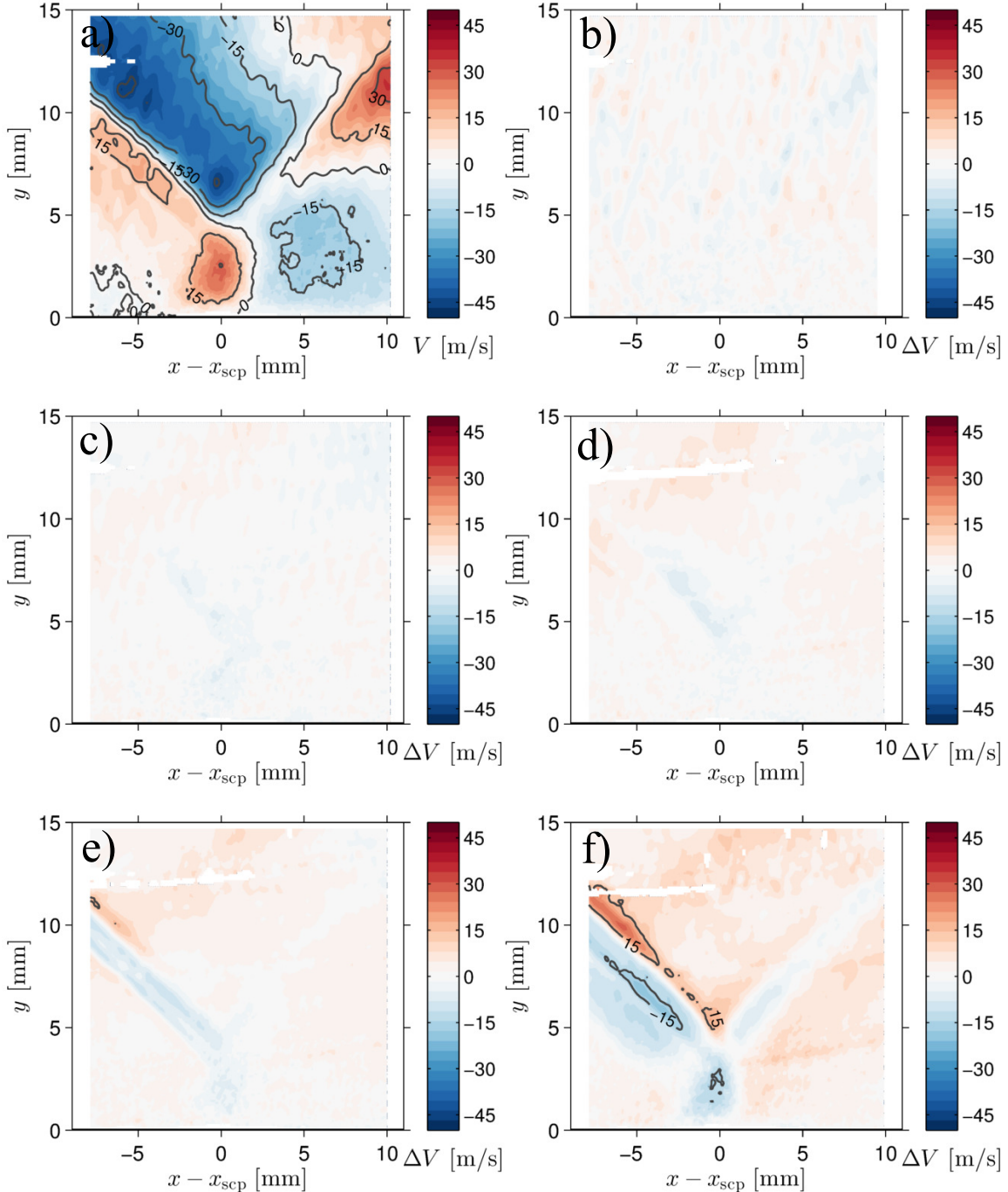


Figure 4.19: Mean vertical velocity difference in the incident SBLI region for perturbations located at  $x_{bump} = -75.2\text{mm}$ . (a)  $h_{bump} = 0$  (unperturbed); (b)  $h_{bump} = 0.11\text{mm}$ ; (c)  $h_{bump} = 0.28\text{mm}$ ; (d)  $h_{bump} = 0.48\text{mm}$ ; (e)  $h_{bump} = 0.66\text{mm}$ ; (f)  $h_{bump} = 0.89\text{mm}$ . The data are shifted to align the shock crossing points in the streamwise direction.

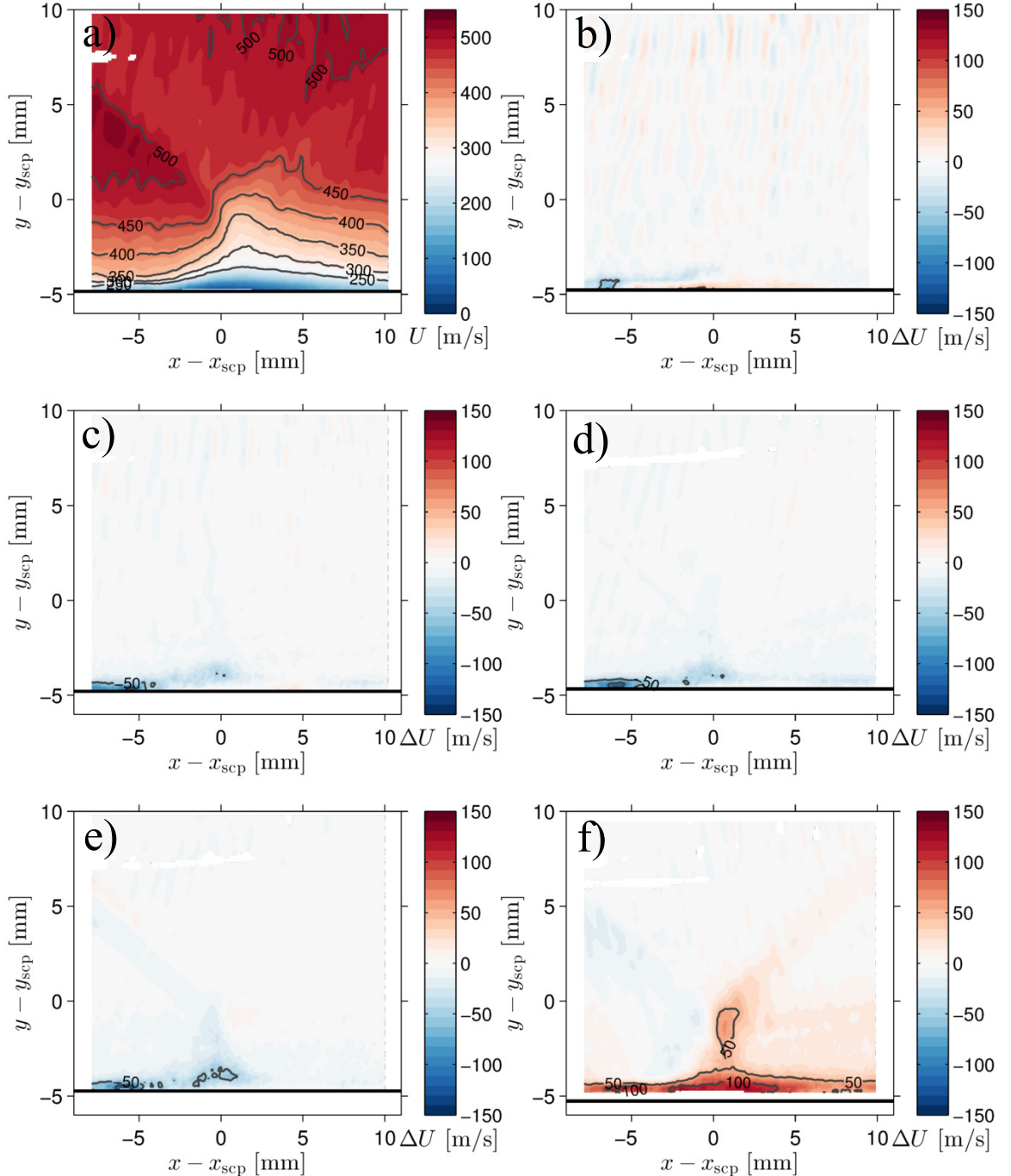


Figure 4.20: Mean streamwise velocity difference in the incident SBLI region for perturbations located at  $x_{bump} = -75.2\text{mm}$ . (a)  $h_{bump} = 0$  (unperturbed); (b)  $h_{bump} = 0.11\text{mm}$ ; (c)  $h_{bump} = 0.28\text{mm}$ ; (d)  $h_{bump} = 0.48\text{mm}$ ; (e)  $h_{bump} = 0.66\text{mm}$ ; (f)  $h_{bump} = 0.89\text{mm}$ . The data are shifted to align the shock crossing points in both the streamwise and vertical directions.

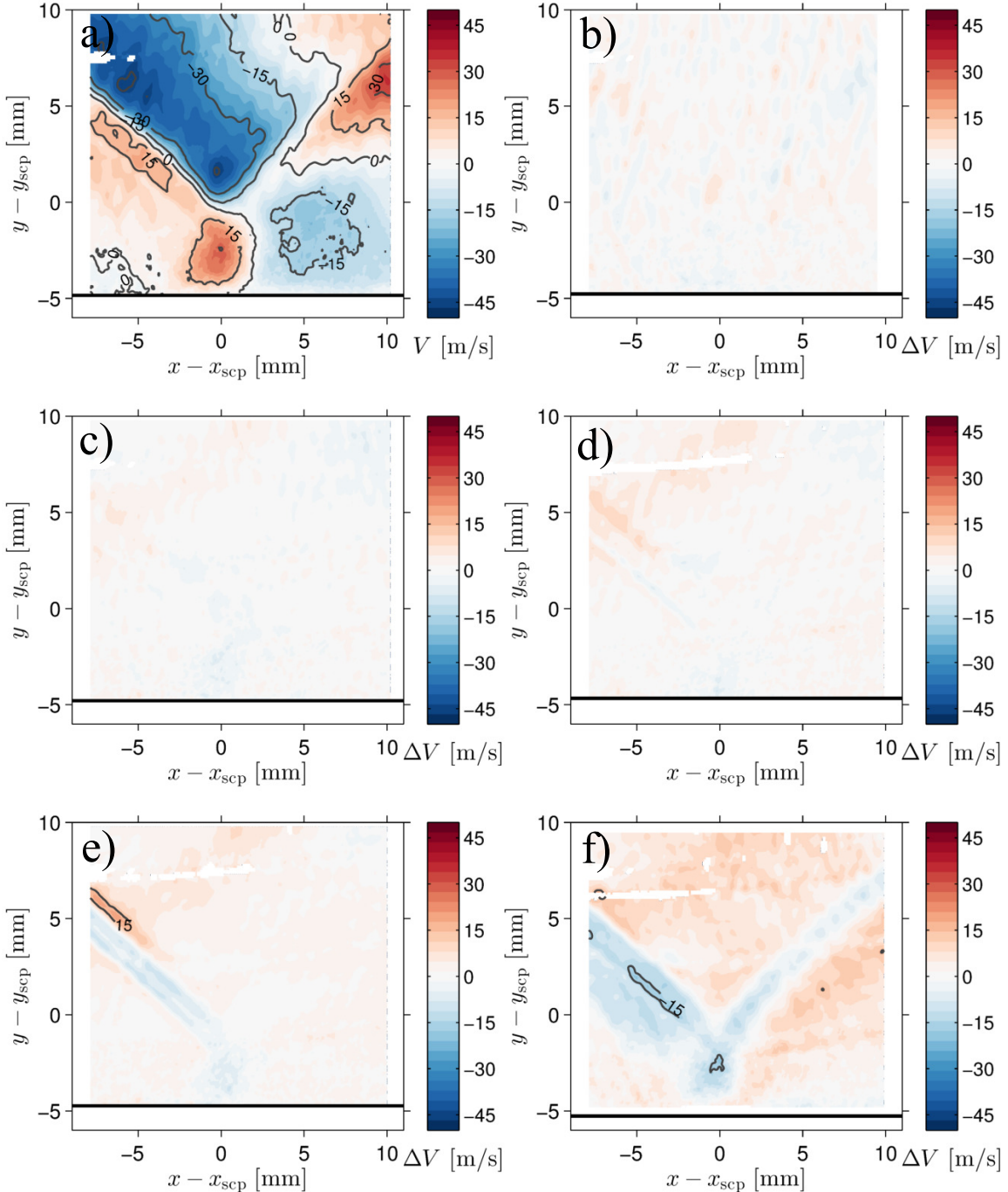


Figure 4.21: Mean vertical velocity difference in the incident SBLI region for perturbations located at  $x_{\text{bump}} = -75.2\text{mm}$ . (a)  $h_{\text{bump}} = 0$  (unperturbed); (b)  $h_{\text{bump}} = 0.11\text{mm}$ ; (c)  $h_{\text{bump}} = 0.28\text{mm}$ ; (d)  $h_{\text{bump}} = 0.48\text{mm}$ ; (e)  $h_{\text{bump}} = 0.66\text{mm}$ ; (f)  $h_{\text{bump}} = 0.89\text{mm}$ . The data are shifted to align the shock crossing points in both the streamwise and vertical directions.

how the data are shifted. Since the differences in the velocity fields are small even when the data are not shifted, it is unsurprising that only minor reductions in  $\Delta U$  and  $\Delta V$  are achieved by applying the small realignments in the streamwise and vertical coordinates.

## 4.5 Quantitative comparisons

The analysis of the previous section is useful for gaining an understanding of the overall effects caused by the addition of perturbations in the upstream boundary layer. However, the color contour plots of the differences between the perturbed and unperturbed velocity fields are still a qualitative representation, and it would be difficult to compare all 45 of the perturbed cases this way. Therefore, this section will explore methods for quantitatively comparing all the perturbed cases.

### 4.5.1 Velocity profile comparisons

This subsection presents velocity profiles extracted throughout the incident shock interaction for all of the perturbed cases. The streamwise positions of the shock crossing points for each case are aligned, and the profiles are extracted at five locations:  $(x - x_{\text{scp}}) = -2, 0, 2, 4,$  and  $6\text{mm}$ . The data are not shifted in the vertical direction; therefore  $y = 0$  represents the position of the bottom wall for every case.

Figure 4.22 shows the evolution of the unperturbed mean velocity throughout the interaction (solid red line). The full range of local mean velocities for all of the perturbed cases is represented by the gray area. This area is shaded between the minimum and maximum measured velocities for a particular location,  $(x - x_{\text{scp}}, y)$ , on each profile. The mean, median, and standard deviation of all of the different realizations of perturbed mean velocities are also computed at each  $(x - x_{\text{scp}}, y)$  point along the profiles. The average of all the perturbed profiles is represented by a dotted

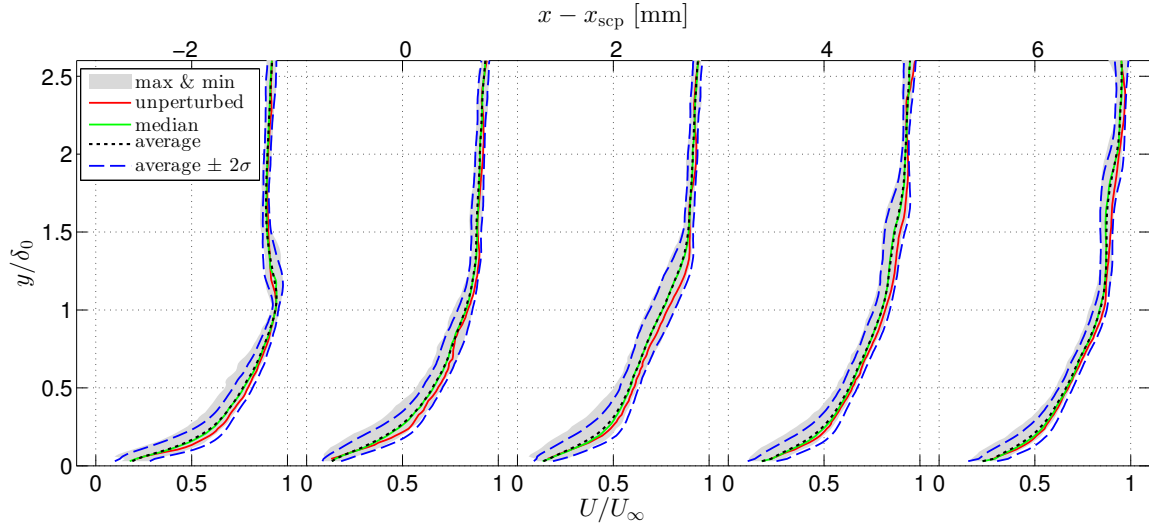


Figure 4.22: Profiles of mean streamwise velocity throughout the incident SBLI zone. The unperturbed case is shown as a solid red line. The full range of velocities for all perturbed cases is spanned by the gray filled area. Profiles of the average velocity, median velocity, and average velocity  $\pm$  two standard deviations are also superimposed.

black line, and the median profile is plotted as a green solid line. The average and median profiles agree very closely, and they show relatively small deviations from the unperturbed profile. The blue dashed lines represent the average profile plus and minus two standard deviations.

In Figure 4.22, all of the profiles show the same general trends as they evolve in the streamwise direction. The velocity deficit grows and the boundary layer thickens between  $(x - x_{scp}) = -2\text{mm}$  and  $2\text{mm}$ , due to the strong adverse pressure gradient and positive vertical velocities imposed by the incident shock wave in this region. Downstream the profiles become fuller as the flow behind the reflected shock wave drives back down toward the bottom wall. No mean flow reversal is observed for the base case or for any of the perturbed cases.

Figure 4.23 shows the same data as Figure 4.22, except that in each case the unperturbed velocity profile is subtracted off. This subtraction allows the data to be

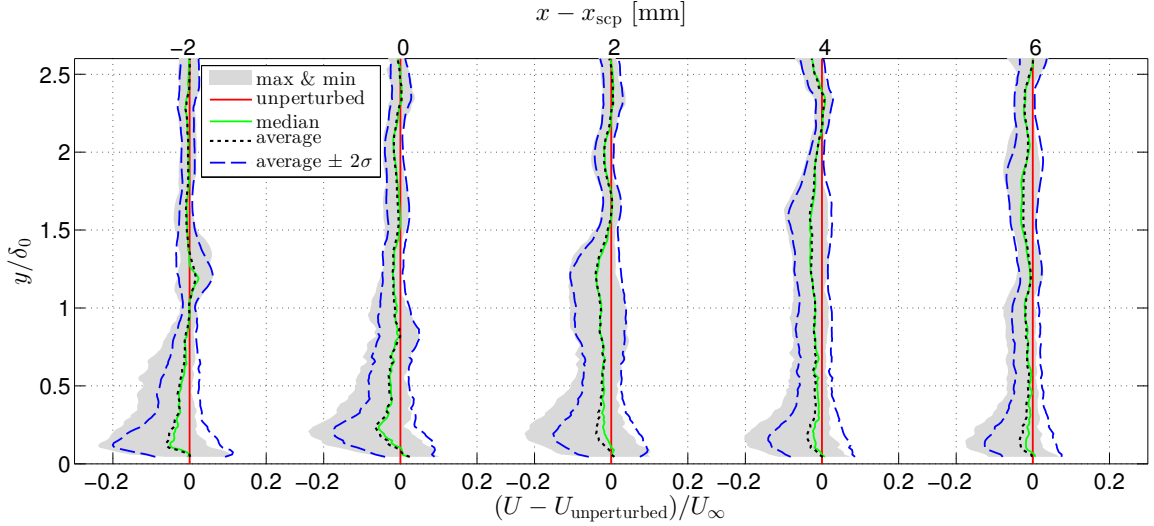


Figure 4.23: Profiles of mean streamwise velocity difference ( $U - U_{\text{unperturbed}}$ ) throughout the incident SBLI zone. The unperturbed case is shown as a solid red line fixed at zero. The full range of velocities for all perturbed cases is spanned by the gray filled area. Profiles of the average velocity, median velocity, and average velocity  $\pm$  two standard deviations are also superimposed.

represented on a more sensitive scale, highlighting the differences in the profiles more clearly. The largest range between max and min velocity profiles occurs below  $y/\delta_0 = 0.5$  throughout the interaction region. The largest discrepancy between a perturbed case and the baseline profile is  $(U - U_{\text{unperturbed}})/U_\infty \approx -0.25$ . For  $y/\delta_0 > 0.5$  the magnitudes of the differences are significantly smaller,  $< 0.1U_\infty$  in most regions.

The average and median profiles are biased negative relative to the unperturbed case in almost all regions of the flow. This indicates that on average, the perturbations cause boundary layer thickening and overall deceleration of the flow. These observations are consistent with the analysis of the color contour plots of the previous section. The profile representation serves to show that the trends can be generalized across the full set of profiles.

The same types of profile plots are presented for the mean vertical velocities in Figures 4.24 and 4.25. Note that the velocity scale is reduced to represent a

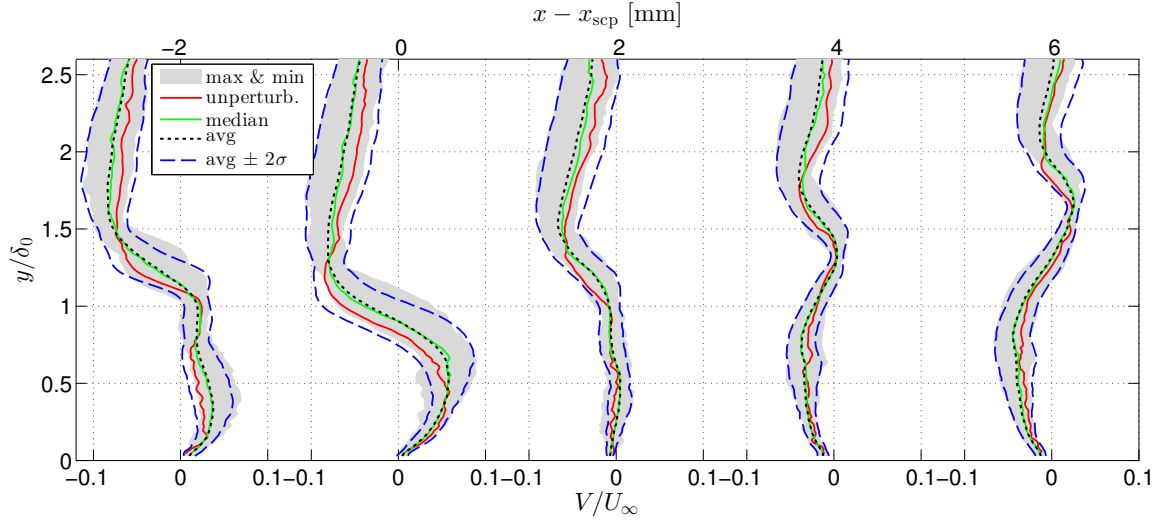


Figure 4.24: Profiles of mean vertical velocity throughout the incident SBLI zone. The unperturbed case is shown as a solid red line. The full range of velocities for all perturbed cases is spanned by the gray filled area. Profiles of the average velocity, median velocity, and average velocity  $\pm$  two standard deviations are also superimposed.

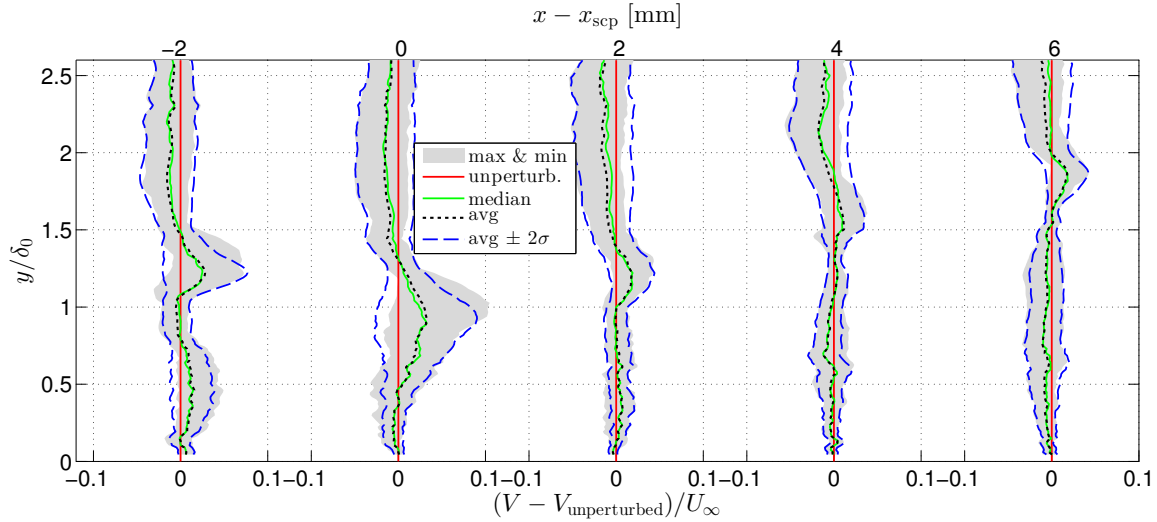


Figure 4.25: Profiles of mean vertical velocity difference ( $V - V_{\text{unperturbed}}$ ) throughout the incident SBLI zone. The unperturbed case is shown as a solid red line fixed at zero. The full range of velocities for all perturbed cases is spanned by the gray filled area. Profiles of the average velocity, median velocity, and average velocity  $\pm$  two standard deviations are also superimposed.

significantly smaller range than in the streamwise velocity profile plots. As the profiles evolve downstream, the region inside  $y/\delta_0 = 1$  transitions from positive to negative vertical velocity, corresponding to the thickening and thinning of the boundary layer. Far from the bottom wall, the vertical velocity becomes less negative as the flow proceeds downstream. This is due to the effects of the expansion fan emanating from the downstream end of the compression ramp on the top wall and the upward deflection imposed by the reflected shock wave.

The discrepancies in the  $V$  velocities are generally smaller than the discrepancies in the  $U$  profiles. Despite their small size in an absolute sense, the  $V$  discrepancies can be large relative to the dynamic range of the mean vertical velocities in the unperturbed case. The smallest discrepancies occur close to the bottom wall where the vertical velocity is near zero for all cases. The largest range between minimum and maximum  $V$  profiles occurs near the shock features in each case. The reason is that the shock crossing point has not been aligned in the vertical direction for all of the cases. A small displacement of the incident or reflected shock wave results in a significantly different vertical velocity in the vicinity of that shock feature. In the color contour plots, the  $V$  discrepancies were mitigated using the  $y - y_{\text{scp}}$  coordinate shift representing the displacement of the outer streamlines by a thicker boundary layer; however that transformation is not applied to the profiles presented here.

### 4.5.2 Integral difference metric

To further quantify the differences, an integral measure of the velocity differences is defined in order to allow  $\Delta U$  and  $\Delta V$  for all of the perturbed cases to be compared. At each point,  $i$ , in the flow, the difference in the mean velocity vector between the perturbed and unperturbed cases is given by:

$$\Delta \mathbf{U}_i = (U_{\text{perturbed},i} - U_{\text{unperturbed},i}, V_{\text{perturbed},i} - V_{\text{unperturbed},i}) \quad (4.3)$$

The magnitude of this vector is:

$$|\Delta \mathbf{U}_i| = \sqrt{(U_{\text{perturbed},i} - U_{\text{unperturbed},i})^2 + (V_{\text{perturbed},i} - V_{\text{unperturbed},i})^2} \quad (4.4)$$

By summing up all of the magnitudes of the velocity differences and dividing by the total number of valid vectors in a region of interest, we arrive at an integral measure of the average velocity magnitude difference:

$$\Lambda = \frac{1}{N} \sum_{i=1}^N |\Delta \mathbf{U}_i| \quad [\text{m/s}] \quad (4.5)$$

The area over which this metric is defined can be chosen arbitrarily. For this work, the region is defined as a rectangle with bounds:  $x \in [-4, 4]\text{mm}$ ,  $y \in [1.5, 9.5]\text{mm}$ . For the cases where the vertical coordinate is shifted by  $y_{\text{scp}}$ , the vertical bounds are chosen as  $y \in [(1.5 - y_{\text{scp}}), (9.5 - y_{\text{scp}})]\text{mm}$  such that the region of interest remains consistent. These regions are illustrated on top of the unshifted and shifted  $\Delta U$  and  $\Delta V$  plots in Figure 4.26. The plots are the same ones as presented previously in Figures 4.8, 4.9, 4.12, and 4.13 – the only difference is that the region of interest is superimposed to help visualize where the integral metric is computed.

The chosen area encompasses a large portion of the flow surrounding the shock crossing point, and therefore includes regions where velocity discrepancies between perturbed and unperturbed cases can be large. It excludes most of the region deep within the boundary layer where differences in  $\Delta U$  are large for the cases where the vertical coordinate is shifted by  $y_{\text{scp}}$ . This is an appropriate choice because the large discrepancies in that region are not physical – they are simply caused by the local shifting and proximity to the wall where  $\partial U / \partial y$  is very high. Those discrepancies indicate that the perturbations thicken the boundary layer; however the lack of discrepancies further from the bottom wall indicates that streamlines in this region are

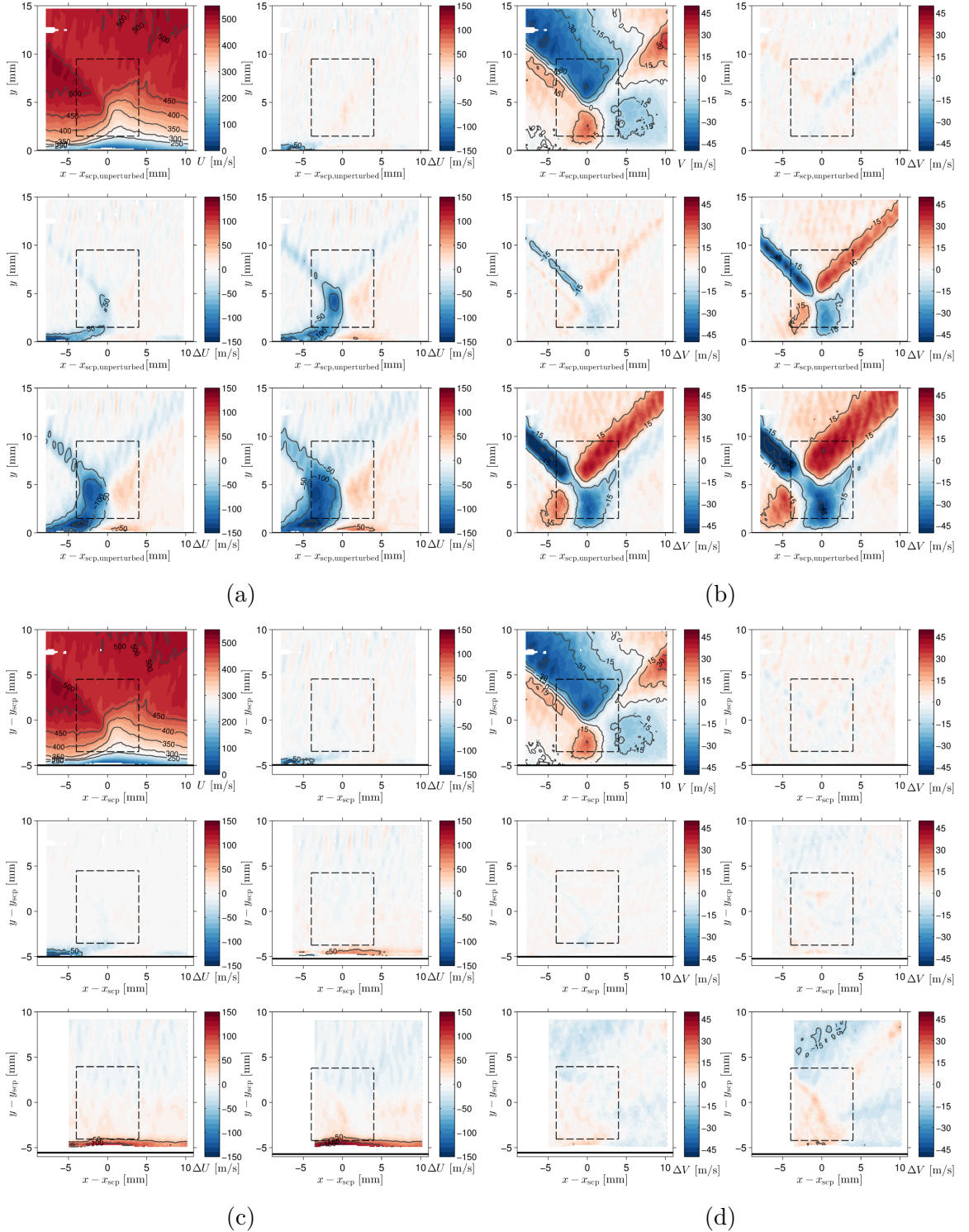


Figure 4.26: Reproduction of Figures 4.8, 4.9, 4.12, and 4.13 showing the region of interest over which the integral metric,  $\Lambda$ , is computed for each case. (a) and (b) are unshifted data; (c) and (d) show data which have been shifted to align the shock crossing point in both the streamwise and vertical directions

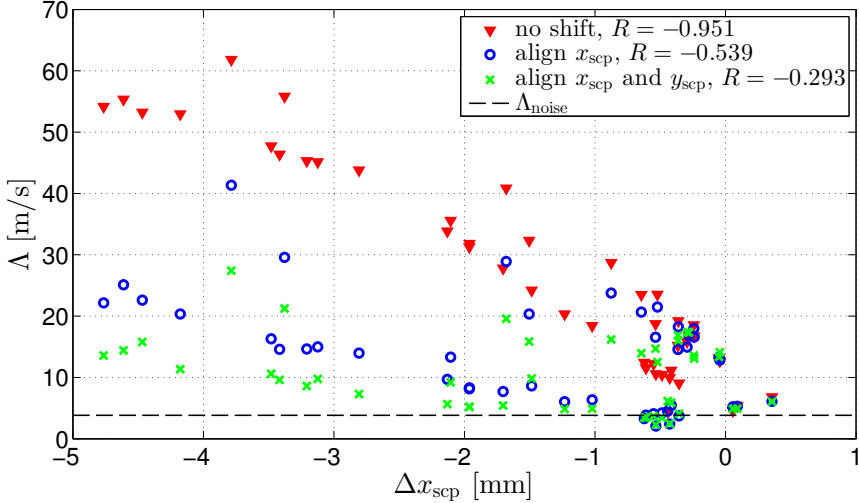


Figure 4.27: Integral velocity difference parameter,  $\Lambda$ , plotted against the change in streamwise position of the shock crossing point,  $\Delta x_{\text{sep}} = x_{\text{sep}} - x_{\text{sep}, \text{unperturbed}}$ . The black dashed line shows the value of  $\Lambda$  corresponding to the noise floor.

simply displaced vertically by a distance approximately equal to the change in the vertical shock crossing position,  $\Delta y_{\text{sep}}$ . Therefore,  $\Delta y_{\text{sep}}$  can be thought of as an approximate measure of boundary layer thickening present in each of the perturbed cases.

The integral difference metric,  $\Lambda$ , is plotted against the change in the shock crossing point from its nominal position,  $\Delta x_{\text{sep}}$ , in Figure 4.27. For comparison,  $\Lambda$  is computed for the unshifted data (red triangles), the data shifted to align the shock crossing point in the streamwise direction only (blue circles), and the data shifted to align the streamwise and vertical positions of the shock crossing point (green  $\times$  marks).

The correlation coefficient between the integral difference parameter,  $\Lambda$ , and the change in the streamwise position of the shock crossing point,  $\Delta x_{\text{sep}}$  is computed as:

$$R = \frac{\text{cov}(\Lambda, \Delta x_{\text{sep}})}{\sqrt{\text{var}(\Lambda)\text{var}(\Delta x_{\text{sep}})}} \quad (4.6)$$

For the unshifted dataset,  $R = -0.95$ , indicating a very strong negative correlation between the change in the shock crossing point and the size of the differences between the perturbed and unperturbed velocity fields. When the data are shifted such that the streamwise positions of the shock crossing points are aligned for all cases, the correlation between  $\Lambda$  and  $\Delta x_{\text{scp}}$  is weakened, with  $R = -0.54$ . The magnitude of the correlation is further reduced when the data are shifted to account for differences in the vertical position of the shock crossing point. For these data,  $R = -0.29$ , which indicates a much weaker negative correlation. These results support the hypothesis that the most significant changes in the velocity field are due to global motion of the entire SBLI, as opposed to local changes in the flow structures.

The noise floor is represented by the black dashed line in Figure 4.27. This quantity is computed assuming that the measurement uncertainty in both the streamwise and vertical velocity components is  $\pm 5 \text{ m/s}$ . The error in the streamwise and vertical velocity measurements vs the true velocity at each point in the domain is modeled by uniform independent jointly distributed random variables,  $e_1$  and  $e_2$ . The joint PDF is  $f(e_1, e_2) = 0.01$  over the domain  $e_1 \in [-5, 5]$ ,  $e_2 \in [-5, 5]$ , and zero elsewhere. Using these assumptions, the integral parameter  $\Lambda$  can be computed for the noise floor:

$$\begin{aligned}\Lambda_{\text{noise}} &= \langle (e_1^2 + e_2^2)^{1/2} \rangle \\ &= \int_{-\infty}^{\infty} \int_{-\infty}^{\infty} f(e_1, e_2) (e_1^2 + e_2^2)^{1/2} de_1 de_2 \\ &= 0.01 \int_{-5}^{5} \int_{-5}^{5} (e_1^2 + e_2^2)^{1/2} de_1 de_2 \\ &= 3.83 \text{ m/s}\end{aligned}$$

By shifting the velocity data to align the streamwise and vertical positions of the shock crossing point, many of the cases have  $\Delta U$  and  $\Delta V$  such that  $\Lambda$  lies very close

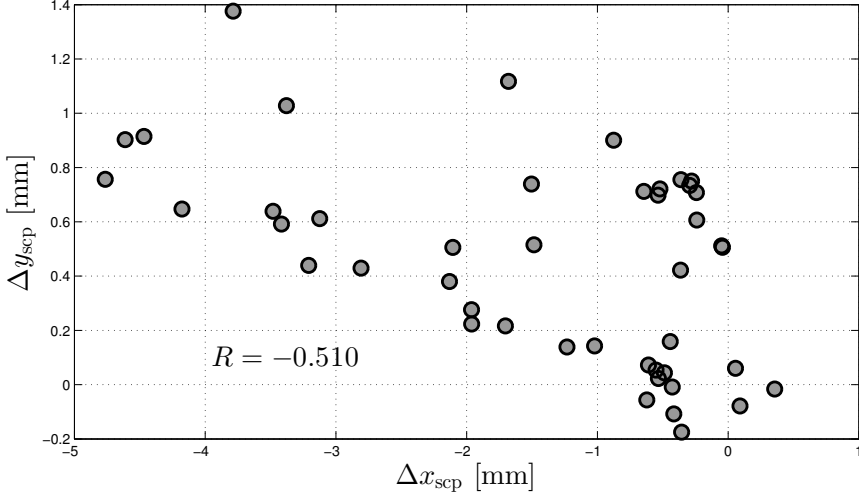


Figure 4.28: Relationship between the changes in the vertical and streamwise positions of the shock crossing point for all perturbed cases

to this noise floor. This indicates minimal actual differences between these perturbed cases and the unperturbed baseline data.

Figure 4.28 shows the relationship between  $\Delta y_{\text{SCP}}$  and  $\Delta x_{\text{SCP}}$ . These variables are moderately correlated with  $R = -0.51$ . This indicates that in general as the shock crossing point moves upstream it also moves away from the bottom wall. While the change in the streamwise position of the interaction can be large (up to 5mm, or  $\approx 0.9\delta_0$ ), the vertical position of the shock crossing point changes over a range of only  $\approx 1.6\text{mm}$ . The extreme cases correspond to  $\Delta y_{\text{SCP}} \approx -0.03\delta_0$  and  $\Delta y_{\text{SCP}} \approx 0.26\delta_0$ .

Furthermore, there are very few cases for which either  $\Delta x_{\text{SCP}}$  is positive or  $\Delta y_{\text{SCP}}$  are negative. This type of trend has interesting implications for design. For example in the case of a scramjet, the mixing of fuel and air is highly dependent on the local flow field at the fuel injector site. If the injector is near a SBLI, the local conditions seen by the fuel jet could drastically change if the SBLI translates in the streamwise direction. Furthermore, if perturbations cause only upstream motion of the SBLI, this information can be leveraged to position features such as the injector in regions

where the flow is less likely to be affected by perturbations.

### 4.5.3 Scalar quantity of interest

Based on both the qualitative and quantitative analyses in the previous sections, the streamwise position of the shock crossing point,  $\Delta x_{\text{scp}}$ , is determined to be the single most important parameter that is affected by the addition of the upstream geometric perturbations. This quantity is a scalar which can easily be extracted from both experimental and computational datasets to facilitate quantitative comparisons.

The location of the shock crossing point in each of the PIV datasets is located using the following procedure. First the positions of the incident and reflected shock waves are located using the maxima in the wall-normal velocity fluctuations. This is the same shock-locating procedure as described previously in Section 3.5 of Chapter 3. A line is fit to the position of each shock wave, using least squares optimization. The shock crossing point is then defined as the  $(x, y)$  location of the intersection of the two lines.

Figure 4.29a shows a sample case where the incident and reflected shocks identified by this algorithm are superimposed upon the wall-normal velocity fluctuation field. Figure 4.29b shows the shocks and shock crossing point superimposed on the mean wall-normal velocity field. This demonstrates that the mean wall-normal velocity field could also have been used in the determination of the shock locations; however the shock waves are more reliably located using  $v'$ .

Due to the particle travel in the streamwise direction between PIV image exposures (up to  $\approx 450\mu\text{m}$ ), the shocks appear slightly further upstream in the measurements than their actual physical location. This bias is expected to be nearly identical for all the perturbed cases considered because only minor variations in the structure of the shock wave outside the boundary layer are observed in the perturbed cases. Therefore, the bias can be removed by examining the change in location of the shock

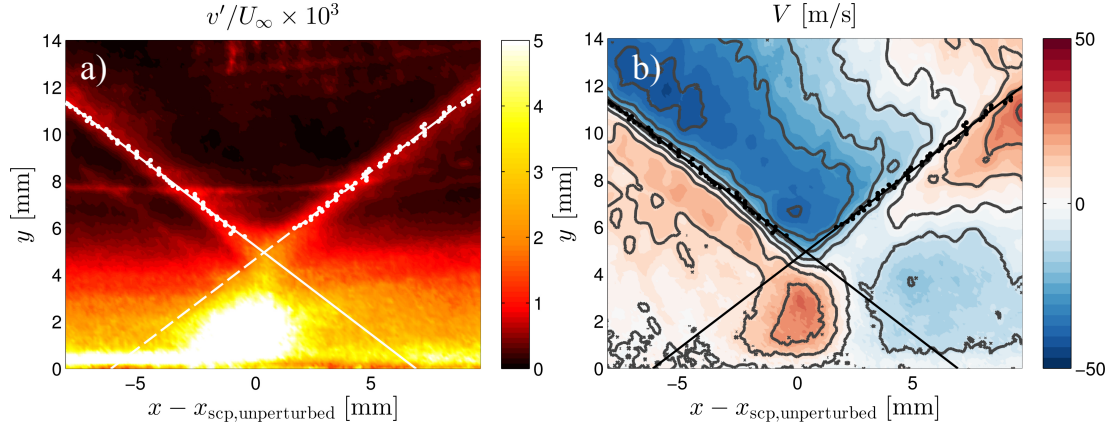


Figure 4.29: a) Results of shock crossing point location algorithm superimposed on the vertical velocity fluctuation field of a sample case. Individual points indicate local maxima in  $v'$ , and the solid lines are the least squares fit to these points. b) Shock positions superimposed on mean vertical velocity plot.

crossing point point from its unperturbed position ( $\Delta x_{\text{scp}} = x_{\text{scp}} - x_{\text{scp,unperturbed}}$ ). Based on repeated baseline experiments and an assessment of the accuracy in locating the overall position and resolution of the PIV datasets, the uncertainty in the measurement of  $\Delta x_{\text{scp}}$  is estimated to be  $\pm 0.25\text{mm}$ .

The deviation in shock crossing point from its unperturbed location is plotted for each case in Figure 4.30. Each set of symbols corresponds to fixed height bumps ( $h_{\text{bump}}$ ) at varying streamwise locations ( $x_{\text{bump}}$ ). This figure emphasizes the strict upstream motion of the SBLI with the addition of perturbations, and also shows that larger perturbations have greater effects on the shock crossing point than smaller ones at the same location. Furthermore, the deviation in shock crossing point is very sensitive to the perturbation location. The flow is most sensitive to perturbations in a very narrow range of  $x_{\text{bump}} \in [-70, -45]\text{mm}$ . The shock crossing point is insensitive to even the largest bumps at either the furthest upstream ( $x_{\text{bump}} = -75.2\text{mm}$ ) or furthest downstream ( $x_{\text{bump}} = -42.2\text{mm}$ ) bump positions tested.

A 2D surface is fitted to the data points to better visualize these trends. This surface is shown in Figure 4.31, and uses a 2nd order polynomial in the bump location

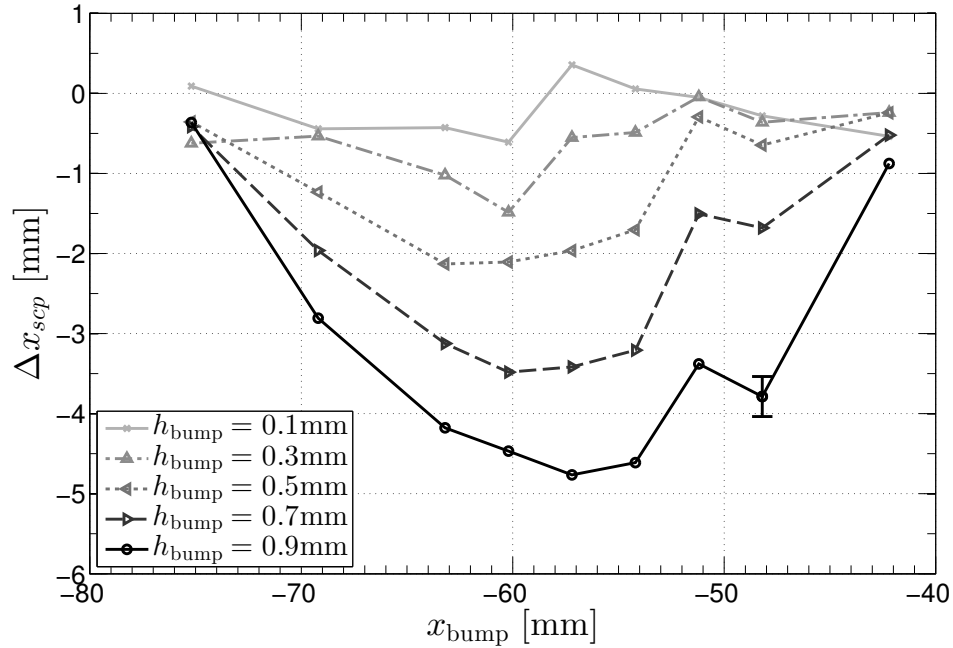


Figure 4.30: Streamwise deviation of shock crossing point from its unperturbed location,  $\Delta x_{\text{SCP}}$ , as a function of streamwise location of the perturbation,  $x_{\text{bump}}$ . The error bar representants the  $\pm 0.25 \text{ mm}$  uncertainty in each measurement of  $\Delta x_{\text{SCP}}$ .

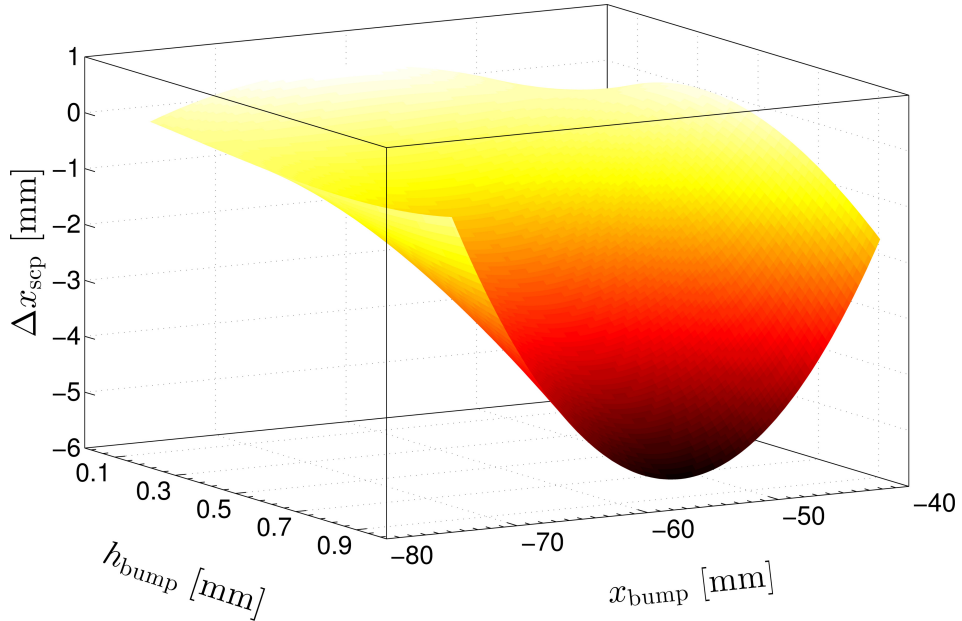


Figure 4.31: 2D polynomial fit to streamwise deviation of shock crossing point data. The fitted function,  $f(x_{\text{bump}}, h_{\text{bump}})$ , is given in equation 4.7.

Table 4.3: Coefficients for equation 4.7.

$a_{00}$	-11.35	$a_{20}$	-14.49
$a_{01}$	-0.3835	$a_{21}$	-0.1873
$a_{02}$	-0.003146	$a_{22}$	0
$a_{10}$	74.78	$a_{30}$	0.9335
$a_{11}$	2.494	$a_{31}$	0
$a_{12}$	0.01986	$a_{32}$	0

and a 3rd order polynomial in the bump height. The form of the polynomial fit is given in equation 4.7, and the coefficients are listed in Table 4.3.

$$f(x_{\text{bump}}, h_{\text{bump}}) = \sum_{m=0}^3 \sum_{n=0}^2 a_{m,n} x_{\text{bump}}^m h_{\text{bump}}^n \quad (4.7)$$

All of the data in Figures 4.27 and 4.28 and 4.30 are listed in Table 4.4.

Table 4.4: Summary of UQ experiment results. These data are plotted in Figures 4.27 and 4.28 and 4.30.

case	$h_{\text{bump}}$ [mm]	$x_{\text{bump}}$ [mm]	$\Delta x_{\text{scp}}$ [mm]	$\Delta y_{\text{scp}}$ [mm]	$\Lambda$ [m/s] unshifted	$\Lambda$ [m/s] align $x_{\text{scp}}$	$\Lambda$ [m/s] align $x_{\text{scp}}$ & $y_{\text{scp}}$
1	0.11	-75.2	0.09	-0.08	5.4	5.3	4.9
2	0.28	-75.2	-0.62	-0.06	12.4	3.3	3.4
3	0.48	-75.2	-0.36	-0.18	9.1	3.7	4.1
4	0.66	-75.2	-0.42	-0.11	11.1	5.4	5.9
5	0.89	-75.2	-0.36	0.42	15.2	14.6	16.8
6	0.11	-69.2	-0.44	0.16	4.4	4.5	6.1
7	0.28	-69.2	-0.53	0.02	10.6	2.1	2.3
8	0.48	-69.2	-1.23	0.14	20.3	6.0	4.9
9	0.66	-69.2	-1.96	0.22	31.8	8.3	5.2

10	0.89	-69.2	-2.81	0.43	43.8	14.0	7.3
11	0.11	-63.2	-0.43	-0.01	10.0	2.4	2.5
12	0.28	-63.2	-1.02	0.14	18.4	6.4	4.9
13	0.48	-63.2	-2.13	0.38	33.8	9.7	5.6
14	0.66	-63.2	-3.12	0.61	45.1	15.0	9.8
15	0.89	-63.2	-4.18	0.65	53.0	20.3	11.3
16	0.11	-60.2	-0.61	0.07	11.5	3.9	3.4
17	0.28	-60.2	-1.49	0.52	24.2	8.6	9.8
18	0.48	-60.2	-2.11	0.51	35.6	13.3	9.2
19	0.66	-60.2	-3.48	0.64	47.7	16.3	10.6
20	0.89	-60.2	-4.47	0.91	53.2	22.6	15.8
21	0.11	-57.2	0.36	-0.02	6.8	6.1	6.1
22	0.28	-57.2	-0.55	0.05	12.2	4.1	3.7
23	0.48	-57.2	-1.96	0.28	31.3	8.2	5.3
24	0.66	-57.2	-3.42	0.59	46.4	14.6	9.6
25	0.89	-57.2	-4.76	0.76	54.2	22.2	13.6
26	0.11	-54.2	0.06	0.06	4.6	5.2	4.9
27	0.28	-54.2	-0.49	0.04	10.4	4.2	3.4
28	0.48	-54.2	-1.70	0.22	27.8	7.7	5.4
29	0.66	-54.2	-3.21	0.44	45.3	14.6	8.6
30	0.89	-54.2	-4.61	0.90	55.3	25.1	14.4
31	0.11	-51.2	-0.05	0.51	13.2	13.3	13.4
32	0.28	-51.2	-0.04	0.51	12.7	12.8	14.1
33	0.48	-51.2	-0.29	0.73	15.8	15.0	17.4
34	0.66	-51.2	-1.50	0.74	32.3	20.4	15.9

35	0.89	-51.2	-3.38	1.03	55.8	29.6	21.2
36	0.11	-48.2	-0.28	0.75	16.9	16.9	17.3
37	0.28	-48.2	-0.36	0.76	19.2	18.3	16.0
38	0.48	-48.2	-0.65	0.71	23.5	20.6	13.9
39	0.66	-48.2	-1.68	1.12	40.8	28.9	19.6
40	0.89	-48.2	-3.79	1.38	61.8	41.3	27.4
41	0.11	-42.2	-0.54	0.70	18.7	16.5	14.7
42	0.28	-42.2	-0.24	0.61	16.7	16.6	13.1
43	0.48	-42.2	-0.24	0.71	18.5	18.0	13.6
44	0.66	-42.2	-0.52	0.72	23.5	21.5	12.5
45	0.89	-42.2	-0.88	0.90	28.7	23.8	16.2

## 4.6 Utility for CFD validation

The UQ experiment cases presented in this chapter were designed for two purposes. The first is to document the sensitivity of the SBLI features to upstream geometric perturbations, as described in Sections 4.4 and 4.5. The other objective is to provide an experimental database suitable for quantitative CFD validation.

Variation of system parameters is an important method for CFD validation. In many cases, models and numerical procedures can be tuned such that a simulation replicates experimental results to within measurement accuracy. However, this process does not guarantee that the code correctly represents the underlying physics of the problem. A more robust validation can be performed if experimental data are available for multiple test cases with small variations in the boundary conditions. This type of database is especially useful if some of the perturbed cases produce substantial changes to the flow field.

The high resolution velocity field data provided here are ideally suited to this type of CFD validation. The measurement domain for each case is limited to a small area in a single plane near the center of the duct; however this area encompasses the most important variations in the flow field. To validate a CFD code intended for simulating SBLI physics in real applications, the code could be tested on the nominal base case geometry (no perturbations) as well as several of the perturbed cases. Perturbations which cause both large and small changes to the baseline flow should be included in the test matrix. A recommended minimum set of four cases includes:

1. the baseline unperturbed case
2.  $h_{\text{bump}} = 0.89\text{mm}$ ,  $x_{\text{bump}} = -57.2\text{mm}$ : perturbation with the maximum effect
3.  $h_{\text{bump}} = 0.48\text{mm}$ ,  $x_{\text{bump}} = -57.2\text{mm}$ : a smaller perturbation with a large effect
4.  $h_{\text{bump}} = 0.66\text{mm}$ ,  $x_{\text{bump}} = -75.2\text{mm}$ : a larger perturbation with a small effect

Detailed comparisons between the simulation results and the experimental measurements can be used to assess of the code's ability to correctly capture the physical mechanisms leading to the observed sensitivity. The use of techniques that utilize the full data field and provide a quantitative measure of the prediction error are highly recommended. Calculation of the integrated difference parameter,  $\Lambda$ , is one example of such a comparison.

As CFD techniques continue to advance, codes should output more information than just the predicted flow field for the nominal flow conditions and geometry. Instead, simulations should provide a range of possible outcomes, taking into account any uncertainties introduced by modeling choices and numerical procedures as well as uncertainties in the specification of inflow and boundary conditions. The present experiments offer a unique database to test compressible flow codes that include these capabilities. The perturbations are precisely defined, and other flow parameters are

held fixed in very narrow ranges. Computing the variation of the quantity of interest over the full range of perturbations would offer a strong test of a code's ability of to estimate the uncertainty interval in a simulation with imperfectly known boundary conditions.

# Chapter 5

## PIV Measurement Biases in SBLI Flows

This chapter describes and quantifies bias errors that are relevant in PIV measurements of high speed compressible flows. The technique involves modeling the effects of these error sources and propagating them through an SBLI flow field generated by CFD simulation. Dr. Ivan Bermejo-Moreno provided all of the CFD results that are used to demonstrate the methodology developed in this chapter. He used wall-modeled LES to compute the flow fields for the  $h_{\text{ramp}}/\delta_0 = 0.56$  and  $0.93$  experimental geometries discussed in Chapters 2 and 3. All of the subsequent modeling of error sources, quantification of PIV biases, and comparisons between CFD and PIV datasets are part of the present work.

### 5.1 Methodology

In order to perform quantitative and meaningful comparisons between an experimental dataset and a simulation result, it is important to understand the magnitudes of the errors and uncertainties associated with the measurements. For example, if the

experimental measurements include some biases, then a “perfect” simulation of the same configuration would not report exactly the same flow field as measured experimentally. If the bias errors associated with the experiments are not reported, then it is not possible to determine whether any discrepancies between the CFD and experimental results arise because of inadequacies in the models or numerical techniques of the simulation or because of measurement biases. Generally the discrepancies may be caused by some combination of both of these factors.

Because it is often difficult or impossible to remove biases from the experimental data, the methodology developed here approaches the problem from the opposite side. First, the PIV error sources are modeled and propagated through the flow field predicted by CFD. Then this modified CFD flow field which accounts for the biases in the measurement technique is directly compared to the PIV data. This framework has the additional benefit of providing information on the spatial non-uniformity of the bias errors as well as how they may be mitigated or increased based on varying the experimental parameters.

Estimates of uncertainties due to peak locking, sample size, and alignment were reported in Chapter 2. However, PIV measurements of high speed compressible flows such as the SBLI test cases presented in this thesis also involve significant biases. The ones that will be explored here include particle inertia, spatial resolution, and spatial averaging due to particle travel between PIV image exposures. Bias errors due to particle inertia and particle travel between PIV image exposures can be sizable in measurements of high speed compressible flows with very large freestream velocities and sharp velocity gradients, but may be negligible in PIV measurements of low speed flows. The methods and results described here apply specifically to PIV measurements of high speed flows; however the idea behind the framework is applicable to comparisons between any experimental result and simulation.

## 5.2 Particle inertia

To understand how particle inertia may cause discrepancies between the actual and measured flow fields, it is important to remember that PIV measures the velocity field associated with particles suspended in the fluid flow of interest. In the limit of infinitesimally small particles with no mass, the particle and fluid velocity fields are identical. This represents the limiting case of  $Re_p \rightarrow 0$  and  $St_p \rightarrow 0$ . However in a real PIV system the particles are finite and may have non-negligible inertia due to physical constraints; i.e. larger particles scatter more laser light and are easier to work with.

The effects of inertia on the particle trajectories through the measurement domain are expected to be most significant in regions of the fluid velocity field where steep spatial gradients exist. The particle paths will deviate from the fluid streamlines in areas where the fluid experiences strong convective acceleration or deceleration, i.e. where  $|\mathbf{U} \cdot \nabla \mathbf{U}|$  is large. Due to the presence of shock waves and expansion fans, as well as the interaction of these features with the boundary layers, the SBLI flow field contains several regions of large convective acceleration and deceleration.

### 5.2.1 Numerical setup

To compute the particle velocity field, the particles are modeled and their trajectories are propagated through the mean fluid velocity field computed by CFD. The trajectories are computed in 2D for a plane of CFD data near the centerline of the duct ( $z/\delta_0 = 3.89$ ). This simplification is made because near the centerplane, the spanwise velocity is generally much smaller than the streamwise velocity,  $|W| \ll |U|$ , and the spanwise gradients  $\partial U / \partial z$  and  $\partial V / \partial z$  are small. To extend this analysis to regions close to the side walls, the full 3D fluid velocity field would be required in order to accurately propagate the particle trajectories.

A higher fidelity method of computing the mean particle trajectories would involve propagating particles through the instantaneous flow field and averaging them over time. However, this method requires the particle simulation to be embedded in the calculation of the flow field, and is not compatible with RANS simulations which provide only mean flow quantities. Therefore, in order to allow the method to be generally applicable to CFD results of varying fidelity, the particle paths are generated using only the mean fluid velocity field from the simulation.

Particles are represented as spheres with density  $\rho_p$  and diameter  $d_p$ . The particle density and diameter are not directly measured in the present experiments. However in the equations of motion for the particle trajectories, these parameters are combined into the expression for particle response time,  $\tau_p = \rho_p d_p^2 / 18\mu$ , which is characterized experimentally (see Section 2.3.2 of Chapter 2). For the olive oil droplets used to seed the PIV experiments in this thesis,  $\tau_p \approx 1\mu\text{s}$ .

The volume fraction of particles is small enough that the particles do not interact with one another or influence the air velocity field. Because the particle density is much larger than the fluid density, the buoyancy force is neglected. Thus, the only forces acting on a particle are gravity and the drag due to the particle slip velocity,  $\mathbf{U}_p - \mathbf{U}_f$ . For the olive oil droplets used to seed the present PIV experiments, the particle Reynolds number,  $Re_p \leq 1$  for slip velocities of magnitude  $\leq 40 \text{ m/s}$  ( $0.075U_\infty$ ). The particle drag will be modeled using Stokes' drag law,  $\mathbf{F}_D = 3\pi\mu d_p(\mathbf{U}_f - \mathbf{U}_p)$ . In regions where the slip velocity exceeds  $40 \text{ m/s}$ , Stokes' law will underpredict the drag force that acts to restore the particle velocity to the fluid velocity. In these regions the differences between particle velocity field and fluid velocity field may be overpredicted. These areas are shown in the following sections to be small and concentrated near shock features.

The force balance is illustrated in Figure 5.1, leading to the following formulation

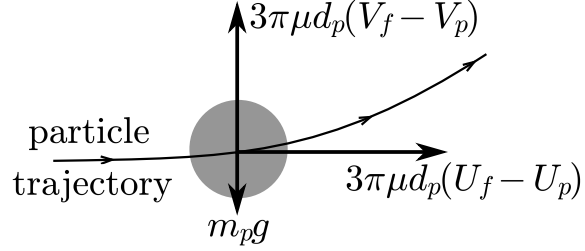


Figure 5.1: Force balance on a particle traveling through a fluid velocity field.

of the horizontal and vertical force balances on a particle suspended in the fluid flow:

$$\begin{aligned} m_p \frac{dU_p}{dt} &= 3\pi\mu d_p (U_f - U_p) \\ m_p \frac{dV_p}{dt} &= 3\pi\mu d_p (V_f - V_p) - m_p g \end{aligned} \quad (5.1)$$

The particle's trajectory is given by  $(x(t), y(t))$ , and its streamwise and vertical velocity components are:

$$U_p = \frac{dx}{dt} \quad \text{and} \quad V_p = \frac{dy}{dt} \quad (5.2)$$

At any point along the particle's trajectory, the fluid velocity relative to the particle is:  $(U_f - U_p) = U_f(x(t), y(t)) - dx/dt$  in the streamwise direction. Similarly, for the vertical direction,  $(V_f - V_p) = V_f(x(t), y(t)) - dy/dt$ . Using these substitutions along with the definition of  $\tau_p$ , equations 5.1 can be re-written as:

$$\begin{aligned} \tau_p \frac{d^2x}{dt^2} &= U_f(x(t), y(t)) - \frac{dx}{dt} \\ \tau_p \frac{d^2y}{dt^2} &= V_f(x(t), y(t)) - \frac{dy}{dt} - \tau_p g \end{aligned} \quad (5.3)$$

The initial conditions for this system of second order ODEs are:

$$\begin{aligned} x(t=0) &= x_0 & \frac{dx}{dt} \Big|_{t=0} &= U_f(x_0, y_0) \\ y(t=0) &= y_0 & \frac{dy}{dt} \Big|_{t=0} &= V_f(x_0, y_0) \end{aligned} \quad (5.4)$$

Note that for these assumed initial conditions, the starting position of a trajectory,  $(x_0, y_0)$  must be chosen away from the SBLI features such that  $\mathbf{U} \cdot \nabla \mathbf{U}$  is negligible and the fluid and particle velocities are well matched.

To facilitate numerical integration of the particle trajectories, equations 5.3 are recast as a system of first order nonlinear ODEs. Making the substitutions  $x_1 = x$ ,  $x_2 = y$ ,  $x_3 = dx/dt$ , and  $x_4 = dy/dt$ , the governing equations are written:

$$\begin{aligned} \frac{dx_1}{dt} &= x_3 \\ \frac{dx_2}{dt} &= x_4 \\ \frac{dx_3}{dt} &= \frac{1}{\tau_p} [U_f(x_1, x_2) - x_3] \\ \frac{dx_4}{dt} &= \frac{1}{\tau_p} [V_f(x_1, x_2) - x_4] - g \end{aligned} \quad (5.5)$$

With initial conditions:

$$\begin{aligned} x_1(t=0) &= x_0 & x_3(t=0) &= U_f(x_0, y_0) \\ x_2(t=0) &= y_0 & x_4(t=0) &= V_f(x_0, y_0) \end{aligned} \quad (5.6)$$

The equations are integrated in time using a custom written Matlab implementation of a 4th order Runge-Kutta (RK4) method. The vectors  $\mathbf{x}$  and  $\mathbf{f}(\mathbf{x}, t)$  are defined such that equations 5.5 can be written as  $d\mathbf{x}/dt = \mathbf{f}(\mathbf{x}, t)$ . A single RK4 time

integration step is given by:

$$\begin{aligned}\mathbf{x}_{n+1} &= \mathbf{x}_n + \frac{1}{6}\mathbf{k}_1 + \frac{1}{3}(\mathbf{k}_2 + \mathbf{k}_3) + \frac{1}{6}\mathbf{k}_4 \\ \mathbf{k}_1 &= \mathbf{f}(\mathbf{x}_n, t_n) \\ \mathbf{k}_2 &= \mathbf{f}(\mathbf{x}_n + \mathbf{k}_1, t_n + h/2) \\ \mathbf{k}_3 &= \mathbf{f}(\mathbf{x}_n + \mathbf{k}_2, t_n + h/2) \\ \mathbf{k}_4 &= \mathbf{f}(\mathbf{x}_n + \mathbf{k}_3, t_n + h)\end{aligned}$$

The time step,  $h$ , is selected such that the distance traveled in a single step never exceeds a user-defined parameter  $\Delta x_{\max}$ . For all of the simulations presented in this chapter,  $\Delta x_{\max} = 0.05\text{mm}$  and  $h = \Delta x_{\max}/U_{\infty} \approx 9.52 \times 10^{-8}\text{s}$ .

A fine rake of 651 particle trajectories is seeded across the height of the channel at a constant streamwise  $x_0$  location. Very close to the top and bottom walls ( $y \in [0.01, 1]\text{mm}$  and  $y \in [44, 44.99]\text{mm}$ ) the starting positions are spaced by 0.02mm in the vertical direction. Further from the walls but still within the boundary layers ( $y \in (1, 5]\text{mm}$  and  $y \in [40, 44]\text{mm}$ ) the starting points are spaced 0.04mm apart, and in the center of the duct the starting points are spaced vertically by 0.1mm. Some paths are also started further downstream in order to ensure that particle paths propagate into the slowest regions of the flow, some of which may include reversed flow. If a particle trajectory impacts the top or bottom wall of the duct, it is terminated at that point. Otherwise, the integration ends at a pre-defined location downstream of the SBLI features of interest.

Because the particle paths are not coupled to one another and the underlying fluid velocity is unaffected by the presence of particles, the particle trajectory calculations are all independent and well suited to parallelization. This is accomplished by iterating over all of the individual trajectories in a `parfor` loop utilizing multiple Matlab workers. A particle's position and velocity are recorded at every step along the RK4

integration throughout the domain. After all the particle paths are integrated, the full two-dimensional two-component particle velocity field is extracted by interpolating all of the saved particle data back onto the CFD grid.

### 5.2.2 Simulation results using $\tau_p = 1\mu\text{s}$

Figure 5.2 shows a zoomed in view of streamlines and particle paths that originate at the same set of initial points  $(x_0, y_0)$  and have been integrated throughout the domain for the  $h_{\text{ramp}}/\delta_0 = 0.56$  SBLI flow. Particle trajectories are computed for two different values of particle time constant:  $\tau_p = 1\mu\text{s}$  (particles used in the present experiments), and  $\tau_p = 4\mu\text{s}$  (larger and/or denser particles) in order to emphasize the effects of varying this parameter. Less than 5% of the total paths computed in this region are displayed. The incident shock wave is visible where the paths turn downward, and the reflected shock wave occurs at the location where the paths are deflected upward. The boundary layer thickening is represented by the displacement of the streamlines and particle paths away from the bottom wall.

The discrepancies between streamlines (black solid lines) and particle trajectories are small for the  $\tau_p = 1\mu\text{s}$  particles (red dashed lines) and significantly larger for the  $\tau_p = 4\mu\text{s}$  particles (blue dash-dot lines). In particular, the particles cannot decelerate and turn as quickly as the surrounding fluid as they pass through the incident shock wave. Therefore, the downward deflection of the particle trajectories is shifted slightly downstream relative to the streamlines. If these  $\tau_p = 4\mu\text{s}$  particles were used for PIV, the apparent shock location would be shifted downstream and the velocity gradient,  $\partial U / \partial x$ , would be smeared in the streamwise direction. The particle paths for  $\tau_p = 4\mu\text{s}$  do not track the streamlines faithfully in the region where the bottom wall boundary layer rapidly thickens. This effect causes the measured velocities within this region to incur a positive bias, resulting in artificially fuller velocity profiles.

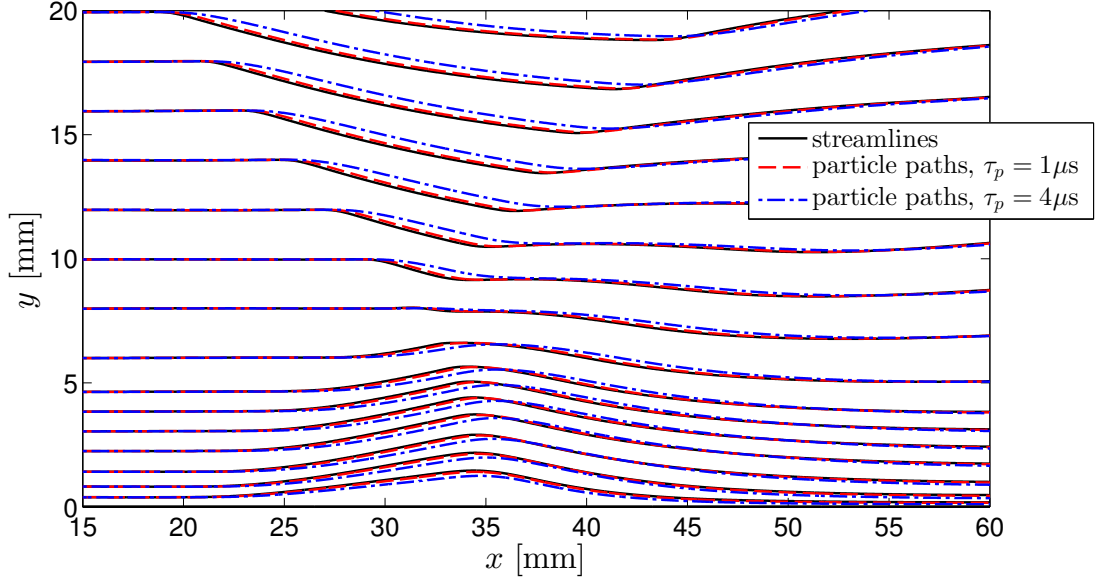


Figure 5.2: Streamlines and particle paths in incident SBLI for  $h_{\text{ramp}}/\delta_0 = 0.56$ . Particle trajectories are computed for  $\tau_p = 1\mu\text{s}$  (corresponding to particles used in present experiments) and  $\tau_p = 4\mu\text{s}$  (slower response, plotted to emphasize the effects of particle inertia).

The particle velocity field can be compared to the fluid velocity field by performing the direct subtractions:  $\Delta U = U_p - U_f$ ,  $\Delta V = V_p - V_f$ . The streamwise and vertical differences between the particle velocity field and the air velocity field for the  $h_{\text{ramp}}/\delta_0 = 0.56$  test geometry are shown in Figures 5.3 and 5.4 respectively. The results presented here are collected from particle simulations using the nominal value of  $\tau_p = 1\mu\text{s}$ .

Figure 5.3 shows that relatively large errors in the streamwise particle velocity are associated with the incident and reflected shock waves. These features cause a positive bias in the streamwise velocity because the particles cannot decelerate through the shocks as quickly as the surrounding fluid due to their finite response time,  $\tau_p$ . The largest errors are very localized near the transmitted shock wave where the maximum velocity discrepancy is  $\approx +60\text{m/s} \approx +0.11U_\infty$ . Another region where large particle velocity errors occur is at the downstream edge of the compression ramp where the

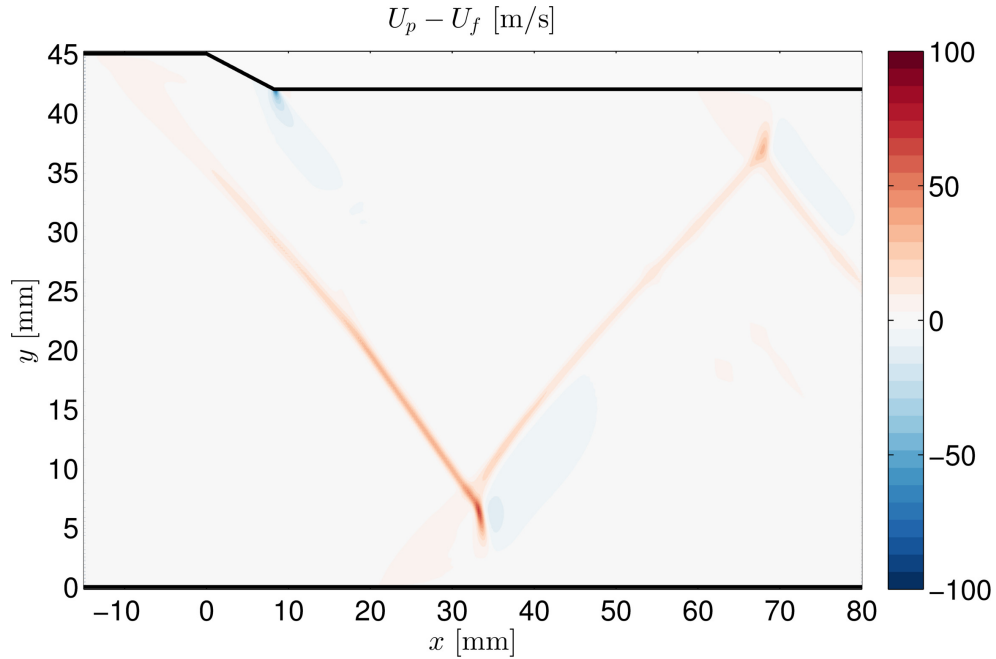


Figure 5.3: Differences between streamwise component of particle velocity field (using nominal value of  $\tau_p = 1\mu\text{s}$ ) and fluid velocity field for the  $h_{\text{ramp}}/\delta_0 = 0.56$  SBLI.

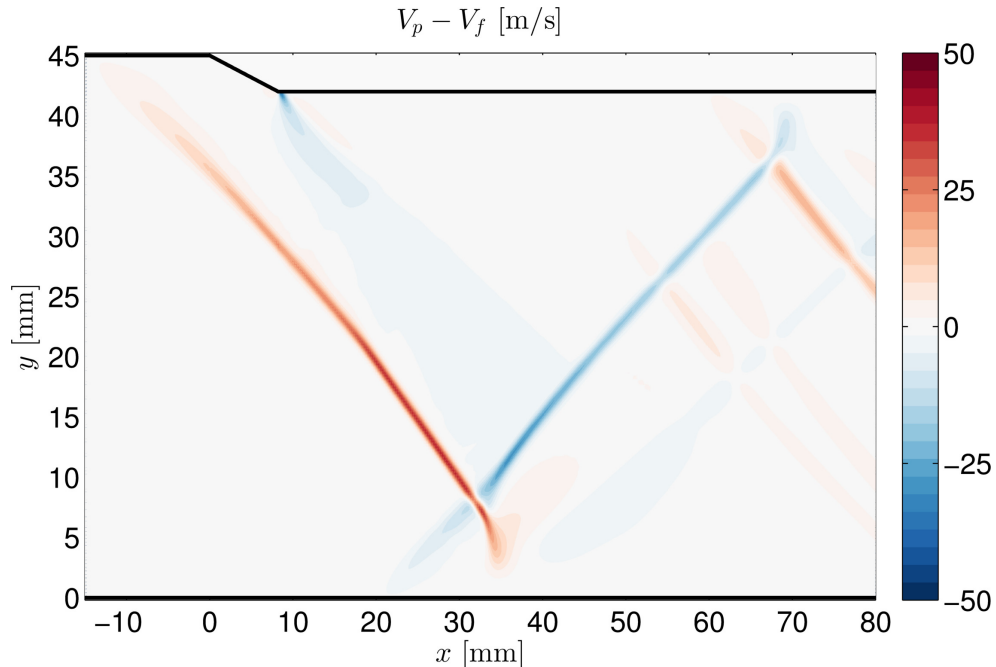


Figure 5.4: Differences between vertical component of particle velocity field (using nominal value of  $\tau_p = 1\mu\text{s}$ ) and fluid velocity field for the  $h_{\text{ramp}}/\delta_0 = 0.56$  SBLI.

top wall turns back to horizontal. At this location an expansion fan accelerates and deflects the flow upward to navigate the sharp corner. The particles lag behind the air velocity field, resulting in a negative velocity bias in this region. The acceleration associated with the expansion fan is strongest directly next to the top wall, and in this region negative  $U$  biases up to  $-120\text{m/s}$  ( $-0.23U_\infty$ ) are observed. Elsewhere in the flow field, the errors incurred due to particle inertia are relatively small.

Figure 5.4 shows that the largest errors in vertical velocity occur in the same regions as the largest errors in the streamwise velocity – localized near the shock and expansion fan features. Due to the particle lag, the vertical particle velocities are biased positively near features that turn the flow downward and negatively near features that turn the flow upward. The error magnitudes for the vertical velocity are generally smaller than for the streamwise velocity; therefore the colorbar range is twice as sensitive in Figure 5.4 as compared to Figure 5.3.

The particle velocity field is computed for the larger  $h_{\text{ramp}}/\delta_0 = 0.93$  geometry using the same procedure as outlined above. The larger ramp case includes even stronger velocity gradients, and therefore larger slip velocities between fluid and particles are possible. The errors in the particle velocity field,  $\Delta U = U_p - U_f$  and  $\Delta V = V_p - V_f$ , are shown in Figures 5.5 and 5.6. As in the  $h_{\text{ramp}}/\delta_0 = 0.56$  case, the largest errors are associated with the shock and expansion fan features. Significantly larger positive velocity biases observed in the vicinity of the Mach stem and the transmitted shock for the  $h_{\text{ramp}}/\delta_0 = 0.93$  case than in the  $h_{\text{ramp}}/\delta_0 = 0.56$  case. The velocity jump across these shocks is very large because the flow decelerates to subsonic downstream. Therefore, the particle overshoot through these shocks appears as a larger error in the measured velocity. In this region, positive velocity biases of up to  $150 \text{ m/s} \approx 0.28U_\infty$  are observed. The maximum negative biases in streamwise velocity associated with the expansion fan are  $\approx -130\text{m/s}$  ( $\approx -0.25U_\infty$ ); these errors are also larger than for the smaller ramp geometry.

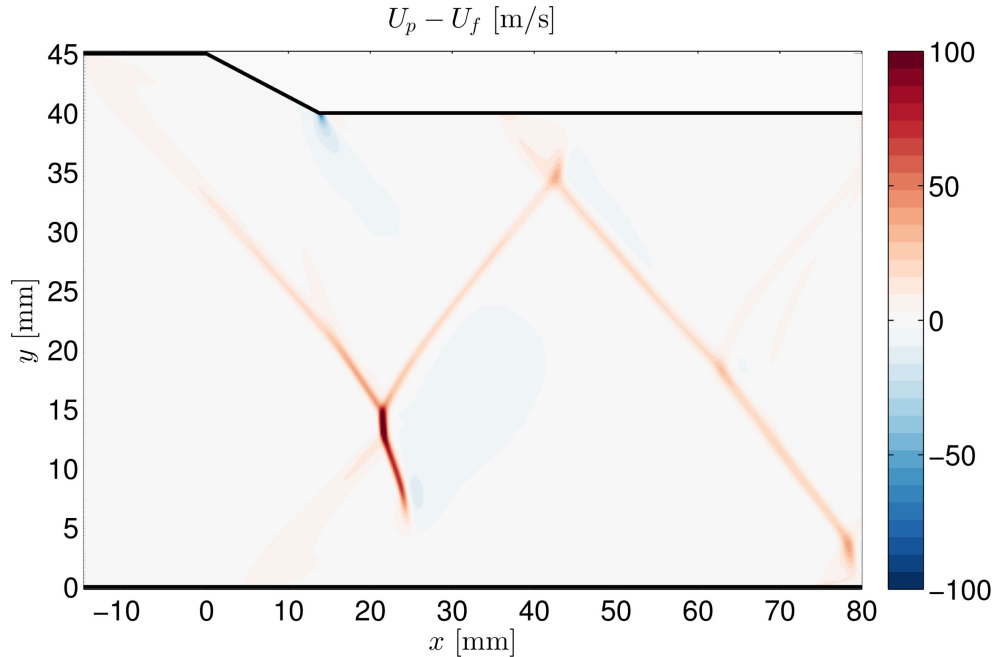


Figure 5.5: Differences between streamwise component of particle velocity field (using nominal value of  $\tau_p = 1\mu\text{s}$ ) and fluid velocity field for the  $h_{\text{ramp}}/\delta_0 = 0.93$  SBLI.

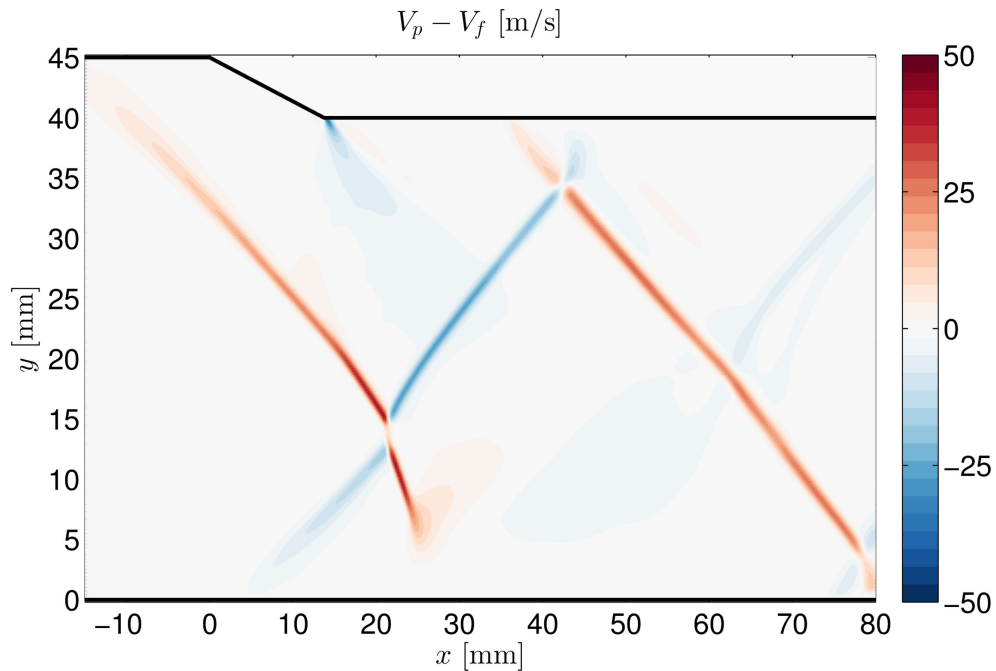


Figure 5.6: Differences between vertical component of particle velocity field (using nominal value of  $\tau_p = 1\mu\text{s}$ ) and fluid velocity field SBLI for the  $h_{\text{ramp}}/\delta_0 = 0.93$  SBLI.

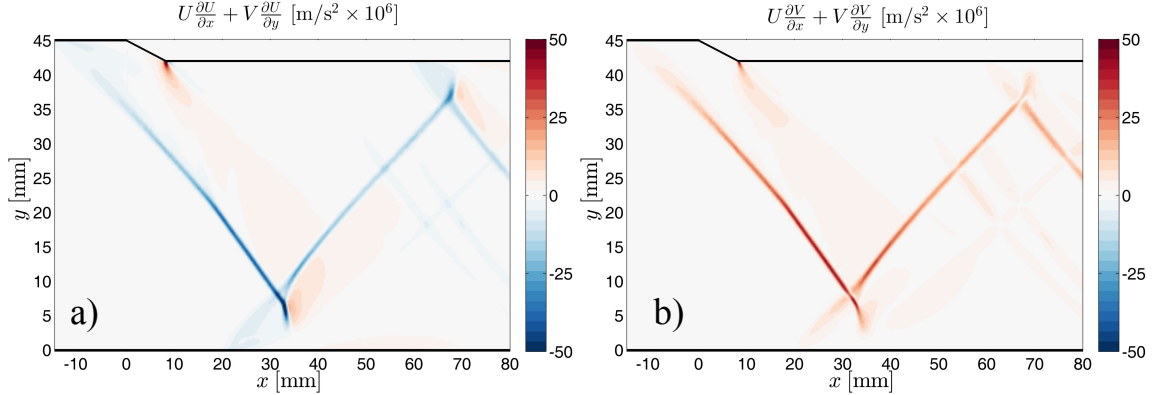


Figure 5.7: Convective acceleration terms throughout the LES flow field for the  $h_{\text{ramp}}/\delta_0 = 0.56$  geometry. a)  $U \frac{\partial U}{\partial x} + V \frac{\partial U}{\partial y}$ ; b)  $U \frac{\partial V}{\partial x} + V \frac{\partial V}{\partial y}$

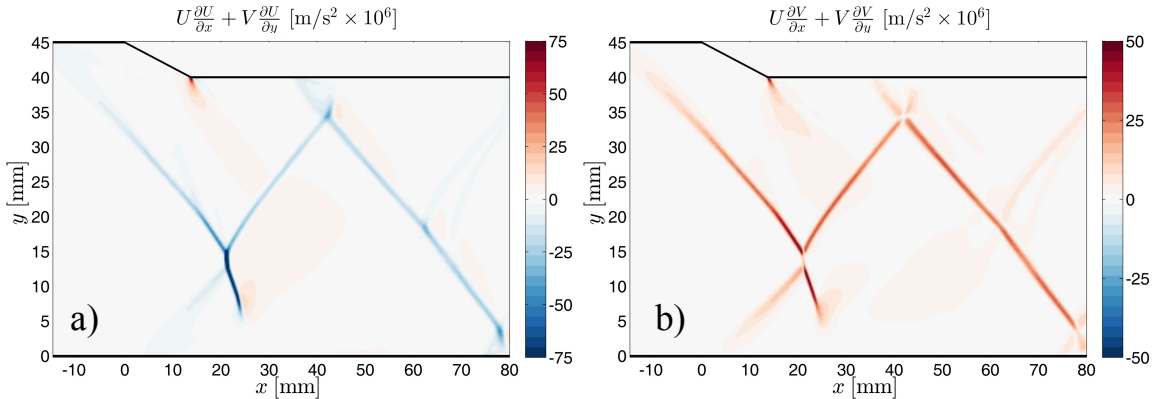


Figure 5.8: Convective acceleration terms throughout the LES flow field for the  $h_{\text{ramp}}/\delta_0 = 0.93$  geometry. a)  $U \frac{\partial U}{\partial x} + V \frac{\partial U}{\partial y}$ ; b)  $U \frac{\partial V}{\partial x} + V \frac{\partial V}{\partial y}$

Figure 5.7 shows the convective acceleration terms,  $U \frac{\partial U}{\partial x} + V \frac{\partial U}{\partial y}$  and  $U \frac{\partial V}{\partial x} + V \frac{\partial V}{\partial y}$  computed directly from the LES fluid flow field for the  $h_{\text{ramp}}/\delta_0 = 0.56$  case. The convective acceleration terms for the  $h_{\text{ramp}}/\delta_0 = 0.93$  case are shown in Figure 5.8. The shock and expansion fan features are apparent, and the overall patterns appear very similar to the ones observed in the  $\Delta U$  and  $\Delta V$  plots for each case (Figures 5.3 – 5.6).

Figures 5.9 and 5.10 show contour lines of the magnitude of the convective acceleration terms overlaid on the  $\Delta U$  and  $\Delta V$  color plots for each case. As expected,

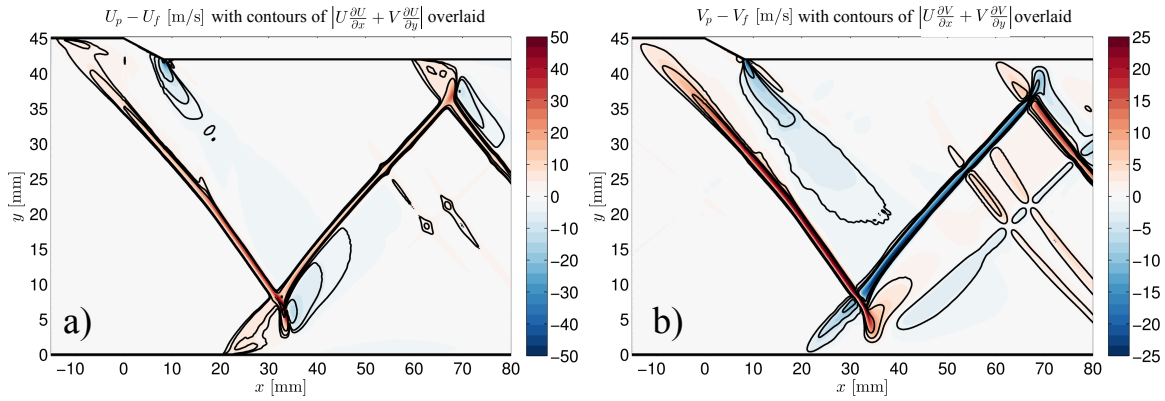


Figure 5.9: Overlap between regions of large particle velocity bias and large convective acceleration magnitude for  $h_{\text{ramp}}/\delta_0 = 0.56$ . a) streamwise:  $U_p - U_f$  with contours of  $|U_{\partial x} + V_{\partial y}|$  overlaid; b) vertical:  $V_p - V_f$  with contours of  $|U_{\partial x} + V_{\partial y}|$  overlaid.

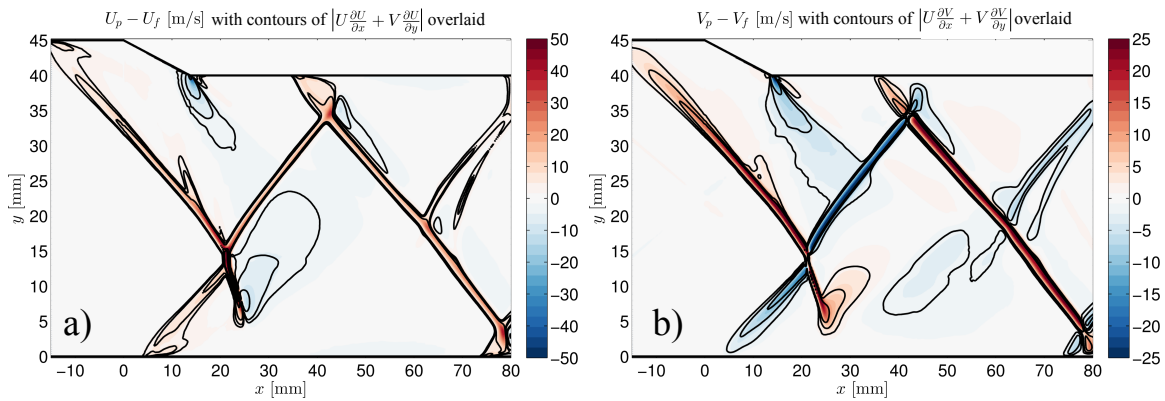


Figure 5.10: Overlap between regions of large particle velocity bias and large convective acceleration magnitude for  $h_{\text{ramp}}/\delta_0 = 0.93$ . a) streamwise:  $U_p - U_f$  with contours of  $|U_{\partial x} + V_{\partial y}|$  overlaid; b) vertical:  $V_p - V_f$  with contours of  $|U_{\partial x} + V_{\partial y}|$  overlaid.

the most severe particle velocity biases are observed in the same regions where the magnitudes of the convective acceleration terms are largest. These results indicate that without computing the particle trajectories, the convective acceleration terms could be used a priori to identify regions of the flow where particle inertia may cause significant deviations between the particle and fluid velocity fields.

While large discrepancies between the particle and fluid velocities do occur in the SBLI flows investigated here, it is important to note that these large errors are concentrated in the vicinity of shock waves and expansion fans. Throughout most of the flow field, the particles with  $\tau_p = 1\mu\text{s}$  track the fluid flow well, resulting in very small particle velocity errors. In particular, the errors in regions of boundary layer thickening, separation, and reattachment are relatively low. This information gives confidence in the measurement accuracy in the primary regions of interest in these SBLI flows.

### 5.2.3 Simulation results using $\tau_p = 0.25\mu\text{s}$ and $\tau_p = 4\mu\text{s}$

This section explores the effects of changing the particle time constant,  $\tau_p$ , in the particle inertia simulations described in the previous sections. The intent of this parameter variation study is to provide information to guide the design of future PIV experiments in high speed compressible flows. PIV studies of SBLI flows typically report particle time constants in the range of  $1 - 10\mu\text{s}$ . The particle trajectory simulations from the previous section are repeated using values of  $\tau_p = 0.25\mu\text{s}$  and  $\tau_p = 4\mu\text{s}$ . These would correspond to olive oil droplets of diameters  $d_p \approx 0.25\mu\text{m}$  and  $1\mu\text{m}$ , respectively. The low value of  $\tau_p = 0.25\mu\text{s}$  is chosen to show that some velocity bias errors occur in the vicinity of shock and expansion features even for a limiting case of very small  $\tau_p$ .

Figures 5.11 and 5.12 show the streamwise and vertical differences between the particle and fluid velocity fields for the  $h_{\text{ramp}}/\delta_0 = 0.56$  case when a particle time

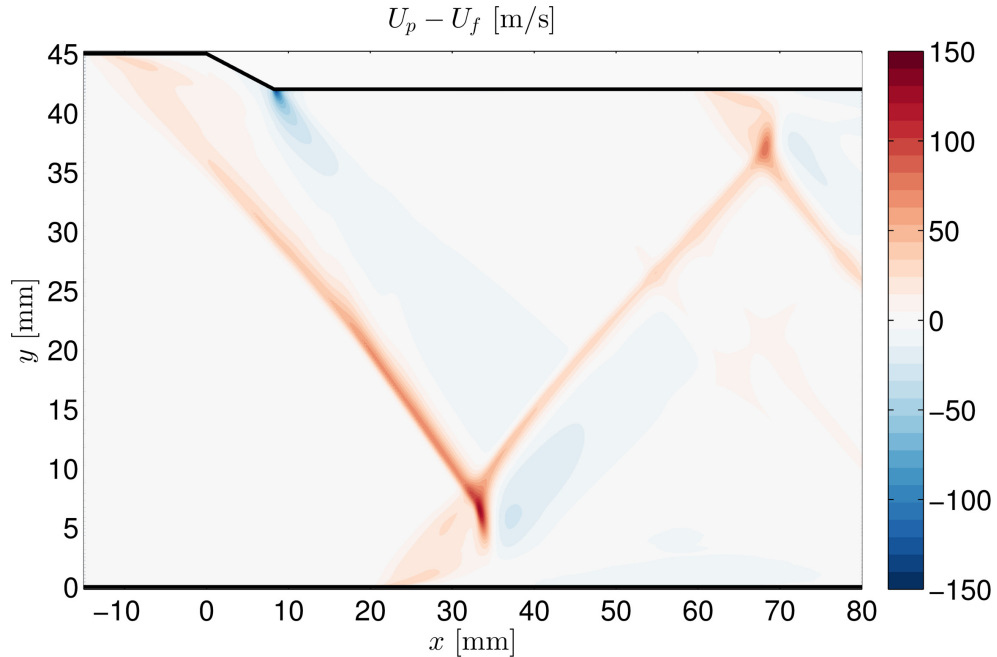


Figure 5.11: Differences between streamwise component of particle velocity field (using  $\tau_p = 4\mu\text{s}$ ) and fluid velocity field for the  $h_{\text{ramp}}/\delta_0 = 0.56$  SBLI.

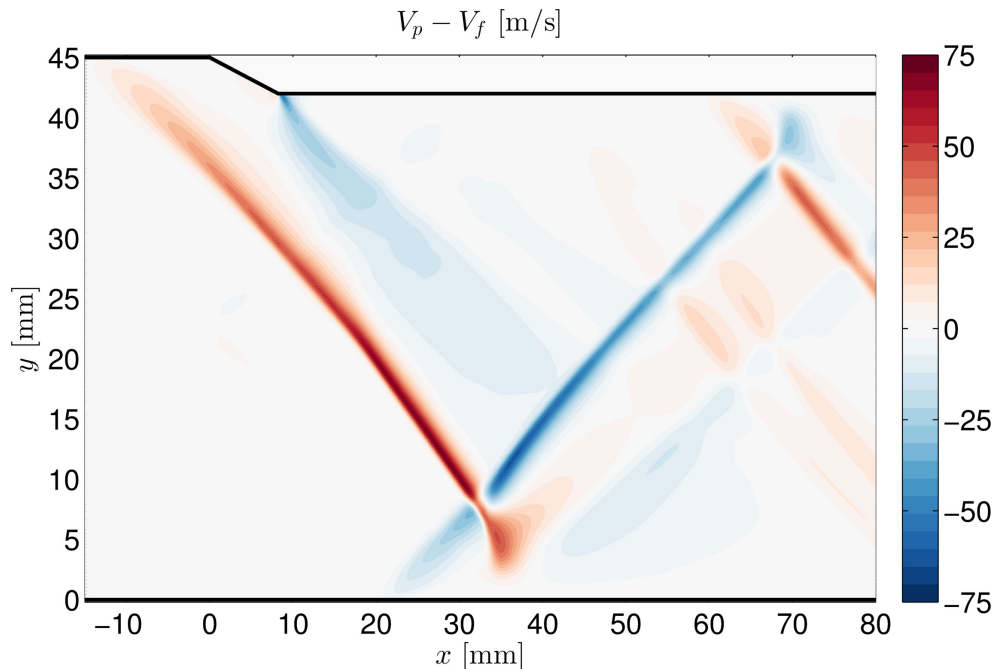


Figure 5.12: Differences between vertical component of particle velocity field (using  $\tau_p = 4\mu\text{s}$ ) and fluid velocity field for the  $h_{\text{ramp}}/\delta_0 = 0.56$  SBLI.

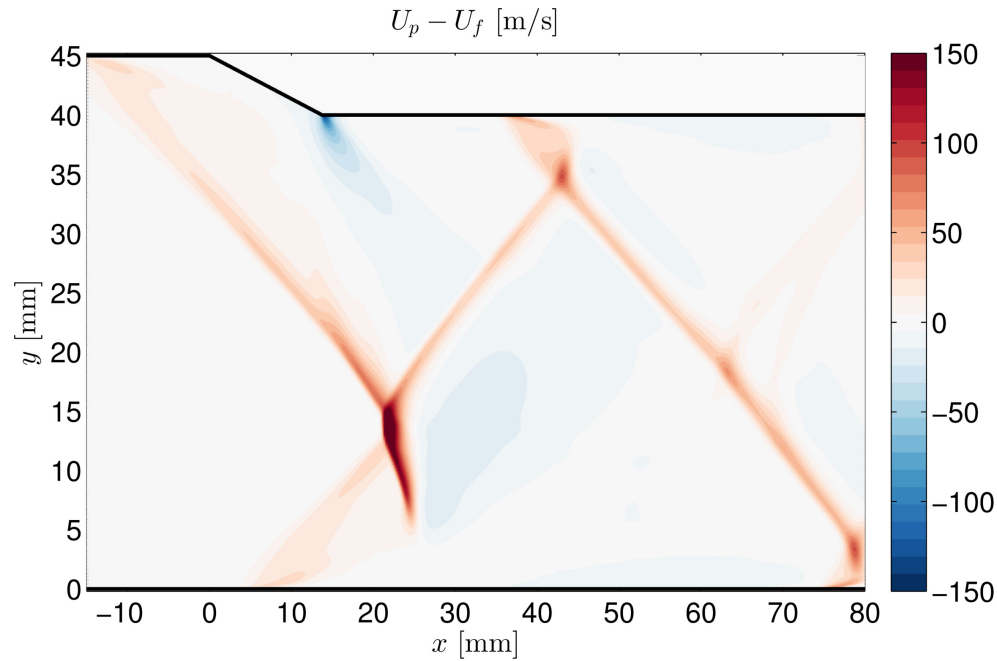


Figure 5.13: Differences between streamwise component of particle velocity field (using  $\tau_p = 4\mu\text{s}$ ) and fluid velocity field for the  $h_{\text{ramp}}/\delta_0 = 0.93$  SBLI.

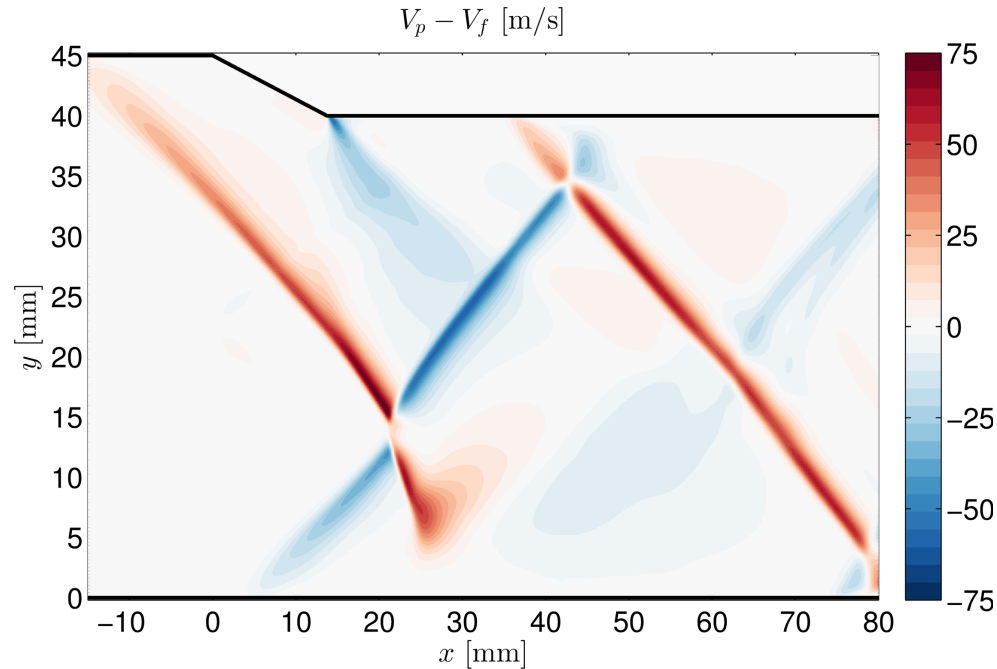


Figure 5.14: Differences between vertical component of particle velocity field (using  $\tau_p = 4\mu\text{s}$ ) and fluid velocity field for the  $h_{\text{ramp}}/\delta_0 = 0.93$  SBLI.

constant of  $\tau_p = 4\mu\text{s}$  is assumed. Likewise, the velocity differences for the  $h_{\text{ramp}}/\delta_0 = 0.93$  case with particle time constant of  $\tau_p = 4\mu\text{s}$  are plotted in Figures 5.13 and 5.14. These results show significantly larger velocity mismatches associated with all of the shock and expansion fan features as compared to the simulations using the nominal  $\tau_p = 1\mu\text{s}$  (Figures 5.3, 5.4, 5.5, and 5.5). Note that the ranges of values in the colorbars have been increased by a factor of 1.5 in the  $\tau_p = 4\mu\text{s}$  figures to better represent the larger errors. The total areas over which the discrepancies are significant is also much larger in the  $\tau_p = 4\mu\text{s}$  case.

Furthermore, for the  $\tau_p = 4\mu\text{s}$  particle velocity fields, non-negligible errors in the streamwise velocity are associated with regions where the boundary layer thickens rapidly. This is observed in Figures 5.11 and 5.13 both near the foot of the compression ramp where the shock wave is generated as well as in regions corresponding to subsequent reflections of that shock. In these regions, the measured velocity is biased positively because the particles do not decelerate as quickly as the surrounding fluid.

In the  $h_{\text{ramp}}/\delta_0 = 0.56$  test case, positive streamwise velocity biases up to  $+125\text{m/s}$  ( $+0.24U_\infty$ ) exist directly downstream of the transmitted shock wave and negative velocity biases of up to  $-140\text{m/s}$  ( $-0.26U_\infty$ ) occur at the origin of the expansion fan. In the  $h_{\text{ramp}}/\delta_0 = 0.93$  case, the particle velocity bias reaches a maximum of  $+240\text{m/s}$  ( $+0.45U_\infty$ ) directly behind the Mach stem. In this case, the largest negative bias observed in the expansion fan is  $-180\text{m/s}$  ( $-0.34U_\infty$ ). The simulated particle velocity errors are very large; however SBLI experiments using particles with similar values of  $\tau_p$  are common in the literature.

Figures 5.15, 5.16, 5.17, and 5.18 show the streamwise and vertical differences between the particle and fluid velocity fields for both test geometries when a particle time constant of  $\tau_p = 0.25\mu\text{s}$  is assumed. These errors are much smaller than the biases observed for both the  $\tau_p = 4\mu\text{s}$  and  $\tau_p = 1\mu\text{s}$  cases, but not zero. In the  $h_{\text{ramp}}/\delta_0 = 0.56$  case with  $\tau_p = 0.25\mu\text{s}$ , the maximum bias errors are  $+20\text{m/s}$

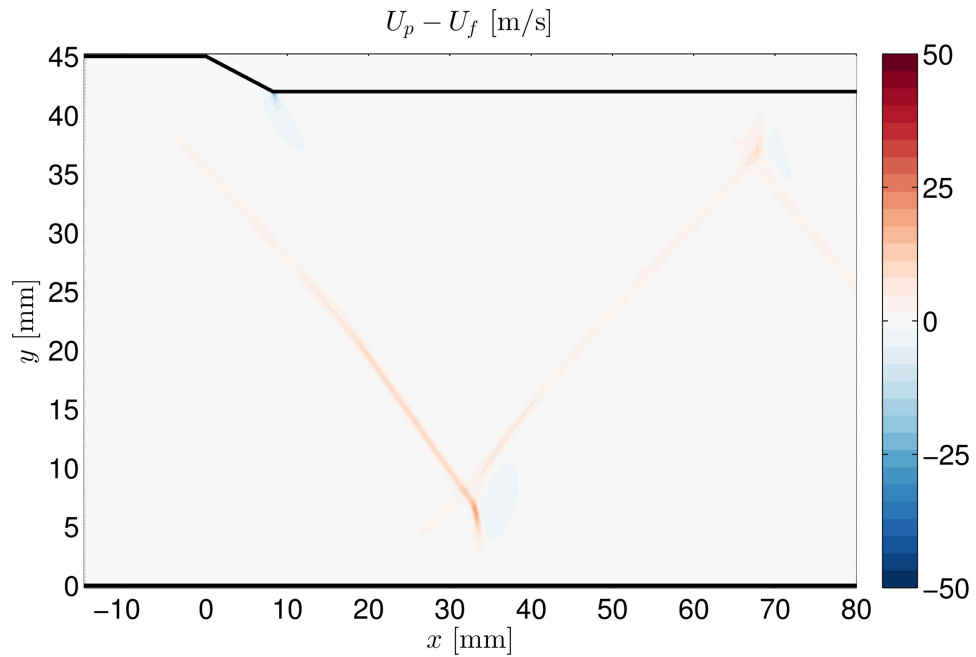


Figure 5.15: Differences between streamwise component of particle velocity field (using  $\tau_p = 0.25\mu\text{s}$ ) and fluid velocity for the  $h_{\text{ramp}}/\delta_0 = 0.56$  SBLI.

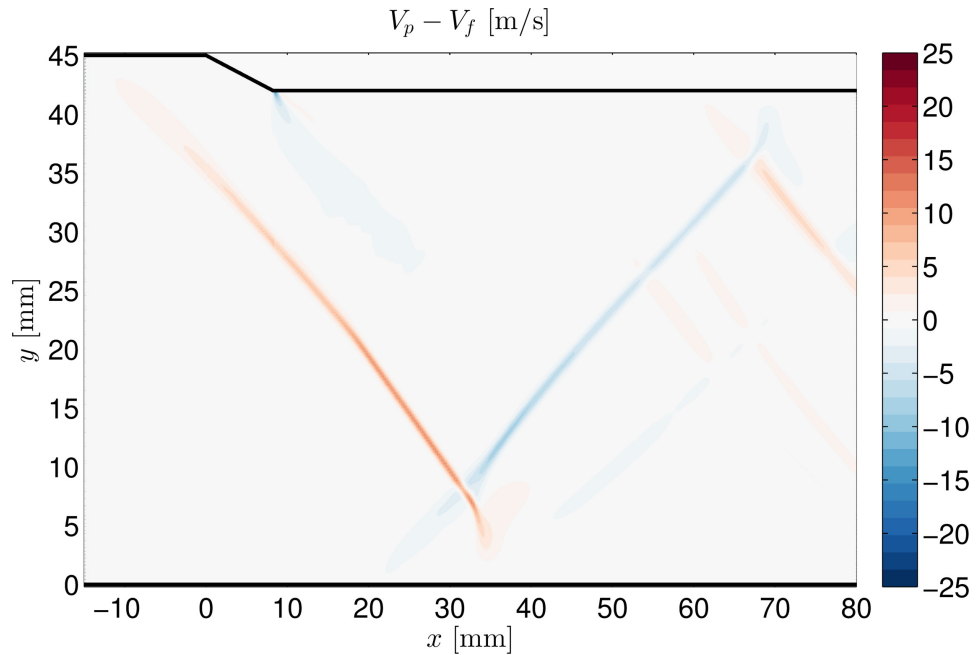


Figure 5.16: Differences between vertical component of particle velocity field (using  $\tau_p = 0.25\mu\text{s}$ ) and fluid velocity field for the  $h_{\text{ramp}}/\delta_0 = 0.56$  SBLI.

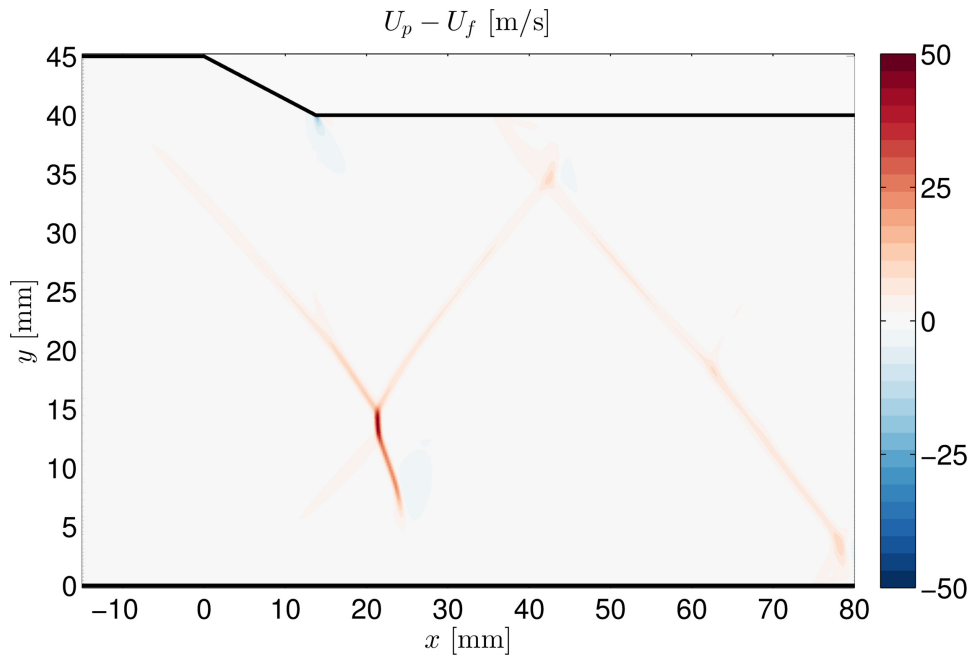


Figure 5.17: Differences between streamwise component of particle velocity field (using  $\tau_p = 0.25\mu\text{s}$ ) and fluid velocity field for the  $h_{\text{ramp}}/\delta_0 = 0.93$  SBLI.

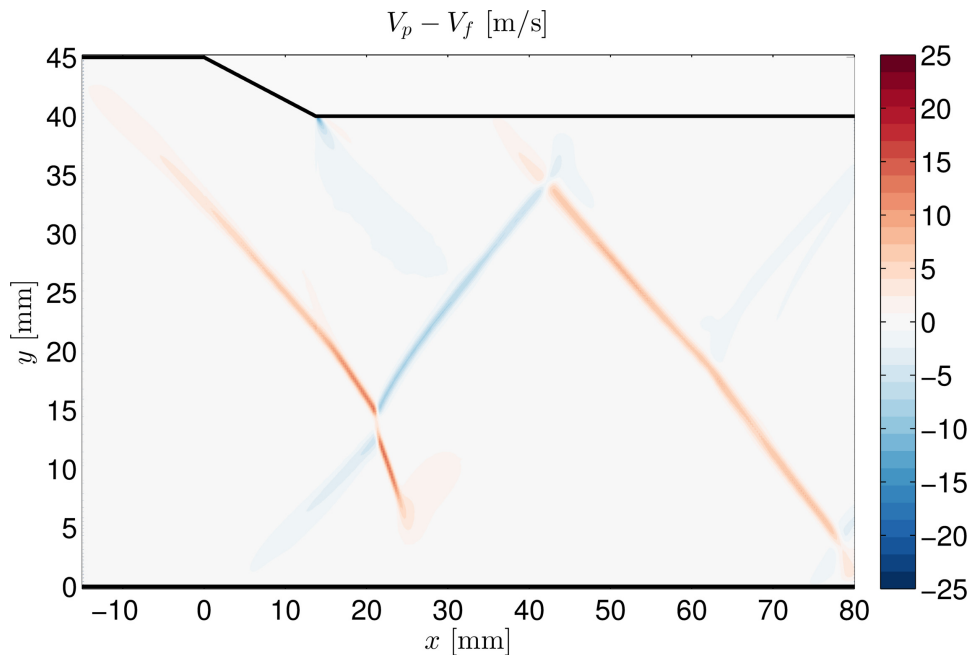


Figure 5.18: Differences between vertical component of particle velocity field (using  $\tau_p = 0.25\mu\text{s}$ ) and fluid velocity field for the  $h_{\text{ramp}}/\delta_0 = 0.93$  SBLI.

( $+0.04U_\infty$ ) and  $-25\text{m/s}$  ( $-0.05U_\infty$ ). For the larger ramp case, the maximum errors for  $\tau_p = 0.25\mu\text{s}$  are  $+50\text{m/s}$  ( $+0.09U_\infty$ ) and  $-30\text{m/s}$  ( $-0.06U_\infty$ ).

Figure 5.19 shows velocity profiles extracted at a constant  $y$  height above the bottom wall for both of the ramp geometries. For  $h_{\text{ramp}}/\delta_0 = 0.56$  the profiles are extracted at  $y = 6\text{mm}$ , and for  $h_{\text{ramp}}/\delta_0 = 0.93$  the profiles are extracted at  $y = 14\text{mm}$ . These positions are chosen because they slice through the regions where the velocity biases are largest, including the Mach stem and the transmitted shock wave. The black solid lines represent the mean streamwise and vertical velocities predicted by CFD. The simulated particle velocity fields corresponding to  $\tau_p = 0.25, 1,$  and  $4\mu\text{s}$  are overlaid for comparison. This allows for a more quantitative comparison between the fluid and particle velocity fields generated using different values of  $\tau_p$ .

In all four subfigures, the large discrepancies between the fluid velocity field and the particle velocity field using  $\tau_p = 4\mu\text{s}$  are highlighted. The shock features appear further downstream and less sharp than in the fluid velocity profiles. Furthermore, in regions where the flow is first quickly decelerated and then reaccelerated shortly downstream, the particles with  $\tau_p = 4\mu\text{s}$  grossly overpredict the minimum streamwise velocity and do not accurately report its position. The discrepancies for  $\tau_p = 0.25\mu\text{s}$  are hardly detectable, and the discrepancies for  $\tau_p = 1\mu\text{s}$  are small but noticeable. These results serve two purposes – first, to validate that the particles chosen for the current PIV experiments track the flow acceptably in most regions, and second to demonstrate the variability in results that could have occurred if the particles had been selected differently. The particle velocity fields calculated for SBLIs of two different strengths with three different values of  $\tau_p$  show an order of magnitude difference in the size of the maximum bias errors. This large variability demonstrates the importance of quantifying such biases before attempting a comparison between CFD and PIV datasets for high speed compressible flows.

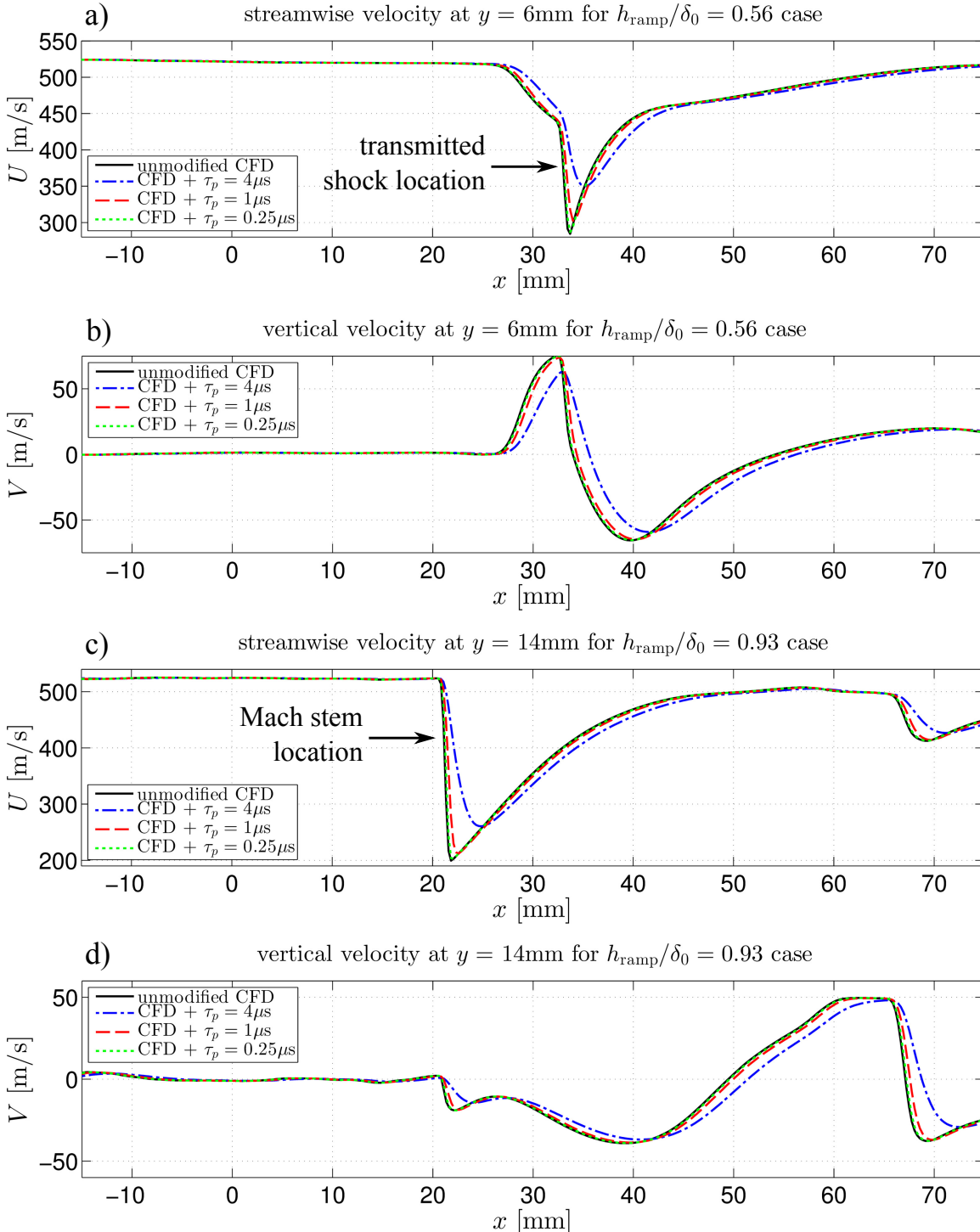


Figure 5.19: Mean streamwise and vertical velocity extracted at a constant  $y$  location for  $h_{\text{ramp}}/\delta_0 = 0.56$  and  $h_{\text{ramp}}/\delta_0 = 0.93$  geometries. The fluid velocity profile from CFD is shown as a black solid line. The particle velocity profiles using  $\tau_p = 0.25, 1$ , and  $4\mu\text{s}$  are overlaid for comparison.

## 5.3 PIV measurement resolution

### 5.3.1 Interrogation region size and overlap

The next source of velocity bias errors in PIV data explored here is the measurement resolution. When comparing CFD and PIV data it is important to examine the differences between the computational mesh and the PIV vector spacing. This is particularly relevant in regions where the CFD mesh has been refined to capture steep velocity gradients. Often the interrogation regions used in PIV experiments are of a fixed size, regardless of their proximity to a boundary layer or shock wave. Usually the areas encompassed by neighboring cells in the PIV grid overlap in order to obtain additional velocity vectors. For the 50% overlap used in all of the experiments presented in this thesis, the distance spanned by an interrogation region is twice the distance between the center of that interrogation region and the center of its nearest neighbor. A zoomed in view of a sample PIV vector grid overlaid on a CFD mesh is shown in Figure 5.20. The left image shows a case with no overlap in the PIV interrogation regions, and the right image shows a case with 50% overlap. In both cases, a total of four equally sized adjacent interrogation windows are shown.

A simple procedure to modify the CFD velocity field to account for the spatial resolution of the PIV measurements is as follows. The velocities associated with any full or partial CFD mesh cells that fall within a particular PIV interrogation region are averaged over the area represented by the PIV vector. The average is performed using weights corresponding to the fraction of the PIV interrogation region occupied by each individual velocity point from the CFD. This area averaged velocity is then assigned to the point at the center of the PIV interrogation region where the corresponding PIV vector is located. In order to account for both particle inertia and the PIV measurement resolution, this area averaging should be performed on the particle velocity field computed using the appropriate value of  $\tau_p$ .

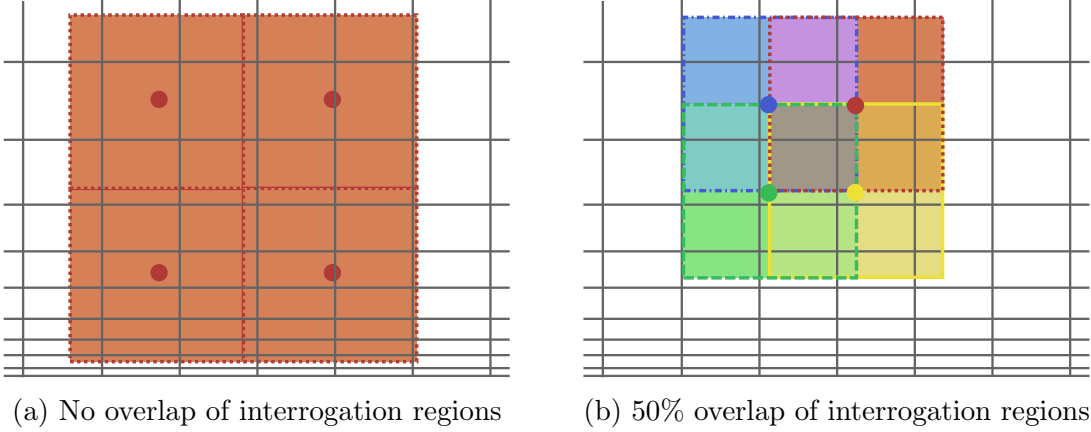


Figure 5.20: Sample CFD mesh (gray lines) and PIV vector grids (color-filled squares). Both (a) and (b) show four equally sized adjacent interrogation regions. The center of each PIV interrogation region is marked by a dot.

It is important to note that assumptions are made in applying the above procedure. First, it is assumed implicitly in using an area average that the PIV measurement uniformly samples the velocity over an interrogation region. This assumption may not be valid if, for example, slow particles are more likely to be detected than fast ones. Secondly, the PIV measurement resolution is assumed to be equal to the interrogation region size. As will be shown in the following section, this is not necessarily the case, particularly for high speed flows. The simple area-averaging method outlined in this section is the minimum amount of post-processing that should be applied to a CFD result prior to comparing it with a PIV dataset. A much higher fidelity method is described in the following section.

### 5.3.2 Particle travel between image exposures

The previous section assumed that the PIV resolution was simply the physical size of an interrogation window. This is typically how PIV measurement resolutions are reported in the literature. Some studies report the PIV resolution to be the spacing between adjacent interrogation region centers even when 50% or 75% overlap is used.

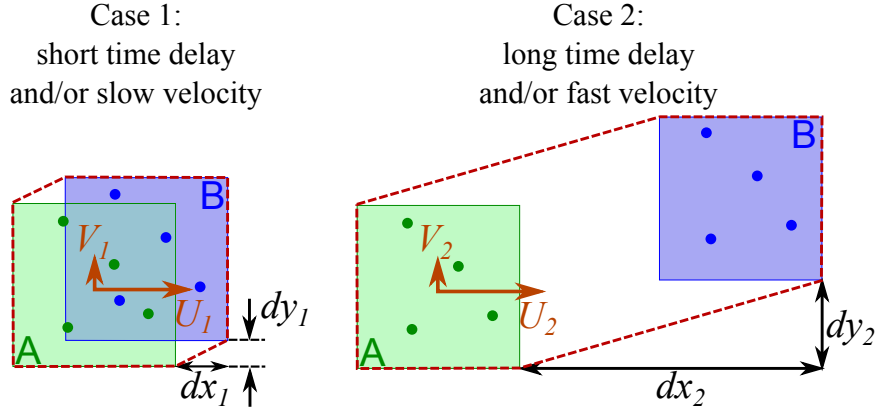


Figure 5.21: Illustration of PIV velocity vector calculation process for cases where the particle displacements are small (case 1) and large (case 2) relative to the size of the interrogation windows.

However, the true measurement resolution includes the full size of the interrogation region plus the area swept out by particles originating inside that interrogation region between image exposures. Recall that PIV finds the most likely particle displacement by cross-correlating the two image frames, A and B. If the time delay between exposures is short and/or the velocity of the particles is slow, then the displacement between interrogation regions A and B will be small. This case is illustrated in case 1 of Figure 5.21. The velocity measurements are estimated as:

$$U_1 = \frac{dx_1}{\Delta t} \quad \text{and} \quad V_1 = \frac{dy_1}{\Delta t} \quad (5.7)$$

and then these velocity estimates are assigned to the  $(x, y)$  location of the centroid of interrogation region A. The full area that is actually represented by measurements  $U_1$  and  $V_1$  is surrounded by the dashed red line. For case 1 where the particle displacements are small relative to the interrogation region size, the overall measurement resolution is approximately the same as the interrogation region area.

If, however, the particle velocities are large and/or the time delay between image exposures is long, the situation illustrated in case 2 of Figure 5.21 occurs. In this

case, the particles travel a significant distance between frame A and frame B. The velocity measurements are again estimated as:

$$U_2 = \frac{dx_2}{\Delta t} \quad \text{and} \quad V_2 = \frac{dy_2}{\Delta t} \quad (5.8)$$

and assigned to the centroid of interrogation region A. The red dashed line surrounds the full area of influence of the measurement. In this case, the velocity measurement represents an average over a much larger area than the interrogation region size; therefore simply stating the interrogation region size as the measurement resolution is misleading.

Large particle displacements between image exposures are common in high speed flows. Furthermore, the velocity calculation from particle displacements assumes a constant particle velocity between frames A and B; therefore, biases arise if the particles accelerate or decelerate between image exposures. For example, if interrogation regions A and B straddle a shock wave, the velocity assigned to the centroid of region A may be biased low because the particles decelerate between image exposures.

In order to account for the combined effects of PIV interrogation region size and particle travel between image exposures, the following filtering scheme can be applied to either the original CFD velocity field or the simulated particle velocity field. This process is illustrated in Figure 5.22

1. Determine the PIV parameters: time delay between images,  $\Delta t$ , physical size of each interrogation region,  $2\Delta x_{IR} \times 2\Delta y_{IR}$ , and percentage overlap between interrogation regions
2. Define the set of centroids of the PIV grid ( $x_{IR}, y_{IR}$ ), which correspond to the locations where PIV vectors are assigned
3. For each PIV grid cell, sample  $n$  points at random over the enclosed area,

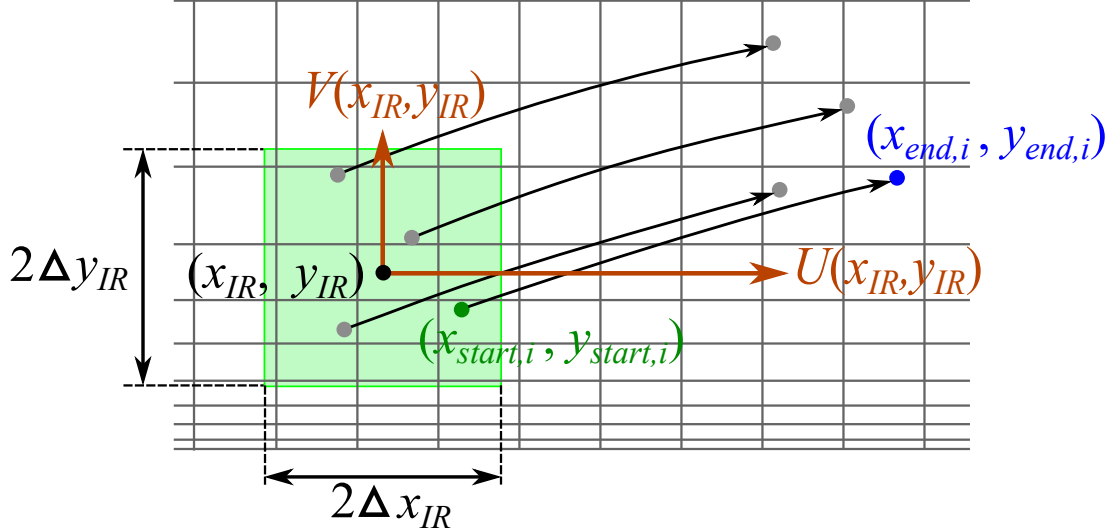


Figure 5.22: Illustration of streamline or particle trajectory integration for an area corresponding to a single PIV vector. A PIV interrogation region from frame A of an image pair (green square) is overlaid on the CFD mesh (grey grid lines). This diagram assumes 50% overlap of interrogation regions.

$$[x_{IR} - \Delta x_{IR}, x_{IR} + \Delta x_{IR}] \cap [y_{IR} - \Delta y_{IR}, y_{IR} + \Delta y_{IR}].$$

4. Use the CFD velocity field or simulated particle velocity field to propagate streamlines or particle paths starting at these  $n$  locations over a time interval of  $\Delta t$ .
5. Save the starting and ending points of each trajectory as  $(x_{start,i}, y_{start,i})$  and  $(x_{end,i}, y_{end,i})$ .
6. Compute the streamwise and vertical velocities as:

$$\begin{aligned} U(x_{IR}, y_{IR}) &= \frac{1}{n\Delta t} \sum_{i=1}^n (x_{end,i} - x_{start,i}) \\ V(x_{IR}, y_{IR}) &= \frac{1}{n\Delta t} \sum_{i=1}^n (y_{end,i} - y_{start,i}) \end{aligned} \quad (5.9)$$

7. Repeat for all the other cells in the PIV grid.

The final modified CFD field using this process represents the true spatial resolution of the PIV measurements. Depending on whether the trajectories are integrated along particle paths ( $\tau_p > 0$ ) or streamlines ( $\tau_p = 0$ ), the effects of particle inertia may or may not be included in the calculation.

## 5.4 Results

### 5.4.1 Simulations of PIV bias error magnitudes

The CFD velocity field and the simulated particle velocity fields ( $\tau_p = 0.25$ , 1, and  $4\mu s$ ) are filtered according to the method laid out in the previous section using three different combinations of  $\Delta x_{IR} = \Delta y_{IR}$  and  $\Delta t$ . This process is repeated for  $h_{ramp}/\delta_0 = 0.56$  and  $0.93$  using  $n = 100$  and 50% overlap of vectors for all cases. All of the different sets of parameters used are listed in Table 5.1. The nominal conditions corresponding to the experiments presented in the previous chapters are highlighted in yellow.

The differences between the velocity fields for the modified and unmodified CFD results are impossible to discern by looking at side-by-side color contour plots. Therefore, color contour plots of only the original unmodified mean streamwise velocity from CFD for both the  $h_{ramp}/\delta_0 = 0.56$  and  $0.93$  cases are presented in Figure 5.23. These surface plots are meant to orient the reader to the overall flow patterns when looking at velocity profile plots extracted at different streamwise ( $x$ ) positions. The subsequent analysis of the differences caused by the various PIV bias sources will be done by examining velocity profiles in the incident shock region for each case, starting with the stronger interaction. Only the lower half of the test section is shown because the analysis focuses on the Mach stem and transmitted shock regions of the incident SBLIs where the PIV biases are most significant.

Table 5.1: Parameters used to filter CFD data for both  $h_{\text{ramp}}/\delta_0 = 0.56$  and  $0.93$  test cases to simulate PIV biases. The nominal conditions corresponding to the PIV parameters used in the current experiments are highlighted.

$\tau_p$ [ $\mu\text{s}$ ]	$\Delta x_{IR} = \Delta y_{IR}$ [mm]	$\Delta t$ [ $\mu\text{s}$ ]
0	0.12	0.8
0	0.12	1.6
0	0.24	0.8
0.25	0.12	0.8
0.25	0.12	1.6
0.25	0.24	0.8
1	0.12	0.8
1	0.12	1.6
1	0.24	0.8
4	0.12	0.8
4	0.12	1.6
4	0.24	0.8

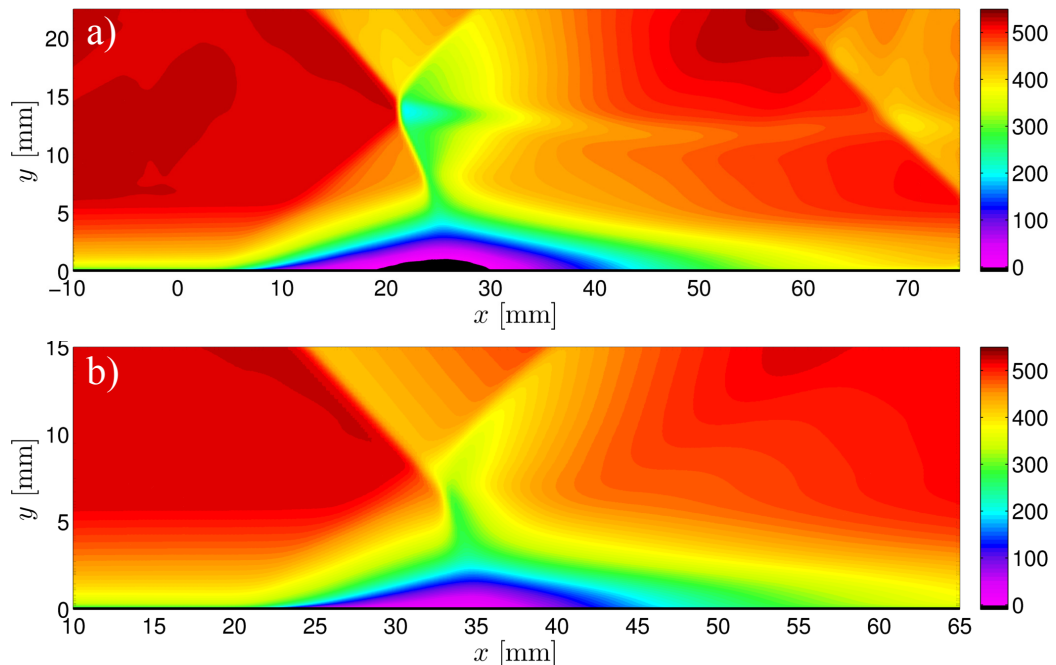


Figure 5.23: Unmodified mean streamwise velocity from CFD simulations of the two different experimental geometries: a)  $h_{\text{ramp}}/\delta_0 = 0.93$ ; b)  $h_{\text{ramp}}/\delta_0 = 0.56$ .

Figure 5.24 shows mean streamwise velocity profiles for the original CFD and the 12 different modified CFD cases using the parameter sets listed in Table 5.1 for the  $h_{\text{ramp}}/\delta_0 = 0.93$  test geometry. The top panel (a) shows that the velocity profiles for all cases collapse in the incoming boundary layer ( $x = 0\text{mm}$ ). Therefore, in this upstream portion of the flow the effects of particle inertia, measurement resolution, and time delay between exposures are negligible.

The profiles in panel (b) are extracted at a station on the upstream edge of the Mach stem ( $x = 21\text{mm}$ ). This location is interesting because depending on the parameter choices ( $\tau_p$ ,  $\Delta x_{IR}$ , and  $\Delta t$ ), the streamwise velocity can be biased either significantly negative or positive relative to the unmodified CFD result. The profile from the original unmodified CFD simulation is shown as a solid gray line. The line types correspond to particular values of particle time constant,  $\tau_p$ , and the colors indicate which combination of  $\Delta x_{IR}$  and  $\Delta t$  parameters are used.

The velocity bias is negative for all of the cases where the particles are assumed to follow the fluid streamlines exactly ( $\tau_p = 0$ , solid lines). This is because the path traveled by an inertialess “particle” crosses from the upstream side to the downstream side of the Mach stem in time  $\Delta t$ . These “particles” have no lag and therefore decelerate to the post-shock fluid velocity instantly. The end effect is that the velocity measurement includes an average of both high velocity (upstream of the MS) and low velocity (downstream of the MS) regions, and the resulting vector is assigned to the center of an interrogation region that sits slightly upstream of the shock. The negative bias is most severe for the case where  $\Delta t = 1.6\mu\text{s}$ , which is intuitive because the “particle” spends a longer time downstream of the shock wave in this case.

The velocity profiles for the cases with very small, but finite particle response time,  $\tau_p = 0.25\mu\text{s}$  (long dash lines), also show a slight negative bias. However, the effect is weaker than for the inertialess particle case. The reason for this is that two competing effects are in play. The effect of the particles crossing from one side of

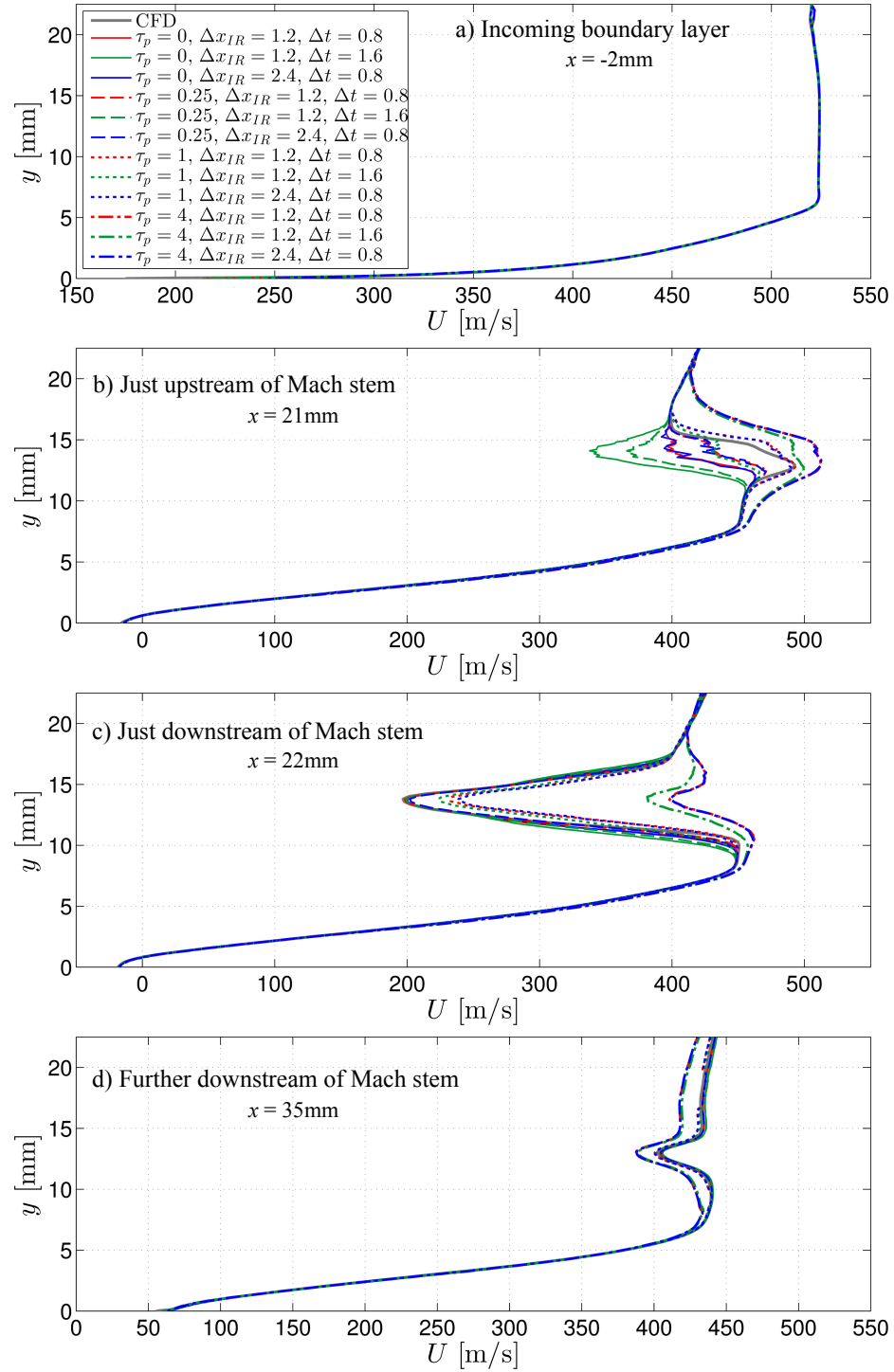


Figure 5.24: Mean streamwise velocity profiles showing simulated PIV biases in the incident shock region for the  $h_{\text{ramp}}/\delta_0 = 0.93$  test case.

the shock to the other during  $\Delta t$  causes a negative velocity bias as before. However, the particles take a finite time to relax to the lower post-shock fluid velocity, so the total distance traveled by a particle with  $\tau_p = 0.25\mu s$  over time  $\Delta t$  is higher than the distance traveled by an inertialess particle originating at the same initial location. The negative bias outweighs the positive bias, particularly for the case with the longer time delay, resulting in a net negative bias for the  $\tau_p = 0.25\mu s$  cases.

Strong positive velocity biases are associated with the profiles for the  $\tau_p = 4\mu s$  cases (dash-dot lines). For these simulations, the particles decelerate significantly slower than the surrounding fluid, and therefore these particles travel an artificially long distance over the time interval  $\Delta t$ . For  $\tau_p = 4\mu s$  with a longer  $\Delta t$  of  $1.6\mu s$ , the positive bias is less severe. This is because for the longer trajectory, the particle has time to decelerate more than for the shorter trajectory, resulting in a less positively biased velocity measurement.

The  $\tau_p = 1\mu s$  profiles (short dash lines) for  $\Delta t = 0.8\mu s$  display a positive bias due to the particle inertia effect dominating over the effect of the trajectory including both pre- and post-shock regions. The  $\tau_p = 1\mu s$  profile for the longer time delay shows a negative bias because in this case the particle trajectory includes a longer portion downstream of the shock where it is decelerating, causing a lower average velocity over  $\Delta t = 1.6\mu s$ .

Panel (c) of Figure 5.24 shows the mean streamwise velocity profiles for all of the cases at a streamwise location at the downstream edge of the Mach stem ( $x = 22\text{mm}$ ). For this location, all of the velocity profiles show either positive or no bias near the local minimum in  $U$ . The magnitude of the bias increases with increasing  $\tau_p$  as expected. The velocity profiles are plotted at a location further downstream of the Mach stem ( $x = 35\text{mm}$ ) in the bottom panel (d) of Figure 5.24. At this location most of the velocity profiles collapse, with significant discrepancies for only the  $\tau_p = 4\mu s$  cases. The  $\tau_p = 4\mu s$  profiles are biased negatively because the particles

cannot reaccelerate as quickly as the surrounding fluid downstream of the Mach stem.

Figure 5.25 shows mean streamwise velocity profiles extracted at four  $x$  locations in the  $h_{\text{ramp}}/\delta_0 = 0.56$  incident SBLI region. The unmodified CFD plus 12 cases where PIV biases have been simulated using the parameter combinations in Table 5.1 are shown in each set of profile plots. The lines are styled in the same way as in Figure 5.24. The data in panel (a) of Figure 5.25 are from an upstream location where all the profiles collapse, and are very similar to the upstream boundary layer profiles for the larger ramp case.

The profiles in panel (b) of Figure 5.24 are extracted at  $x = 33\text{mm}$ , which is just upstream of the transmitted shock wave in a region of strong deceleration. The trends in the velocity profile biases for the 12 different cases are qualitatively similar to the trends observed just upstream of the Mach stem in the large ramp case (panel (b) of Figure 5.24). The primary discrepancies occur around  $y = 4$  to  $y = 10\text{mm}$  where the velocity profile has a distinct non-monotonic shape and where the streamwise deceleration is strongest.

Panel (c) shows profiles extracted at a slightly further downstream location of  $x = 35\text{mm}$ . At this station, the velocity gradient,  $\partial U / \partial y$ , is less severe in the non-monotonic portion of the profiles, and the particles for all the cases except  $\tau_p = 4\mu\text{s}$  have mostly relaxed back to the underlying CFD fluid velocity. Even further downstream where the flow reaccelerates (panel (d),  $x = 45\text{mm}$ ), slight negative biases are observed for the  $\tau_p = 0.25$  and  $1\mu\text{s}$  cases and large negative biases occur for the  $\tau_p = 4\mu\text{s}$  cases, similar to the behavior in the reaccelerating flow downstream of the Mach stem for the larger ramp case.

Based on the results of all 24 simulated PIV bias cases, doubling the size of  $\Delta x_{IR}$  has negligible overall effect. This is shown by the very close agreement between the red ( $\Delta x_{IR} = 0.12\text{mm}$ ) and blue ( $\Delta x_{IR} = 0.24\text{mm}$ ) lines for each individual value of  $\tau_p$ . Therefore, the most important PIV bias error sources to consider are the particle

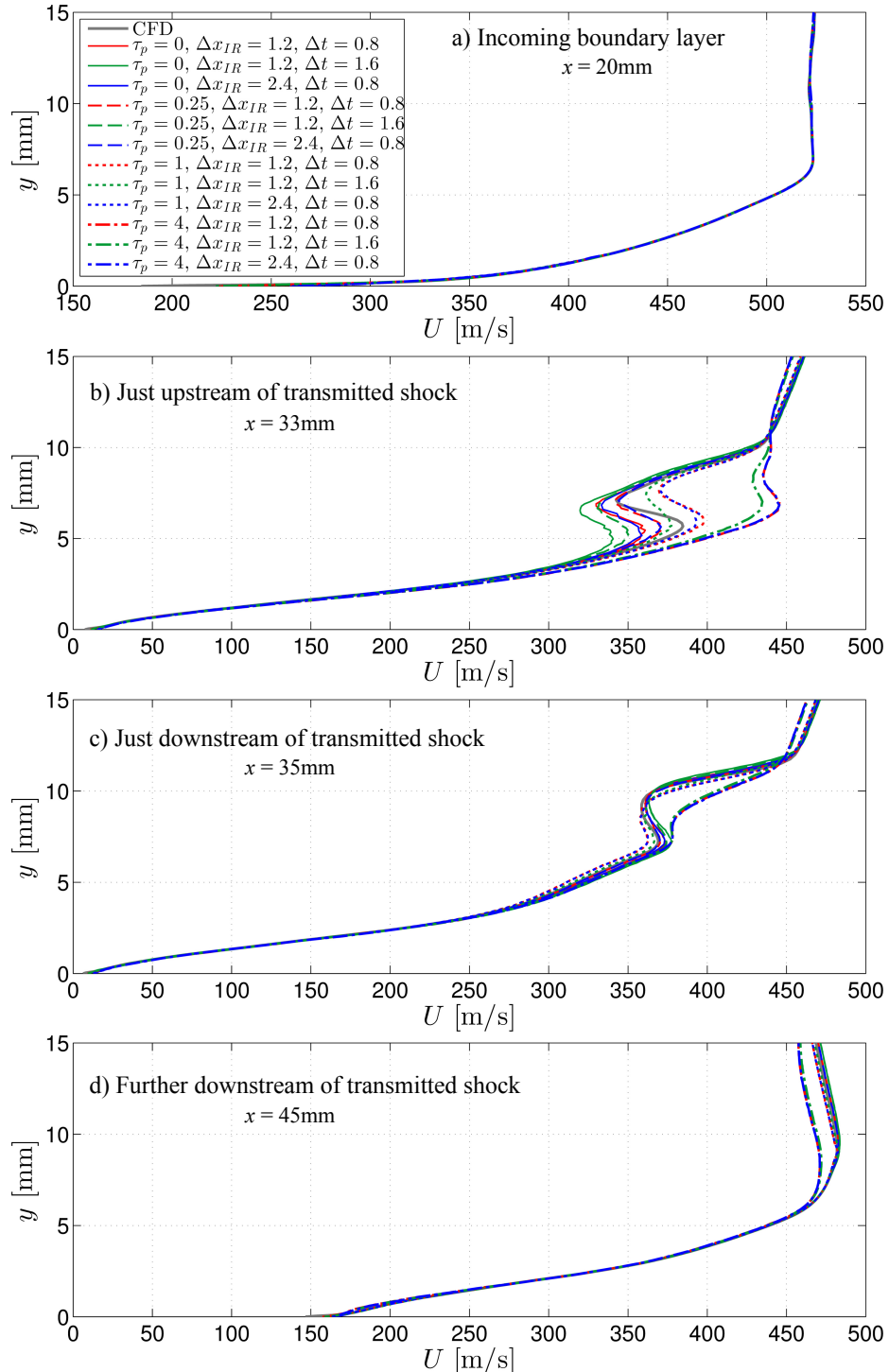


Figure 5.25: Mean streamwise velocity profiles showing simulated PIV biases in the incident shock region for the  $h_{\text{ramp}}/\delta_0 = 0.56$  test case.

relaxation time,  $\tau_p$ , and the time between PIV image exposures,  $\Delta t$ . The comparisons shown in panels (b) and (c) of Figures 5.24 and 5.25 represent the extreme case where the convective acceleration terms are very large in magnitude due to the Mach stem and transmitted shock. In most other regions of the flow, the magnitudes of the velocity biases are significantly smaller. Notably, the regions close to the bottom wall ( $y < 7\text{mm}$  for  $h_{\text{ramp}}/\delta_0 = 0.93$  and  $y < 2.5\text{mm}$  for  $h_{\text{ramp}}/\delta_0 = 0.56$ ) are largely unaffected by the addition of simulated PIV bias sources.

#### 5.4.2 Comparisons to PIV data

Now that the signs and approximate magnitudes of bias errors incurred due to varying PIV parameters  $\tau_p$ ,  $\Delta t$ , and  $\Delta x_{IR}$  are understood, comparisons between PIV data and the baseline and modified CFD results are presented. The modified CFD results shown in this section use the nominal experimental values of  $\Delta x_{IR} = 0.12\text{mm}$  and  $\Delta t = 0.8\mu\text{s}$ . Results from  $\tau_p = 0, 0.25, 1$ , and  $4\mu\text{s}$  are shown for comparison because changing  $\tau_p$  has the greatest effect on the velocity bias. The actual assessment of the agreement between the PIV data and the simulation results should be made by comparing the PIV data profiles to the  $\tau_p = 1\mu\text{s}$  profiles.

Figure 5.26 shows the unmodified CFD and PIV mean velocity fields for  $h_{\text{ramp}}/\delta_0 = 0.56$  with profile locations 1 – 6 superimposed. Qualitatively, the overall structure of the flow is captured quite well by the CFD. There is a slight shift of all of the features in the streamwise direction between the CFD and PIV cases. Therefore, the profile locations are referenced to the shock crossing point in each case. This is the same type of streamwise shift that was made in Chapter 4 to compare the overall flow structures between different perturbed cases. The velocity profile locations are selected throughout the decelerating and accelerating portions of the SBLI.

Profile comparisons for the  $h_{\text{ramp}}/\delta_0 = 0.56$  case at stations 1 – 6 are shown in Figure 5.27. At station 1, the profiles show good qualitative agreement, but the

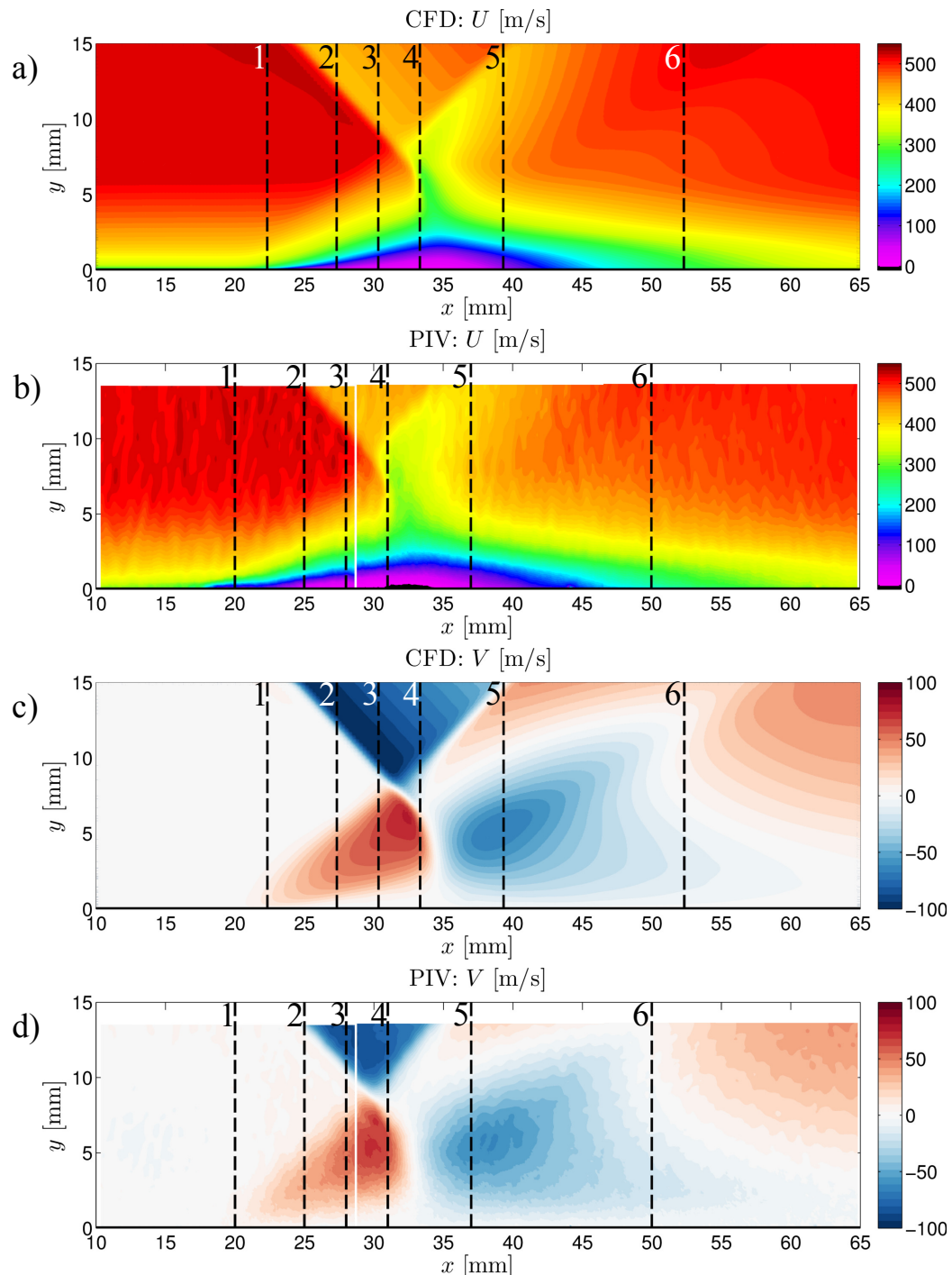


Figure 5.26: Side-by-side comparison of mean velocity surface plots for the unmodified CFD and PIV datasets ( $h_{\text{ramp}}/\delta_0 = 0.56$ ).

boundary layer is slightly thicker for the PIV data than for any of the modified or unmodified CFD cases. The asymptotic velocity is well matched. At station 2, the profile agreement is very good for  $y < 12\text{mm}$ . However, above  $y = 12\text{mm}$ , the profiles deviate where they intersect the incident shock wave. In the PIV data, this shock wave is displaced further from the bottom wall than in the CFD simulations. The vertical position of the shock crossing point is also pushed  $\approx 1.5\text{mm}$  further from the bottom wall in the PIV data as compared to the CFD results.

At station 3, the agreement between PIV and CFD is again excellent except for the vertical displacement of the incident shock feature, which cannot be accounted for strictly by PIV measurement bias. At stations 2 and 3, the  $\tau_p = 4\mu\text{s}$  profiles appear to match the location of the incident shock wave in the PIV data better than any of the other CFD profiles. This is a coincidence, and it should also be noted that the  $\tau_p = 4\mu\text{s}$  predict excessively full boundary layer profiles, which leads to worse agreement lower in the boundary layer.

The comparison at station 4 shows the same displacement of the shock feature as in 2 and 3; however at this location the modified CFD profile for  $\tau_p = 1\mu\text{s}$  indicates that a larger portion of the mismatch between  $y = 4\text{mm}$  and  $y = 10\text{mm}$  may be due to PIV bias errors. Stations 5 and 6 show the beginning of the boundary layer recovery in the accelerating part of the SBLI. The qualitative profile shapes are very similar, but there is a systematic difference where the PIV profiles show consistently lower velocities than the CFD results. This may indicate that the overall strength of the SBLI is slightly higher for the PIV measurements than for the simulations, leading to lower overall velocities downstream of the shock waves.

The profile comparisons presented here indicate that there are true physical differences between the PIV and CFD, and that the discrepancies cannot be attributed solely to biases inherent in the measurement technique. Still, the CFD and modified CFD profiles show a remarkable ability to capture the correct profile shapes

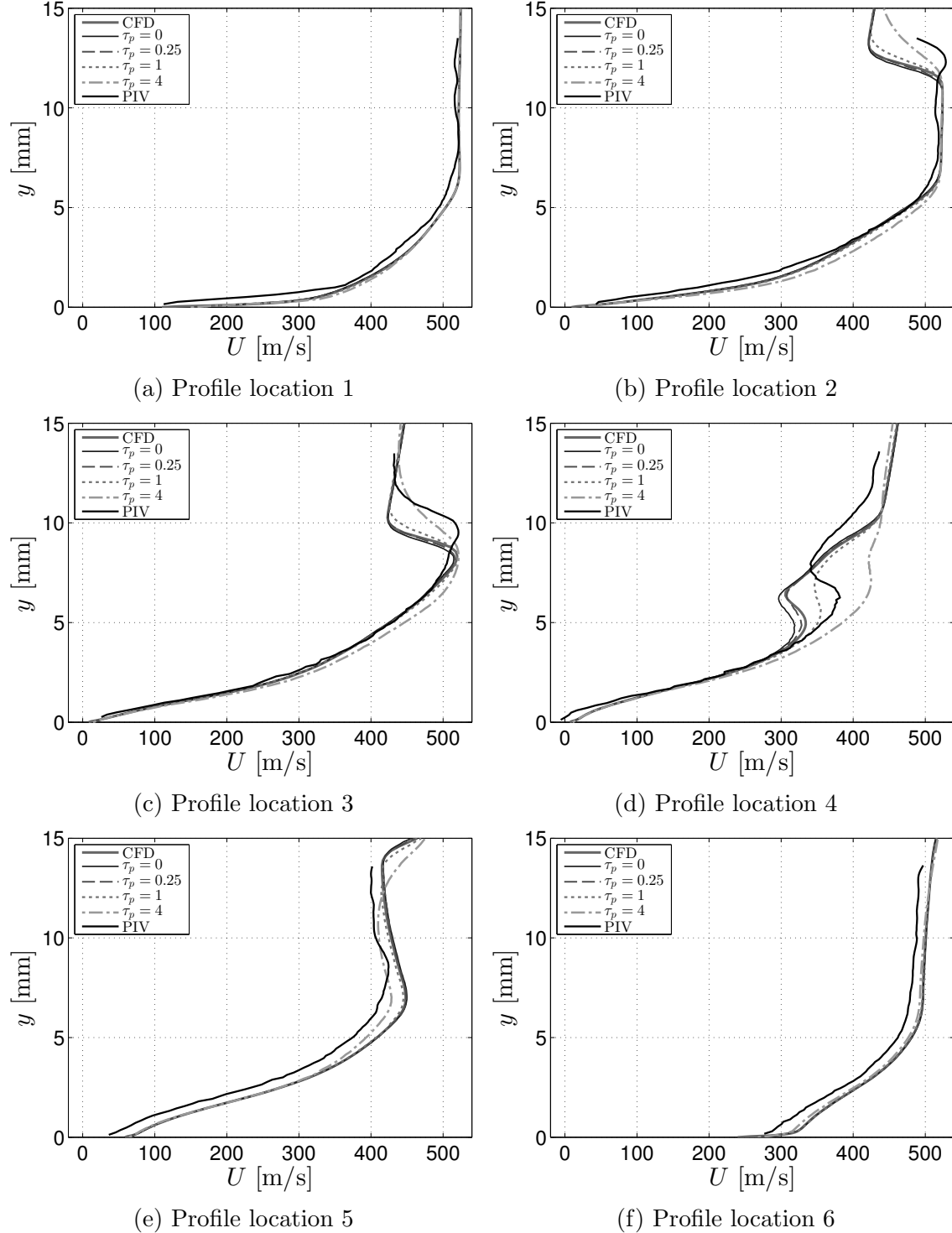


Figure 5.27: Comparison of mean streamwise velocity profiles for CFD, modified CFD, and PIV data for  $h_{\text{ramp}}/\delta_0 = 0.56$  incident shock region. The modified CFD profiles simulate PIV bias errors using nominal  $\Delta t = 0.8\mu\text{s}$  and  $\Delta x_{IR} = \Delta y_{IR} = 0.12\text{mm}$  with varying  $\tau_p$ .

throughout the full streamwise extent of the interaction, particularly given the complex physics and highly non-equilibrium character of the boundary layer. Depending on the desired application, these CFD results may provide sufficient accuracy to be of practical use. If the CFD results are deemed trustworthy, then they can be used to explore flow features and quantities that cannot be measured in experiments. The CFD and experimental results can then be jointly leveraged to facilitate better understanding of the flow physics involved.

Figure 5.28 shows color contour plots of mean velocity in the  $h_{\text{ramp}}/\delta_0 = 0.93$  test case for the PIV and unmodified CFD results. There are some notable discrepancies that are apparent in the surface plots. The Mach stem is considerably larger and occurs further upstream and further from the bottom wall in the PIV data. There is also a significantly larger region of mean flow reversal (black area) in the PIV data, and it begins further upstream relative to the Mach stem location. Despite the discrepancies in the sizes and locations of these features, the overall flow patterns share a very similar overall character qualitatively.

Six profile locations are superimposed throughout the interaction zone. These profiles are positioned at constant distances relative to the Mach stem. This is analogous to the shift based on the shock crossing point for the previous profile comparisons, and it allows for a better direct comparison of the features within the interaction.

To assess the discrepancies in more detail and to evaluate their magnitudes relative to any potential biases due to PIV parameter choices, profile plots at stations 1–6 are shown in Figure 5.29. The incoming boundary layer profiles at station 1 show excellent agreement. Upstream of the Mach stem at station 2, there are a few discrepancies between the PIV and CFD. First, there is a larger velocity deficit and reversed flow for the PIV data as compared to any of the CFD profiles below  $y = 8\text{mm}$ . Second, the positions of the separation shock and incident shock are displaced, with the vertical distance between them much larger for the PIV data than the CFD results. The

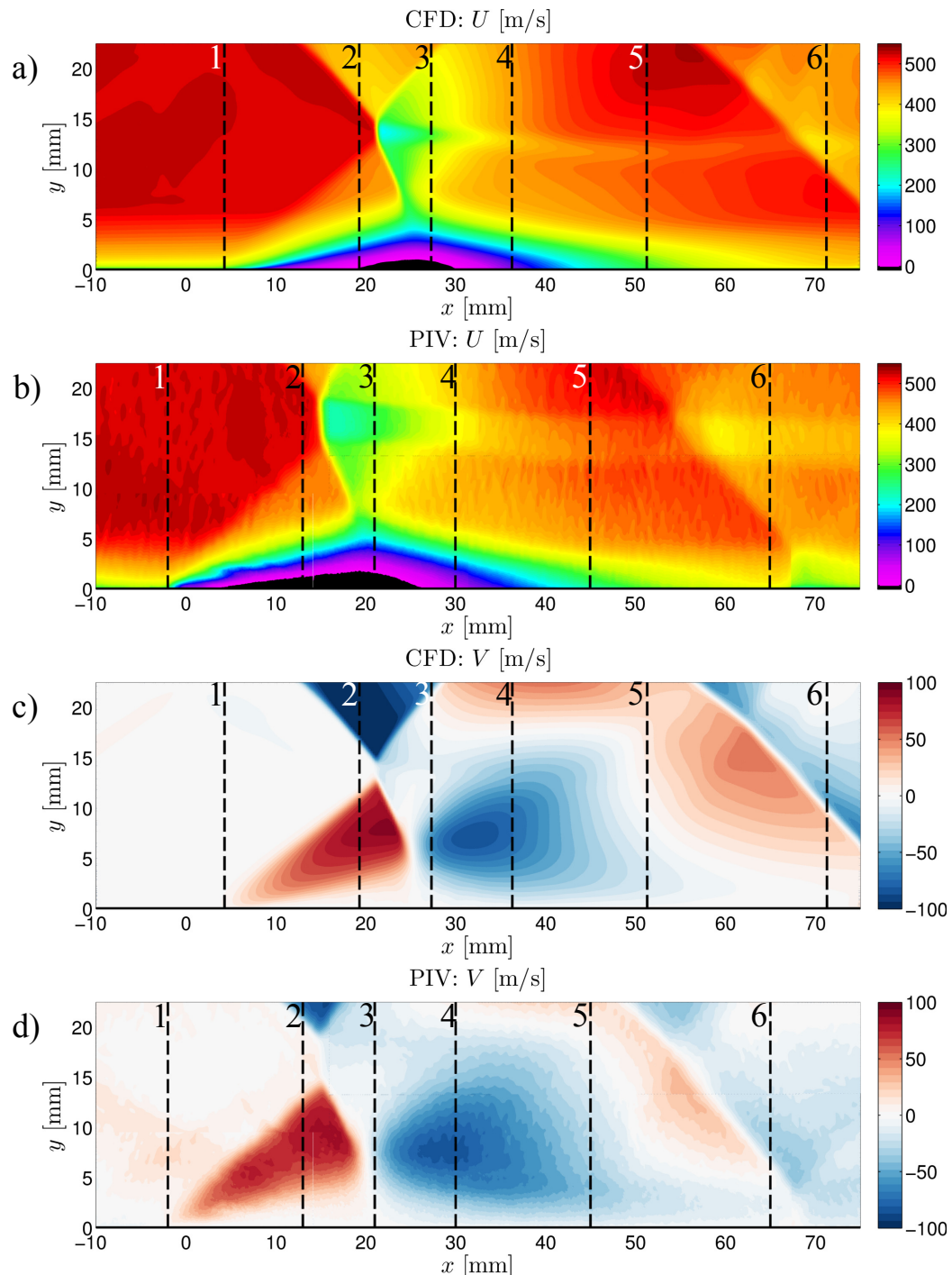


Figure 5.28: Side-by-side comparison of mean velocity surface plots for the unmodified CFD and PIV datasets ( $h_{\text{ramp}}/\delta_0 = 0.93$ ).

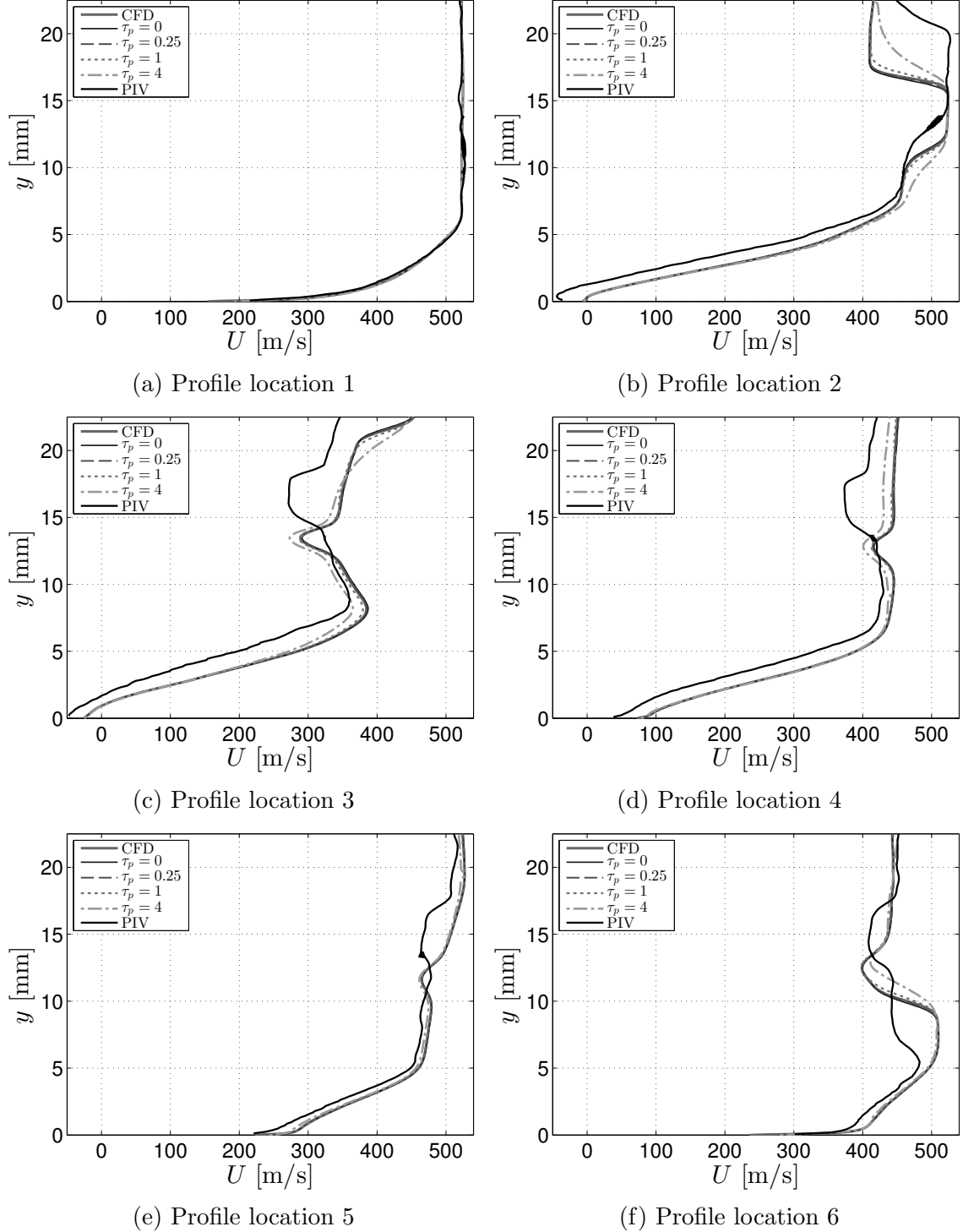


Figure 5.29: Comparison of mean streamwise velocity profiles for CFD, modified CFD, and PIV data for  $h_{\text{ramp}}/\delta_0 = 0.93$  incident shock region. The modified CFD profiles simulate PIV bias errors using nominal  $\Delta t = 0.8\mu\text{s}$  and  $\Delta x_{IR} = \Delta y_{IR} = 0.12\text{mm}$  with varying  $\tau_p$ .

region between the separation and incident shock waves is the portion of the profile that resembles a top hat with the largest streamwise velocity.

The discrepancies noted at station 2 persist downstream of the Mach stem at stations 3 and 4. The velocity deficit below the wake of the Mach stem is higher for the PIV data than the CFD results. The Mach stem wake is also positioned further from the bottom wall and covers a larger region in the PIV data. Similar discrepancies are also visible in the profile comparisons further downstream at stations 5 and 6 where the flow is accelerating. Like in the  $h_{\text{ramp}}/\delta_0 = 0.56$  comparisons, the CFD profiles are consistently fuller than the PIV profiles, indicating that the experiment shows a stronger overall interaction. However, the profile shapes close to the bottom wall are again qualitatively very similar.

Performing velocity profile comparisons between the PIV data and the CFD data modified to account for PIV biases due to  $\tau_p$ ,  $\Delta t$ , and  $\Delta x_{IR}$  provides much more information than simply comparing the PIV data directly to the original CFD results. This method shows which discrepancies may be partially or fully due to measurement errors and which discrepancies are actual physical differences. With this quantitative information, the parameters, models, and inlet/boundary conditions of the CFD code can be modified to attempt to better capture the physics of the experiment.

Furthermore, the simulation of experimental bias error sources using a CFD flow field allows both experimentalists and CFD users to estimate the sizes of biases inherent in the PIV technique. This is helpful in the experimental design stage for evaluating whether or not a particular selection of PIV parameters will yield acceptable results. The methodology and results presented here are intended to help bridge the gap between experiments and simulations and to foster a better understanding of true experimental uncertainties and biases for experimentalists and CFD users alike. Future validations of CFD results against PIV experiments of high speed compressible flows are encouraged to use this type of procedure. Furthermore, if comparisons

between different CFD simulations are to be made, integral metrics (such as the ones described in Chapter 4) that utilize the full PIV dataset for quantitative comparison are suggested.



# Chapter 6

## Conclusions

### 6.1 Effects of shock strength & confinement

PIV measurements are acquired for SBLI flows in a low aspect ratio duct with an  $M_\infty = 2.05$  inlet. In order to gain physical insight into the three-dimensional structure of the flow and provide relevant data for CFD validation, data are acquired in multiple streamwise-vertical planes across the span. These include a plane near the spanwise centerline as well as in four off-center planes, two of which are embedded within the side wall boundary layer. The primary oblique shock wave is generated by a fully-spanning  $20^\circ$  ramp on the top wall of the duct. In the present work, two ramp heights are considered:  $h_{\text{ramp}} = 3\text{mm}$  and  $5\text{mm}$  ( $h_{\text{ramp}}/\delta_0 = 0.56$  and  $0.93$ , respectively). These results are compared to the  $h_{\text{ramp}} = 1.1\text{mm}$  ( $h_{\text{ramp}}/\delta_0 = 0.20$ ) data of Helmer (2011). The experimental geometry and parameters other than ramp height are maintained constant between all three cases.

For each case, the PIV measurement domain includes two SBLIs – one near the foot of the compression ramp where the shock wave is generated, and another in the vicinity of the first reflection of the shock wave on the opposite wall. The strength of the primary oblique shock wave increases with increasing ramp height, despite the

fact that all of the ramps are inclined at the same angle to the incoming flow. This is because the ramps are embedded in the incoming boundary layer on the top wall. Therefore the properties of the shock wave in the core of the flow are coupled to the viscous effects at the foot of the ramp where compression waves coalesce into a shock. For all three test geometries, the angle of the incident shock wave is shallower than the  $-52^\circ$  predicted by 2D inviscid theory for a  $M_\infty = 2.05$  air flow impinging on a surface inclined at  $20^\circ$ .

In both the small and medium ramp geometries, no mean flow reversal is observed near the foot of the compression ramp. The maximum probability of instantaneous flow reversal in the medium ramp case ( $h_{\text{ramp}}/\delta_0 = 0.56$ ) is  $\approx 53\%$ , which is significantly greater than the maximum probability of flow reversal for the smaller ramp geometry investigated by Helmer (2011). In the large ramp geometry ( $h_{\text{ramp}}/\delta_0 = 0.93$ ), the SBLI associated with the compression ramp includes a small region where the flow is reversed on average. In this region the maximum probability of instantaneous flow reversal is  $\approx 79\%$ . In all of the test geometries, no mean flow reversal is observed in the planes closer to the side wall, and the probability of observing instantaneously reversed flow decreases as the distance to the side wall is decreased.

A regular reflection of the shock wave occurs for the small and medium ramp cases. In the large ramp case a Mach reflection occurs instead. This phenomenon involves a nearly normal shock wave – the Mach stem – located in the core of the duct. A significant region of subsonic flow exists downstream of the Mach stem. This flow is re-accelerated to supersonic speed by the faster surrounding fluid; however a noticeable wake persists to the downstream extent of the measurement domain. The shear layers at the edges of the wake are marked by regions of relatively high streamwise velocity fluctuations. The Mach stem is only present near the core of the duct; the data planes closer to the side wall do not include this feature.

Confinement of the flow is caused by the thickening of the boundary layers on all

four walls of the duct. The streamwise-vertical PIV data planes explicitly show that the thickening of the top and bottom wall boundary layers is significantly more severe as the shock strength is increased due to increasing ramp height. Comparison of the off-center data planes between each of the three test cases shows that the side wall boundary layers are also significantly more distorted as the shock strength increases. This results in significantly higher levels of blockage for the largest ramp case as compared to the smaller two ramp geometries.

Bermejo-Moreno et al. (2014) performed two wall-modeled large eddy simulations of the largest ramp geometry presented here. One of the simulations treated the side walls as no-slip surfaces upon which boundary layers would grow, and the other treated the side walls using spanwise periodic boundary conditions. The differences between the two cases were drastic; a Mach stem was predicted for the case with more realistic no-slip side walls, but not for the case with spanwise periodic boundary conditions. Therefore, it is evident that the degree of confinement and blockage caused by the thickening of the side wall boundary layers plays a significant role in determining the overall characteristics of the whole SBLI flow field. This is particularly important for realistic low-aspect ratio geometries, and highlights the importance of collecting experimental data in off-centerline locations for validation of 3D simulations.

In the incident shock interaction region, mean flow reversal is observed on the bottom wall near the spanwise centerline of the duct in both the  $h_{\text{ramp}}/\delta_0 = 0.56$  and  $0.93$  cases. This causes a blockage near the center of the duct, forcing higher momentum fluid to divert upward and toward the side walls, energizing the bottom wall boundary layer at locations away from the spanwise centerplane. This is consistent with the lesser degree of boundary layer thickening and lack of mean flow reversal observed away from the centerline in both ramp cases. While the boundary layer thickening is most severe near the centerline, the re-acceleration of the flow downstream of the reflected shock wave is also strongest in this plane, leading to faster boundary layer

recovery. The size of the mean flow reversal is significantly larger for the stronger interaction produced by the larger ramp.

Throughout the incident SBLI for the  $h_{\text{ramp}}/\delta_0 = 0.93$  case, the maximum values of  $u'$  occur at approximately the same locations as where the mean velocity profiles exhibit inflection points. Despite the complexity and compressible nature of this flow, this is the same behavior observed in canonical subsonic boundary layer reattachment and mixing layer flows. The match between location of maximum  $u'$  and the inflection point in the mean velocity profile is verified in both the near-centerline ( $z/\delta_0 = 3.89$ ) and off-centerline ( $z/\delta_0 = 1.02$ ) data planes. Furthermore the shapes of the loci of  $\max u'$  vary significantly across the span of the duct.

The relevant length scales of the various interactions and shock features near the spanwise centerline are extracted from the PIV measurements. The non-dimensional shock excursion lengths,  $L_{ex}/\delta_0$ , are found to be small relative to other studies in the literature, indicating that the shock features in the present experiments exhibit less unsteadiness. Furthermore, for the reflected shock wave, no dependence of  $L_{ex}/\delta_0$  on the strength of the incident shock wave or degree of boundary layer separation is noted.

The experiments are designed and conducted specifically with the intent of using the resulting data for validation of CFD simulations of complex three-dimensional non-equilibrium flows. Both the mean velocity and turbulence statistics indicate that the SBLIs in these low aspect ratio ducts are highly three-dimensional. In the case of the largest ramp geometry, there is no nominally two-dimensional region near the spanwise centerline. In order to accurately capture the effects imposed by the confinement and thickening of side wall boundary layers, CFD simulations of these flows must include adequate treatment of all four walls of the duct. The detailed mean and turbulence measurements over a large region of the flow at several stations across the span of the duct provide physical insight into the shock and interaction

structures, as well as a wealth of information for detailed CFD validation.

## 6.2 Effects of geometric perturbations

The objectives of the UQ experiment are to quantitatively document the sensitivity of the incident shock interaction to a large number of small, steady, geometric perturbations and to produce a high quality experimental dataset suitable for validation of CFD simulations. The experiments are carried out in the same  $h_{\text{ramp}}/\delta_0 = 0.20$  test section as used by Helmer (2011), with a modification to allow bumps to be introduced in the bottom wall surface.

A total of 45 different perturbations ranging in height from  $h_{\text{bump}} = 0.1$  to 0.9mm are set in the bottom wall at streamwise locations in the range  $x_{\text{bump}} \in [-80, -40]$ mm. The downstream shock features are extremely sensitive to even the smallest perturbations located within a narrow range of streamwise position from  $x_{\text{bump}} = -69$ mm to  $x_{\text{bump}} = -48$ mm. The flow is largely insensitive to perturbations of all sizes placed outside this region.

The most notable effect caused by the addition of perturbations in the sensitive region is their tendency to force the whole SBLI to shift upstream. The streamwise shift in the position of the shock crossing point for each case relative to its location in the unperturbed case,  $\Delta x_{\text{scp}}$ , is extracted as a quantity of interest for CFD validation. The dependence of  $\Delta x_{\text{scp}}$  on  $h_{\text{bump}}$  and  $x_{\text{bump}}$  is modeled by a 2D polynomial fit to the experimental data.

An integral metric,  $\Lambda$ , is defined and used to quantify the size of the differences between the perturbed and unperturbed flow fields.  $\Lambda$  represents the average difference in velocity magnitude over a user-defined region of interest. If the perturbed flow fields are shifted such that the shock crossing point in each case is aligned with the shock crossing point in the unperturbed case,  $\Lambda$  is greatly reduced. Furthermore,

\Lambda and  $\Delta x_{\text{scp}}$ .

Profiles of mean streamwise and wall-normal velocities are presented at various streamwise positions (relative to  $x_{\text{scp}}$ ) throughout the interaction. The maximum and minimum velocity profiles as well as median and average profiles are plotted at each location. These statistics give quantitative bounds on the changes in local velocity that can be induced by the addition of geometric perturbations in the inflow. A CFD validation based on these data should include an analysis of the agreement between the simulation and experiment using quantitative metrics such as  $\Lambda$  and  $\Delta x_{\text{scp}}$  as well as velocity profile comparisons.

### 6.3 PIV measurement biases for SBLI flows

A methodology for quantitative comparisons between PIV measurements and CFD results for high speed compressible flows is presented. PIV bias error sources are modeled and propagated through an SBLI flow field predicted by CFD. Then the modified CFD flow field which accounts for the biases in the measurement technique is directly compared to the PIV data. This framework has the additional benefit of providing information on the spatial non-uniformity of the PIV bias errors as well as how they may be mitigated or increased by varying the experimental parameters. The effects of finite particle size and inertia, size and overlap of PIV interrogation regions, and particle travel between PIV image exposures are considered.

Finite particle inertia causes particle trajectories to differ from fluid streamlines, particularly in the direct vicinity of shock and expansion fan features where the magnitudes of the convective acceleration terms are very large. The mismatch between the particle and fluid velocity fields is exacerbated by using particles with larger time constant,  $\tau_p$ . The effect on the measured velocity field is that shock waves appear

downstream of their physical locations and the velocity gradients are smeared in the streamwise direction. The magnitude of this effect increases with increasing shock strength.

The actual resolution of a PIV measurement is simulated by accounting for the full area that influences the velocity assigned to a particular cell in the PIV grid. This area includes the size of the interrogation window as well as the area swept out by particle trajectories originating inside that interrogation window over the time  $\Delta t$  between image exposures. For high speed flows, the distance traveled by particles between image frames can be significant, and may even exceed the size of the interrogation window. When coupled with the effects of particle inertia, the modeling of the true PIV resolution may cause either positive or negative velocity biases in the vicinity of the shock wave. The results are much more sensitive to changes in  $\Delta t$  than to changes in the interrogation region size,  $\Delta x_{IR}$ . An optimal selection of PIV parameters will strike a balance between mitigating these biases while still achieving a large dynamic range of pixel displacements and using particles large enough to scatter sufficient laser light for imaging.

The simulations of PIV biases using the CFD data predict large errors in the direct vicinity of shock waves, but relatively small errors elsewhere in the field. For the PIV parameters used in the present experiments, only minimal errors are predicted in regions of boundary layer thickening, separation, and reattachment. Users of PIV datasets should exercise caution when interpreting PIV data directly downstream of a strong shock feature where the experimental biases may be large.

CFD simulations of the  $h_{ramp}/\delta_0 = 0.56$  and  $h_{ramp}/\delta_0 = 0.93$  test geometries are compared to the PIV databases using the methodology outlined here. The agreement between the modified CFD and PIV is generally good, but there are some discrepancies that are not accounted for by the PIV biases inherent in the experimental dataset, particularly for the larger ramp case with the stronger shocks and larger separated

regions.

This framework is developed to inform both experimentalists and CFD users about biases that arise in all PIV measurements of high speed compressible flows. Future validations of CFD codes and models against PIV databases should follow a similar procedure such that the largest sources of PIV bias are removed from the comparisons between PIV and CFD results. This requires close cooperation between experiments and simulations as well as thorough documentation of experimental parameters so the experimental biases may be accurately modeled.

## 6.4 Recommendations for future work

The present work has provided quantitative documentation of the three-dimensional nature of two SBLI flows in low aspect ratio test geometries, as well as the sensitivity of an SBLI to perturbations in the upstream boundary conditions. Recommendations for further work are summarized below.

- The present UQ experiment for SBLIs could be expanded to include the effects of geometric perturbations on the flow in off-center planes. It could also be repeated for the larger ramp cases ( $h_{\text{ramp}}/\delta_0 = 0.56$  and  $0.93$ ) in order to determine whether the larger interactions demonstrate stronger or weaker sensitivity to the same set of perturbations. Future experiments that apply the idea behind the UQ experiment – testing sensitivity to a wide range of well defined inlet and/or boundary condition perturbations – to other types of flows are also encouraged. These studies could be extremely useful in providing both physical insight and validation data for a wide range of flow applications, particularly in cases of incipiently or fully separated flows.
- For the unperturbed SBLI flows presented here, PIV measurements could be

made in additional streamwise-vertical planes or in streamwise-spanwise oriented planes at varying heights from the bottom wall. These measurements would provide further information on the spanwise non-uniformity of the bottom wall boundary layer separation induced by the incident/reflected shock interaction. They could also supply additional evidence of the confinement caused by separation of the side wall boundary layers as well as more data for CFD validation. PIV measurements in streamwise-spanwise planes may be more challenging and less accurate than PIV measurements in streamwise-vertical planes due to the large vertical velocities associated with the shock and expansion fan features. However, the effects of particle loss between image pairs due to out-of-plane velocity could be added to the PIV bias simulations in order to help account for these challenges.

- The simulations of PIV bias errors could be expanded to allow for more accurate modeling of the particle velocity field. In the case of LES or DNS, the particle simulations could be embedded in the original computations, allowing the particle trajectories to evolve in the instantaneous flow as opposed to propagating them through only the mean field. This method would be more computationally expensive, but would also allow any biases on the velocity statistics ( $u'$ ,  $v'$ , and  $\langle u'v' \rangle$ ) to be explored. Additionally, a higher fidelity model for the particle drag can be used to improve the accuracy of the computations in regions where the particle slip velocities are large, leading to  $Re_p > 1$ .
- Future validations of CFD codes against the experimental database provided here are highly encouraged. The data set described in Appendix B is available by contacting Professor John Eaton at Stanford University. It is hoped that the detailed velocity and turbulence measurements provided for simple low-aspect ratio SBLIs will aid in the improvement of models and methods for accurately

simulating the complex non-equilibrium flow phenomena involved in these test cases.

# Appendix A

## Characterization & Modeling of Perturbation Shapes

### A.1 Confocal microscopy

The detailed shapes of individual bumps and two-bump configurations are characterized using a series of high resolution confocal microscopy measurements. Images are captured on a  $1280 \times 1024$  pixel CCD camera using a  $10\times$  objective, resulting in a physical resolution of  $1.15 \mu\text{m}/\text{pixel}$  in the in-plane directions. The out-of-plane spacing between successive images in a set is  $4\mu\text{m}$ . Sample raw images of the peak of a single bump are shown in Figure A.1. Due to the high in-plane resolution of the measurements, data from several different camera positions are stitched together to provide a composite representation over a region extending from the peak of a bump to the flat surrounding surface.

The raw data are reconstructed to represent the perturbation surfaces using a set of custom written Matlab codes. The reconstructed surfaces of two different bump configurations are shown in Figure A.2. Note that the axis scales are not equal so the shapes appear slightly skewed.

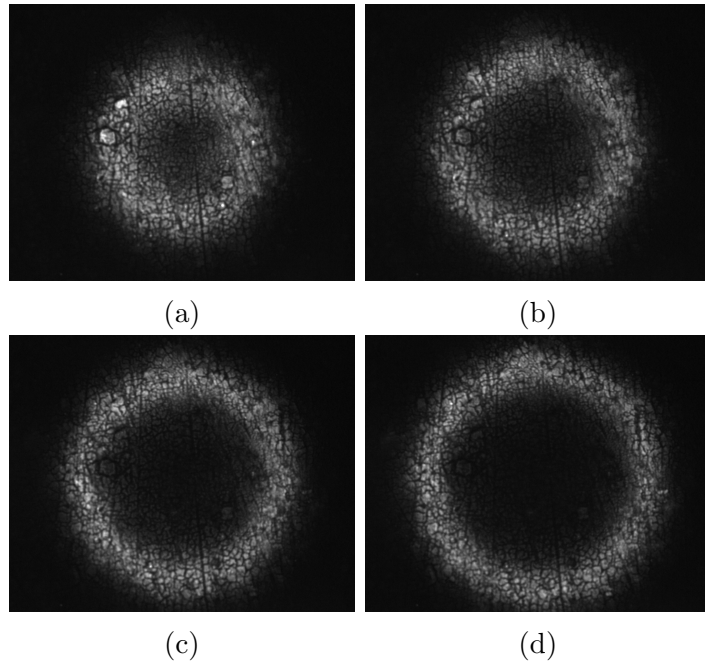


Figure A.1: Samples from a sequence of confocal microscopy images showing the peak of a single bump. The images represent horizontal "slices" at vertical positions spaced  $4\mu\text{m}$  apart.

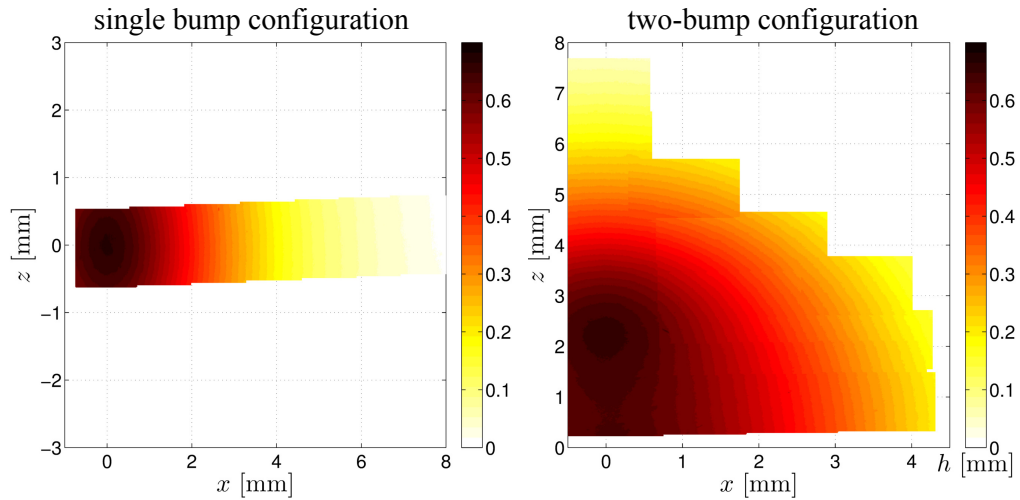


Figure A.2: Surface reconstruction from confocal microscopy data for a single bump (left) and two-bump configuration (right). The two-bump configuration is achieved by raising two neighboring screws (spaced by 4.5mm in the  $z$  direction) to equal heights. The single bump surface is axisymmetric and the two-bump configuration is symmetric across both the  $x$  and  $z$  axes.

Table A.1: Coefficients for 5th order polynomial fits to single bump profiles of varying heights.

screw turns	$h_{\text{bump}}$ [mm]	$a_5$ [mm $^{-4}$ ]	$a_4$ [mm $^{-3}$ ]	$a_3$ [mm $^{-2}$ ]	$a_2$ [mm $^{-1}$ ]	$a_1$ [-]	$a_0$ [mm]
0.5	0.11	4.982e-3	-0.04020	0.12426	-0.16491	0.02815	0.11038
1.0	0.28	1.111e-4	-0.00232	0.01785	-0.05448	-0.00326	0.27854
1.5	0.48	8.540e-5	-0.00214	0.01925	-0.06577	-0.01760	0.47433
2.0	0.66	1.159e-4	-0.00284	0.02541	-0.08849	-0.01867	0.65533
2.5	0.89	7.456e-5	-0.00217	0.02301	-0.09524	-0.01102	0.88406

## A.2 Polynomial & Gaussian fits for single bumps

Profiles of the axisymmetric single bump shapes are extracted from the reconstructed surfaces of the confocal microscopy images. These profiles are shown in Figure 4.4 of chapter 4. The profiles can be reasonably approximated by either fifth-order polynomial or Gaussian fits of the forms:

$$h_{\text{poly5}}(z) = a_5 z^5 + a_4 z^4 + a_3 z^3 + a_2 z^2 + a_1 z + a_0 \quad (\text{A.1})$$

$$h_{\text{gauss}}(z) = A \exp\left(\frac{-(z - z_0)^2}{2\sigma^2}\right) \quad (\text{A.2})$$

The optimum coefficients  $\mathbf{a} = [a_0, a_2, \dots, a_5]$  for the polynomial fits are determined using Matlab's `polyfit` function. This routine optimizes the coefficients in a least squares sense such that the cost function  $S = \sum_{i=1}^N (h(z_i) - h_{\text{poly5}}(z_i, \mathbf{a}))^2$  is minimized. These coefficients are listed in Table A.1 for each of the five bump heights tested.

For the Gaussian approximations, the peak height of the bump,  $A$ , is defined directly from the measured heights. With  $A$  fixed, the parameter  $\sigma$  is optimized in the least squares sense such that the cost function  $S = \sum_{i=1}^N (h(z_i) - h_{\text{gauss}}(z_i, \sigma))^2$  is minimized. Table A.2 lists the optimum parameters for each of the five bump heights tested.

Table A.2: Parameters for Gaussian fits to single bump profiles of varying heights.

screw turns	$h_{\text{bump}}$ [mm]	$A$ [mm]	$\sigma$ [mm]
0.5	0.11	0.110	0.988
1.0	0.28	0.280	2.089
1.5	0.48	0.475	2.367
2.0	0.66	0.655	2.446
2.5	0.89	0.886	2.778

### A.3 Modeling a spanwise row of 5 bumps

Given the good agreement of both the Gaussian and fifth-order polynomial fits to the single-bump data, it is reasonable to model the larger spanwise row of bumps using a piecewise combination of these functions. The five peaks across the span are each modeled using Gaussian distributions with the parameters  $A$  and  $\sigma$  as determined for the single bump configurations of the appropriate height. The valleys in between are modeled using fifth order polynomial splines. The constraints used to define these splines are:

- match the values at the endpoints:

$$h_{\text{poly5}}(z_L) = h_{\text{gauss}}(z_L) = A \exp\left(\frac{-(z_L - z_{\text{peak}})^2}{2\sigma^2}\right) \quad (\text{A.3})$$

$$h_{\text{poly5}}(z_R) = h_{\text{gauss}}(z_R) = A \exp\left(\frac{-(z_R - z_{\text{peak}})^2}{2\sigma^2}\right) \quad (\text{A.4})$$

- match the first derivatives at the endpoints:

$$h'_{\text{poly5}}(z_L) = h'_{\text{gauss}}(z_L) = \frac{-(z_L - z_{\text{peak}})}{\sigma^2} h_{\text{gauss}}(z_L) \quad (\text{A.5})$$

$$h'_{\text{poly5}}(z_R) = h'_{\text{gauss}}(z_R) = \frac{-(z_R - z_{\text{peak}})}{\sigma^2} h_{\text{gauss}}(z_R) \quad (\text{A.6})$$

- set the value at the midpoint to the minimum measured height

$$h_{\text{poly5}}(z_M) = h_{\min,\text{meas.}} \quad (\text{A.7})$$

- set the slope at the midpoint to zero

$$h'_{\text{poly5}}(z_M) = 0 \quad (\text{A.8})$$

The coefficients for each of the fifth order polynomial splines are determined by solving the following matrix equation for  $\mathbf{a} = [a_5, a_4, a_3, a_2, a_1, a_0]^T$ :

$$\mathbf{M}\mathbf{a} = \mathbf{b} \quad (\text{A.9})$$

where:

$$\mathbf{M} = \begin{bmatrix} z_L^5 & z_L^4 & z_L^3 & z_L^2 & z_L & 1 \\ z_R^5 & z_R^4 & z_R^3 & z_R^2 & z_R & 1 \\ z_M^5 & z_M^4 & z_M^3 & z_M^2 & z_M & 1 \\ 5z_L^4 & 4z_L^3 & 3z_L^2 & 2z_L & 1 & 0 \\ 5z_R^4 & 4z_R^3 & 3z_R^2 & 2z_R & 1 & 0 \\ 5z_M^4 & 4z_M^3 & 3z_M^2 & 2z_M & 1 & 0 \end{bmatrix}$$

$$\mathbf{b} = [h_{\text{gauss}}(z_L), h_{\text{gauss}}(z_R), h_{\text{gauss}}(z_M), h'_{\text{gauss}}(z_L), h'_{\text{gauss}}(z_R), 0]^T$$

Table A.3 lists the locations where the Gaussian and fifth-order polynomial splines are matched ( $z_L$  and  $z_R$ ), the midpoints ( $z_M$ ), and the minimum measured heights ( $h_{\min,\text{meas.}}$ ) for each of the splines shown in Figure 4.5 of chapter 4.

Table A.3: Spanwise ( $z$ ) coordinates of matching points between Gaussian and 5th order spline fits and measured minimum heights,  $h_{\min,\text{meas}}$ , for each of the 5-bump perturbation configurations. All quantities have units of mm.

$h_{\text{bump}}$	spline #1				spline #2			
	$z_L$	$z_R$	$z_M$	$h_{\min,\text{meas}}$	$z_L$	$z_R$	$z_M$	$h_{\min,\text{meas}}$
0.1	10.25	10.25	10.25	0	19.25	19.25	19.25	0
0.3	7.75	12.75	10.25	0.075	16.75	21.75	19.25	0.075
0.5	7.75	12.75	10.25	0.180	16.75	21.75	19.25	0.180
0.7	7.10	13.40	10.25	0.286	16.10	22.40	19.25	0.490
0.9	7.10	13.40	10.25	0.458	16.10	22.40	19.25	0.852

$h_{\text{bump}}$	spline #3				spline #4			
	$z_L$	$z_R$	$z_M$	$h_{\min,\text{meas}}$	$z_L$	$z_R$	$z_M$	$h_{\min,\text{meas}}$
0.1	24.0	28.0	26.0	0.090	32.75	32.75	32.75	0
0.3	24.0	28.0	26.0	0.260	35.25	30.25	32.75	0.075
0.5	24.0	28.0	26.0	0.450	35.25	30.25	32.75	0.180
0.7	24.0	28.0	26.0	0.628	35.9	29.60	32.75	0.325
0.9	24.0	28.0	26.0	0.853	35.9	29.60	32.75	0.490

## **Appendix B**

### **Experimental database**

The data presented in this thesis may be requested by contacting Prof. John Eaton at Stanford University.

The data from chapter 3 are available as a set of Matlab data files (.mat). A Matlab script that reproduces Figures 3.8 – 3.15 and Figures 3.26 – 3.41 is also available. A detailed readme file describes how to use and plot the data.

The data from chapter 4 are available in three file formats: Matlab (.mat) with associated plotting script, Tecplot (.dat) with associated layout files, and tab-delimited ASCII files. The information from Table 4.4 is available as a Matlab data file or ASCII tab-delimited file. A detailed readme file describes the organization of the files and variables as well as instructions on how to get started using the database.



# Bibliography

- Adamson, T., & Messiter, A. (1980). Analysis of two-dimensional interactions between shock waves and boundary layers. *Annu. Rev. Fluid Mech.*, **12**(1), 103–138.
- Adrian, R., & Westerweel, J. (2011). *Particle Image Velocimetry*. Cambridge University Press.
- Adrian, R. J. (1997). Dynamic ranges of velocity and spatial resolution of particle image velocimetry. *Meas. Sci. Technol.*, **8**, 1393–1398.
- Andreopoulos, J., & Muck, K. (1987). Some new aspects of the shock-wave/boundary-layer interaction in compression-ramp flows. *J. Fluid Mech.*, **180**, 405–428.
- Ardonceau, P., Lee, D., Alziary de Roquefort, T., & Goethals, R. (1980). Turbulence behaviour in a shock wave/boundary layer interaction. In *AGARD-CP-271, paper 8*.
- Babinsky, H., Li, Y., & Pitt Ford, C. W. (2009). Microramp control of supersonic oblique shock-wave/boundary-layer interactions. *AIAA J.*, **47**(3), 668–675.
- Bell, J. H., & Mehta, R. D. (1990). Development of a two-stream mixing layer from tripped and untripped boundary layers. *AIAA J.*, **28**(12), 2034–2042.

- Beresh, S., Clemens, N., & Dolling, D. (2002). Relationship between upstream turbulent boundary-layer velocity fluctuations and separation shock unsteadiness. *AIAA J.*, **40**(12), 2412–2422.
- Bermejo-Moreno, I., Campo, L., Larsson, J., Bodart, J., Helmer, D., & Eaton, J. (2014). Confinement effects in shock wave/turbulent boundary layer interactions through wall-modeled large-eddy simulations. *J. Fluid Mech.*, *in revision*.
- Bisek, N. J., Rizzetta, D. P., & Poggie, J. (2013). Plasma control of a turbulent shock boundary-layer interaction. *AIAA J.*, **51**(8), 1789–1804.
- Bogdonoff, S. (1955). *Some experimental studies of the separation of supersonic turbulent boundary layers*. Ph.D. thesis, Princeton University.
- Bookey, P., Wyckham, C., & Smits, A. (2005). Experimental investigations of Mach 3 shock-wave turbulent boundary layer interactions. In *35th AIAA Fluid Dynamics Conference*. Toronto, Ontario Canada, 6-9 June 2005.
- Bruce, P. J. K., & Babinsky, H. (2012). Experimental study into the flow physics of three-dimensional shock control bumps. *J. Aircraft*, **49**(5), 1222–1233.
- Brusniak, L., & Dolling, D. (1994). Physics of unsteady blunt-fin-induced shock wave/turbulent boundary layer interactions. *J. Fluid Mech.*, **273**, 375–409.
- Bur, R., Corbel, B., & Déler, J. (1998). Study of passive control in transonic shock wave/boundary-layer interaction. *AIAA J.*, **36**(3), 394–400.
- Burton, D. M. F., & Babinsky, H. (2012). Corner separation effects for normal shock wave/turbulent boundary layer interactions in rectangular channels. *J. Fluid Mech.*, **707**, 287–306.

- Campo, L., Helmer, D., & Eaton, J. (2012). Validation experiment for shock boundary layer interactions: Sensitivity to upstream geometric perturbations. In *14th AIAA Non-Deterministic Approaches Conference*. Honolulu, HI, 23-26 April 2012.
- Chapman, D. R., Kuehn, D. M., & Larson, H. K. (1958). Investigation of separated flows in supersonic and subsonic streams with emphasis on the effect of transition. Report, NACA.
- Christensen, K. T. (2004). The influence of peak-locking errors on turbulence statistics computed from PIV ensembles. *Exp. Fluids*, **36**(3), 484–497.
- Chyu, W. J., Rimlinger, M. J., & Shih, T. I. P. (1995). Control of shock-wave/boundary-layer interactions by bleed. *AIAA J.*, **33**(7), 1239–1247.
- Clemens, N. T., & Narayanaswamy, V. (2014). Low-frequency unsteadiness of shock wave/turbulent boundary layer interactions. *Annu. Rev. Fluid Mech.*, **46**(1), 469–492.
- Cohen, G., & Motallebi, F. (2008). Influence of the height of vortex generators in the control of shock induced separation of the boundary layers. *Aeronaut. J.*, **112**(1133), 415–420.
- Colliss, S., Babinsky, H., Nubler, K., & Lutz, T. (2013). Vortical structures on three-dimensional shock control bumps. In *51st AIAA Aerospace Sciences Meeting*. Grapevine, TX, 7-10 Jan 2013.
- Davis, D., & Gessner, F. (1989). Further experiments on supersonic turbulent flow development in a square duct. *AIAA J.*, **27**(8), 1023–1030.
- Davis, D., Gessner, F., & Kerlick, G. (1986). Experimental and numerical investigation of supersonic turbulent flow through a square duct. *AIAA J.*, **24**(9), 1508–1515.

- Délery, J., & Marvin, J. (1986). Shock-wave boundary layer interactions. Report, AGARD-AG-280.
- Do, H., Im, S.-k., Mungal, M. G., & Cappelli, M. A. (2011). The influence of boundary layers on supersonic inlet flow unstart induced by mass injection. *Exp. Fluids*, **51**(3), 679–691.
- Dolling, D., & Murphy, M. (1983). Unsteadiness of separation shock wave structure in a supersonic compression ramp flowfield. *AIAA J.*, **21**(12), 1628–1634.
- Dolling, D., & Or, C. (1985). Unsteadiness of the shock wave structure in attached and separated compression ramp flows. *Exp. Fluids*, **3**, 24–32.
- Dolling, D. S. (2001). Fifty years of shock-wave/boundary-layer interaction research: what next? *AIAA J.*, **39**(8), 1517–1531.
- Dupont, P., Haddad, C., Ardissonne, J. P., & Debièvre, J. F. (2005). Space and time organisation of a shock wave/turbulent boundary layer interaction. *Aerospace Sci. Technol.*, **9**(7), 561–572.
- Dupont, P., Haddad, C., & Debièvre, J. F. (2006). Space and time organization in a shock-induced separated boundary layer. *J. Fluid Mech.*, **559**, 255–277.
- Dupont, P., Piponnai, S., Sidorenko, A., & Debièvre, J. F. (2008). Investigation by particle image velocimetry measurements of oblique shock reflection with separation. *AIAA J.*, **46**(6), 1365–1370.
- Dussauge, J.-P., Dupont, P., & Debièvre, J.-F. (2006). Unsteadiness in shock wave boundary layer interactions with separation. *Aerospace Sci. Technol.*, **10**(2), 85–91.
- Eagle, W. E. (2012). *An experimental study of three-dimensional inlet shock-boundary layer interactions*. Ph.D. thesis, University of Michigan.

- Eaton, J. K., & Johnston, J. P. (1981). A review of research on subsonic turbulent flow reattachment. *AIAA J.*, **19**(9), 1093–1100.
- Erengil, M., & Dolling, D. (1991). Correlation of separation shock motion with pressure fluctuations in incoming boundary layer. *AIAA J.*, **29**(11), 1868–1877.
- Ferri, A. (1940). Experimental results with airfoils tested in the high-speed tunnel at guidonia. Report, NACA Technical Report No. 946.
- Gaitonde, D. V., Visbal, M. R., Shang, J. S., Zheltovodov, A. A., & Maksimov, A. I. (2001). Sidewall interaction in an asymmetric simulated scramjet inlet configuration. *J. Propul. Power*, **17**(3), 579–584.
- Galbraith, D., Turner, M., Orkwis, P., & Weils, S. (2013). The effect of aspect ratio on a Mach 2.75 shock boundary layer interaction configuration. In *51st AIAA Aerospace Sciences Meeting*. Grapevine, TX, 7-10 Jan 2013.
- Ganapathisubramani, B., Clemens, N. T., & Dolling, D. S. (2007). Effects of upstream boundary layer on the unsteadiness of shock-induced separation. *J. Fluid Mech.*, **585**, 369–394.
- Green, J. (1970). Interactions between shock waves and turbulent boundary layers. *Prog. Aerosp. Sci.*, **11**, 235–340.
- Hadjadj, A., Larsson, J., Morgan, B. E., Nichols, J., & Lele, S. K. (2010). Large-eddy simulation of shock boundary-layer interaction. *Proc. of Center for Turbulence Research Summer Program*, **13**, 141–152.
- Han, D. (2001). *Study of turbulent nonpremixed jet flames using simultaneous measurements of velocity and CH distribution*. Ph.D. thesis, Stanford University.

- Hanada, T., Mitsuhashi, M., & Matsuo, K. (2005). Three-dimensional normal shock-wave/boundary-layer interaction in a rectangular duct. *AIAA J.*, **43**(10), 2182–2187.
- Helmer, D., Campo, L., & Eaton, J. (2011). Sensitivity of a shock-boundary layer interaction to geometric perturbations. In *7th International Symposium on Turbulence and Shear Flow Phenomena*. Ottawa, Canada, 28–31 July 2011.
- Helmer, D. B. (2011). *Measurements of a three-dimensional shock-boundary layer interaction*. Ph.D. thesis, Stanford University.
- Helmer, D. B., Campo, L. M., & Eaton, J. K. (2012). Three-dimensional features of a Mach 2.1 shock/boundary layer interaction. *Exp. Fluids*, **53**(5), 1347–1368.
- Herges, T., Kroeker, E., Elliott, G., & Dutton, C. (2010). Microramp flow control of normal shock/boundary-layer interactions. *AIAA J.*, **48**(11), 2529–2542.
- Holden, H. A., & Babinsky, H. (2005). Separated shock-boundary-layer interaction control using streamwise slots. *Journal of Aircraft*, **42**(1), 166–171.
- Hornung, H., & Robinson, M. (1982). Transition from regular to Mach reflection of shock waves, Part 2: The steady-flow criterion. *J. Fluid Mech.*, **123**, 155–164.
- Hou, Y., Clemens, N., & Dolling, D. (2003). Wide field study of shock induced turbulent boundary layer separation. In *41st AIAA Aerospace Sciences Meeting*. Reno, NV, 6–9 Jan 2003.
- Humble, R. A., Elsinga, G. E., Scarano, F., & van Oudheusden, B. W. (2009). Three-dimensional instantaneous structure of a shock wave/turbulent boundary layer interaction. *J. Fluid Mech.*, **622**, 33–62.

- Humble, R. A., Scarano, F., & Oudheusden, B. W. (2007). Particle image velocimetry measurements of a shock wave/turbulent boundary layer interaction. *Exp. Fluids*, **43**(2-3), 173–183.
- Hunter, L. G., & Reeves, B. L. (1971). Results of a strong interaction, wake-like model of supersonic separated and reattaching turbulent flows. *AIAA J.*, **9**(4), 703–712.
- Ivanov, I., Markelov, G., Kudryavtsev, A., & Gimelshein, S. (1998). Numerical analysis of shock wave reflection transition in steady flows. *AIAA J.*, **36**(11), 2079–2086.
- Ivanov, M., Vandromme, D., Fomin, V., Kudryavtsev, A., Hadjadj, A., & Khotyanovsky, D. (2001). Transition between regular and Mach reflection of shock waves: new numerical and experimental results. *Shock Waves*, **11**, 199–207.
- Kalra, C., Zaidi, S., Shneider, M., & Miles, R. (2009). Shockwave induced turbulent boundary layer separation control with plasma actuators. In *47th AIAA Aerospace Sciences Meeting*. Orlando, FL, 5-8 Jan 2009.
- Kalra, C. S., Zaidi, S. H., Miles, R. B., & Macheret, S. O. (2010). Shock-wave?turbulent boundary layer interaction control using magnetically driven surface discharges. *Exp. Fluids*, **50**(3), 547–559.
- Kistler, A. (1964). Fluctuating wall pressure under a separated supersonic flow. *J. Acoustical Soc. of America*, **36**(3), 543–550.
- Krishnan, L., Sandham, N. D., & Steelant, J. (2009). Shock-wave/boundary-layer interactions in a model scramjet intake. *AIAA J.*, **47**(7), 1680–1691.
- Lapsa, A. (2009). *Experimental study of passive ramps for control of shock-boundary layer interactions*. Ph.D. thesis, University of Michigan.

- Loginov, M., Adams, N. A., & Zheltovodov, A. A. (2007). Shock-wave system analysis for compression-decompression ramp flow. In *5th International Symposium on Turbulence and Shear Flow Phenomena*, vol. 1, (pp. 87–92). Munich, Germany, 27-29 Aug 2007.
- Mattheis, J., Budich, B., & Hickel, S. (2013). Large eddy simulation of the transition process from regular to irregular shock-wave boundary-layer interaction. In *8th International Symposium on Turbulence and Shear Flow Phenomena*. Poitiers, France, 28-30 Aug 2013.
- Mitchell, D., Honnery, D., & Soria, J. (2011). Particle relaxation and its influence on the particle image velocimetry cross-correlation function. *Exp. Fluids*, **51**(4), 933–947.
- Morkovin, M. V. (1962). Effects of compressibility on turbulent flows. In A. J. Favre (Ed.) *Mécanique de la Turbulence*, (pp. 367–380). CNRS.
- Narayanaswamy, V., Raja, L. L., & Clemens, N. T. (2012). Control of a shock/boundary-layer interaction by using a pulsed-plasma jet actuator. *AIAA J.*, **50**(1), 246–249.
- Neiland, V. (1969). On the theory of laminar separation in supersonic flow. *Izv. Akad. Nauk. SSSR, Mech. Zhidk. Gaza*, **4**, 53–57.
- Ogawa, H., Babinsky, H., Pätzold, M., & Lutz, T. (2008). Shock-wave/boundary-layer interaction control using three-dimensional bumps for transonic wings. *AIAA J.*, **46**(6), 1442–1452.
- Piponnau, S. (2009). *Instationnarités dans les décollements compressibles: cas des couches limites soumises à ondes de choc*. Ph.D. thesis, L'Université de Provence.

- Piponnau, S., Dussage, J., Debièvre, J., & Dupont, P. (2009). A simple model for low-frequency unsteadiness in shock-induced separation. *J. Fluid Mech.*, **692**, 87–108.
- Pirozzoli, S., & Bernardini, M. (2011). Direct numerical simulation database for impinging shock wave/turbulent boundary-layer interaction. *AIAA J.*, **49**(6), 1307–1312.
- Pirozzoli, S., Bernardini, M., & Grasso, F. (2010). Direct numerical simulation of transonic shock/boundary layer interaction under conditions of incipient separation. *J. Fluid Mech.*, **657**, 361–393.
- Priebe, S., & Martin, M. (2012). Direct numerical simulation of a reflected-shock-wave/turbulent-boundary-layer interaction. *J. Fluid Mech.*, **699**, 1–49.
- Priebe, S., Wu, M., & Martin, M. P. (2009). Direct numerical simulation of a reflected-shock-wave/turbulent-boundary-layer interaction. *AIAA J.*, **47**(5), 1173–1185.
- Raffel, M., Willert, C., Wereley, S., & Kompenhans, J. (2007). *Particle Image Velocimetry: A Practical Guide*. Springer, 2 ed.
- Raghunathan, S. (1987). Effect of porosity strength on passive shock-wave/boundary-layer control. *AIAA J.*, **25**(5), 757–758.
- Raghunathan, S., & Mabey, D. G. (1987). Passive shock-wave/boundary-layer control on a wall-mounted model. *AIAA J.*, **25**(2), 275–278.
- Reda, D. C., & Murphy, J. D. (1973). Sidewall boundary-layer influence on shock wave/turbulent boundary-layer interactions. *AIAA J.*, **11**(10), 1367–1368.
- Ringuette, M. J., Bookey, P., Wyckham, C., & Smits, A. J. (2009). Experimental study of a Mach 3 compression ramp interaction at  $\text{Re}_\theta = 2400$ . *AIAA J.*, **47**(2), 373–385.

- Rose, W., & Johnson, D. (1975). Turbulence structure in a shock wave boundary layer interaction. *AIAA J.*, **13**(7), 884–889.
- Settles, G., Fitzpatrick, T., & Bogdonoff, S. (1979). Study of attached and separated compression corner flowfields in high Reynolds number supersonic flow. *AIAA J.*, **17**(6), 579–585.
- Settles, G. S., & Dodson, L. J. (1994). Supersonic and hypersonic shock/boundary-layer interaction database. *AIAA J.*, **32**(7), 1377–1383.
- Skews, B. (1997). Aspect ratio effects in wind tunnel studies of shock wave reflection transition. *Shock Waves*, **7**, 373–383.
- Skews, B. (2000). Three-dimensional effects in wind tunnel studies of shock wave reflection. *J. Fluid Mech.*, **407**, 85–104.
- Smith, A., Babinsky, H., Fulker, J. L., & Ashill, P. R. (2004). Shock wave/ boundary-layer interaction control using streamwise slots in transonic flows. *Journal of Aircraft*, **41**(3), 540–546.
- Smits, A. J., & Muck, K. (1987). Experimental study of three shock wave/turbulent boundary layer interactions. *J. Fluid Mech.*, **182**, 291–314.
- Souverein, L. J., Dupont, P., Debive, J.-F., Van Oudheusden, B. W., & Scarano, F. (2010). Effect of interaction strength on unsteadiness in shock-wave-induced separations. *AIAA J.*, **48**(7), 1480–1493.
- Stewartson, K., & Williams, P. (1969). Self induced separation. *Proc. Roy. Soc. A*, **312**, 181–206.
- Thomas, F., Putnam, C., & Chu, H. (1994). On the mechanism of unsteady shock oscillation in shock wave/turbulent boundary layer interactions. *Exp. Fluids*, **18**, 69–81.

- Tieng, S., Chang, K., & Yu, F. (1992). Holographic interferometric investigation of shock wave interaction with a ramp. *Shock Waves*, **2**, 133–138.
- Touber, E., & Sandham, N. D. (2009). Large-eddy simulation of low-frequency unsteadiness in a turbulent shock-induced separation bubble. *Theor. Comp. Fluid Dyn.*, **23**(2), 79–107.
- Ünalmis, Ö., & Dolling, D. (1994). Decay of wall pressure field structure of a Mach 5 adiabatic turbulent boundary layer. In *25th AIAA Fluid Dynamics Conference*. Colorado Springs, CO, 20-23 June 1994.
- Vicharelli, A., & Eaton, J. K. (2006). Turbulence measurements in a transonic two-passage turbine cascade. *Experiments in Fluids*, **40**(6), 897–917.
- Viswanath, P. R., Sankaran, L., Narasimha, R., Prabhu, A., & Sagdeo, P. M. (1983). Injection slot location for boundary-layer control in shock-induced separation. *Journal of Aircraft*, **20**(8), 726–732.
- von Neumann, J. (1943). Oblique reflection of shock waves. Report, Navy Dept. Bureau of Ordnance, Washington DC, USA. Explosive Research Report No. 12.
- Wagner, J. L., Yuceil, K. B., Valdivia, A., Clemens, N. T., & Dolling, D. S. (2009). Experimental investigation of unstart in an inlet/isolator model in mach 5 flow. *AIAA J.*, **47**(6), 1528–1542.
- White, M. E., & Ault, D. A. (1996). Expansion corner effects on hypersonic shock wave/turbulent boundary-layer interactions. *J. Propul. Power*, **12**(6), 1169–1173.
- White, M. E., Lee, R. E., Thompson, M. W., Carpenter, A., & Yanta, W. J. (1991). Tangential mass addition for shock/boundary-layer interaction control in scramjet inlets. *J. Propul. Power*, **7**(6), 1023–1029.

Wu, M., & Martin, M. P. (2008). Analysis of shock motion in shockwave and turbulent boundary layer interaction using direct numerical simulation data. *J. Fluid Mech.*, **594**, 71–83.

Zheltovodov, A., Maksimov, A., Shevchenko, A., Vorontsov, S., & Knight, D. (1994). Experimental study and computational comparison of crossing shock wave-turbulent boundary layer interaction. In *International Conference on Methods of Aerophysical Research*. Novosibirsk, Russia, Aug 1994: Inst. of Theoretical and Applied Mechanics.

Zheltovodov, A., & Yakovlev, V. N. (1986). Stages of development, flowfield structure and turbulence characteristics of compressible separated flows in the vicinity of 2-d obstacles. Tech. rep., ITAM, USSR Academy of Sciences, Siberian Branch, Novosibirsk. Preprint 27-86 (in Russian).